RAYLEIGH WAVE GROUP VELOCITIES
AND
ATTENUATION COEFFICIENTS

A THESIS SUBMITTED FOR THE DEGREE OF

DOCTOR OF PHILOSOPHY

at the

AUSTRALIAN NATIONAL UNIVERSITY

by

JOSEPH M. MILLS, JR.

April 1977

This thesis is dedicated to

CAROL ANN

ANDREW THOMAS

AARON DONALD

and to the memory of

JOHN W. GRAHAM

who introduced me to Geophysics.

STATEMENT

This thesis is a description of a research project undertaken during the period October, 1973 to March, 1977, while I was a full-time student in the Research School of Earth Sciences at the Australian National University.

The research work described in this thesis is entirely my own except as cited in the acknowledgements and in the text. This thesis has never been submitted to another university or similar institution.

Joseph M Mills, Jr.

....

Joseph M. Mills, Jr.

Canberra, A.C.T.
1 April, 1977.

RAYLEIGH WAVE GROUP VELOCITIES AND ATTENUATION COEFFICIENTS

TABLE OF CONTENTS

Page No.

Chapter 6 (contd.)

Page No.

FIGURES

Chapter 2

CHAPTER 3

Chapter 4

Page No.

Chapter 4 (contd.)

Chapter 5

Chapter 6

Page No.

Chapter 6 (contd.)

Chapter 7

Page No.

TABLES

Page No.

TABLES (contd.)

ACKNOWLEDGEMENTS

I am indebted to my supervisor Professor Anton L. Hales, whose insight into geophysical problems and academic politics has never ceased to amaze me. His advice and encouragement has been a continual aid in the completion of this thesis.

Professor Adam Dziewonski of Harvard University introduced me to the methods of analysis of surface waves in his course on seismology at the University of Texas at Dallas. He has contributed greatly to my development with many discussions, suggestions and in his guidance in the development of the Residual Dispersion Measurement.

I also extend my thanks to Dr. Thomas J. Fitch (now at Massachusetts Institute of Technology, Lincoln Laboratory) for suggesting our joint analysis of the Picton earthquake (Chapter 6) in which he is primarily responsible for the determination of the source mechanism solution, aftershock locations and determination of seismograph constants.

The idea of inversion of surface wave dispersion data using a controlled Monte Carlo inversion technique was first suggested to me by Dr. Joseph F. Gettrust (now at the University of Hawaii).

Professor Dziewonski and Drs. R.S. Anderssen and R.L. Parker (University of California at San Diego) enlightened me in the pitfalls and problems of inversion techniques and their application to geophysical data.

Drs. R.S. Anderssen and F.R. de Hoog of the Computer Center and Professor P.A.P. Moran of the Research School of Social Sciences are thanked for their assistance in the formulation of the variance of phase velocities calculated by integration of group velocities (Sec. 4.3.1).

I have benefited greatly from conversations with Professor Mark Landisman while I was a student at the University of Texas at Dallas.

Drs, R.C. Liebermann, J.R. Cleary and J.M.W. Rynn have critically read papers for publication and made many constructive comments to my benefit. Dr. J.M.W. Rynn was most helpful in his critical comments on early drafts of this thesis.

The following individuals allowed me to use their computer programs: Dr Brian Mitchell (stochastic inversion program for Q_β^{-1}); Professor A.M. Dziewonski (multiple filter analysis and free oscillation period calculation programs); Dr. John Goncz (surface wave dispersion calculation program); Dr. David Harkrider (surface wave dispersion and synthetic seismogram programs); Mr. Lee Belbin (global map generation program); Dr. R.L. Parker (line printer contouring program); and Dr. B.R. Julian (ray tracing program).

Mrs. I.J. Weekes, Mrs. L. Hodgson and Mrs. Clementine Krayshek have drafted some of the figures which are included in this thesis. The operations and programming staff at the Computer Center have been of enormous aid throughout the course of the research described in this thesis.

My special thanks is also extended to the faculties and to my fellow students at both the University of Texas at Dallas and at R.S.E.S. who have contributed to my knowledge of the earth sciences.

EARLIER PUBLICATIONS

Dziewonski, A.M., Mills, J.M. Jr. and Bloch, S., 1972. Residual dispersion measurement - a new method of surface-wave analysis. Bull. Seis. Soc. Am., 62, 129-139.

PUBLICATIONS DURING THE COURSE OF THIS WORK

Mills, J.M. Jr. and Fitch, T.J., 1977. Thrust faulting and crust-upper mantle structure in east Australia. Geophys. J. Roy. Astr. Soc. (Accepted for publication.)

Mills, J.M. Jr. and Hales, A.L., 1977. Great circle Rayleigh wave attenuation and group velocity, Part I: Observations for periods between 150 and 600 seconds for 7 great circle paths. Phys. Earth Planet. Int. (Accepted for publication.)

Mills, J.M. Jr. and Hales, A.L., 1977. Great circle Rayleigh wave attenuation and group velocity, Part II: Observations for periods between 50 and 200 seconds for 9 great circle paths and global averages for periods between 50 and 600 seconds. Submitted to Phys. Earth Planet. Int.

ABSTRACT

The analysis of group velocities and attenuation coefficients for Rayleigh Waves in the period range 50 to 600 seconds provides information on the average elastic and anelastic properties of the earth at upper mantle depths. The Direct Filtering Method has been developed for this analysis and provides objective estimates of group arrival times, their standard errors and spectral amplitudes from Gaussian filtered seismograms. Estimates of the period at the envelope maximum are also made to estimate the purity of the filtered signal at the group arrival time.

The Direct Filtering Method has been applied to seismograms of 4 Kurile Islands earthquakes ranging in magnitude from 6.6 to 8.3. These events are located within a small region so that Rayleigh waves from all events traverse the same great circle paths. Great circle group velocities for the period range 100 to 600 seconds have been determined for the magnitude 8.3 event by averaging of group velocities of Rayleigh phases arriving after R_3. Attenuation coefficients for periods between 100 and 450 seconds have been determined from spectral amplitudes determined (1) from the rate of decay of envleope maxima of Gaussian filtered Rayleigh phases and (2) from the rate of decay of spectral amplitudes taken as the sum of the products of a pure sine wave with segments of each Rayleigh phase within a group velocity window. Both methods provide similar estimates of attenuation coefficients.

Group velocities and spectral amplitudes determined for 3 other Kurile Islands earthquakes have extended the range of accurate measurements to periods as short as 50 seconds. These measurements taken with those for the larger event provide averages for group velocities and attenuation coefficients for 9 great circle paths which are evenly distributed in azimuth at the source region. Averaging of path group velocities and

attenuation coefficients over all paths provides a reliable estimate of global average group velocities for periods between 50 and 600 seconds and attenuation coefficients for periods between 50 and 450 seconds. Global average phase velocities have been calculated by integrating global average gorup velocities. Global average group velocities and equivalent spheroidal oscillation periods derived from the global average phase velocities are in poor agreement with those calculated for most recent earth models, including QM2, of Hart et al. (1977b). In future inversions of data sets for average earth models equivalent free oscillation periods on surface wave phase or group velocities in the period range 50 to 150 seconds are necessary since body wave travel times together with free oscillation data for periods in excess of 140 seconds do not adequately constrain upper mantle structure of such models.

Upper mantle shear velocities and Q_β^{-1} have been determined from global average group velocities and attenuation coefficients for periods between 50 and 300 seconds. Shear velocity models determined from global average group velocities alone show that the average thickness of the lithosphere cannot be determined with precision. Global average models for shear wave specific attenuation (Q_β^{-1}) indicate that a zone of high attenuation is coincident with the low velocity zones beginning at depths ranging from 70 to 100 km. Average Q_β for the lithosphere, low-velocity zone and sub-low velocity layer (asthenosphere) are approximately 200, 85 to 110 and 170 to 200 respectively.

Pure Path averages for group velocities and specific attenuation have been calculated from individual observations and from path averages for 2 regionalizations, one original to this study and the other devised by Wu (1972). Both are based on 4 upper mantle provinces: ocean basins, continent, island arc and mid-ocean ridge. Pure path group velocities and specific attenuation have also been calculated for combinations of regions and provide well separated regional measurements for such composite regions.

Shear velocity models for pure and combined regions indicate that a low velocity zone is required beneath the oceans, but is not required beneath continents. A regional study of group velocity dispersion thrust faulting in eastern Australia shows that a low velocity zone is required at depths greater than 140 and probably greater than 180 km in order to fit observed fundamental and higher mode Love and Rayleigh wave group velocities and ScS travel times.

Q^{-1}_R determined from path average group velocities and attenuation coefficients has been regionalized successfully for 2 and 3 region combinations. The resulting pure path Q^{-1}_R for continents is much lower than that for ocean basins and ocean-ridge provinces. Inversion of Q^{-1}_R for ocean-ridge provinces shows that the average Q_β for the upper 200 km of these regions is between 85 and 100.

CHAPTER 1

INTRODUCTION

Since 1912 when Alfred Wegener (1929) proposed the theory of continental drift, our knowledge of the dynamics of continental and oceanic plates and the internal structure of the earth has increased manyfold. Our understanding of the nature of the ocean floor and its relation to the motion of the lithospheric plates was greatly advanced during the 1960's and early 1970's by Hess (1962), Vine and Matthews (1963), Wilson (1965), McKenzie and Parker (1967), Morgan (1968), Le Pichon (1968) and others.

The observation and modelling of seismic wave travel times and amplitudes provide direct evidence on the state of material in regions of the earth's interior which are not otherwise readily available to our investigation. Of the body phases, neither compressional (P) or shear (S) waves will bottom in a pronounced low velocity zone. The additional property, that body phases do not average laterally over large portions of the earth's mantle, makes them less suitable than surface waves for studies of the average regional properties of the earth's upper mantle. The study of the graver free oscillation modes leads to problems in the opposite sense, namely that of averaging over extensive portions of the earth's interior. Thus, the most suitable method for the investigation of the average regional elastic and anelastic properties of the earth at upper mantle depths is the study of the dispersion and attenuation of long period surface waves.

Adequate methods of filtering and modelling of surface wave trains have been possible only since the advent of digital computers. However, even without the aid of computer modelling, Press, in 1959, realized that a low velocity zone must be present in the upper mantle of the Pacific Ocean and beneath continental paths passing through the Bering Sea to Pasadena, the inference being based on S-wave travel times from explosions and on G wave group velocities. Toksoz and Anderson (1966) demonstrated that the upper mantle structure is laterally heterogenous. Shear velocity models derived from pure path phase velocities (Toksoz, et al. 1967) indicated that a pronounced low velocity zone exists beneath the oceans and tectonic regions. This was the first indication that mantle shear velocities beneath continents, oceans and tectonic regions were genuinely different.

The motion of the oceanic lithosphere, whether by mantle convection (Ringwood and Green 1966, Ringwood 1969, McKenzie 1969b) or by gravity sliding (Hales 1969) requires flow in some region of mantle and probably, therefore, zones of low viscosity. These low viscosity regions are generally thought to coincide with regions of high seismic wave attenuation and low shear velocity (Anderson 1966). Recent studies show that the shear wave low velocity zone is present beneath the oceans beginning at depths of 30 to 90 km, depending on the age of the oceanic lithosphere (Forsyth 1977), and beneath the continents at depths of 100 km or more (Knopoff 1972). Such low velocity / high attenuation zones are thought to be caused by partial melting of mantle material (Walsh 1968) from which basaltic magmas are formed by processes of partial fusion and fractional crystallization (Green and Ringwood 1967). Whether low viscosity is restricted to zones of high attenuation has, however, been questioned recently by O'Connell (1977).

Studies of attenuation of surface waves have only recently begun to provide information on attenuation in the crust and upper mantle. Kanamori's (1970a) estimates of attenuation for great circle Rayleigh and Love waves pioneered the study of attenuation in the upper mantle. More recent studies have provided information on attenuation for surface waves which sample the crust and the uppermost mantle but do not sample to depths great enough to augment Kanamori's (1970a) data.

It is thus the intention of this study to provide global average and regional estimates of attenuation for Rayleigh waves which traverse the crust and upper mantle.

Sec. 1.1 SURFACE WAVE INVESTIGATIONS OF THE ANELASTICITY OF THE UPPER MANTLE.

Surface waves which sample the crust and upper mantle to depths of several hundred kilometers provide information on anelasticity not available through body wave studies, since measurements of body wave attenuation require pure phases (Kanamori 1967). S-wave arrivals which sample the low velocity zone appear as late arrivals and do not bottom in the low velocity zone. Consequently measurements of attenuation in this zone are at best difficult.

As early as 1958, Satô calculated attenuation from G wave spectral amplitudes. For each spectral component, the amplitude of a surface wave decays as exp $(-\pi\Delta Q^{-1}/TU)$, where T is the period, Δ the epicentral distance, U the group velocity and Q^{-1} the specific attenuation. Since Q^{-1} is defined as the ratio of energy lost per cycle to energy stored in the wave, Q^{-1} is a direct measure of anelasticity. At least two measurements of the amplitude of a surface wave along its path of propagation, as well as a measurement of the group velocity for that segment of the path between the stations, are needed to compute Q^{-1} for the path. This measurement of the specific attenuation is an average of Q^{-1}_{β} for Love waves and Q^{-1}_{α} and Q^{-1}_{β} for Rayleigh waves weighted by the surface wave amplitudes as a function of depth. Q^{-1} can be measured from seismograms recorded at two or more stations along a great circle path or from a single seismogram which contains multiple passages of a surface wave phase which travels two or more full circuits of the earth.

The precision of Q^{-1} measurements is dependent upon the precision of both group velocity and spectral amplitude measurements. For accurate determination of Q^{-1}, paths must be long enough to provide decrements in amplitude over the path length which are large enough for accurate calculation of the amplitude ratio and yet short enough so that amplitudes of the phase recorded at the second station are relatively uncontaminated by noise. For a path with a Q of 200 measured at a period of 300 seconds, a 10 per cent decrement in amplitude requires a path length of 7500 km, a 25 per cent decrement, a path length of 20500 km, and a 50 per cent decrement a path length of 49500 km. Pure paths of such lengths are difficult to find either between standard seismic stations or between seismic zones in which large earthquakes occur and standard stations. At a period of 50 seconds and a Q of 100 these path lengths cause decrements of 70, 96.3 and 99.97 per cent, respectively. For one full circuit of the earth the decrement in amplitude at 50 seconds for a Q of 100 is 99.84 per cent. Since the amount of energy arriving per unit of time generated by a large earthquake on the average decreases with time, so also the noise level (i.e. other modes excited by the earthquake) decreases with time. For this reason measurement of heavily attenuated surface waves is still possible even after attenuation by factors as great as two hundred.

Since Satô's (1958) early investigation of the attenuation of G waves, a number of advances have been made in both the determination of group and phase velocity as well as spectral amplitudes (e.g. Alexander 1963, Pilant and Knopoff 1964, Ben-Menahem 1965, Landisman _et al_. 1969, Dziewonski and Hales 1972, Forsyth 1975a). These techniques have provided methods for accurate measurements of surface wave velocities and have been applied to paths over many portions of the earth's surface. A summary of velocity observations and crust-upper mantle shear velocities measured prior to 1972 has been compiled by Knopoff (1972). Since that time important contributions have been made in the determination of shear velocities and the thickness of the lithosphere in the oceans (Forsyth 1975b, Kausel _et al_. 1974, Leeds _et al_. 1974, Yoshii 1975). Additional observations extending to periods of as great as a few hundreds of seconds have also increased our knowledge of the crust and upper mantle structure beneath the continents (Gupta _et al_. 1977 - southern Asia, Knopoff and Fouda 1975 -

Arabia, Goncz 1974 - Australia, Sherburne 1975 - South America, Biswas and Knopoff 1974 - North America). These observations complement observations of great circle phase and group velocities made by Kanamori (1970a), Dziewonski (1971a) and Wu (1972) which have produced pure path velocities at periods between 160 and 360 seconds for 3 or 4 different kinds of regions that can be described as _either_ shield, ocean, tectonic _or_ continent, deep ocean basin, arc, and ridge. The major difference between these regionalizations is a matter of interpretation: Kanamori (1970a) and Dziewonski (1971a) based their tectonic regionalization on Umbgrove's (1947) global classification of Cenozoic folding belts, whereas Wu's (1972) classification is based on global tectonic regimes.

The study of the average anelastic properties of the earth has not progressed as quickly as the study of the elastic properties. A summary of Q^{-1} observations measured prior to 1972 has been compiled by Smith (1972). Since 1972 measurements of attenuation have been made in North America by Solomon (1972) and Mitchell (1973b, 1975a, 1975b) for periods as great as 80 seconds. Similar measurements have also been made to 110 seconds for Pacific Ocean paths by Mitchell _et al_. (1975) and have been inverted by Mitchell (1977). Other measurements of Q^{-1} for Rayleigh waves have been made and inverted by Burton (1974, 1977) and appear to represent an average Q^{-1} for mixed oceanic and continental paths, many of which cross the Eurasian continent. Q^{-1} observations from fundamental and higher mode torsional and spheroidal oscillation modes for periods between 100 and 600 seconds have also been reported by Roult (1974, 1975) and Jobert and Roult (1976). These measurements employ many of the techniques used in long period surface wave analyses developed by Pilant and Knopoff (1964) and Cara (1973) and are comparable to Q^{-1} determined from long period surface waves.

The importance of accurate long period measurements of Q^{-1} has only recently been recognized (Randall 1976, Liu _et al_. 1976) although

Jeffreys (1965, 1967) had made the point that the anelasticity of the mantle would cause shifts in free oscillation periods which could lead to errors in earth modelling. Anderson and Archambeau (1964) and Anderson _et al_. (1965) presented a method for calculating observed free oscillation and surface wave Q^{-1} from a Q_{α}^{-1} and Q_{β}^{-1} model. Liu _et al_. (1976) have formulated corrections for free oscillation periods and surface wave phase velocity measurements caused by anelasticity. Recently these corrections have been incorporated into average earth models derived from free oscillation periods and body wave travel times (Hart _et al_. 1977a, 1977b). However, little high quality average earth or regional Q^{-1} data exist for surface wave or free oscillation periods which sample the upper mantle - the region in earth models most affected by attenuative dispersion. Such a set of data for Rayleigh waves is provided in this thesis.

Sec. 1.2 SCOPE OF THIS THESIS

A new method of analysis for the determination of surface wave group velocities and spectral amplitudes has been developed (Chapter 2) which provides objective estimates of error in group velocity measurements. These methods have been applied to 4 Kurile Islands earthquakes of surface wave magnitude 6.6 to 8.3 (Chapters 3 and 4). Analysis of the largest event yields group velocities for periods between 150 and 600 seconds and attenuation coefficients between 150 and 450 second periods for 7 great circle paths. Analysis of the smaller 3 events extend the range of each of these types of measurements to periods as short as 50 seconds for each of the 7 paths and for 2 additional paths. Global average group velocities are slow compared with all recent earth models for periods between 70 and 200 seconds. Phase velocities and equivalent free oscillation periods are calculated by integrating global average group velocities. Average earth models generated by controlled Monte Carlo inversion (Chapter 5) of global average group velocities corrected for anelastic dispersion show that average lithospheric thicknesses of 70 km and 100 km are both possible Models for Q_β^{-1} indicate that the mean Q_β of the lithosphere is about 200 while a high attenuation zone at depths of 100 to 200 km with a Q_β between 85 and 110 produces satisfactory models for observed attenuation for periods between 50 and 300 seconds. Q_β for the mantle beneath 400 km exceeds 180.

Regional models for shear velocity have been derived by controlled Monte Carlo inversion of pure path group velocities corrected for anelastic dispersion (Chapter 7). Pure path oceanic group velocities require a low velocity zone beginning at depths of 70 or 100 km. Pure path continental group velocities do not require the presence of a low velocity zone. A regional study of group velocity dispersion and thrust faulting in eastern Australia (Chapter 6), however, shows that a low velocity zone is required at depths of greater than 140 km and probably greater than

180 km in order to fit both ScS travel times and observed fundamental and higher mode group velocities for both Love and Rayleigh waves. Surface wave group velocities, alone, do not require the presence of a pronounced low velocity zone with a high velocity lid but preclude its presence at depths shallower than 140 km. Pure path attenuation models have been produced for both continental and oceanic upper mantle structures (Chapter 7).

A summary of the results of this study appears in Chapter 8.

CHAPTER 2

DETERMINATION OF GROUP VELOCITY AND SPECTRAL AMPLITUDE BY NARROW-BAND FILTERING

Sec. 2.1 INTRODUCTION

Group velocity dispersion of surface waves is a measure of the average elastic properties of the earth. The rate of decay of amplitudes of surface waves is a measure of the average anelastic properties of the earth and is commonly expressed as the attenuation coefficient γ or the specific attenuation Q^{-1}. For two stations on the same great circle as the source

$$\gamma = \frac{1}{\Delta} \ln\left(\frac{A_1}{A_2}\right) ,$$

$$Q^{-1} = \frac{TU}{\pi\Delta} \ln\left(\frac{A_1}{A_2}\right) = \frac{TU\gamma}{\pi} \qquad (2.1)$$

where Δ is the station separation in kilometers, U the interstation group velocity, A_1 the spectral amplitude measured at the station closest to the source and A_2 the spectral amplitude measured at the station most distant from the source. Therefore the measurement of both group velocity and amplitude decrement along a path are necessary for the determination of the specific attenuation, Q^{-1}. The method of band-pass filtering (Alexander 1963) has been used to determine both group arrival time and spectral amplitude. In later chapters the techniques developed here will be applied to multiple passage Rayleigh phases (R_1, R_3, R_5, etc. or R_2, R_4, R_6 etc.) to produce estimates of group velocity and attenuation for periods between 50 and 600 seconds. These measurements will, in turn, be used to derive the regional and global average shear velocity and variation of Q_R^{-1}, the specific attenuation for Rayleigh waves, as a function of depth.

Sec. 2.2 GAUSSIAN FILTERS AND THE DETERMINATION OF GROUP ARRIVAL TIMES AND SPECTRAL AMPLITUDES

Several refinements to the technique introduced by Alexander (1963) have recently been made by Pilant and Knopoff (1964) - Time Variable Filtration, Dziewonski et al. (1969) - Multiple Filter Technique and, Levshin et al. (1972) - Frequency Time Analysis. The more recent of these techniques use Gaussian filters of the form

$$F(\omega,\omega_o) = \exp\left(-\alpha\left(\frac{\omega-\omega_o}{\omega_o}\right)^2\right) \tag{2.2}$$

in the frequency domain, and

$$f(t,\omega_o) = \frac{\sqrt{\pi}\,\omega_o}{2\alpha}\cos(\omega_o t)\exp\left(-\left(\frac{\omega_o t}{2\sqrt{\alpha}}\right)^2\right) \tag{2.3}$$

in the time domain (Dziewonski et al. 1969). Gaussian filters allow optimal frequency and time resolution to be achieved (Papoulis 1962) in the sense that

$$D_t D_\omega = \sqrt{\pi/2} \tag{2.4}$$

where D_t and D_ω are the time and frequency duration of the filter:

$$D_t^2 = \int_{-\infty}^{\infty} t^2 |f(t,\omega_0)|^2 dt$$

and (2.5)

$$D_\omega^2 = \int_{-\infty}^{\infty} \omega^2 |F(\omega,\omega_0)|^2 d\omega ,$$

For other types of non-band-limited filters, D_tD_ω is always greater than $\sqrt{\pi}/2$. Other filters thus provide poorer frequency-time resolution than the Gaussain filter. In practice such filters are always truncated and, hence, band-limited. As Dziewonski et al. (1969) pointed out

> "The highest possible energy concentration of the impulse response corresponding to a band-limited filter is achieved when the filter is a truncated prolate spheroidal wave function of zero order (see also Papoulis, 1962, sec 4-5). If, however, the Gaussian function is truncated at a value of the order of 30 db down from the maximum, the energy concentration of its impulse response is only 0.1 per cent lower than that of the corresponding prolate spheroidal wave function."

More recently, several authors have discussed the optimization of filter resolution in terms of the determination of the value of the filter parameter (α in the case of the Gaussian filter described in Equation 2.2 and 2.3) which produces the sharpest filter which "rings" least (Inston et al. 1971, Cara 1973, Denny and Chin 1976, Canitez 1977). The effect of choosing a filter parameter which is not optimal results in the loss of resolution in the time domain. The choice of such an optimal value of the filter parameter is dependent upon the dispersive character of the signal being analyzed. Errors in estimation of group velocity are systematic when group velocity changes rapidly with frequency (Dziewonski et al. 1972).

An alternative method for minimizing error in group velocity estimation is the Residual Dispersion Measurement of Dziewonski et al. (1972). This technique requires cross-correlation of a synthetic seismogram, which approximates the dispersion of the signal to be analyzed within a few percent, with the original seismogram. The analysis of the resulting cross-correlogram gives the differences in dispersion between the two signals. The rate of change of group velocity with frequency in the cross-correlogram should be very small compared to the original seismogram and errors in estimation of the group velocity difference (residual dispersion) are consequently much smaller. If the residual dispersion is large, then a new synthetic should be produced and the process repeated.

Dziewonski et al. (1972) noted that the maximum amplitude of a Gaussian filtered seismogram does not, in general, coincide with the group arrival time. The errors in determination of the group arrival time caused by Gaussian filtering depend on second and higher order derivatives (with respect to frequency) of the amplitude spectrum and wave number of the seismic signal. Second and third order derivatives of the wave number are related to the slope and curvature of the group velocity dispersion curve. However, errors of this kind can be suppressed by increasing the frequency resolution and sacrificing time resolution. This, of course, also sacrifices precision in the group velocity measurement. With this approach, a narrower band estimate of the spectral amplitude is obtained which is more suitable for spectral amplitude estimation.

It was clear from the analysis carried out at the time that the "residual dispersion" paper (Dziewonski et al. 1972) was written, that errors in the determination of group velocity by any of the multiple filter methods (e.g. Dziewonski et al. 1969, Levshin et al. 1972) tended to be large when the amplitude of the seismic signal varied rapidly with frequency so that the change in amplitude between successive center frequencies was large. In such cases the frequencies at which amplitudes are large leak through into adjacent low amplitude frequencies (see Figure 2.1) unless the filter parameter α is sufficiently large. The use of sufficiently large α's avoids errors in both group velocity and spectral amplitude estimation at the expense of time (group velocity) resolution.

The approach adopted in this thesis is to use filters with large α and verify directly that the difference between the frequency at the

<u>Figure 2.1</u> PURITY OF FILTERED RAYLEIGH PHASES -

R_4 recorded at HNR has been filtered with a Gaussian filter of the form shown in Equation 2.3 with 4 different values of the filter parameter α. Each filtered trace is shown starting at 1027 GMT on 13 October 1963 with relative amplitudes of each peak in each trace shown in large numbers and effective periods (in seconds) measured from adjacent zero crossings shown in small numbers beneath each zero crossing. Note that peak amplitudes of R_4 filtered with $\alpha = 20$ and 40 occur at periods considerably different from the center period of the filter (340 seconds). Amplitudes of peaks adjacent to the maximum decay more slowly as large values of α are used for filtering.

R_4 Phase Filtered at 340 s

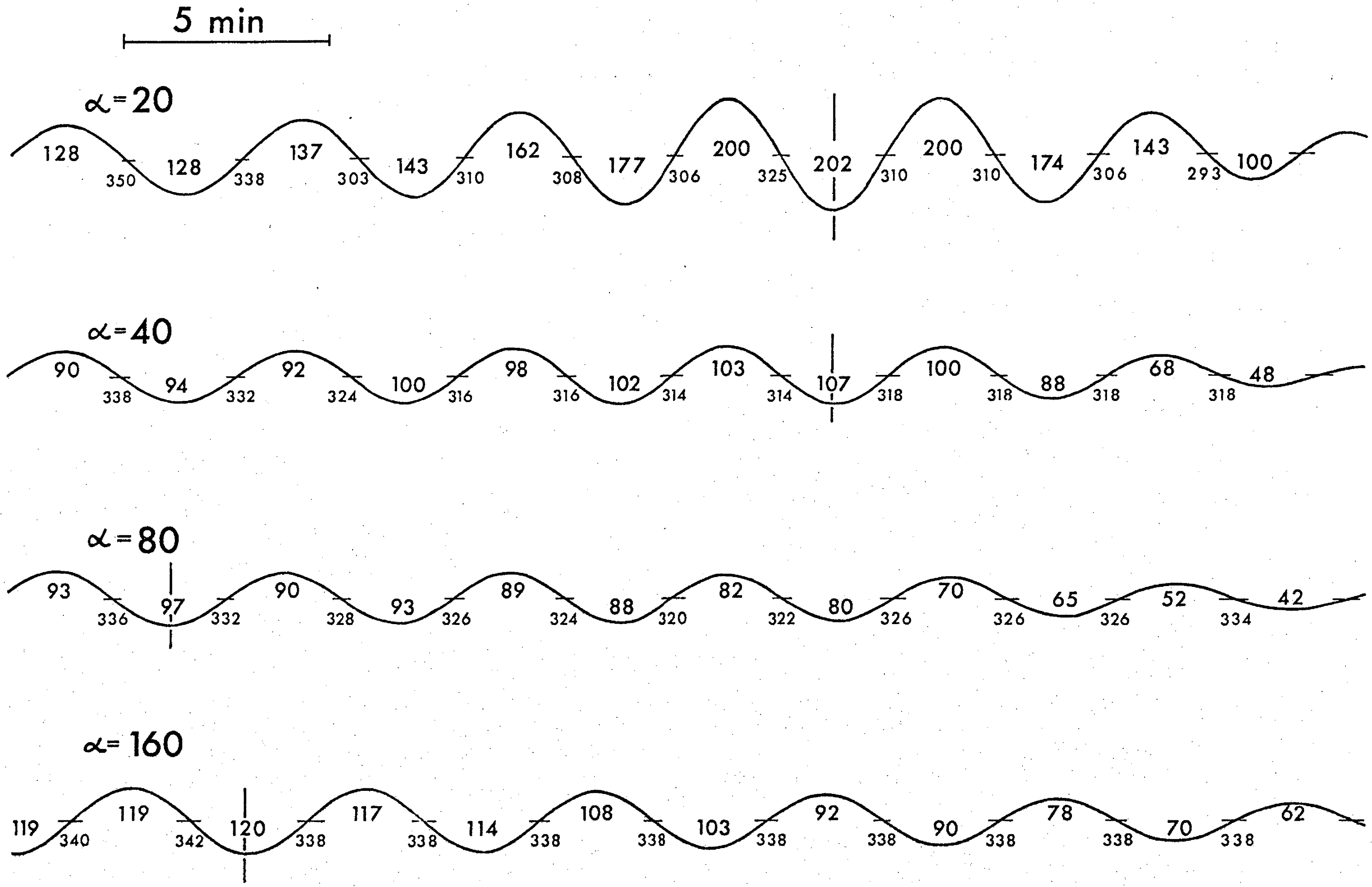

maximum of the envelope of the filtered signal and the center frequency of the filter is much less than the separation between center frequencies. Since almost all paths used in this study (with the exception of the Picton earthquake discussed in Chapter 6) were of lengths greater than 10,000 km, the loss of time resolution was not serious and was more than offset by the gain in purity of the spectral amplitudes.

It is probable that a "residual dispersion/residual amplitude analysis" using a synthetic seismogram with an amplitude function of spectral content which is the inverse of the amplitude spectrum of the seismic signal to be analysed would produce a cross-correlogram with minimal variation with frequency. This would, in effect, be an inverse filter technique and should eliminate error in measured dispersion due to variation of the signal's amplitude with frequency as well as dispersion. In addition, this technique should, with the inclusion of source phase shift in the synthetic, allow the direct, accurate and simultaneous determinations of phase velocity, group velocity and spectral amplitude. Such cross-correlograms can also be stacked without weighting since each cross-correlogram will be of unit amplitude. Path averages can be calculated from a number single station observations, if cross-correlograms for all seismograms recorded on a path are "equalized" to the same effective epicentral distance.

Sec. 2.3 THE DIRECT FILTERING METHOD AND THE ANALYSIS OF LONG PERIOD SEISMIC DATA

Sec. 2.3.1 Computers

The routine processing and analysis programs used in this thesis were developed for use on a small computer. Most were used on one of two computers: a Datacraft 6024/4 with 32k (1k = 1024 words) of 750 nanosecond 24 bit core memory and a Scientific Arithmetic Unit (floating point arithmetic hardware unit), or a Univac 1108 with 256k of 750 nanosecond 36 bit words (eventually upgraded to a Univac 1100/42 dual arithmetic processor system). In general it was found that both the 6024/4 and 1108 computers ran programs at comparable speeds, and that only programs for calculating phase or group velocity partial derivatives were required to be run in double precision on the 1108-1100/42 system. Approximately equal amounts of time were used on both computers due to heavy usage of the 6024/4 and availability of the 1108-1100/42 systems.

Sec. 2.3.2 Data, Digitization, Decimation and Detrending

All seismograms processed in this study were recorded by the World Wide Standard Seismograph Network (WWSSN) or the High-Gain, Long-Period Network (HGLP). Other data used in the focal mechanism determination for the Picton earthquake of 9 March 1973 are listed in Chapter 6.

WWSSN long-period seismograms used for surface wave group velocity determination were digitized using a DMAC digitizer at the Commonwealth Scientific and Industrial Research Organization, Division of Computing Research, Canberra, and later at the Division of Land Use Research, Canberra. These seismograms were sampled at a variable rate depending upon the complexity of the seismic trace, and interpolated to a constant sample interval of 1 sample per second. Only the seismograms of the 13 October 1963 Kurile Islands earthquake ($M_s = 8.3$) were low pass filtered and decimated to 1 sample per 4 seconds. All records were processed to remove linear trend and the mean.

Sec. 2.3.3 Filtering

Since almost all of the programs used in this study were designed to be run on a small computer the most direct (although sometimes somewhat pedestrian) methods were employed which would require only a modest amount of memory. For this reason filtering was performed in the time domain using the filter described by Equation 2.3 truncated at 30 db amplitude level of the envelope. Values of the filter parameter, α, were determined in accordance with the philosophy described in Section 2.2 (see Figure 2.1). Values of 40, 80, and 160 were found to produce adequately pure spectral amplitudes for the period ranges 5 to 80, 60 to 200 and 100 to 600 seconds respectively. Center-frequencies, ω_o, were chosen at 5 second intervals in period for periods shorter than 100 seconds, at 10 second intervals for periods between 100 and 200 seconds, and at 20 second intervals for periods greater than 200 seconds. This ensured that any particular frequency is passed by two or three filtrations since filters have half amplitude filter widths of approximately two to four times the interval between adjacent center periods for filtration. Redundancy in the group velocities and spectral amplitude estimates was thus achieved.

Early versions of the filtering program were designed as a single program, however, in later versions the functions of the Direct Filtering Method program were combined with the filtering program so that only selected group velocity windows in the time series were filtered. All Rayleigh phases from one seismogram were filtered at one time with repeated runs for different frequencies or series of frequencies.

Sec. 2.3.4 The Direct Filtering Method

For the determination of group velocities, the Direct Filtering Method (Figure 2.2) locates maxima in the envelope of a filtered seismogram by locating successive maxima and minima within a specified group velocity window. Estimates of group arrival time are made by least-squares fitting a parabola to a specified number of maxima and minima about each rectified envelope maximum. Usually between 5 and 11 points are used in the least squares fit. Standard errors of group arrival times are calculated from (1) regression statistics for each parabola and (2) the half-amplitude width of each envelope maximum (also calculated from the equation of the parabola within each group velocity window. Group travel times are calculated as the difference between the United States Coast and Geodetic Service (USCGS) origin time and the group arrival time corrected for instrumental group delay by Hagiwara's 1958) formulae. For this correction theoretical values for constants for the WWSSN long period seismograph system were assumed.

Results of analyses for each envelope maximum are displayed in line printer output as shown in Figure 2.3. Part 1 of the output displays the residuals of the parabola fit, group arrival time estimate, standard error estimates, coefficients of the parabola and their standard errors, the resulting group velocity estimate, corrected for instrumental group delays, and the two standard error estimates (from regression statistics and envelope maximum half-width). Part 2 is a graphical display of rectified maxima (+) and minima (-) about the maxima of the envelope of the filtered seismogram. Part 3 is a graph of the effective period at each maximum or minimum, calculated as twice the time interval between the two zero crossings adjacent to the maximum or minimum. After all envelope maxima within the specified group velocity window for each phase are displayed, a summary table (Figure 2.4) of phase index, group arrival time and

Figure 2.2 DIRECT FILTERING METHOD -

The flow diagram describes the processes involved in the Direct Filtering Method for determining group arrival times and group velocities.

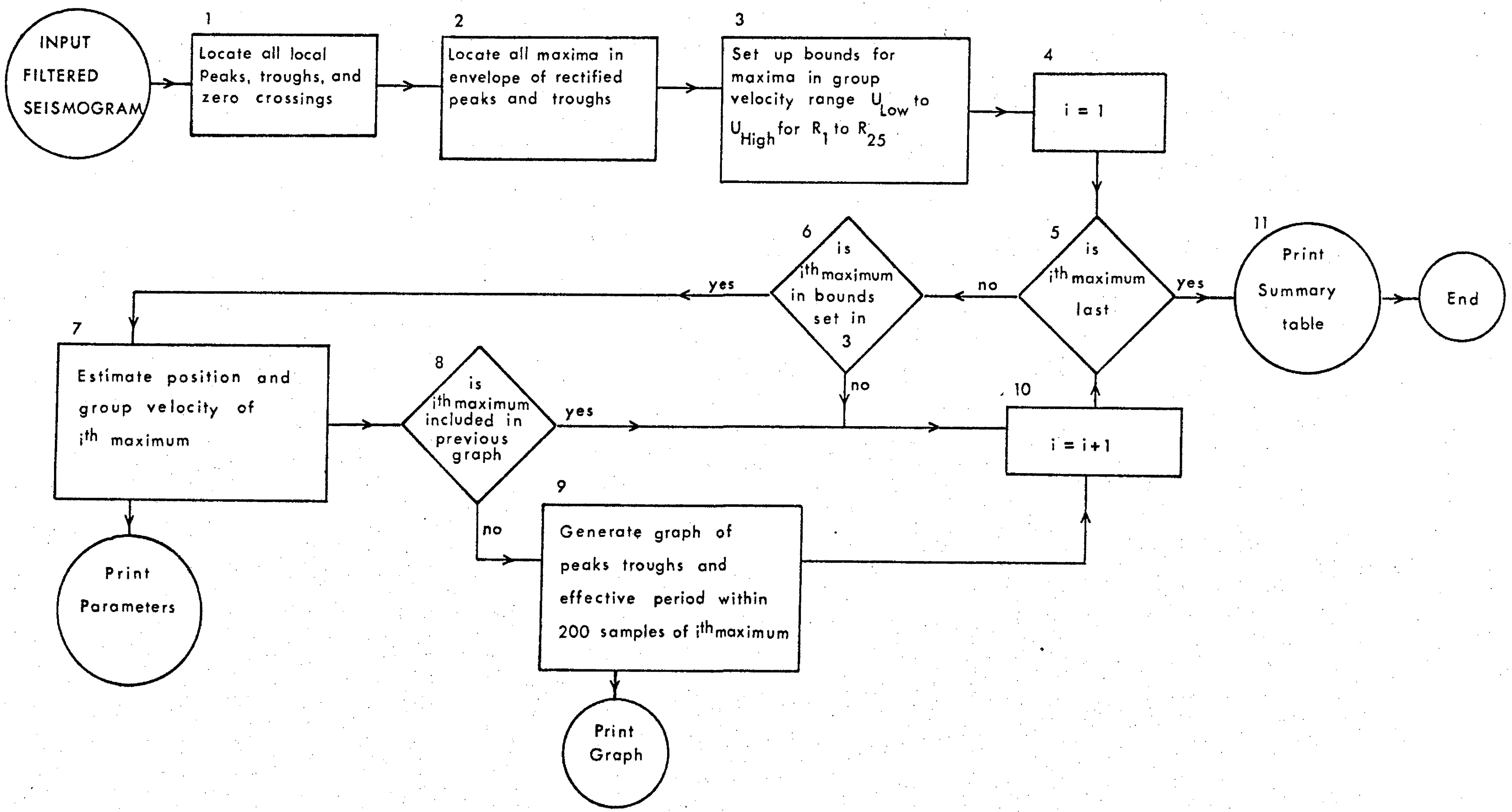
INPUT FILTERED SEISMOGRAM
1
Locate all local Peaks, troughs, and zero crossings
2
Locate all maxima in envelope of rectified peaks and troughs
3
Set up bounds for maxima in group velocity range U_{Low} to U_{High} for R_1 to R_{25}
4
i = 1
5
is i^{th} maximum last
yes
11
Print Summary table
End
no
6
is i^{th} maximum in bounds set in 3
yes
no
7
Estimate position and group velocity of i^{th} maximum
Print Parameters
8
is i^{th} maximum included in previous graph
yes
no
9
Generate graph of peaks troughs and effective period within 200 samples of i^{th} maximum
Print Graph
10
i = i+1

Figure 2.3 DIRECT FILTERING METHOD DISPLAY OF ENVELOPE MAXIMUM -

(1) Least squares parabola residuals and fit to the envelope maximum are shown with the position of the maximum (XMAX) and two estimates of the standard error of the maximum, coefficients of the parabola and their standard errors (C), maximum of the envelope estimated from the parabola (YMAX) and from the largest peak (ACTUAL MAX). Estimates of group velocity and its standard errors calculated from the two estimates of standard error of the position of the maximum,

(2) The envelope maximum is plotted with "+" and "-" indicating the position (sample number) and height of each rectified maximum or minimum.

(3) The effective period is plotted corresponding to twice the interval between zero crossings adjacent to each maximum or minimum.

DIRECT FILTERING METHOD DISPLAY OF ENVELOPE MAXIMUM

1

```
   RES   =      .01693368 CALC Y=     9.36138320 X=  9277. Y= 9.3783169
   RES   =     -.04692340 CALC Y=    10.29066479 X=  9318. Y=**********
   RES   =      .03921366 CALC Y=    10.68670106 X=  9359. Y=10.7259147
   RES   =     -.00548363 CALC Y=    10.54949236 X=  9400. Y=**********
   RES   =     -.00374043 CALC Y=     9.85602415 X=  9442. Y= 9.8522837
    DXMAX(PEAK UNCERTAINTY) =        23.038      DMAX(1/2 WIDTH)=    183.680
 XMAX = 9369. D(XMAX) =    23.04 / 183.68    C=-.158609531-03 .707353996-05 .347365288-02 .346906898-03 .106833861+02 .313554015-01
      YMAX = 10.702405       ACTUAL MAX =10.725915
          U(XMAX) =      3.7809 +/-    .0105 /   .0834          U(XZ(IMX)) =     3.78547
PLOT NO.   5
          PLOT OF MAXIMUM AT (   9359.,   10.72591) PER =     82
```

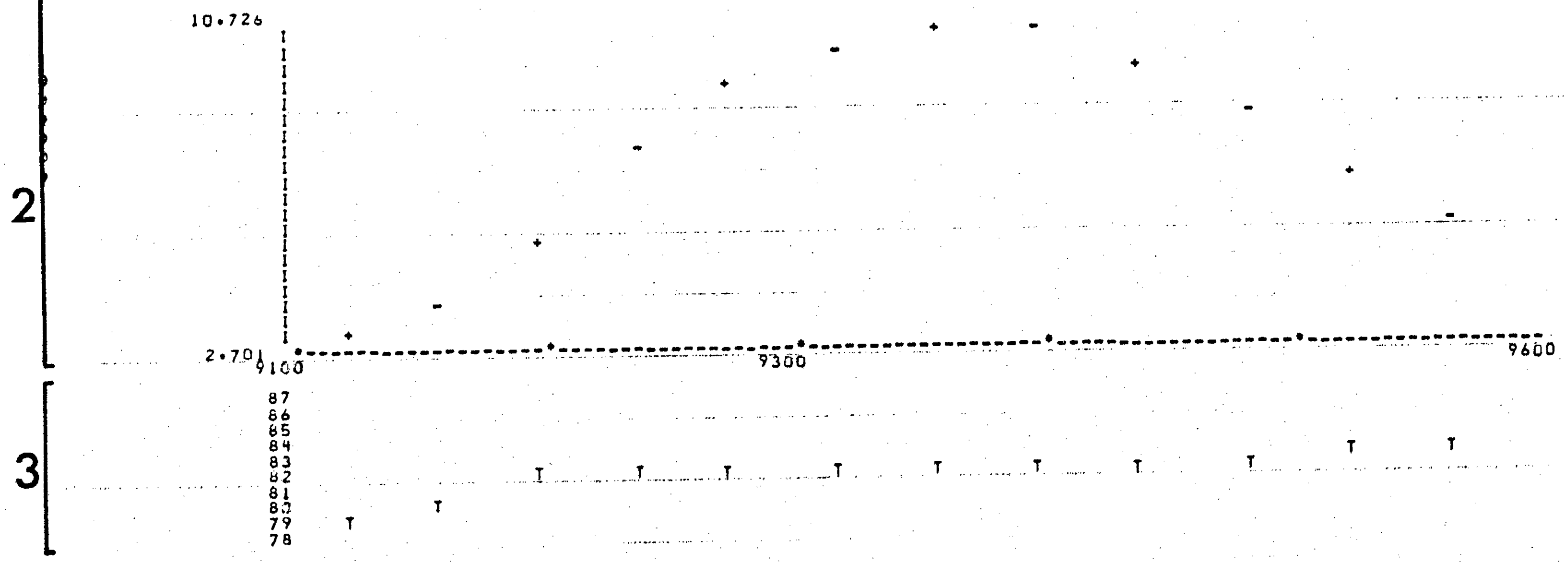

Figure 2.4 DIRECT FILTERING METHOD SUMMARY TABLE - A label, period of filter, number of samples in the record (N), number of points used in the Gaussian filter (NFILT), filter parameter (ALPHA), origin time to beginning of record time difference, instrumental group delay calculated for the period of the filter, filter half width and group velocity window and number of maxima processed are listed at the top of the table. The 9 columns in the table contain the surface wave phase index, estimated sample number of the envelope maximum, the estimate of standard errors calculated from the least-squares fitted parabola coefficients and half-amplitude width. Amplitude of the envelope maximum, effective period at the maximum, the group velocity of the maximum and estimated standard errors of the group velocity calculated from the two standard error estimates of the group arrival time of the maximum.

DIRECT FILTERING METHOD SUMMARY TABLE

```
ALQ 13V175 MS=6.6 17:58:13.1 BGRT=-599.7        VRTCL  PER = 80.00 CONVL
   N =23287     NFILT =          847      ALPHA =  80.00000
ORIGIN TIME TO BEGIN OF RECORD TIME =         -599.70INSTRUMENTAL GROUP DELAY =   19.9401
 HALF FILTER WIDTH =  424
 NUMBER OF POINTS TO ADD = -1043
           3.0000 < U <  5.0000

   31 MAXIMA PLOTTED
1          3380.29       7.74     178.70      122.8084        81       3.6574  .0121  .2796
2          7626.99       8.31     182.38       13.6289        81       4.7812  .0060  .1324
2          8463.88      22.98     189.33       12.1131        78       4.2421  .0131  .1082
2          8796.12      22.81     213.60        7.8412        72       4.0603  .0119  .1119
2          9368.95      23.04     183.68       10.7024        82       3.7809  .0105  .0834
2          9991.25       6.98     144.58        5.8391        79       3.5180  .0027  .0568
2         10805.68      75.53     292.03        3.4464        81       3.2245  .0249  .0965
2         11075.36      33.39     244.13        3.7602        80       3.1379  .0104  .0764
3         11530.10      16.86     132.23        3.8931        80       4.6323  .0074  .0584
3         12090.29      68.15     164.69        2.2792        79       4.3974  .0271  .0656
3         12659.80      43.16     252.97        4.0197        81       4.1818  .0155  .0911
3         12843.30       8.01     295.42        3.9855        82       4.1168  .0028  .1031
3         13226.45      67.27     149.65        1.9582        75       3.9873  .0220  .0490
3         13499.98      49.15     157.16        1.4344        80       3.8998  .0154  .0492
3         13821.36       5.17     104.01        1.3019        78       3.8017  .0015  .0309
3         14225.33       4.84     143.89        2.5462        77       3.6852  .0014  .0402
3         14528.34      24.48     168.28        1.7300        74       3.6024  .0065  .0450
3         14971.25      45.30     187.81        2.5823        78       3.4878  .0113  .0470
3         15420.86      38.03     183.35        3.8132        78       3.3788  .0089  .0431
3         16005.80      14.40     130.03        1.5751        77       3.2467  .0031  .0282
3         16650.52      24.87     172.07        4.4820        78       3.1126  .0050  .0343
3         17159.21      36.71     232.92        4.1963        81       3.0143  .0069  .0436
4         17541.00     506.62     557.42        3.3020        77       4.3345  .0000  .0000
4         18150.62      54.89     171.97        1.5803        77       4.1801  .0134  .0420
4         18374.03      31.03     165.49        1.9329        77       4.1262  .0074  .0394
4         19035.25      33.12     229.25        2.2256        80       3.9745  .0073  .0506
4         19933.71       4.35     221.58        3.3887        79       3.8889  .0009  .0468
4         19977.32      57.68     156.57        1.1738        81       3.7768  .0115  .0312
4         20664.28      34.16     164.85        1.9010        82       3.6446  .0063  .0306
4         21485.27      40.40     222.63        1.3037        78       3.4982  .0069  .0381
4         22010.06      69.05     258.79        1.5791        82       3.4106  .0112  .0421
```

standard error estimates, effective period at the envelope maximum, amplitude, and group velocity and its standard error estimates are displayed. In practice, the largest maxima for each phase are selected from the summary table, and the display and statistics for those peaks are inspected.

Sec. 2.3.5 Tests and Comparison with the Multiple Filter Technique

Although the Direct Filtering Method may appear to be a pedestrian method of group velocity analysis it is the only one known to the author which provides an objective measure of the quality of each estimate. The two estimates of error usually are a reasonable set of bounds on the real error in group velocity estimation. This method also provides a check on purity of the filtered signal which is not available through other techniques of display, although they may be considerably more convenient.

In Figure 2.5 the analyses of two synthetic seismograms by the Direct Filtering Method and the Multiple Filter Technique are shown with circles and indicating the actual group velocities used to general the synthetics. Horizontal and vertical bars indicate the group velocities and standard errors, respectively, estimated from Direct Filtering Method regression statistics fit (of the parabola) at each period. The Multiple Filter Technique display in each case is the linear normalized display with positions of the ridge maximum displayed as diamonds and the range of the maximum value in a column shown by "-" or "Λ" and "V". The synthetic in parts (a) and (b) corresponds to a vertical seismogram recorded at an epicentral distance of 40°. A filter with α equal 40 was used in the analyses of both cases. In part (a) the beginning of record time corresponds to 850 seconds after origin time so that the first sample corresponds to a group velocity of 5.23 km/s. In part (b) the synthetic time series begins 1050 seconds after origin time so that the first recorded sample corresponds to a group velocity of 4.24 km/s. Both the

Figure 2.5 ANALYSIS OF TWO SYNTHETIC SEISMOGRAMS BY THE DIRECT FILTERING METHOD AND THE MULTIPLE FILTER TECHNIQUE - Seismograms in (a) and (b) were synthesized for an epicentral distance of 40° with group velocities (shown as circles). The synthetic in (a) begins 850 seconds after origin time and (b) begins 1050 seconds after origin time. Error bars for Direct Filtering Method estimates indicate standard errors estimated from regression statistics of the least-squares fitted parabola. Differences in measured dispersion are caused by filter ramping.

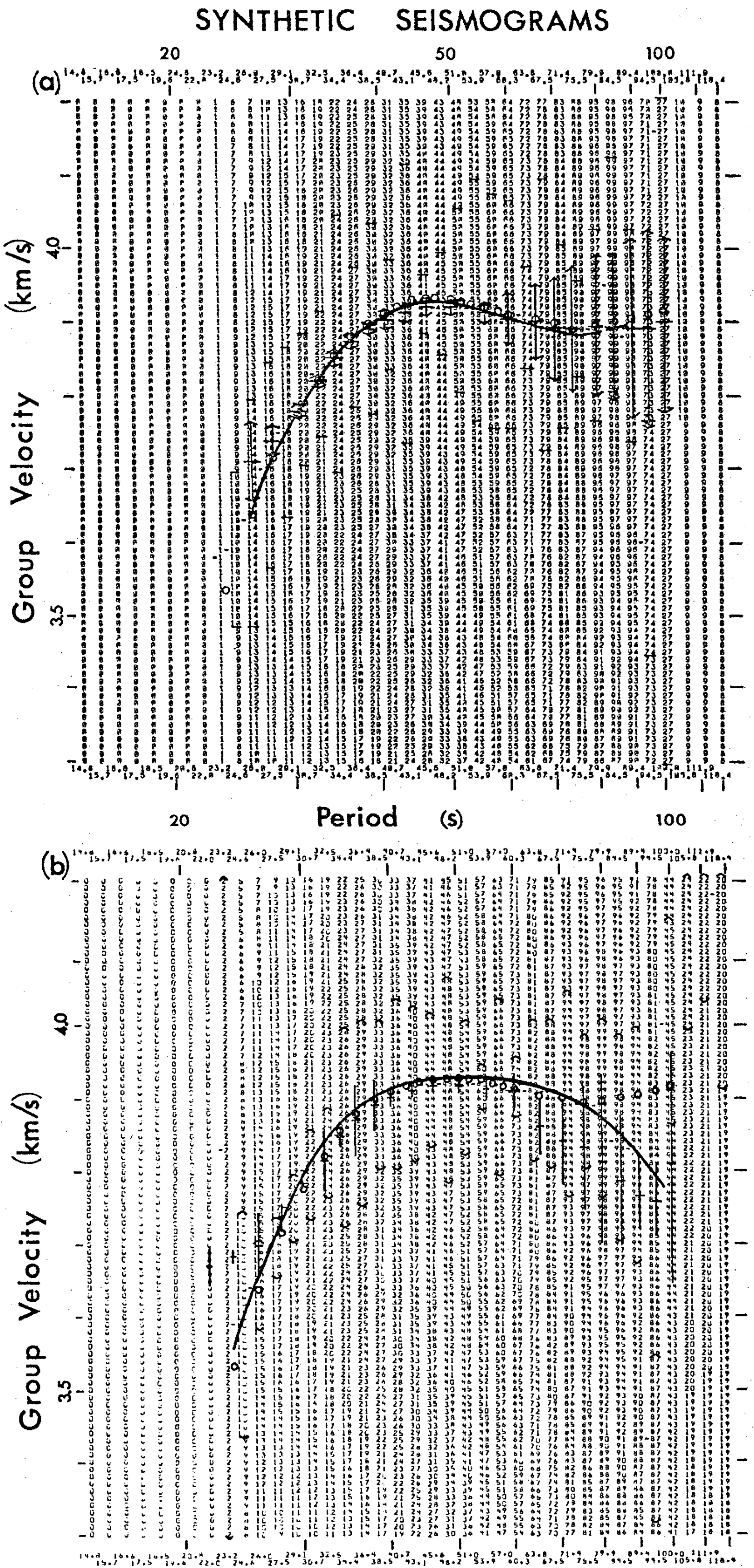
SYNTHETIC SEISMOGRAMS
(a)
(b)
20
50
100
Group Velocity (km/s)
4.0
3.5
Period (s)

Direct Filtering Method and the Multiple Filter Technique give comparable results for both seismograms in the period range 26 to 80 seconds. Errors at short periods, 20 to 26 seconds, in the Direct Filter Method group velocity estimates may be caused by wide spacing of frequencies used in generation of the synthetics. As is shown later (Figure 2.6), results from the Multiple Filtering Method are comparable in this short period range.

The difference between results shown in Figure 2.5(a) and (b) is caused by the effect of filter ramping and can be a major pitfall in the analysis of time series. At each end of a record the equivalent of a half a filter length of the time series is ramped after the application of the filter. For this reason it is necessary to digitize a long enough segment of the seismogram to allow for the loss at long periods for which filter lengths are longest. Truncation of the time series or addition of zeros to the trace constitutes a change in the character of the noise. When filters are applied in the time domain these losses are easily recognized. The situation is more complex in frequency domain filtering, however, because the time domain effects are not so readily apparent. Half-widths in seconds of Gaussian filters of the type shown in Equations 2.2. and 2.3 for a filter parameter of 40 are listed as a function of period for the length of the time domain filter to decay to a given percentage of its peak amplitude. This corresponds to the half filter length at which the envelope of the time domain filter would achieve 25, 12.5, and 3 per cent of its maximum amplitude if a delta function were filtered. These percentages determine how closely the band-limited Gaussian filter approximates the non-band-limited Gaussian filter. An arrival travelling with a group velocity of 3.9 km/s (as in the synthetics in Figure 2.5 for periods greater than 60 seconds) will arrive about 1140.5 seconds after origin time. Such an arrival will appear 290.5 seconds after the beginning of the first synthetic (Figure 2.5(a)) and 90.5 seconds

Figure 2.6 RAYLEIGH WAVE DISPERSION FROM THE PICTON EARTHQUAKE (9 MARCH 1973) RECORDED AT CHARTERS TOWERS, QUEENSLAND - Fundamental mode Rayleigh waves recorded by the low-gain analogue vertical HGLP instrument at CTA which have been processed using the Direct Filtering Method (DFM) (black dots with vertical error bars) are superimposed on the Multiple Filter Technique (MFT) linear amplitude matrix contoured at an interval of 10 amplitude units. Open circles show maxima in the envelope picked by the MFT analysis. For both methods a filter parameter value of 40 was used. All arrivals picked by DFM are shown in Figure 4.8.

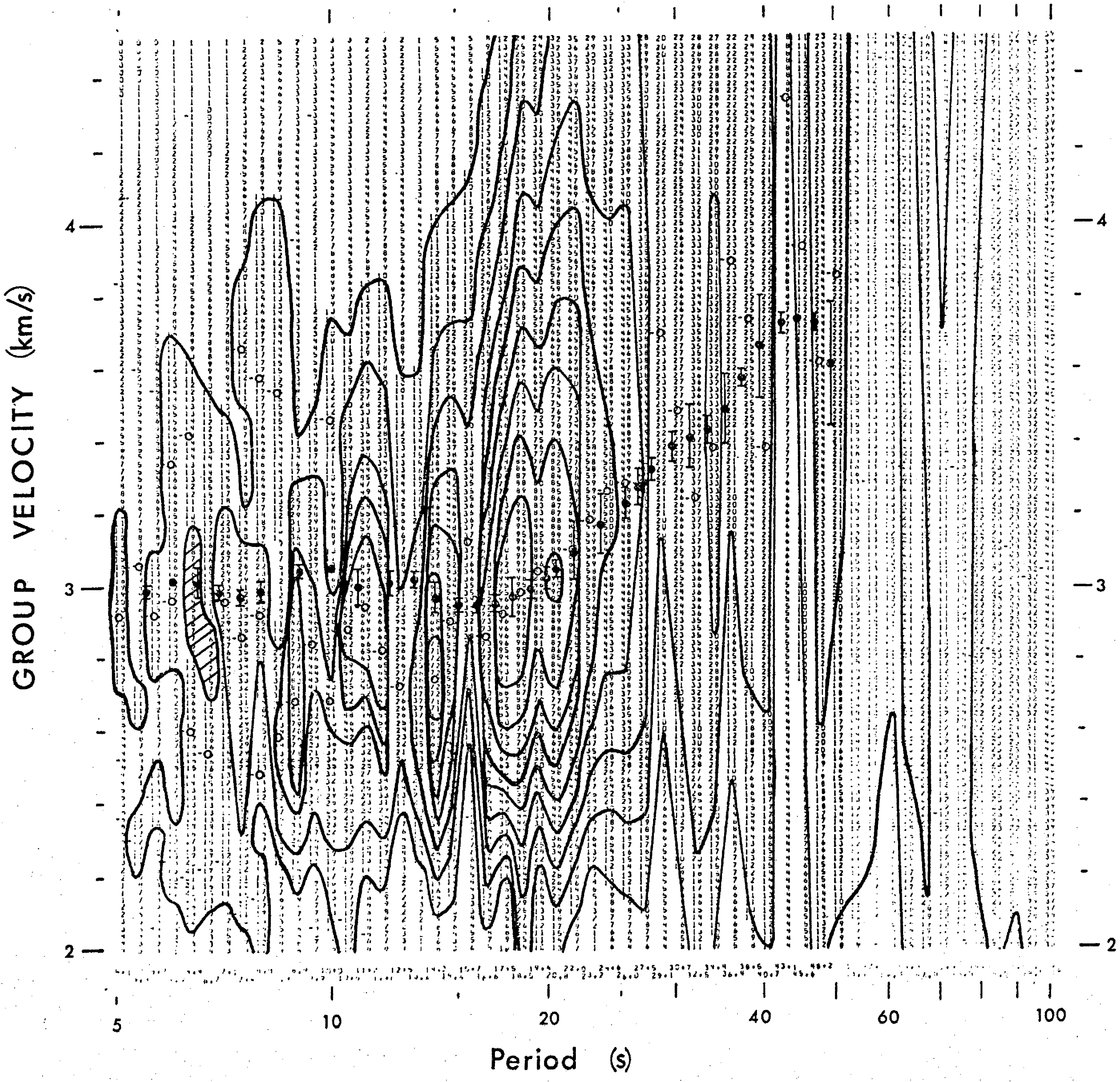
GROUP VELOCITY (km/s)
4
3
2
Period (s)
5
10
20
40
60
100

after the beginning of the second synthetic (Figure 2.5(b)). Consequently filter ramping will be a problem for filters truncated at the 30 db level, as Dziewonski et al. (1969) recommended, for periods greater than 80 seconds for the synthetic in Figure 2.5(a) and at less than 40 seconds for the synthetic in Figure 2.5(b). This effect becomes increasingly more acute at longer periods (see Table 2.1).

Filter ramping causes group arrival time estimates within a half filter width of the beginning or end of the filtered record to migrate away from the ends of the filtered trace. If we consider the effect of not including the contribution of one wing of a Gaussian filter for points beyond some fraction of the maximum amplitude of the envelope, we find that the output of the filter will be diminished by a factor corresponding to the ratio of the area enclosed by the neglected part of the envelope to the area enclosed by the complete envelope. These ratios have been listed in Table 2.2 as percentages of the total filter output. The effect of filter ramping may be a serious problem in the analysis of Goncz (1974) who filtered 1024 second time series to periods as great as 200 seconds (see Chapter 6 for a comparable eastern Australian study of group velocity dispersion.

The problem of filter ramping is avoided in the Direct Filtering Method because no arrivals which are ramped are considered in the analysis. A special version of the analysis program which did not exclude filter ramped arrivals was used to generate group velocities that are shown in Figure 2.5.

Figure 2.6 compares group velocity determinations for Rayleigh waves generated by the Picton earthquake of 9 March 1973 recorded at Charters Towers, Queensland (CTA) analyzed by the Direct Filtering Method (black dots with vertical error bars) with the contoured matrix of the Multiple Filter Technique. Only Direct Filtering Method determinations for the fundamental mode are shown. A complete dispersion analysis

TABLE 2.1 HALF-WIDTHS OF GAUSSIAN FILTERS (IN SECONDS) COMPUTED FOR A FILTER PARAMETER OF 40

Period	Percentage of Maximum Amplitude		
	25	12.5	3
40	68	95	150
50	84	119	188
60	101	142	225
70	118	166	262
80	135	190	300
90	151	214	337
100	168	238	375
120	202	285	449
140	235	332	524
160	269	380	599
180	302	427	679
200	336	475	749

TABLE 2.2 DECREMENT IN FILTERED AMPLITUDES CAUSED BY FILTER TRUNCATION

Truncation Amplitude*	Decrement in Filter Output
1%	0.3%
5%	2.0%
10%	4.9%
15%	8.0%
20%	12.0%
25%	26.7%

* Percentage of maximum amplitude

with higher mode and laterally refracted arrivals is included in Chapter 6 (Figures 6.7 and 6.8)).

Sec. 2.3.6 Amplitudes and Determination of Q^{-1}

Ewing et al. (1957) and Brune (1962) have pointed out that the displacement for a given surface wave mode can be written in the form

$$u(X,t) \cong \frac{1}{2\pi}\int_0^\infty \frac{A(\omega)}{\sqrt{\sin\theta}} \exp[-\frac{\omega t}{2Q}] \cos(\omega t-kX-\pi/4-m\pi/2)d\omega \quad (2.6)$$

and that the application of the stationary phase approximation gives results for non-Airy phases

$$u(X_o,t_o) = \frac{A_2(\omega_o)\exp[-\frac{\omega_o t_o}{2Q}]}{\sqrt{\sin\theta}\left(X\left|\frac{d^2k}{d\omega^2}\right|_o\right)^{1/2}} \cos(\omega_o t-k_o X_o-\pi/4-m\pi/2+\pi/4) \quad (2.7)$$

and for periods in the vicinity of Airy phases (when $d^2\omega/dk^2$ is small)

$$u_a(X_o,t_o) = \frac{A_3(\omega_o)\exp[-\frac{\omega_o t_o}{2Q}]}{\sqrt{\sin\theta}\left(X\frac{d^3k}{d\omega^3}\right)^{1/3}} \cos(\omega_o t_o-k_o X_o-\pi/4-m\pi/2) \ . \quad (2.8)$$

These two equations imply that a wave packet should decrease in amplitude at least as fast as $X^{-1/3}$ and usually as fast as $X^{-1/2}$. In Section 3.2.2 the results of an experiment are presented which was designed to determine which of these expressions should be used for Rayleigh waves in the period range 100 to 275 seconds. This period range represents a broad minimum in group velocity in which variations as a function of period are slow. When a group velocity window was used (which spreads faster than either of the above cases and hence includes successive passages of a Rayleigh wave train filtered for a particular frequency) for cross-correlation with a sine or cosine wave it was found that a decay in signal amplitude similar to that for narrow-band filtered phases occurred.

The major reason for this effect appears to be that in choosing filters as sharp as have been used in the determination of group velocities in this thesis, the time domain filter is long enough to include all energy in the wave train in the pass-band of the filter even at passages as late as R_4 generated by the smaller events discussed in Chapter 4 and much later arrivals discussed in Chapter 3. For these reasons, maximum filtered amplitudes of successive passages of the same Rayleigh phase have been used without a correction for spreading, and the determination of Q^{-1}_{R} for each circuit has been made using amplitudes of envelope maxima of the filtered seismogram in Equation 2.1.

CHAPTER 3

GREAT CIRCLE RAYLEIGH WAVE ATTENUATION AND GROUP VELOCITY, OBSERVATIONS FOR PERIODS BETWEEN 150 AND 600 SECONDS FOR 7 GREAT CIRCLE PATHS

Sec. 3.1 INTRODUCTION

Since Anderson and Archambeau (1964) and Anderson *et al*. (1965) presented a theory for the inversion of surface wave attenuation measurements, few additional measurements of attenuation of mantle surface waves have been attempted (e.g. Kanamori 1970a). The importance of attenuation in the upper mantle was recently demonstrated by Randall (1976) who showed that Jeffreys was correct in suggesting that dispersion caused by the earth's anelasticity would cause shifts in free oscillation periods of as great as 1 percent. Randall showed also that the effect was significant for the dissipation models proposed by Futterman (1962), Jeffreys (1965) and Jackson (1971) and was highly dependent on the particular Q model used. Liu *et al* (1976) computed the absorption and dispersion using the concept of a relaxation sprectum. They showed that a broad absorption band could be obtained by the superposition of absorption peaks of individual relaxation mechanics. Hart *et al*. (1977a, 1977b) have shown that when the effect of Q on the periods of the free oscillations is taken into account in the inversion of these data in conjunction with the travel time data, this leads to significantly increased shear velocities in the upper mantle relative to their starting model, C2. This development lends added importance to the determination of Q for the full range of surface waves which have their maximum amplitudes in the upper mantle.

In this chapter measurements of group velocities and attenuation coefficients are presented which are appropriate for determining Q for Rayleigh waves in the upper mantle. By using long records (Table 3.1) containing many passages of the same Rayleigh phase,the precision of attenuation estimates is improved at long periods and the range of these measurements is extended to periods as great as 500 seconds. Nine great circle paths were selected which provide an even azimuthal coverage of most regions of the earth (Figure 3.1). Of these 9 paths, results for 7 are presented in this chapter. The remaining 2 paths, primarily sample stable continents and ocean basins and will be included in an analysis of several smaller magnitude Kurile Islands earthquakes in Chapter 4. The ultimate goal of this project is to determine average and regional earth models for Q.

The Kurile Islands earthquake of 13 October 1963 (M_s=8.3) was selected for this study because it was one of the largest earthquakes recorded by the World Wide Standard Seismograph Network (WWSSN) in the period of time during which the long period seismographs were operated at a free period of 30 seconds. Operation of these instruments at this free period provided a sensitivity to long period waves which is four times greater than that allowed by their subsequent operation (free periods of all WWSSN long period seismographs were adjusted to 15 seconds beginning early in 1964). The major disadvantage in choosing an earthquake of large magnitude for this study is that in most cases the amplitudes of Rayleigh phases earlier than R_4 are too large for recording on standard WWSSN photographic recorders operated at magnifications greater than 750. For this reason this study does not extend to periods shorter than 100 seconds since the energy at these periods has been highly attenuated before R_4 arrives. In Chapter 4, a separate study of several Kurile Islands earthquakes of magnitudes 6 to 7, measurements of attenuation and dispersion will be presented for all 9 paths shown in Figure 3.1 for periods between 50 and 200 seconds.

Figure 3.1 GREAT CIRCLE PATHS -

Equal area projections of two hemispheres of the earth are shown with the Kurile Islands earthquake ($M_s = 8.3$) of 13 October 1963 located at one pole. Azimuth windows for 9 great circle paths are numbered in both hemispheres. Azimuth windows not used in this study are dashed. Coastlines and continental margins are shown for all continents. Stations recording the 13 October 1963 event of 05:17:52 GMT which were used in this study are shown as boxes.

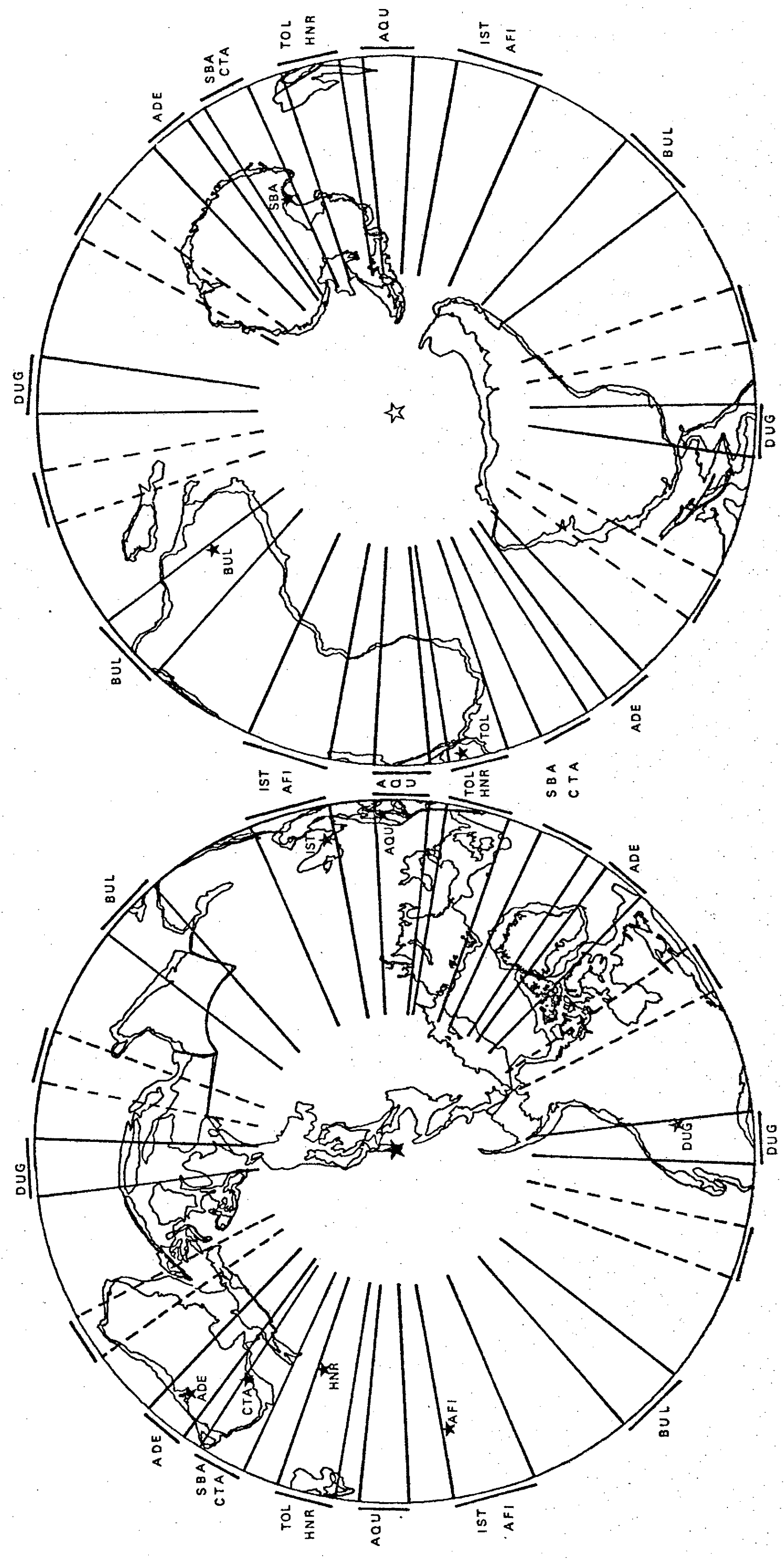
TOL
HNR
AQU
IST
AFI
SBA
CTA
ADE
BUL
DUG
SBA
BUL
DUG
BUL
TOL
IST
AFI
A
Q
U
TOL
HNR
SBA
CTA
ADE
BUL
IST
AQU
ADE
DUG
DUG
DUG
ADE
CTA
HNR
AFI
BUL
ADE
SBA
CTA
TOL
HNR
AQU
IST
AFI

A focal mechanism for the 13 October 1963 Kurile Islands earthquake has been presented by Stauder and Bollinger (1966). Kanamori (1970b) has refined the Stauder and Bollinger solution by modelling long period Rayleigh waves. Both solutions indicate that the sense of motion at the source is dip-slip. These solutions are important since the amplitudes of Rayleigh waves are affected by source orientation (see Ben-Menahem 1961).

Sec. 3.2 DATA AND PROCESSING METHODS

WWSSN long-period vertical seismograms from each station listed in Table 3.1 were digitized using a DMAC digitizer at the Commonwealth Scientific and Industrial Research Organization, Division of Computing Research, Canberra. These digitized seismograms were interpolated to a constant sample interval of 1 sample per second, low-pass filtered, decimated to one sample per 4 seconds and processed to remove the linear trend.

Sec. 3.2.1 Measurement of Group Velocity

Group velocities were determined using the Direct Filtering Method (DFM) as described in Chapter 2. Values of the Gaussian filter parameter α (equations 2.2 and 2.3) of 160 or greater were required to ensure an adequately narrow bandpass for accurate group velocity determinations at periods greater than 300 seconds (Figure 2.1 in Chapter 2). Values of α smaller than 160 gave filters sufficiently broad for envelope maxima of the filtered seismograms to occur sometimes at frequencies substantially different from the centre angular frequencies, ω_n, of the filters. Group travel times were calculated as the difference between USCGS origin time and group arrival time corrected for instrumental group delay by Hagiwara's (1958) formulae, assuming theoretical values for WWSSN seismograph constants. Group velocities of individual Rayleigh phases were calculated as the total path length, corrected for ellipticity, divided by the group travel time. This method of determining group velocities gives independent and more precise estimates than the differential measurement of arrival times of successive odd or even Rayleigh wave trains, since uncertainties in arrival times are a much smaller fraction of total time. In the DFM method, the only large uncertainty arises from the group arrival time estimate, whereas in the differential arrival time method there are uncertainties associated with both group arrival

TABLE 3.1

List of stations and digitization parameters for Kurile Islands earthquake of 13 October 1963, $05^h17^m57^s$ GMT, at 44°8N, 149°5E, h=60 km (USCGS) $M_s = 8.3$

Station code	Station coordinates		Azimuth at epicenter	Epicentral distance (degrees)	Great circle circumference (km)	Magnification	Digitization			
	Latitude ° ′	Longitude ° ′					Beginning h	m	Length h	m
SBA	77 51.0 S	166 45.4 E	184.3	123.4	40008.2	750	7	57	13	07
HNR	9 25.9 S	159 56.8 E	192.7	54.8	40009.6	1500	8	50	14	52
TOL	39 52.9 N	4 02.9 W	20.1	91.2	40011.9	1500	9	15	16	18
BUL	20 08.6 S	28 36.8 E	83.4	125.8	40041.3	750	8	34	14	08
DUG	40 11.7 N	112 48.8 W	124.9	67.7	40030.7	3000	9	14	12	28
ADE	34 58.0 S	138 42.5 E	171.	80.0	40008.8	750	8	34	13	03
AFI	13 54.6 S	171 46.6 W	40.9	68.2	40022.4	750	8	12	11	36
IST	41 02.6 N	28 59.1 E	41.5	79.2	40022.8	1500	9	06	13	26
AQU	42 21.2 N	13 24.2 E	31.1	84.7	40016.9	3000	9	48	18	53
CTA	20 05.3 S	146 15.3 E	176.6	64.5	40008.1	3000	9	16	14	45

time estimates. Group velocity error estimates by the method of differences in arrival times are also larger because the path length is one earth circumference, as compared with at least one and a half earth circumferences by the direct method.

Great circle group velocities were calculated by averaging all group velocity estimates for Rayleigh phases arriving later than R_3. In the first column of graphs in Figures 3.2 to 3.5 the centerpoint of each x indicates the mean of all estimates for each period; vertical error bars indicate the standard deviation of all estimates for that period. It is not strictly accurate to use the estimates for R_4 group velocity and the later passages as estimates of the great circle group velocity, but it can be shown that the errors are small (in general considerably smaller than the errors in determination of the corresponding group arrival times on the filtered records). Since the error changes sign with successive Rayleigh phases, the error in the mean of determinations for several successive passages is even smaller.

To first order the measured group velocity of the phase R_i deviates from the great circle group velocity by

$$(U_{R_i} - U_{CG}) = \begin{cases} \dfrac{-2\ell_1}{i-2\ell_1}\,\delta U & \text{,for even } i \\[2ex] \dfrac{+2\ell_1}{i-1+2\ell_1}\,\delta U & \text{,for odd } i \end{cases} \qquad (3.1)$$

where ℓ_1 is the R_1 path length divided by the circumference of the great circle path and δU is the difference between R_1 and great circle group velocities. At 150 seconds R_1 group velocities differ from great circle group velocities by no more than 0.15 km/s. At the worst, for BUL at an epicentral distance of 125°, the error introduced by averaging R_4, R_5, and R_6 group velocities is less than -0.0097 km/s. At most periods above

Figure 3.2 GROUP VELOCITY AND ATTENUATION COEFFICIENTS FOR STATIONS CTA AND SBA -

Means and standard deviations of all group velocity estimates at each period are shown as x's and error bars in the first column of graphs. Attenuation coefficients (GAMMA) are calculated from the slope of the least squares straight line fitting the logarithm of the spectral amplitude of the successive odd or even Rayleigh phases as a function of epicentral distance. Spectral amplitudes estimated from envelope maxima of Rayleigh phases in each filtered seismogram are used in calculation of attenuation coefficients shown in the second column of graphs, while monochromatic estimates of spectral amplitude for a group velocity window are shown in the third column of graphs. Note that the scales for the plots are not all the same.

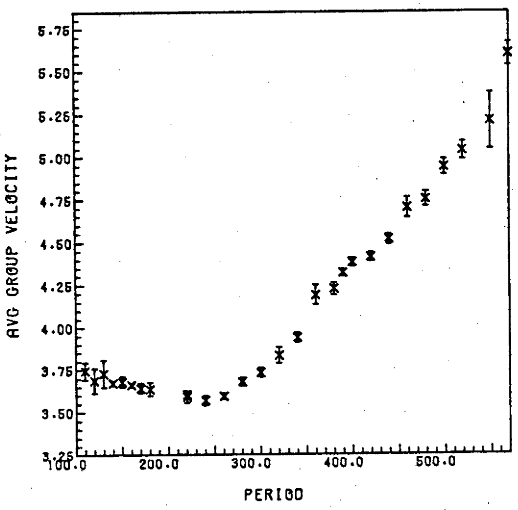
CTA 13X63 MS=8.4 KURILE IS EQ

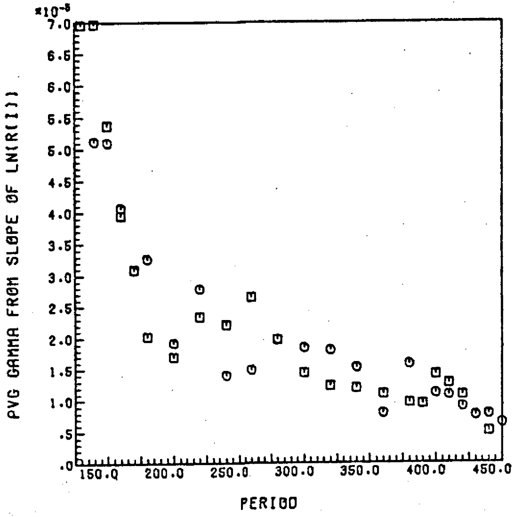
CTA 13X63 MS=8.4 KURILE IS EQ

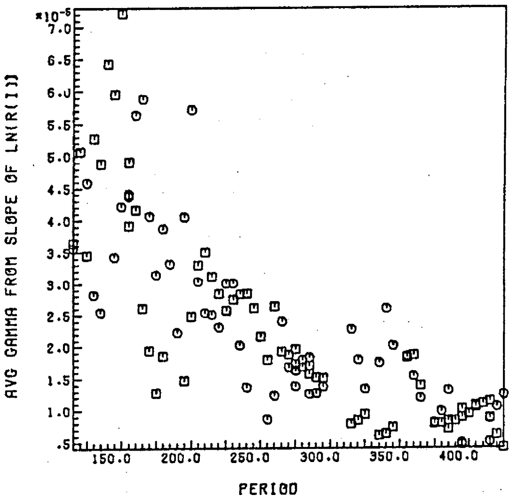
CTA - FAMP DATA1

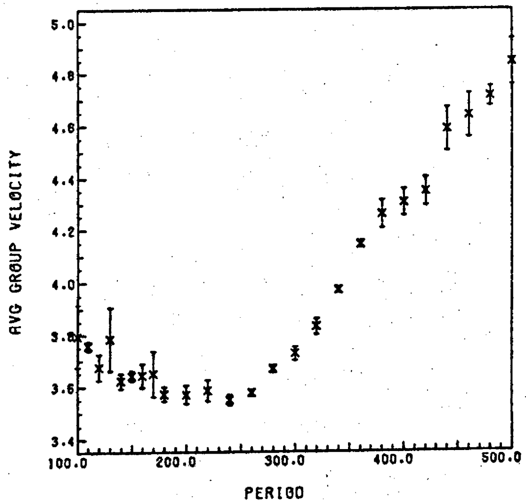
SBA 13X63 MS=8.4 KURILE IS EQ

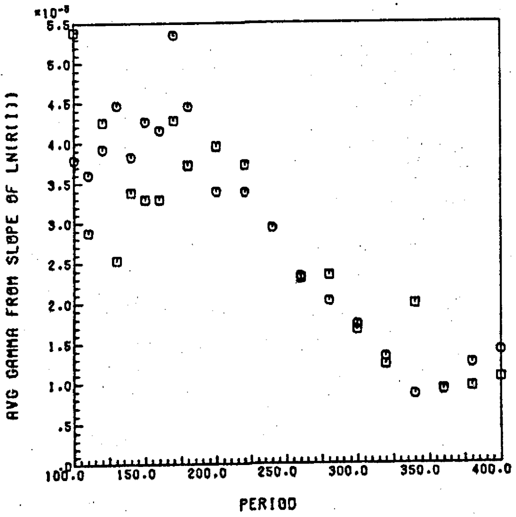
SBA 13X63 MS=8.4 KURILE IS EQ

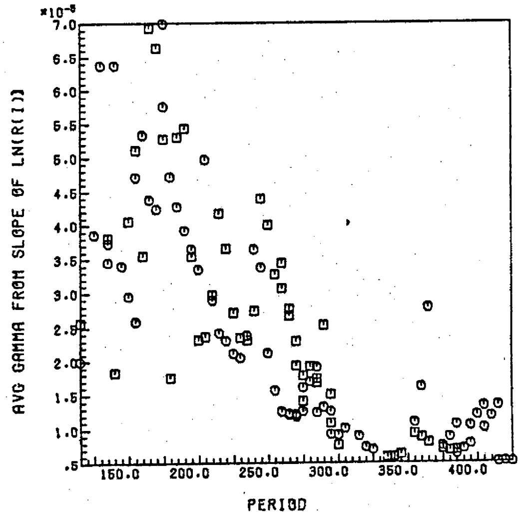
SBA - FAMP DATA1

Figure 3.3 GROUP VELOCITY AND ATTENUATION COEFFICIENTS FOR STATIONS TOL AND HNR -

See caption for Figure 3.2.

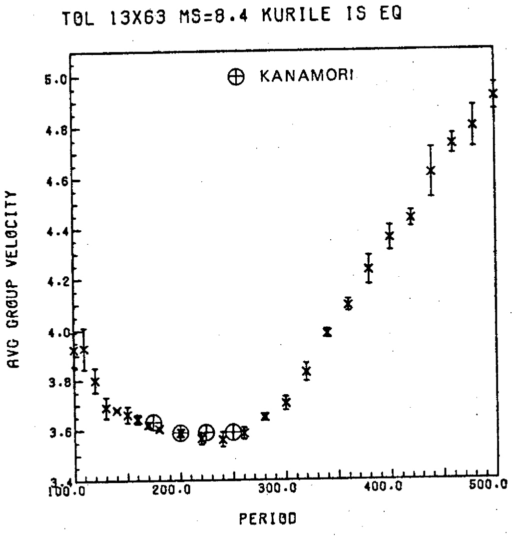
TOL 13X63 MS=8.4 KURILE IS EQ

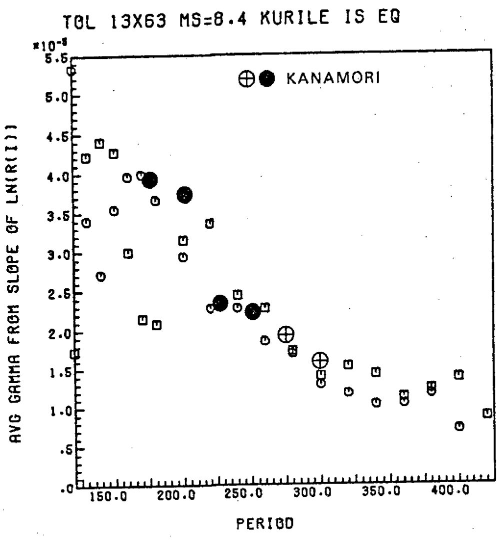
TOL 13X63 MS=8.4 KURILE IS EQ

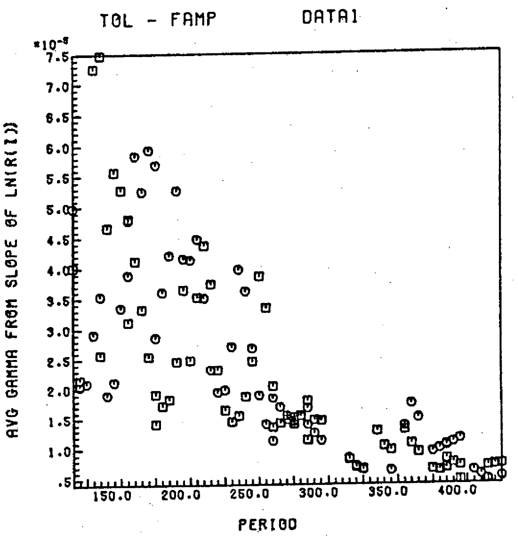
TOL - FAMP DATA1

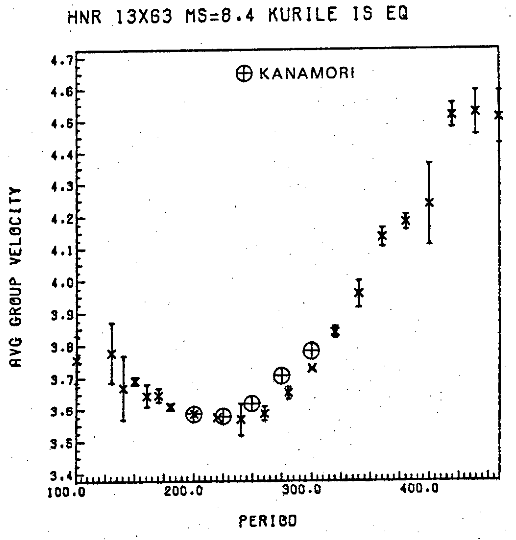
HNR 13X63 MS=8.4 KURILE IS EQ

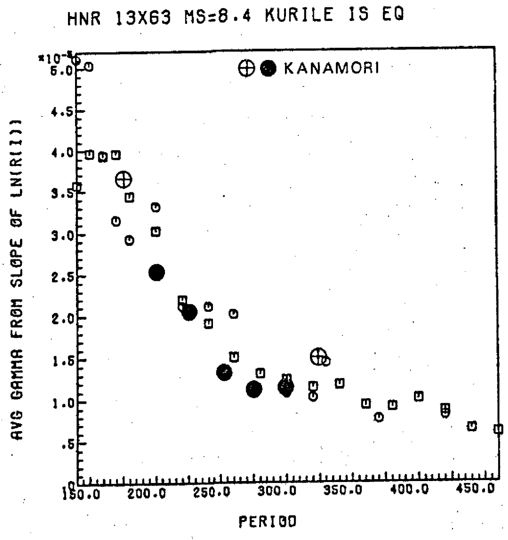
HNR 13X63 MS=8.4 KURILE IS EQ

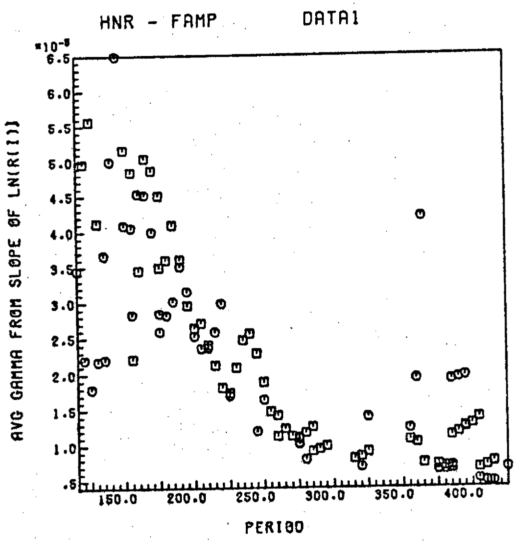
HNR - FAMP DATA1

Figure 3.4 GROUP VELOCITY AND ATTENUATION COEFFICIENTS FOR STATIONS BUL, DUG AND ADE -

See caption for Figure 3.2.

BUL 13X63 MS=8.4 KURILE IS EQ

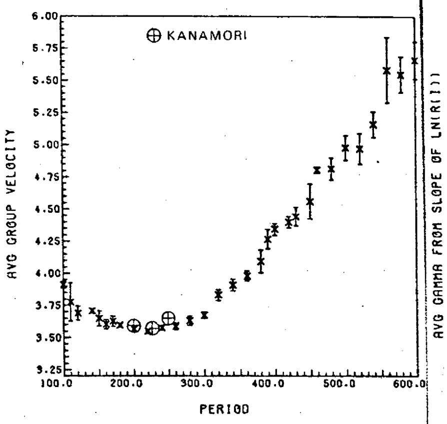

BUL 13X63 MS=8.4 KURILE IS EQ

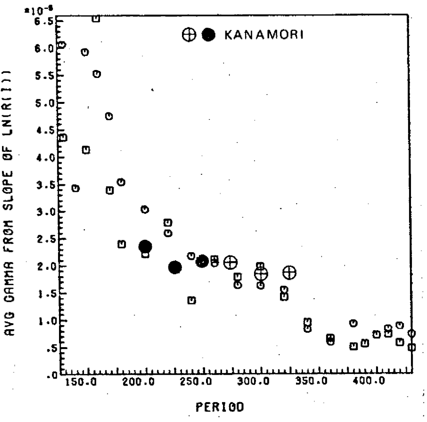

BUL - FAMP DATA1

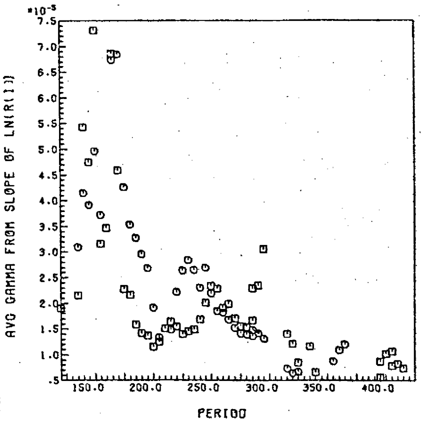

DUG 13X63 MS=8.4 KURILE IS EQ

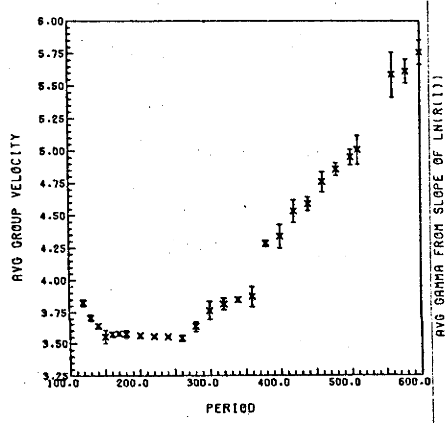

DUG 13X63 MS=8.4 KURILE IS EQ

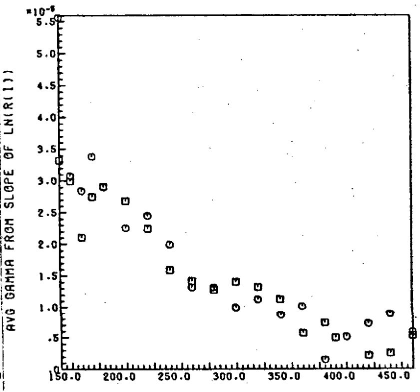

DUG - FAMP DATA1

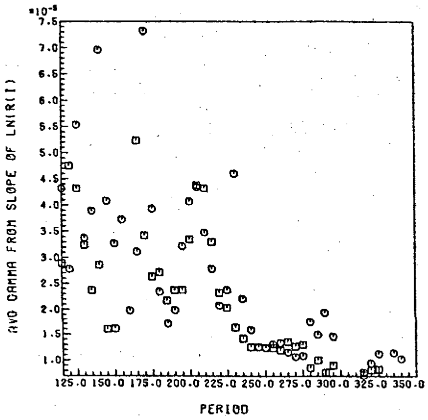

ADE 13X63 MS=8.4 KURILE IS EQ

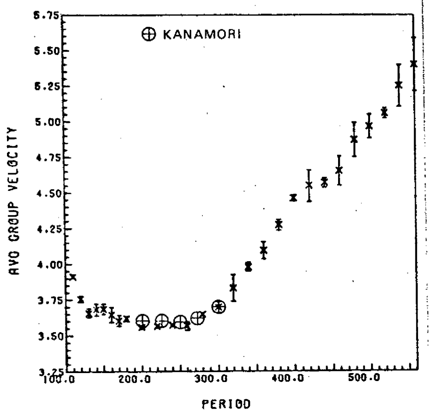

ADE 13X63 MS=8.4 KURILE IS EQ

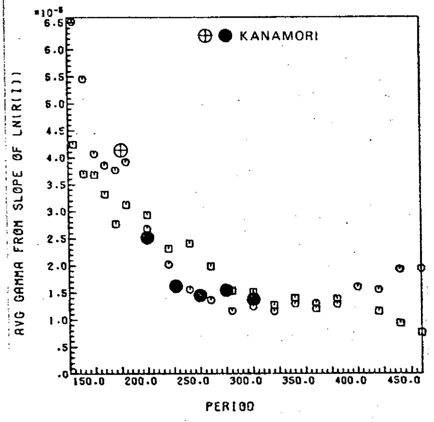

ADE - FAMP DATA0

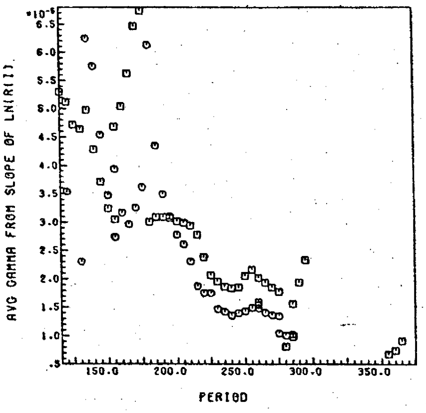

Figure 3.5 GROUP VELOCITY AND ATTENUATION COEFFICIENTS FOR STATIONS AFI, IST AND AQU -

See caption for Figure 3.2.

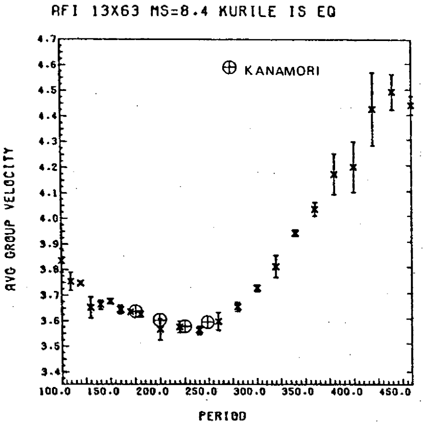
AFI 13X63 MS=8.4 KURILE IS EQ

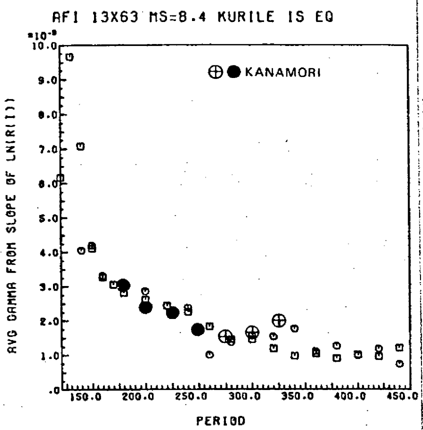
AFI 13X63 MS=8.4 KURILE IS EQ

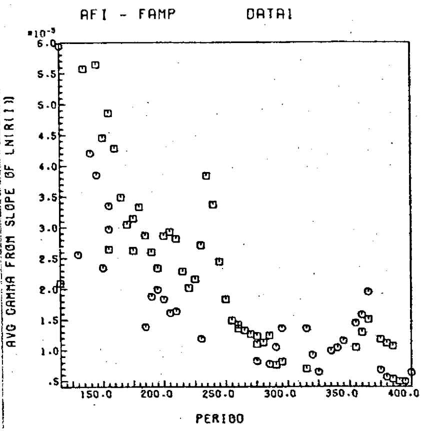
AFI - FAMP DATA1

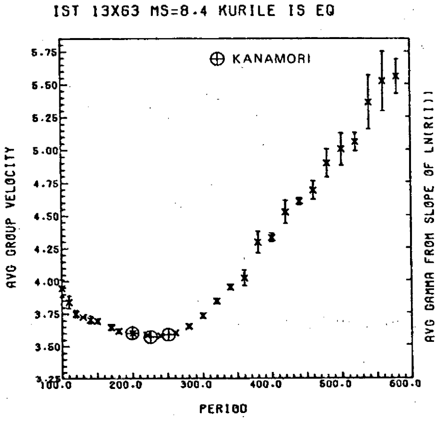
IST 13X63 MS=8.4 KURILE IS EQ

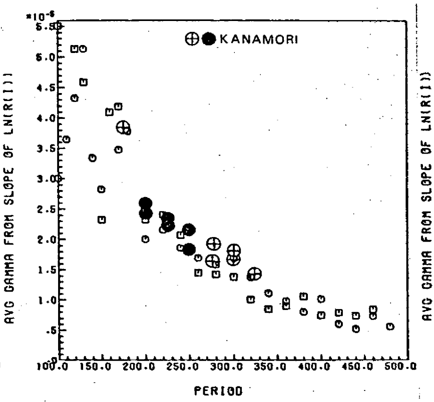
IST 13X63 MS=8.4 KURILE IS EQ

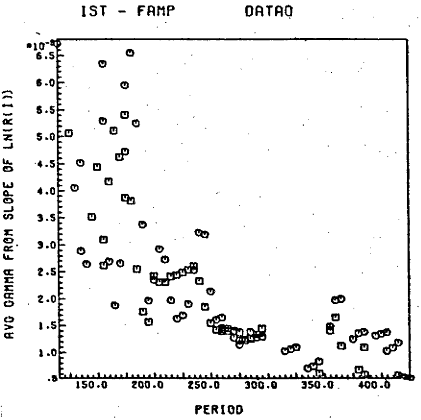
IST - FAMP DATA0

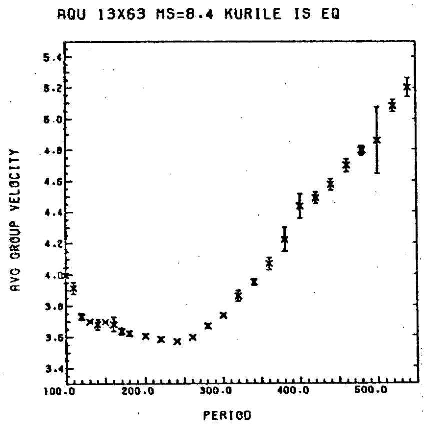
AQU 13X63 MS=8.4 KURILE IS EQ

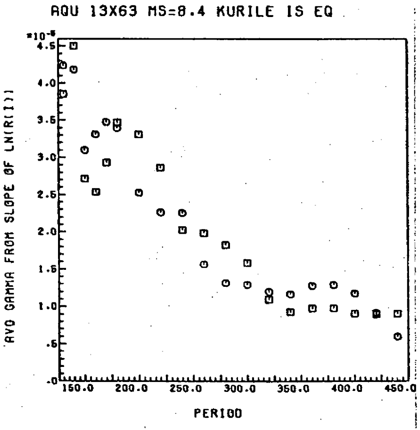
AQU 13X63 MS=8.4 KURILE IS EQ

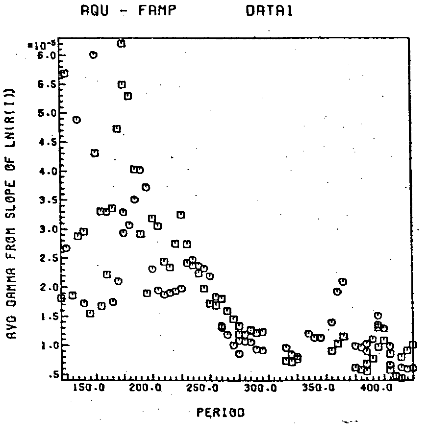
AQU - FAMP DATA1

150 seconds at least 4 Rayleigh phases were used in calculating average group velocities. Differences between R_1 and great circle group velocities are much smaller at longer periods and as more arrivals later than R_6 are averaged, this difference decreases further. Averaging of equal numbers of group velocities for successive Rayleigh phases also averages out the effect of a propagating source.

Clearly, the method of averaging described above cannot be used to determine great circle group velocities from measurements for paths such as R_1 and R_2 (as shown in Chapter 4). Instead, the group travel times of R_1 and R_2 must be added to give one estimate of the great circle group velocity while others can be obtained by taking the difference of the group travel times for R_3 and R_1 and the sum of travel times for R_2 and R_3.

As an added check, auto-correlograms of seismograms for stations AFI and IST were summed and group velocities determined from single and double passage arrivals were found to agree well with group velocities determined as described above and averaged for the two stations (Figure 3.6). The group velocity and attenuation coefficient measurements averaged for overlapping 20 second windows for station IST are shown in Figure 3.7. Only half of the points in each graph are independent.

Sec. 3.2.2 Measurement of Relative Spectral Amplitudes and Attenuation Coefficients

Attenuation measurements have appeared in many different forms in recent articles. In Figure 3.8 attenuation measurements for station AQU are presented in three different formats -

(a) Q_R as a function of period (T),

(b) attenuation coefficient (γ) as a function of period (T), and

(c) attenuation coefficient (γ) as a function of angular frequency (ω).

Figure 3.6 GROUP VELOCITIES COMPUTED FROM THE SUM OF AUTOCORRELOGRAMS FOR STATIONS AFI AND IST.

Results derived by this method are comparable to averaged group velocities for only station IST as shown in Figure 3.8.

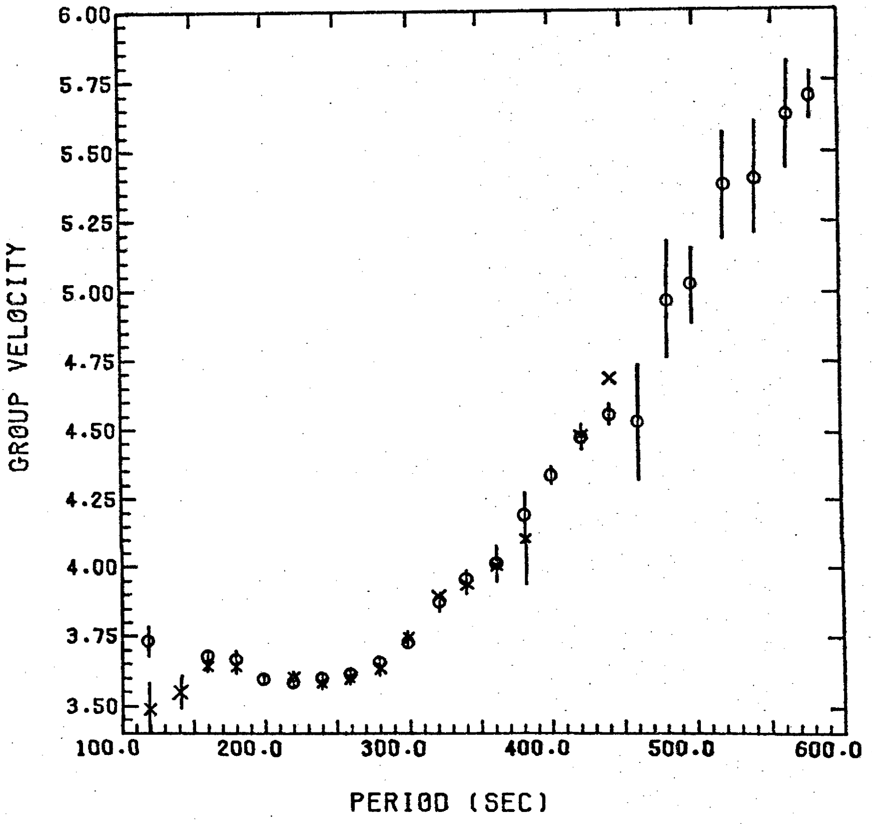

Autocorrelogram Sum - AFI + IST

Figure 3.7 AVERAGED GROUP VELOCITY AND ATTENUATION COEFFICIENTS FOR STATION IST -

Group velocities and attenuation coefficients for station IST appearing in Figure 3.5 have been averaged over 20 second windows centered at 10 second intervals. Not all points are independent.

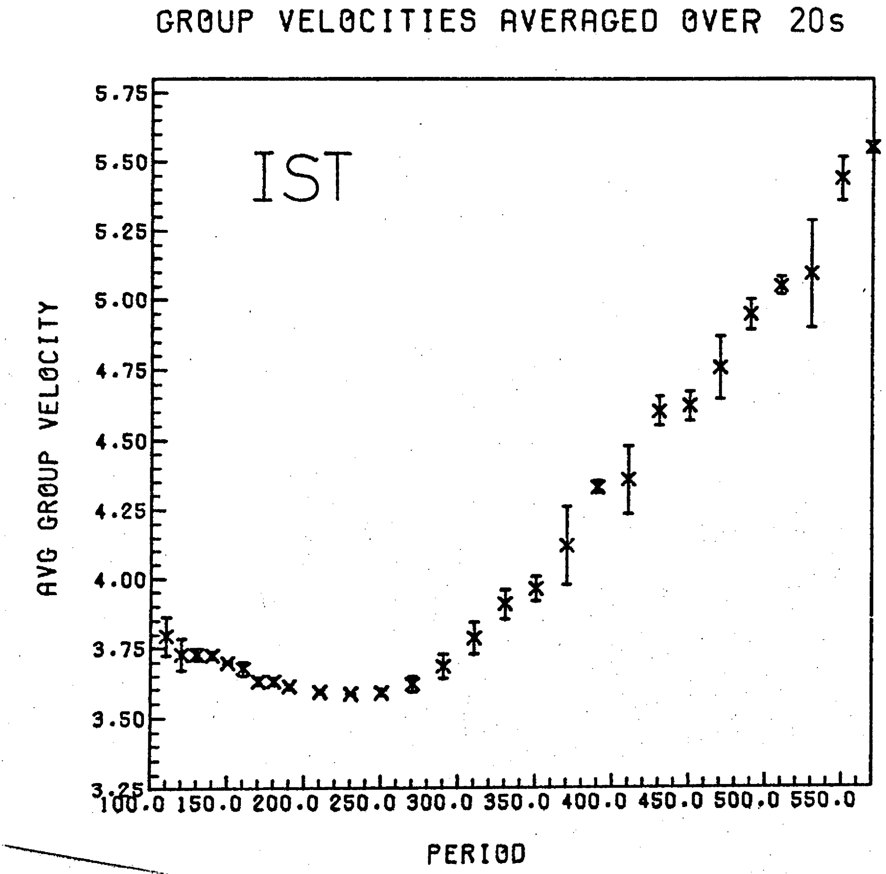
GROUP VELOCITIES AVERAGED OVER 20s
IST
AVG GROUP VELOCITY
5.75
5.50
5.25
5.00
4.75
4.50
4.25
4.00
3.75
3.50
3.25
100.0
150.0
200.0
250.0
300.0
350.0
400.0
450.0
500.0
550.0
PERIOD

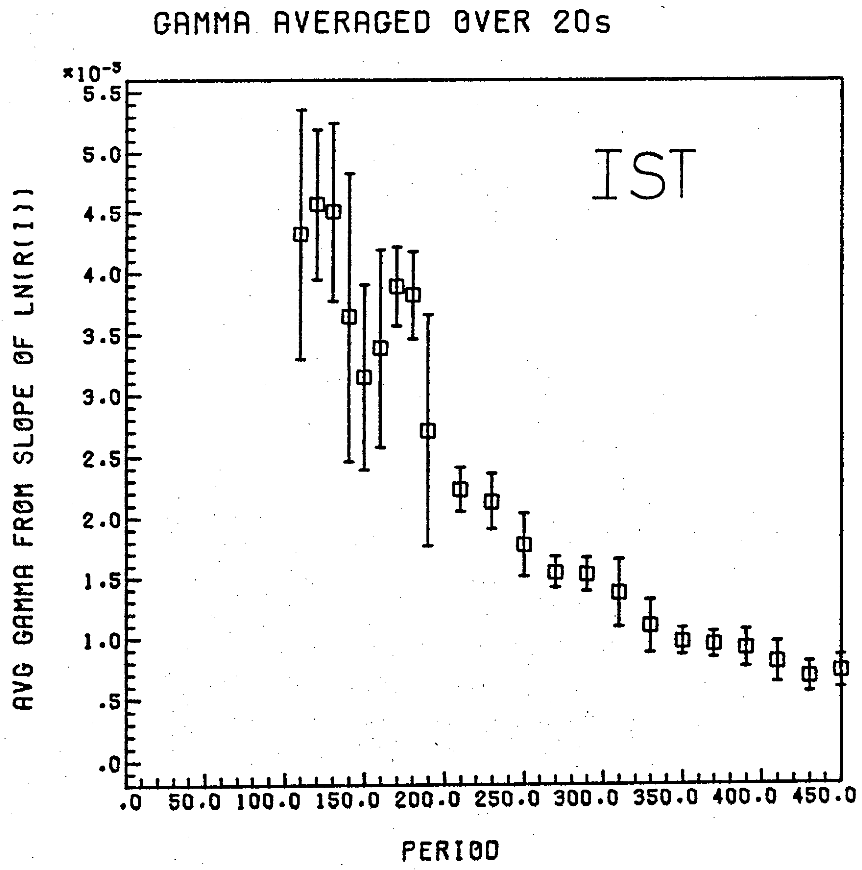
GAMMA AVERAGED OVER 20s
IST
AVG GAMMA FROM SLOPE OF LN(R(I))
×10⁻³
5.5
5.0
4.5
4.0
3.5
3.0
2.5
2.0
1.5
1.0
.5
.0
.0
50.0
100.0
150.0
200.0
250.0
300.0
350.0
400.0
450.0
PERIOD

Figure 3.8 ATTENUATION COEFFICIENTS AND Q_R's ARE DISPLAYED IN THREE DIFFERENT FORMATS -

(a) Q_R's are displayed as a function of period.

(b) Attenuation coefficients are displayed as a function of period.

(c) Attenuation coefficients are displayed as a function of angular frequency.

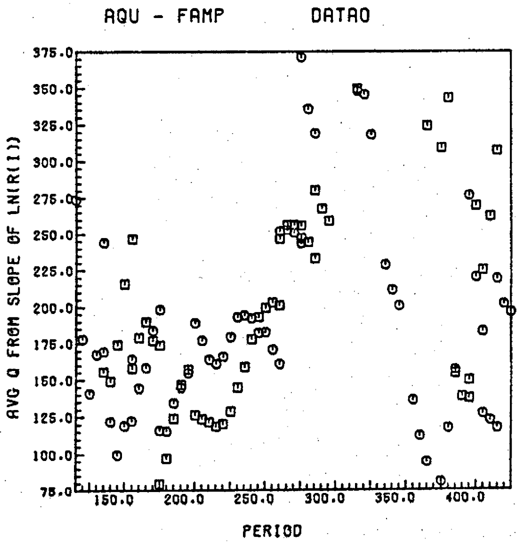

AQU - FAMP DATAO

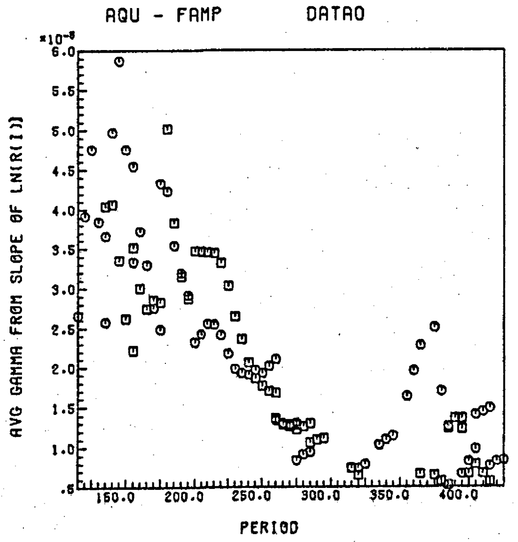

AQU - FAMP DATAO

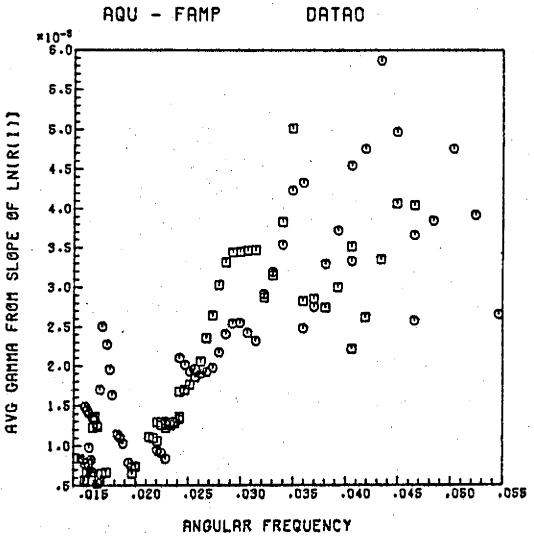

AQU - FAMP DATAO

In the first graph, Figure 3.8 (a), the estimates of Q_R are scattered because small changes in the amplitude ratio $(A_{R_i}/A_{R_{i+2}})$ appear as large changes in Q_R since

$$Q_R = \frac{\pi}{UT\gamma} \quad , \qquad (3.2)$$

the attenuation coefficient (γ) being defined as

$$\gamma = \frac{1}{c} \ln \left(A_{R_i}/A_{R_{i+2}}\right) \qquad (3.3)$$

where c is the circumference of the earth and U the group velocity at period T. Q_R also includes the uncertainties in the group velocity as well as those associated with the amplitude ratio. Since errors in amplitude due to interference between multipath arrivals can be large the attenuation coefficient (γ) will be displayed and used for averaging rather than Q_R. Figure 3.8 (b) and 3.8 (c) show the AQU attenuation data as $\gamma(T)$ and $\gamma(\omega)$ respectively. Since the measurements were made at a constant interval in period, $\gamma(T)$ rather than $\gamma(\omega)$ has been displayed in the remaining figures.

In Figures 3.2 to 3.5 measurements of the attenuation coefficient (γ or GAMMA) which have been calculated from spectral amplitude estimates by two different methods are presented. In the first method, maximum amplitudes of group arrivals in each filtered seismogram were used as smoothed spectral amplitudes. In the second method, values of the sum of the products of a pure sine wave with segments of each seismogram within a group velocity window were used as a monochromatic estimator of spectral amplitudes of the successive Rayleigh phases in each seismogram. The group velocity window spreads faster than $r^{-1/3}$ or $r^{-1/2}$, the theoretically predicted rates of spreading for Airy and non-Airy phases, so that if the first Rayleigh phase is entirely within the group velocity window all later Rayleigh arrivals should be also. Narrow and wide group velocity windows were tried for each seismogram. Widths of each narrow window were chosen to include group velocities up to 0.1 km/sec faster and slower than the measured group velocity. Each wide group velocity window was twice the width of the corresponding narrow window. In most cases the narrow group velocity window was slightly too narrow to include all energy in the earliest Rayleigh phase in each seismogram.

In both of these methods, the attenuation coefficient is calculated from the slope of the logarithm of successive spectral smplitude estimates as a function of epicentral distance. This method provides two independent estimates for the attenuation coefficient at each frequency since even and odd indexed Rayleigh arrivals are treated separately. The estimates of the attenuation coefficient produced in this manner are more immune to noise contamination than those calculated from the ratio of the amplitudes in successive even or odd Rayleigh trains.

Estimates of the attenuation coefficient using the filtered amplitudes appear in the second column of graphs in Figures 3.2 to 3.5. Estimates from the second method appear in the third column of the same figures. For each station used by Kanamori, attenuation coefficients calculated from Q_R's and group velocities (Kanamori 1970a, Tables 5a and 7a) are shown as solid dots. Open circles with crosses appear for values of attenuation coefficients calculated from Kanamori's Q for which no corresponding group velocity appears in his Table 5a. Good agreement is found between values of attenuation coefficients produced by both methods and with those calculated from Kanamori's (1970a) Q's where available.

Sec. 3.3. DISCUSSION

The measurements of group velocity and attenuation coefficients for 10 stations on 7 great circle paths are in good agreement with similar measurements by Kanamori (1970a), but provide new information (1) over a substantially increased period range and (2) with 3 more great circle paths. These measurements can be used to describe the average elastic and anelastic properties of the earth. In Figure 3.9, attenuation coefficients and group velocities for all stations have been averaged over 20 second overlapping windows. Averages of attenuation coefficients and group velocities by paths are given in Table 3.2. A comparison of global mean group velocities is also made with group velocities determined by the Residual Dispersion Measurement technique of Dziewonski et al. (1972, Table 1) and with group velocities derived by differentiation of the Gilbert and Dziewonski fundamental spheroidal mode data (1975, Table 4). It is noteworthy that all three data sets shown in Figure 3.9 tend to show changes in slope at periods of 420 seconds. These are also prominent in the difference between observed and computed spheroidal oscillation periods (residuals) for models 1066A and 1066B (Gilbert and Dziewonski 1975) and C2 (Anderson and Hart 1976). The roughness and larger error bars for our data between 310 and 370 seconds also appear as a break in slope in spheroidal oscillation period residuals near ${}_0S_{20}$ for the above mentioned models. It is probable that these changes are too abrupt to be represented by any physically plausible model. It is, however, possible that these effects are the result of interference between adjacent modes. The roughness of the derivatives of the free oscillation periods for periods of less than 250 seconds leads to poor estimates of group velocity from these data. For this reason, accurate surface wave dispersion measurements at periods shorter than 250 seconds can contribute substantially to the data required for accurate earth modelling, especially in the upper mantle. The global

TABLE 3.2

Global average attenuation coefficients and group velocities.

T	T_{Lower}	T_{Upper}	Attenuation Coefficient (Km^{-1})	Standard Deviation	Group Velocity (Km/s)	Standard Deviation
110.	100.	120.	4.1884E-05	3.5215E-06	3.8066	2.5606E-02
120.	110.	130.	4.2460E-05	5.7904E-06	3.7448	2.1600E-02
130.	120.	140.	4.2550E-05	5.0048E-06	3.7064	1.3512E-02
140.	130.	150.	4.1408E-05	2.1214E-06	3.6897	1.4601E-02
150.	140.	160.	3.9269E-05	2.5695E-06	3.6802	1.4778E-02
160.	150.	170.	3.3152E-05	3.3531E-05	3.6294	1.7002E-02
170.	160.	180.	3.2653E-05	2.1226E-06	3.5788	2.1970E-02
180.	170.	190.	3.2312E-05	1.1950E-06	3.5184	1.6999E-02
190.	180.	200.	2.9111E-05	9.3976E-07	3.5895	9.1639E-03
200.	190.	210.	2.9982E-05	2.7368E-06	3.5852	1.6656E-02
210.	200.	220.	2.5109E-05	9.5156E-07	3.5659	9.7765E-03
220.	210.	230.	2.4014E-05	3.3758E-06	3.5788	8.0257E-03
230.	220.	240.	2.2425E-05	1.0364E-06	3.5665	5.9215E-03
240.	230.	250.	2.1659E-05	1.5234E-07	3.5649	6.0706E-03
250.	240.	260.	1.8847E-05	7.9338E-07	3.5724	6.3704E-03
260.	250.	270.	1.8173E-05	2.1179E-06	3.5871	2.0100E-02
270.	260.	280.	1.4244E-05	2.1383E-06	3.6162	1.2972E-02
280.	270.	290.	1.5902E-05	2.4297E-06	3.6528	1.1491E-02
290.	280.	300.	1.5042E-05	1.0167E-06	3.6863	1.1765E-02
300.	290.	310.	1.4571E-05	1.2497E-06	3.7301	1.8610E-02
310.	300.	320.	1.3381E-05	6.4693E-07	3.7696	1.4659E-02
320.	310.	330.	1.3033E-05	4.4565E-07	3.8329	1.1498E-02
330.	320.	340.	1.2071E-05	5.1741E-07	3.8787	2.3230E-02
340.	330.	350.	1.2692E-05	7.6455E-07	3.9459	3.2718E-02
350.	340.	360.	1.1513E-05	9.9965E-07	3.9041	4.0348E-02
360.	350.	370.	9.8808E-06	2.6912E-07	4.0471	7.3599E-02
370.	360.	380.	1.1370E-05	1.3666E-06	4.1307	4.7471E-02
380.	370.	390.	8.9028E-06	1.3201E-06	4.2576	2.0379E-02
390.	380.	400.	1.0260E-05	1.2632E-06	4.2983	2.9068E-02
400.	390.	410.	8.9448E-06	1.1425E-06	4.3966	3.1884E-02
410.	400.	420.	9.2827E-06	1.3061E-06	4.4147	2.5080E-02
420.	410.	430.	8.4504E-06	1.1915E-06	4.4458	2.8085E-02
430.	420.	440.	7.9289E-06	1.3616E-06	4.5312	3.9609E-02
440.	430.	450.	6.9432E-06	8.6199E-07	4.5594	1.8826E-02
450.	440.	460.	6.8704E-06	2.4246E-06	4.6022	3.4420E-02
460.	450.	470.			4.6900	5.5247E-02
470.	460.	480.			4.8003	9.0407E-02
480.	470.	490.			4.7688	3.5355E-02
490.	480.	500.			4.8721	2.4104E-02
500.	490.	510.			4.9490	2.7844E.02
510.	500.	520.			4.9766	5.4174E-02
520.	510.	530.			5.0619	2.3595E-02
530.	520.	540.			5.0715	1.7015E-02
540.	530.	550.			5.2073	4.8291E-02
550.	540.	560.			5.3038	8.1190E-02
560.	550.	570.			5.5223	3.5291E-02
570.	560.	580.			5.5774	4.8023E-02
580.	570.	590.			5.5923	1.7515E-02
590.	580.	600.			5.6259	4.1181E-02
600.	590.	610.			5.7295	5.2345E-02

Figure 3.9 GLOBAL AVERAGE GREAT CIRCLE GROUP VELOCITIES AND ATTENUATION COEFFICIENTS -

Global mean group velocities calculated from mean group velocities for each station averaged over 20 second overlapping windows and weighted inversely proportional to the variance of each station's average group velocity are shown in the first graph. In the second graph, global means (connected by straight lines) are compared with group velocities of Dziewonski, Mills, and Bloch (1972) (dots) and with group velocities derived from differentiation of spheroidal oscillation periods of Gilbert and Dziewonski (1975) (x's). Error bars for global means are shown at 20 - 30 second intervals. Global average attenuation coefficients shown in the third graph were calculated as the 20 second window averages of the attenuation coefficients for all stations estimated from amplitudes of filtered seismograms.

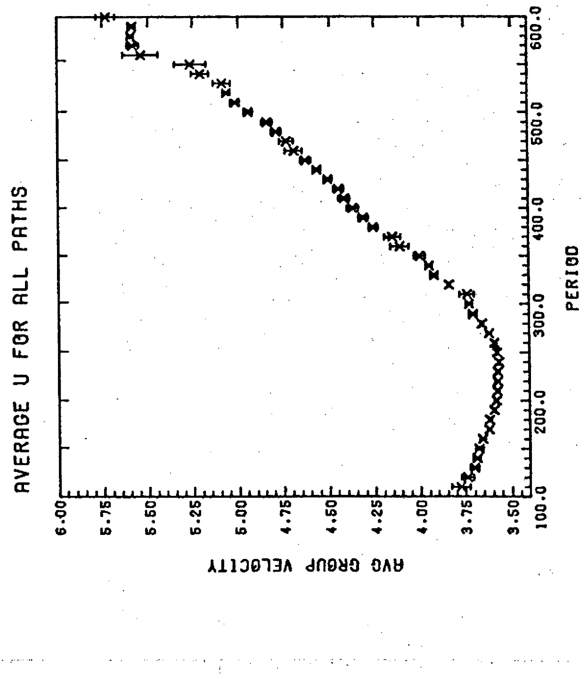
AVERAGE U FOR ALL PATHS
AVG GROUP VELOCITY
6.00
5.75
5.50
5.25
5.00
4.75
4.50
4.25
4.00
3.75
3.50
100.0
200.0
300.0
400.0
500.0
600.0
PERIOD

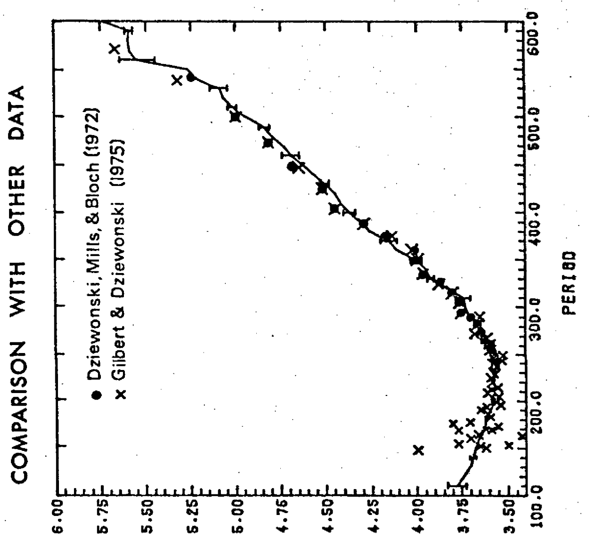
COMPARISON WITH OTHER DATA
● Dziewonski, Mills, & Bloch (1972)
x Gilbert & Dziewonski (1975)
AVG GROUP VELOCITY
6.00
5.75
5.50
5.25
5.00
4.75
4.50
4.25
4.00
3.75
3.50
100.0
200.0
300.0
400.0
500.0
600.0
PERIOD

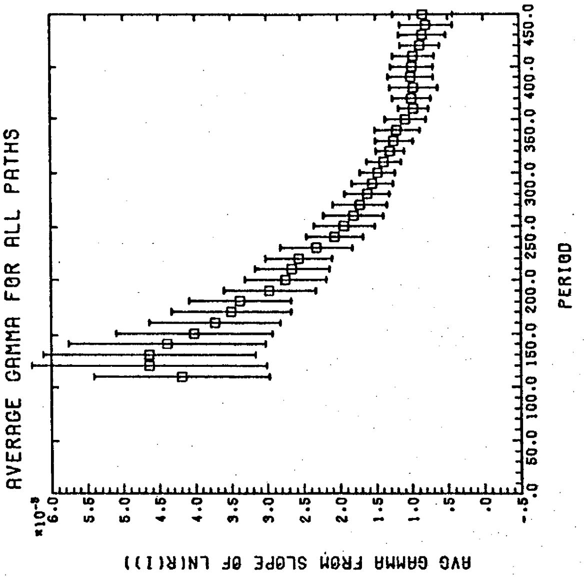
AVERAGE GAMMA FOR ALL PATHS
AVG GAMMA FROM SLOPE OF LN(R(I))
x10⁻³
6.0
5.5
5.0
4.5
4.0
3.5
3.0
2.5
2.0
1.5
1.0
.5
.0
-.5
.0
50.0
100.0
150.0
200.0
250.0
300.0
350.0
400.0
450.0
PERIOD

average attenuation coefficients presented in Figure 3.9, when combined with out global average group velocities indicate that Q for Rayleigh waves (Q_R) is approximately 145 for periods of 140 to 220 seconds and increases at longer periods to about 200 at 400 seconds. These are comparable with the lowest Q's represented in Anderson and Archambeau (1964) Figure 2 for Rayleigh waves and spheroidal oscillations.

The group velocity data presented in this chapter do provide a substantial improvement in the 150 to 250 second period range. Deviations of individual path means from the global mean group velocities in 20 second averaging windows centred at 290, 250, 210, 180 and 150 seconds are less than 0.034, 0.028, 0.024, 0.048, and 0.071 km/s, respectively. At periods shorter than 180 seconds, scatter in averaged values of group velocity increases to almost 0.2 km/s at 100 seconds. Measurements of the attenuation coefficients are also of much lower precision at periods shorter than 150 seconds. The analysis of records of the smaller magnitude Kurile Islands earthquakes for the same great circle paths used in this study are presented in Chapter 4. This analysis yields reliable great circle group velocities and attenuation coefficients for periods as short as 50 seconds and provides additional data to improve both the group velocity and attenuation estimates in the period range from 100 to 150 seconds.

CHAPTER 4

GREAT CIRCLE RAYLEIGH WAVE GROUP VELOCITY AND ATTENUATION COEFFICIENTS OBSERVATIONS FOR PERIODS BETWEEN 50 AND 200 SECONDS FOR 9 GREAT CIRCLE PATHS

Sec. 4.1 INTRODUCTION

Measurements of the group or phase velocities and attenuation of surface waves fall into two classes:

1. Regional studies (e.g. Solomon 1971, Hamada 1972, Madariaga and Aki 1972, Mitchell 1975, Mitchell *et al*. 1975) which are usually restricted to periods less than 160 seconds,

and

2. Studies of great circle average velocities of attenuation coefficients (e.g. Kanamori 1970a, Dziewonski 1971a, Jobert and Roult 1976).

Studies of the second type are not as a rule carried to periods of less than 160 seconds because instrumentation in use today in the standard seismograph networks WWSSN, HGLP, and SRO (Seismic Research Observatory) do not adequately record ground motion of the first few passages of surface wave trains from earthquakes larger than magnitude 7. Few of these studies, if any, contain information about the same great circle paths.

In Chapter 3 measurements of great circle Rayleigh wave group velocity and attenuation were presented for 7 great circle paths for periods from 150 to 600 seconds. In this chapter, the range of such measurements is extended to periods as short as 50 seconds. Further measurements are also given for periods between 150 and 250 seconds complementing the determinations of group velocities and attenuation coefficients discussed in Chapter 3. Measurements for two additional paths (2 and 9 in Figure 4.1) are also presented. Global average group velocities and attenuation coefficients are calculated for the combined data sets in the period range 50 to 600 seconds. Phase velocities and equivalent spheroidal oscillation periods were determined for periods between 50 and 330 seconds by integrating group velocities. Comparisons of group and phase velocities and equivalent spheroidal oscillation periods determined in this study with other similar observations and values calculated from several recent earth models show that shear velocities in the upper mantles of these models are too high to fit global average data in the 80 to 200 second period range.

Sec. 4.2 DATA AND PROCESSING TECHNIQUES

Kurile Islands earthquakes (Table 4.1) with surface wave magnitudes (M_s) 6.6 to 7.1 were selected for this part of the study. These events were recorded either by WWSSN stations prior to 1 January 1964 or by the High-Gain Long-Period (HGLP) seismograph network stations (Figure 4.1 and Table 4.1). Long period seismometers at all of these stations were operated with natural periods of 30 seconds for each of these events. Close proximity of the epicenters of these events to the 13 October 1963 epicenter discussed in Chapter 3 ensures that the paths used in the following analysis do not deviate significantly from those used in Chapter 3 (Figure 4.1). The focal mechanism solution for the 12 October 1963 earthquake, determined from P-wave first motions and S-wave polarizations by Stauder and Bollinger (1966) indicates predominately dip-slip motion. P-wave first motions for the 10 and 13 June 1975 earthquakes, plotted from data given in the United States Geological Survey (USGS) Earthquake Data Report, also yielded predominantly dip-slip solutions, which are substantially in agreement with mechanisms determined by Stauder and Mauchlin (1975) for earthquakes in the same epicentral region (Stauder and Mauchlin, 1975, No. 54 and 55 in Table 2 and Appendix).

Vertical seismograms for the 12 October 1963 event were obtained on 70 mm film chips, printed at full size and digitized using a DMAC digitizer at the Commonwealth Scientific and Industrial Research Organization, Division of Land Use Research, Canberra. These digitized seismograms were interpolated to a constant sample interval of 1 sample per second, low-pass filtered and processed to remove linear trend. Vertical seismograms for the 10 and 13 June 1975 events were, obtained in digital form and only required demultiplexing and linear trend removal.

Figure 4.1 GREAT CIRCLE PATHS -

Equal area projections of two hemispheres of the earth are shown with the Kurile Islands earthquakes of 12 October 1963 (square) and 10 and 13 June 1975 (triangle) located at one pole. Stations used in this study recording each event are also shown with triangles for HGLP stations and squares for WWSSN stations. Azimuth windows for 9 great circle paths are numbered in both hemispheres. Coast lines and continental margins are shown for all continents.

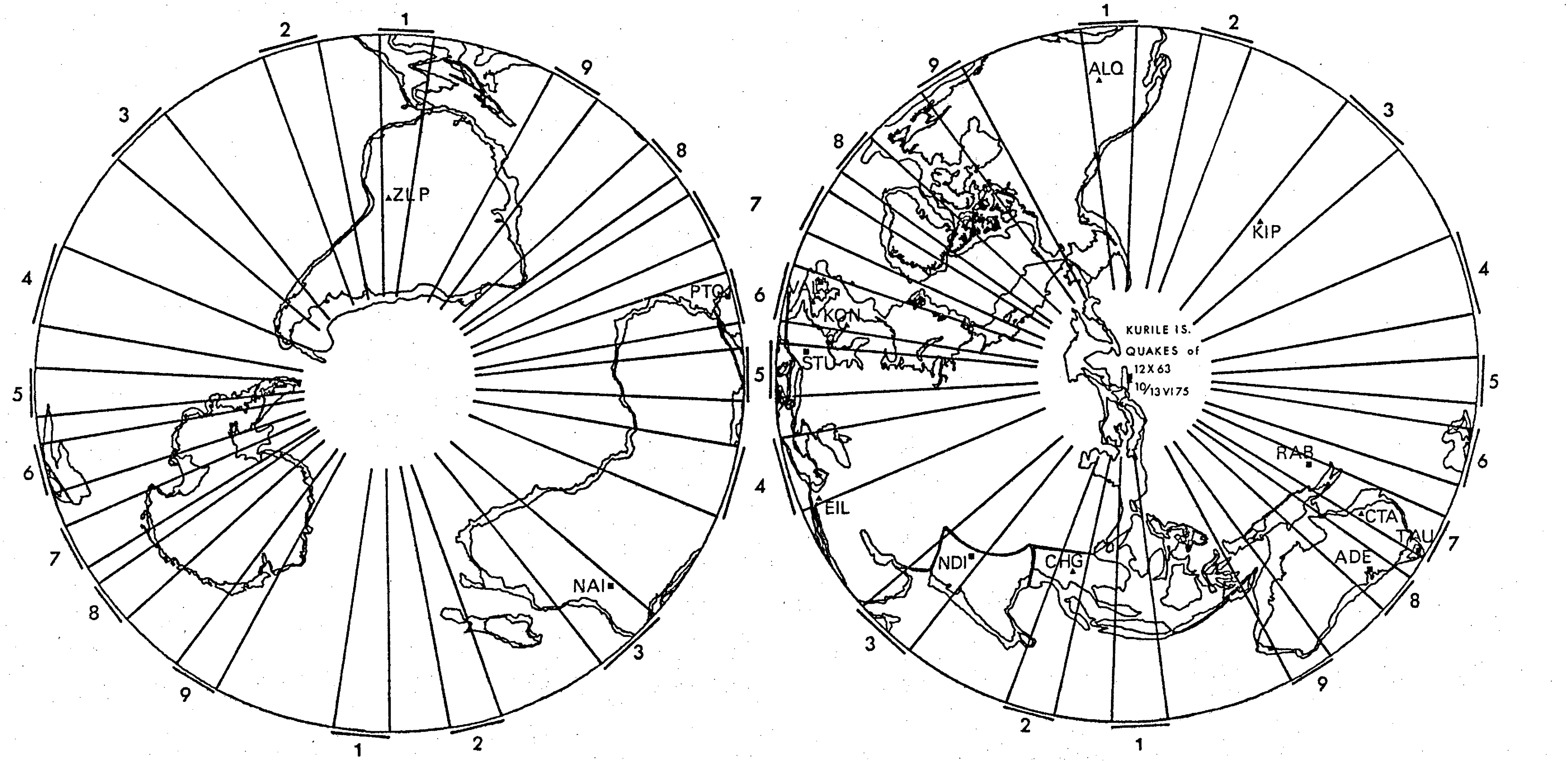
ZLP
PTO
NAI
ALQ
KIP
KURILE IS.
QUAKES of
12 X 63
10/13 VI 75
KON
STU
EIL
NDI
CHG
RAB
CTA
TAU
ADE
1
2
3
4
5
6
7
8
9

TABLE 4.1 KURILE IS. EARTHQUAKES

DATE	ORIGIN TIME (GMT)	LOCATION (USGS)	MS	ABBREVIATION
12 October 1963	11 : 26 : 57.9	44°8N 149°0E	7.0	12X63
10 June 1975	13 : 47 : 21.7	43°3N 147°0E	7.1	10V175
13 June 1975	18 : 08 : 12.8	43°6N 147°4E	6.6	13V175

STATIONS	AZIMUTH AT EVENT AND WINDOW No.	EVENT DATE	EPICENTRAL DISTANCE (km)	GREAT CIRCLE CUMFERENCE (km)	BEGINNING OF DIGITIZATION (GMT)	NO. OF SAMPLES	TYPE OF RECORD
ALQ	124°4(1)	13V175	8549.7	40031.0	17:58:13.1	22440	HGLP
ZLP	119°5(1)	10V175	15565.2	40034.0	13:32:01.6	23100	HGLP
		13V175	15493.7	40033.8	17:50:46.4	22440	HGLP
CHG	104°8(2)	10V175	5232.2	40040.9	13:37:43.0	24420	HGLP
		13V175	5272.4	40040.6	17:52:43.0	22440	HGLP
NDI	79°6(3)	12X63	6440.4	40040.7	11:31:00	17665	WWSSN
NAI	74°6(3)	12X63	11837.3	40039.4	11:40:00	13685	WWSSN
KIP	79°4(3)	10V175	5595.9	40043.0	13:34:25.3	12766	HGLP
		13V175	5568.2	40042.5	18:03:37.8	22440	HGLP
EIL	54°2(4)	10V175	9385.8	40031.3	13:35:55.9	23100	HGLP
		13V175	9392.3	40031.0	17:57:12.1	8580	HGLP
STU	25°4(5)	12X63	8926.9	40014.2	11:36:00	17889	WWSSN
VAL	12°5(6)	12X63	9102.7	40009.5	11:37:00	15990	WWSSN
PTO	16°4(6)	12X63	9702.2	40010.6	11:35:00	15422	WWSSN
KON	20°3(6)	10V175	7947.4	40012.6	13:37:41.3	23100	HGLP
		13V175	7928.0	40012.5	17:56:26.3	22440	HGLP
CTA	176°6(7)	10V175	7018.3	40008.0	13:38:16.6	23430	HGLP
		13V175	7052.2	40008.0	17:53:33.6	22440	HGLP
TAU	178°4(7)	12X63	9716.4	40008.0	11:35:00	16915	WWSSN
RAB	3°5(7)	12X63	5435.3	40008.1	11:27:00	20629	WWSSN
ADE	171°0(8)	12X63	8894.2	40008.8	11:38:00	15168	WWSSN
MUN	151°9(9)	12X63	9127.8	40015.4	11:35:00	14886	WWSSN
OGD*	148°2(9)	10V175	9775.3	40016.9	13:38:39.6	23100	HGLP
		13V175	9730.2	40016.9	17:56:01.0	22770	HGLP

* DATA NOT INCLUDED DUE TO DIGITIZER MALFUNCTION.

Sec. 4.2.1 Measurement of Group Velocity

Group velocities were determined by the Direct Filtering Method (described in Chapter 2) for each Rayleigh phase in each seismogram for as broad a range of periods as possible. For periods shorter than 80 seconds a value of 40 for the filter parameter α, was found to produce a sufficiently sharp filter, while for longer periods, a value of 80 for α was more suitable. No determinations were attempted for periods shorter than 40 seconds since problems of multipathing caused by mid-ocean ridges are acute at shorter periods (Capon 1970) and since R_3 amplitude data does not extend to periods shorter than 50 seconds. Figures 4.2 (a) and 4.2(b) show R_1, R_2 and R_3 group velocities and amplitudes for station ADE (Adelaide, South Australia) for the 12 October 1963 earthquake. Each measurement of group velocity in Figure 4.2(a) has two sets of error bars. The smaller errors are based on the accuracy of the best fitting parabola used for estimating the travel time of a group arrival. The larger set indicates the uncertainity in group velocity based on the half-amplitude width of the group arrival peak. Of these two estimates of the standard errors, the narrower set of error bars probably gives too optimistic an estimate of uncertainity in group velocity while the wider set underestimates the accuracy of these determinations. Estimates of group velocities for all other seismograms are shown in Figures 4.2(e) to 4.2(k).

Sec. 4.2.2 Calculation of Great Circle Group Velocities and their Variances

Great circle group velocities can be calculated in terms of combinations of group velocities for individual Rayleigh phases since some multiple of a great circle travel time can be formed from the sum or difference of travel times for any two Rayleigh phases observed at a single station. For R_1 and R_2 this relationship can be written

Figure 4.2 GROUP VELOCITIES, AMPLITUDES AND ATTENUATION COEFFICIENTS FOR STATIONS

(a) Group velocities of Rayleigh waves recorded at Adelaide, South Australia (ADE) are shown for phases R_1 (circles), R_2 (X's) and R_3 (diamonds). Error bars for each observation indicate 1 standard deviation as estimated from regression statistics from a parabola fit to each filtered group arrival peak (narrow error bars) and 1 standard deviation as estimated from the half-amplitude width of each filtered group arrival peak.

(b) Relative amplitudes for each filtered group arrival peak are shown for each Rayleigh phase shown in 4.2(a).

(c) Great circle group velocities are shown as determined by combining R_1 and R_2 (X's), R_1 and R_3 (bars) and R_2 and R_3 (diamonds) group velocities.

(d) Attenuation coefficients determined from ratios of filtered amplitudes of R_1 and R_3 shown in Figure 4.2(b).

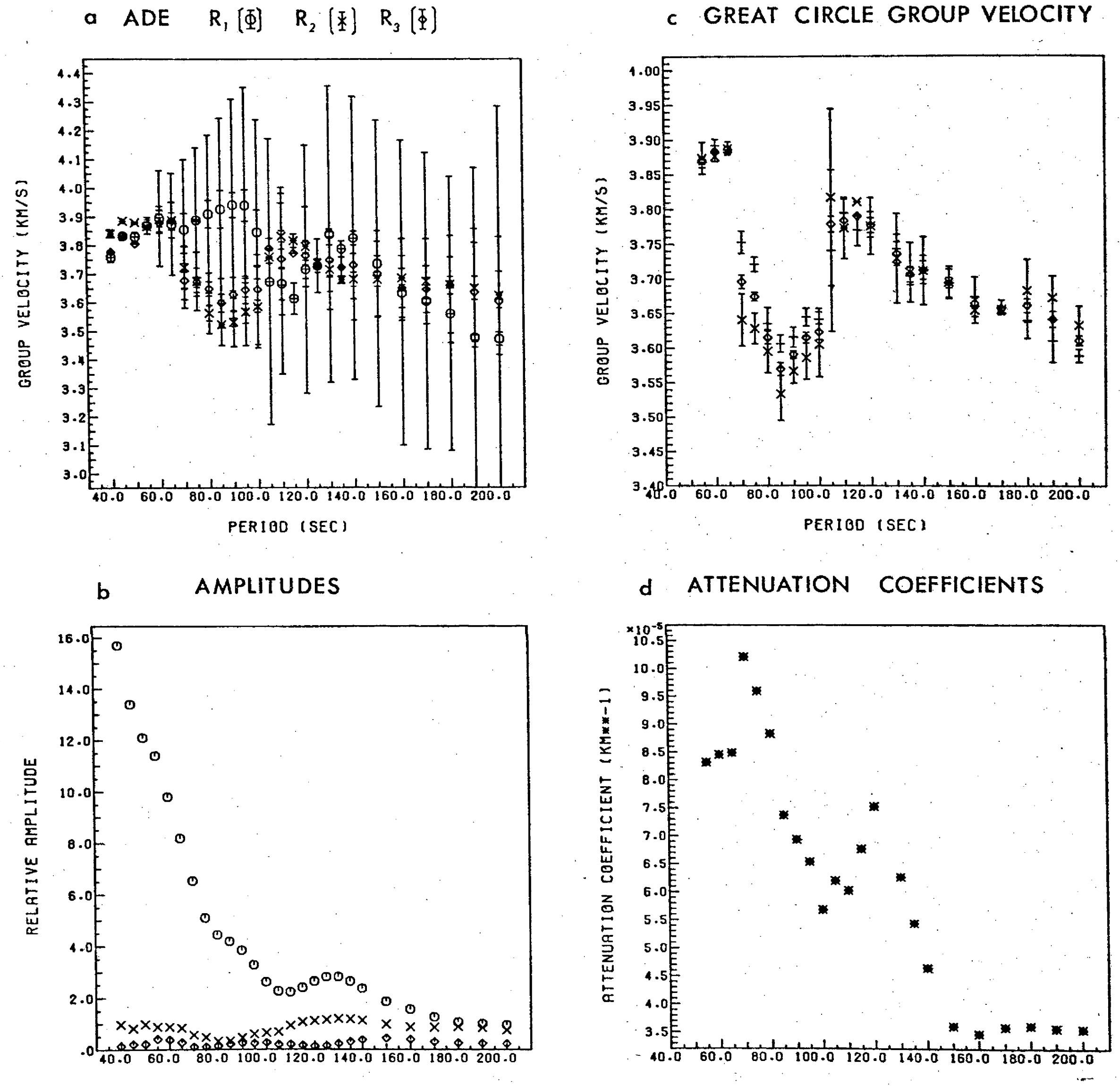
a ADE R₁ [Φ] R₂ [Ẋ] R₃ [Φ̇]
GROUP VELOCITY (KM/S)
3.0 3.1 3.2 3.3 3.4 3.5 3.6 3.7 3.8 3.9 4.0 4.1 4.2 4.3 4.4
PERIOD (SEC)
40.0 60.0 80.0 100.0 120.0 140.0 160.0 180.0 200.0
c GREAT CIRCLE GROUP VELOCITY
GROUP VELOCITY (KM/S)
3.40 3.45 3.50 3.55 3.60 3.65 3.70 3.75 3.80 3.85 3.90 3.95 4.00
PERIOD (SEC)
40.0 60.0 80.0 100.0 120.0 140.0 160.0 180.0 200.0
b AMPLITUDES
RELATIVE AMPLITUDE
.0 2.0 4.0 6.0 8.0 10.0 12.0 14.0 16.0
40.0 60.0 80.0 100.0 120.0 140.0 160.0 180.0 200.0
d ATTENUATION COEFFICIENTS
ATTENUATION COEFFICIENT (KM**-1)
×10⁻⁵
3.5 4.0 4.5 5.0 5.5 6.0 6.5 7.0 7.5 8.0 8.5 9.0 9.5 10.0 10.5
40.0 60.0 80.0 100.0 120.0 140.0 160.0 180.0 200.0

Figure 4.2(e) OBSERVED GROUP VELOCITIES AND ATTENUATION COEFFICIENTS FOR STATIONS EIL, TAU, AND VAL FOR KURILE ISLANDS EARTHQUAKES -

The first 3 characters of each 5 character identifier for each analysis indicate the station identification call for that analysis, while the last 2 characters are the day of the month of the event (Table 4.1) analysed (e.g. EIL 10 is the 10 July 1970 Kurile Islands earthquake recorded at station EIL).

Group velocities for $R_,$, R_2, R_3 and R_4 are shown as circles, triangles, X's, and diamonds respectively. The smaller set of error bars for each measurement is the standard error of the measurement calculated by the Direct Filtering Method from regression statistics for the parabola fitted to the group arrival envelope. The wider set of standard errors bounds are calculated from the half-amplitude width of the parabola.

Attenuation coefficients for each analysis, shown as circles and triangles, are calculated from R_1/R_3 and R_2/R_4 amplitude ratios respectively.

EIL10 GROUP VELOCITIES

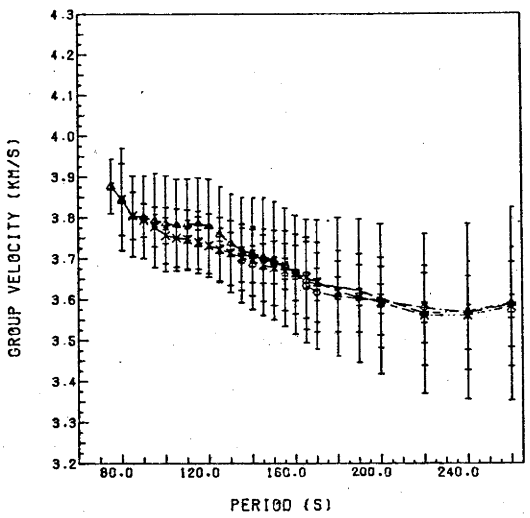

EIL10 ATTENUATION COEFFICIENTS

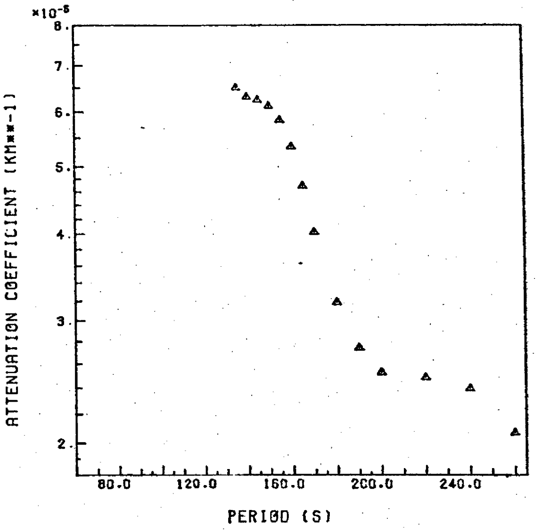

TAU12 GROUP VELOCITIES

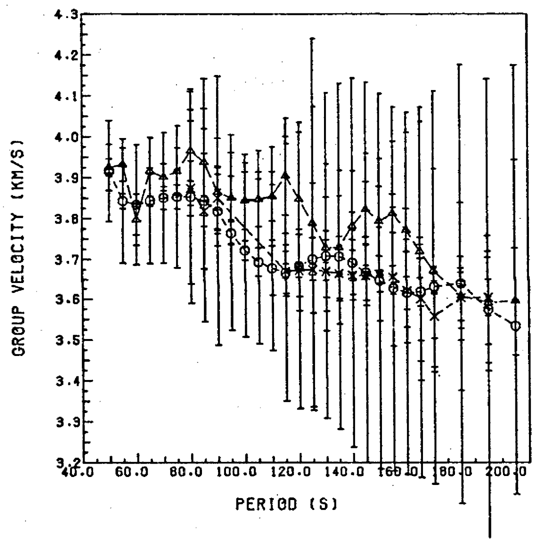

TAU12 ATTENUATION COEFFICIENTS

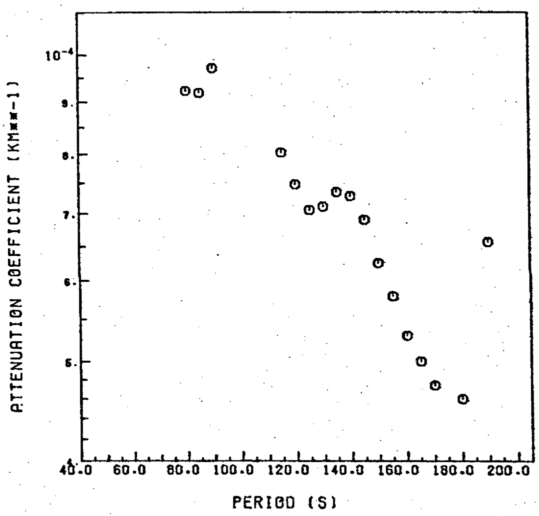

VAL12 GROUP VELOCITIES

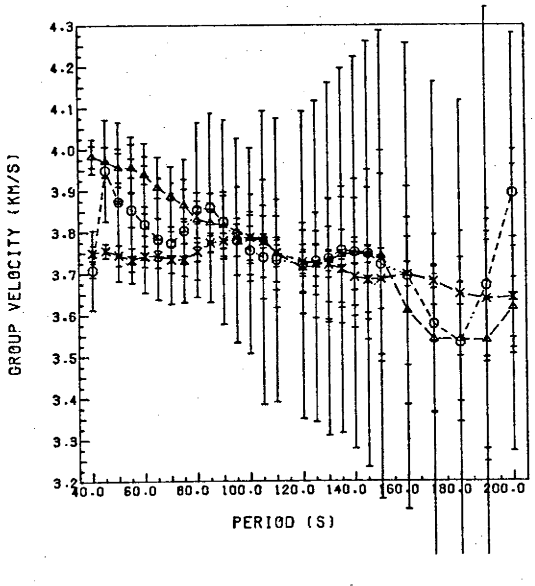

VAL12 ATTENUATION COEFFICIENTS

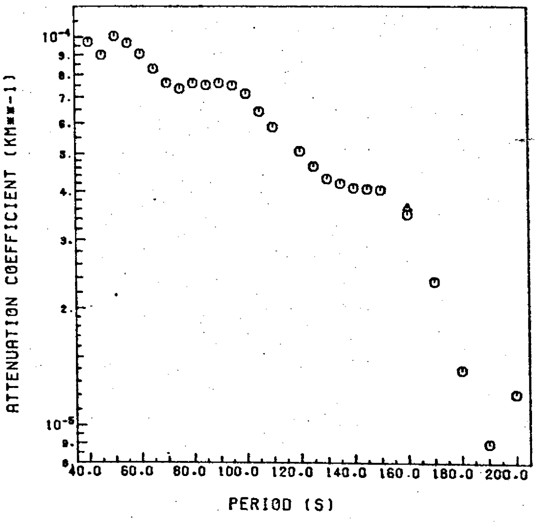

Figure 4.2(f) OBSERVED GROUP VELOCITI$S AND ATTENUATION COEFFICIENTS FOR STATIONS KIP, AND ZLP - see caption to Figure 4.2(e).

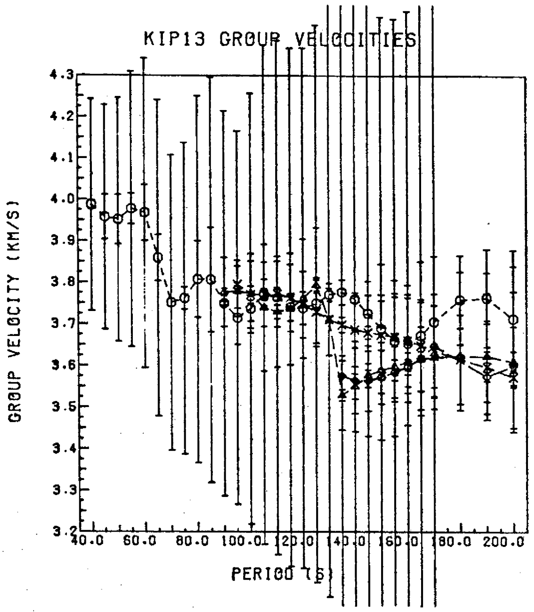

KIP13 GROUP VELOCITIES

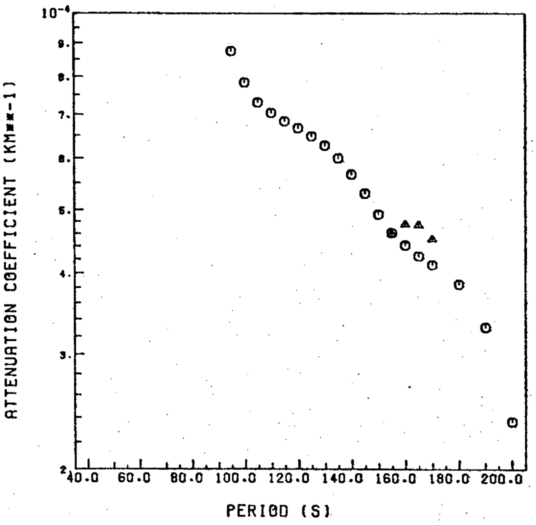

KIP13 ATTENUATION COEFFICIENTS

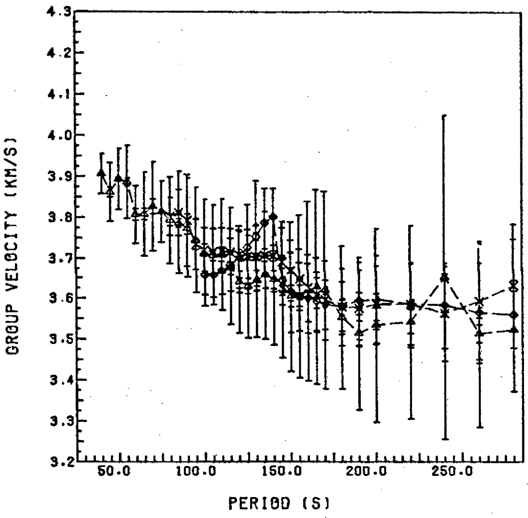

ZLP10 GROUP VELOCITIES

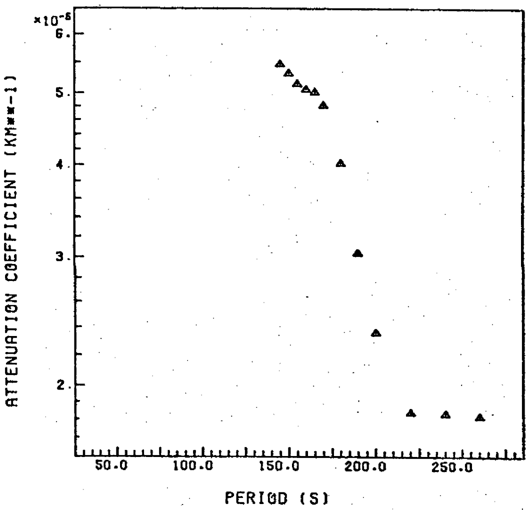

ZLP10 ATTENUATION COEFFICIENTS

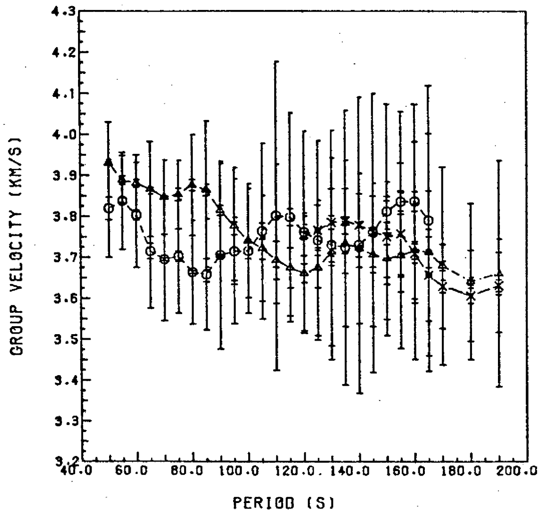

ZLP13 GROUP VELOCITIES

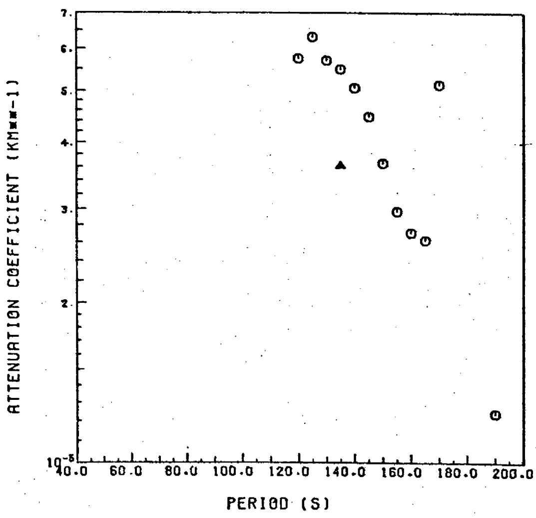

ZLP13 ATTENUATION COEFFICIENTS

Figure 4.2(g) OBSERVED GROUP VELOCITIES AND ATTENUATION COEFFICIENTS FOR STATIONS CTA AND ALQ -

see caption to Figure 4.2(e).

CTA10 GROUP VELOCITIES

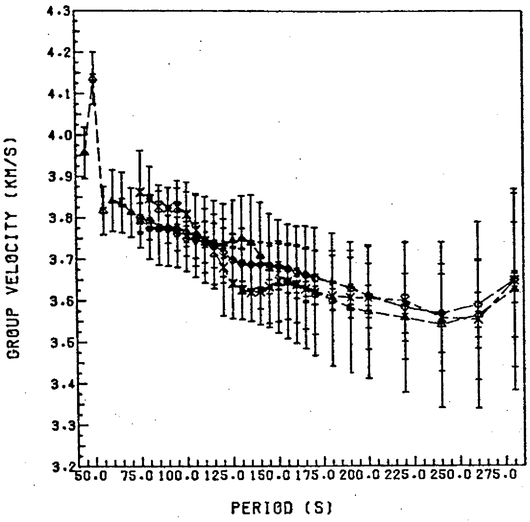

CTA10 ATTENUATION COEFFICIENTS

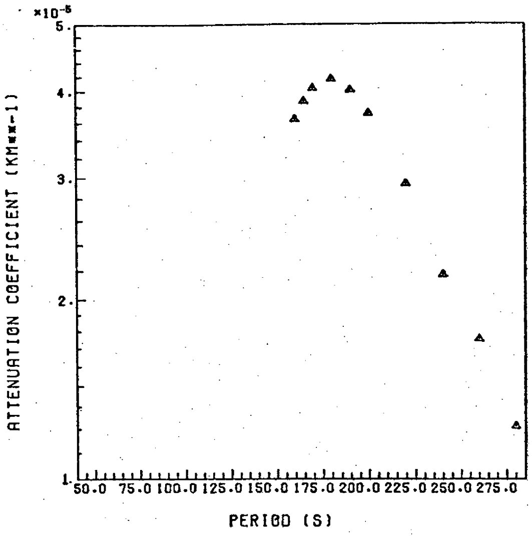

CTA13 GROUP VELOCITIES

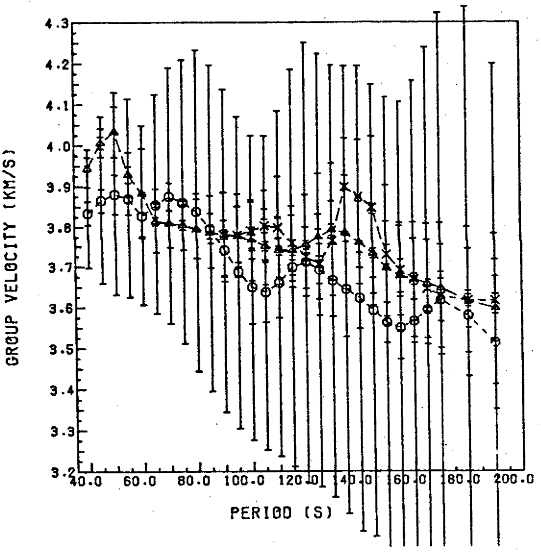

CTA13 ATTENUATION COEFFICIENTS

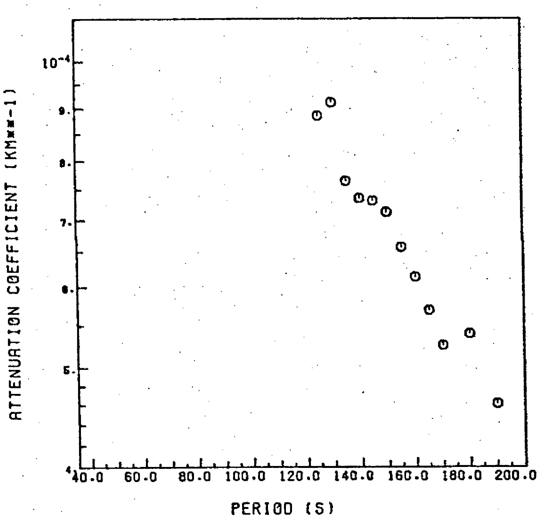

ALQ13 GROUP VELOCITIES

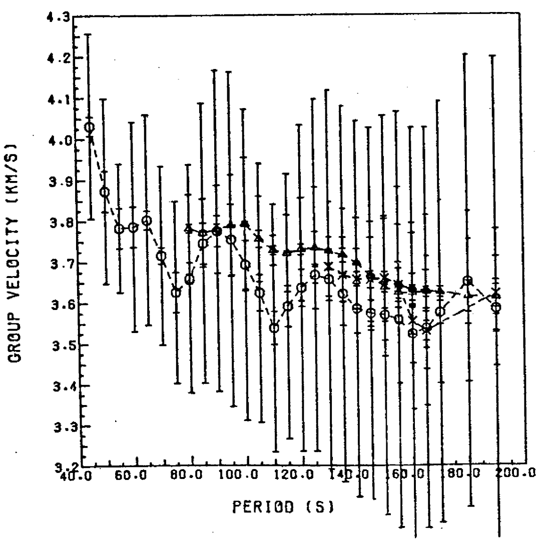

ALQ13 ATTENUATION COEFFICIENTS

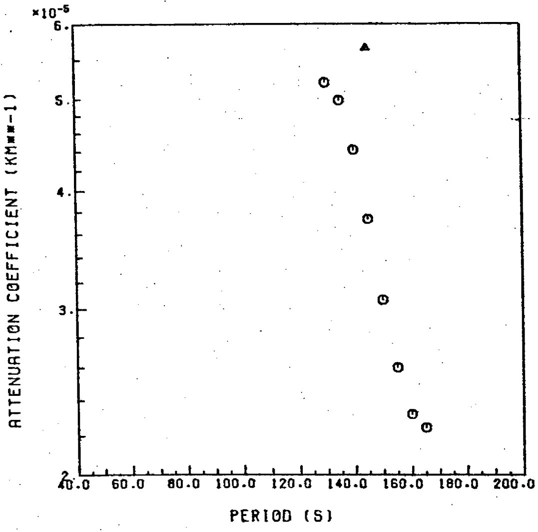

Figure 4.2(h) OBSERVED GROUP VELOCITIES AND ATTENUATION COEFFICIENTS FOR STATIONS KON, KIP AND NAI -
see caption to Figure 4.2(e).

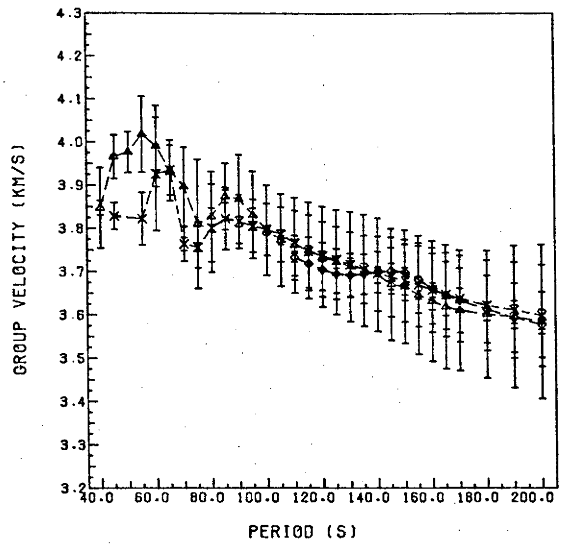
KON10 GROUP VELOCITIES

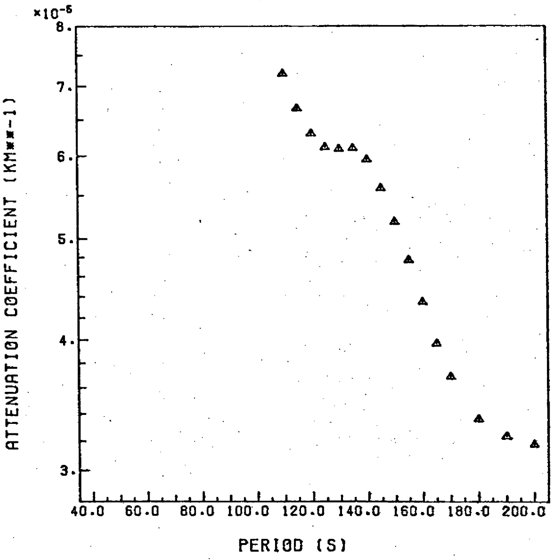
KON10 ATTENUATION COEFFICIENTS

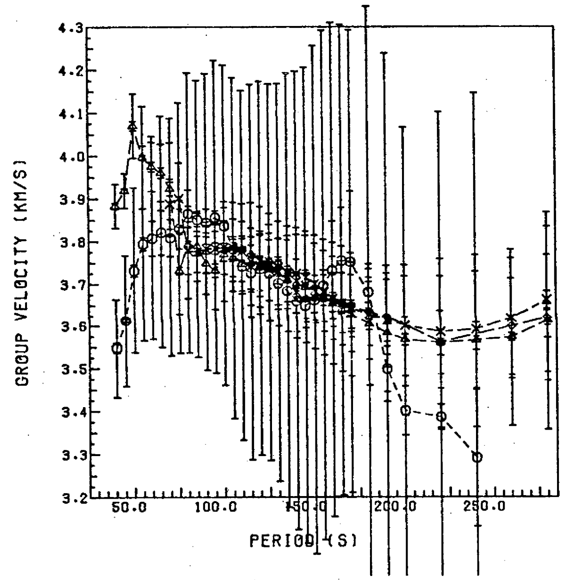
KON13 GROUP VELOCITIES

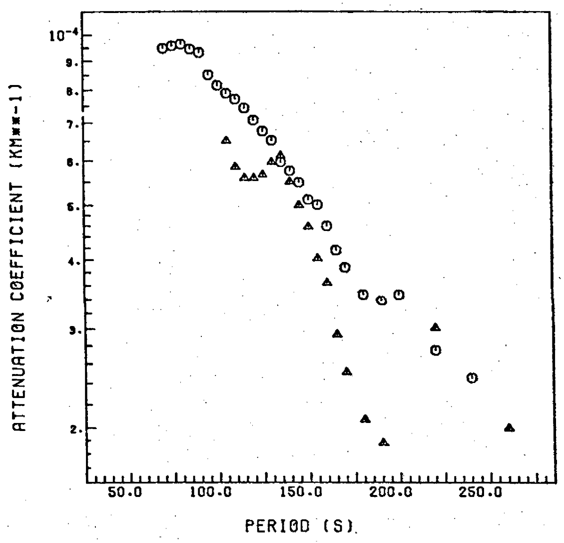
KON13 ATTENUATION COEFFICIENTS

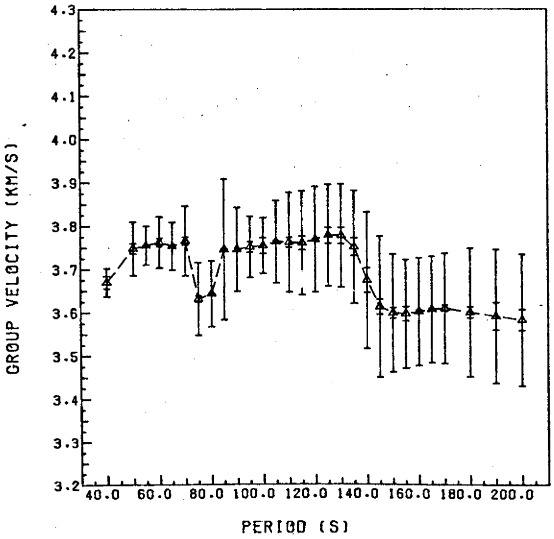
KIP10 GROUP VELOCITIES

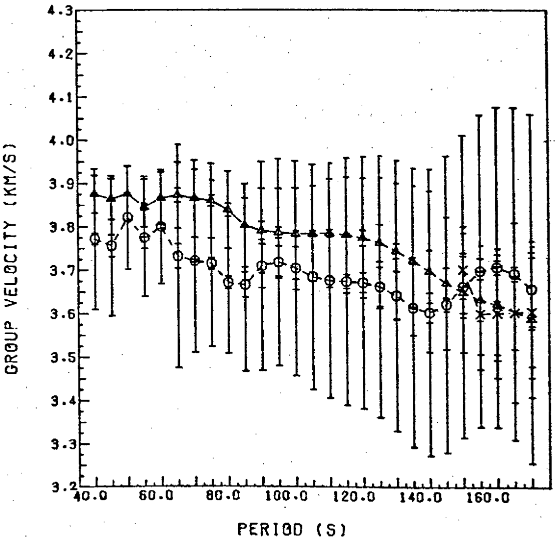
NAI12 GROUP VELOCITIES

Figure 4.2(i) OBSERVED GROUP VELOCITIES AND ATTENUATION COEFFICIENTS FOR STATIONS STU, ADE AND PTO -

see caption to Figure 4.2(e).

STU12 GROUP VELOCITIES

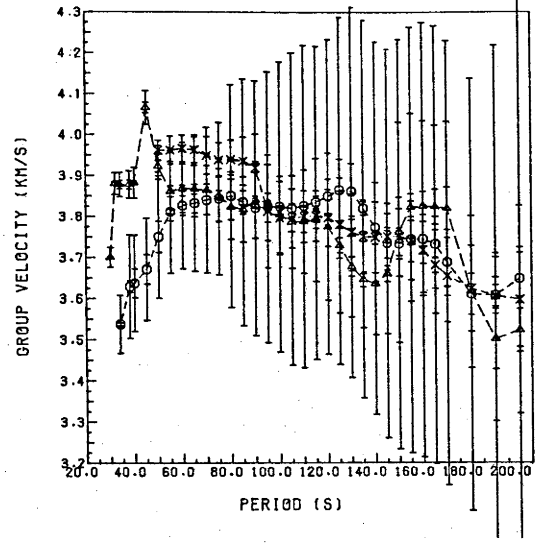

STU12 ATTENUATION COEFFICIENTS

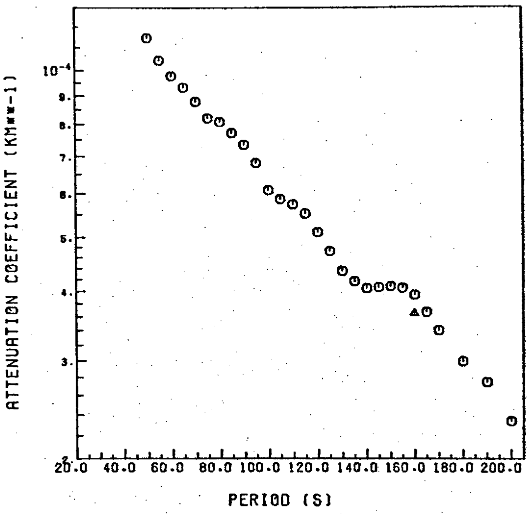

ADE12 GROUP VELOCITIES

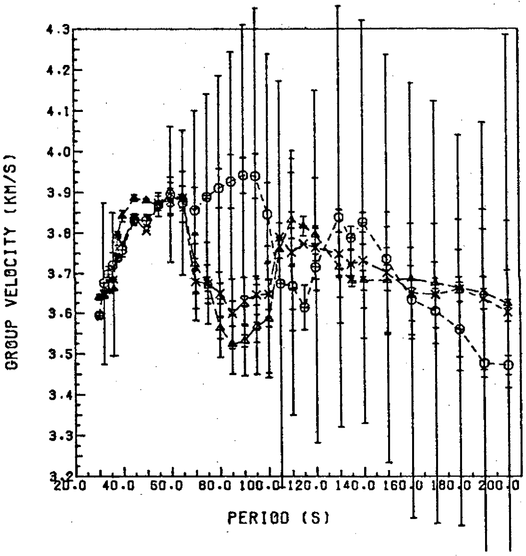

ADE12 ATTENUATION COEFFICIENTS

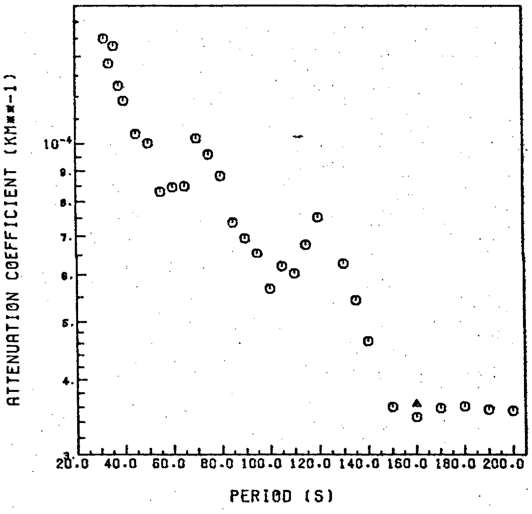

PT012 GROUP VELOCITIES

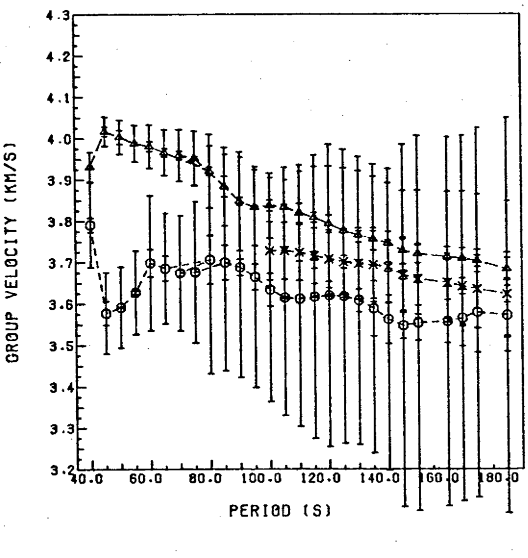

PT012 ATTENUATION COEFFICIENTS

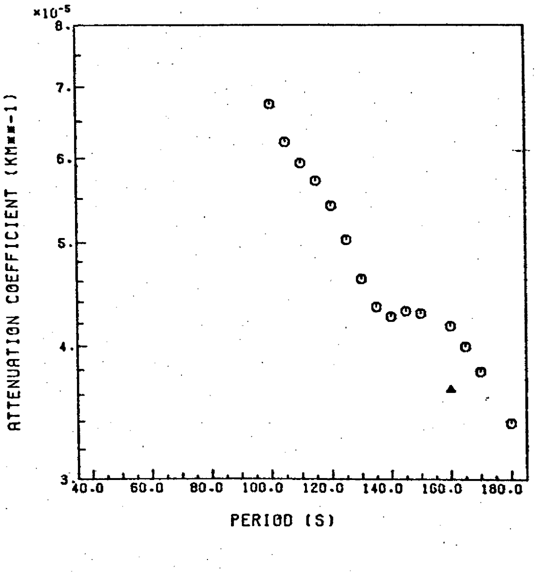

Figure 4.2(j) OBSERVED GROUP VELOCITIES AND ATTENUATION COEFFICIENTS FOR STATIONS CHG AND RAB -

see caption to Figure 4.2(e).

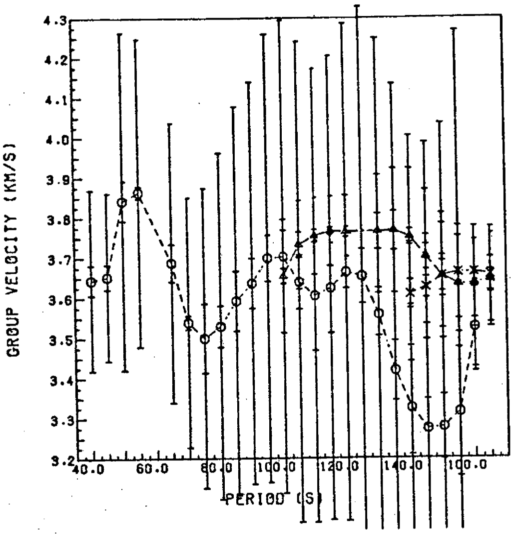
CHG13 GROUP VELOCITIES

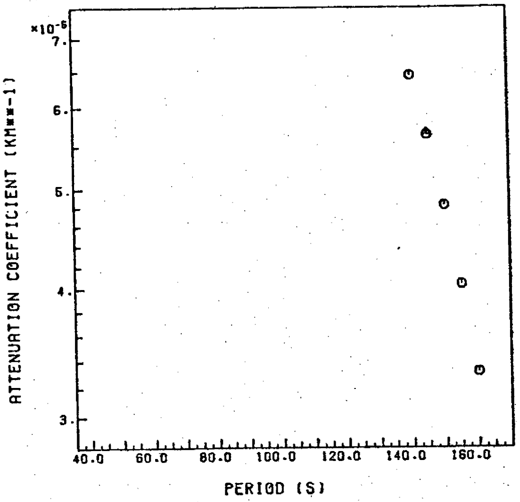
CHG13 ATTENUATION COEFFICIENTS

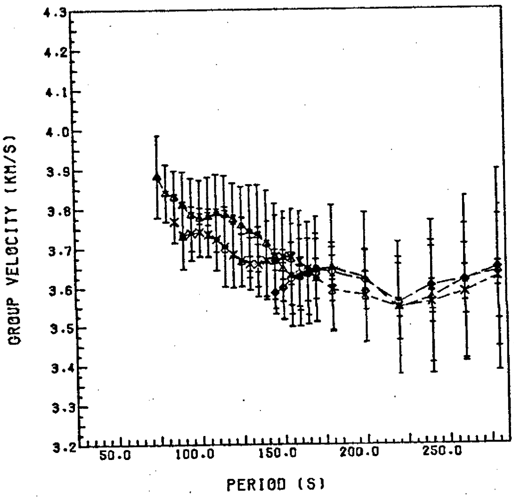
CHG10 GROUP VELOCITIES

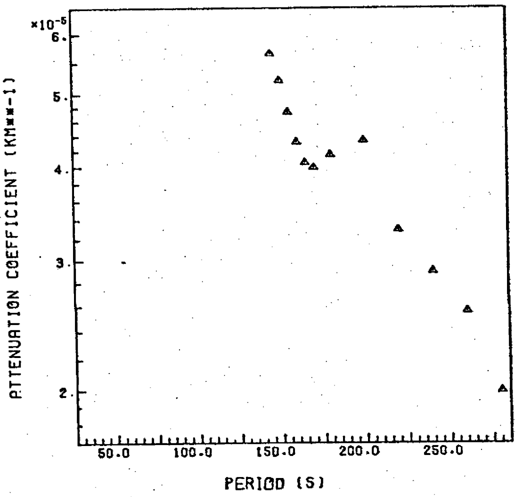
CHG10 ATTENUATION COEFFICIENTS

RAB12 GROUP VELOCITIES

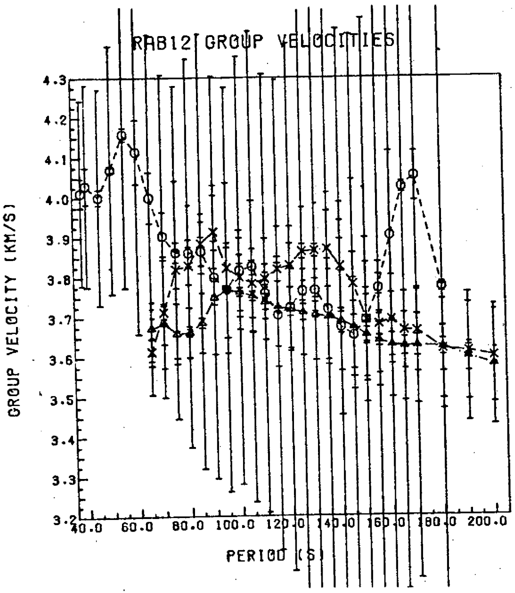

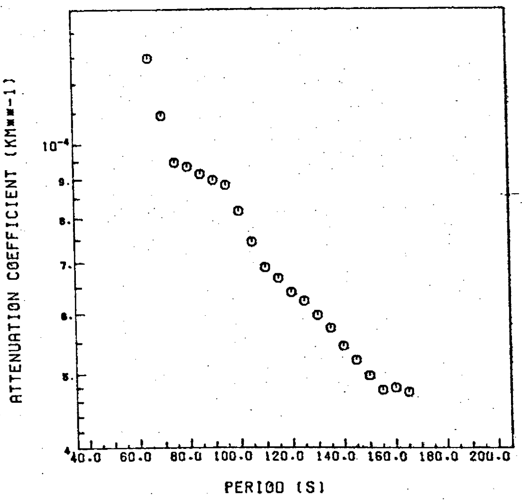
RAB12 ATTENUATION COEFFICIENTS

Figure 4.2(k) OBSERVED GROUP VELOCITIES FOR ATTENUATION COEFFICIENTS FOR STATION EIL -

see caption to Figure 4.2(e).

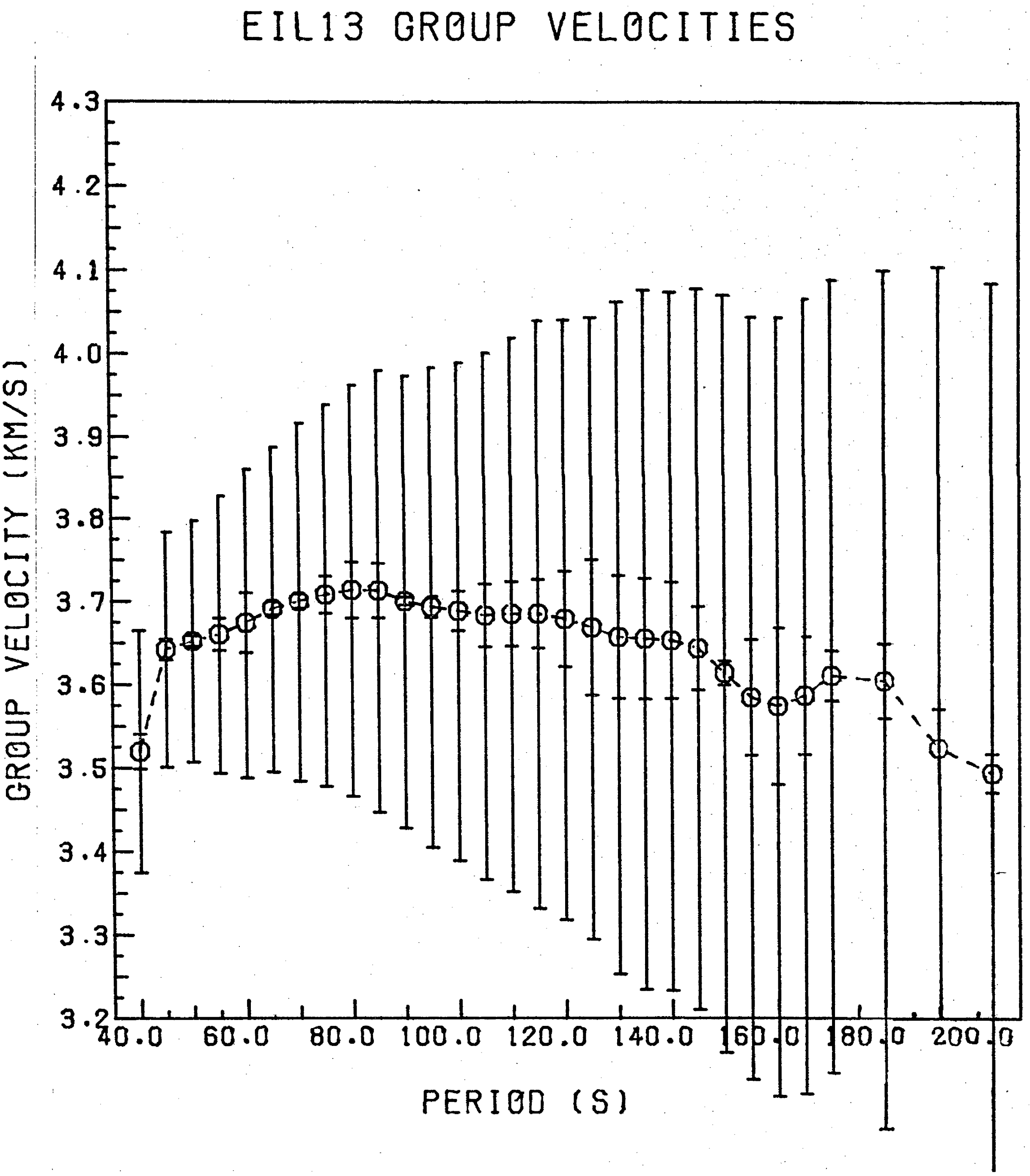
EIL13 GROUP VELOCITIES
GROUP VELOCITY (KM/S)
4.3
4.2
4.1
4.0
3.9
3.8
3.7
3.6
3.5
3.4
3.3
3.2
40.0
60.0
80.0
100.0
120.0
140.0
160.0
180.0
200.0
PERIOD (S)

$$u_{GC}\,[U_{R_1}, U_{R_2}] = \left(\frac{\ell_1}{U_{R_1}} + \frac{\ell_2}{U_{R_2}} \right)^{-1} \qquad (4.1)$$

where ℓ_i is the fraction of an earth circumference traversed by phase R_i with group velocity U_{R_i}. An example is shown in Figure 4.2(c) for the 12 October 1963 event recorded at station ADE (Table 4.1). Consider now the problem of calculating the variance of each great circle group velocity estimate.

The expansion of a function F of n random variables, x_1, x_2, ..., x_n by Taylor series expansion accurate to first order about some experimentally determined $\overline{X}_o$ is

$$F(\overline{X}) = F(\overline{X}_o) + \sum_{i=1}^{n} \left(\frac{\partial F}{\partial X_i} \right) (X_i - X_{io}) + 0(X_i^2). \qquad (4.2)$$

The variance of a linear function $F(\overline{X})$ is

$$\mathrm{var}[F] = \mathrm{var}[F(X_o)] + \sum_{i=1}^{n} \sum_{j=1}^{n} \left(\frac{\partial F}{\partial X_i} \right) \left(\frac{\partial F}{\partial X_j} \right) \mathrm{covar}\,[X_i, X_j] \quad (4.3)$$

(Jenkins and Watts 1968, p.76). If the value $\overline{X}$ is coincident with the mean μ and if all variables X_i are independent, then

$$\mathrm{var}[F(\overline{X})] \cong \sum_{i=1}^{n} \left(\frac{\partial F}{\partial X_i} \right)^2 \mathrm{var}\,[X_i] \,. \qquad (4.4)$$

The validity of this expansion is dependent upon the second and higher order partial derivatives of the function being small compared to the first order partials.

TABLE 4.2 EXPRESSIONS FOR GREAT CIRCLE GROUP VELOCITY AND THE VARIANCES DERIVED FROM GROUP VELOCITIES FOR R_1, R_2, R_3 AND R_4 COMBINATIONS.

Combination	Great Circle Group Velocity	Variance
R_1, R_2	$\left[\frac{\ell_1}{U_{R_1}} + \frac{\ell_2}{U_{R_2}}\right]^{-1}$	$U_{GC}^4 \frac{\ell_1^2}{U_{R_1}^4} \text{var } [U_{R_1}] + \frac{\ell_2^2}{U_{R_2}^2} \text{var } [U_{R_2}]$
R_1, R_3	$\left[\frac{\ell_3}{U_{R_3}} - \frac{\ell_1}{U_{R_1}}\right]^{-1}$	$U_{GC}^4 \frac{\ell_1^2}{U_{R_1}^4} \text{var } [U_{R_1}] + \frac{\ell_3^2}{U_{R_3}^4} \text{var } [U_{R_3}]$
R_1, R_4	$2\left[\frac{\ell_1}{U_{R_1}} + \frac{\ell_4}{U_{R_4}}\right]^{-1}$	$\frac{U_{GC}^4}{4} \frac{\ell_1^2}{U_{R_1}^4} \text{var } [U_{R_1}] + \frac{\ell_4^2}{U_{R_4}^4} \text{var } [U_{R_4}]$
R_2, R_3	$2\left[\frac{\ell_3}{U_{R_3}} + \frac{\ell_2}{U_{R_2}}\right]^{-1}$	$\frac{U_{CG}^4}{4} \frac{\ell_2^2}{U_{R_2}^4} \text{var } [U_{R_2}] + \frac{\ell_3^2}{U_{R_3}^4} \text{var } [U_{R_3}]$
R_2, R_4	$\left[\frac{\ell_4}{U_{R_4}} - \frac{\ell_2}{U_{R_2}}\right]^{-1}$	$U_{GC}^4 \frac{\ell_2^2}{U_{R_2}^4} \text{var } [U_{R_2}] + \frac{\ell_4^2}{U_{R_4}^4} \text{var } [U_{R_4}]$
R_3, R_4	$\left[\frac{\ell_3}{U_{R_3}} + \frac{\ell_4}{U_{R_4}}\right]^{-1}$	$\frac{U_{GC}^4}{9} \frac{\ell_3^2}{U_{R_3}^4} \text{var } [U_{R_3}] + \frac{\ell_4^2}{U_{R_4}^3} \text{var } [U_{R_4}]$

ℓ_i = ratio of the path length for phase R_i to the circumference of the great circle.

The variance of the great circle group velocity, U_{GC}, is

$$\mathrm{var}[U_{GC}] = \left(\frac{\partial U_{GC}}{\partial U_{R_1}}\right)^2 \mathrm{var}\,[U_{R_1}] + \left(\frac{\partial U_{GC}}{\partial U_{R_2}}\right)^2 \mathrm{var}[U_{R_2}]$$

$$= \frac{U_{GC}^4}{U_{R_1}^4}\,\ell_1^{\,2}\,\mathrm{var}[U_{R_1}] + \frac{U_{GC}^4}{U_{R_2}^4}\,\ell_2^{\,2}\,\mathrm{var}[U_{R_2}]\ . \qquad (4.5)$$

To verify that this expression for the variance of U_{GC} is indeed valid, consider the higher order partial derivatives of U_{GC} which were neglected in Equations 4.3 and 4.5:

$$\frac{\partial^2 U_{GC}}{\partial U_{R_1}\,\partial U_{R_2}} = 2\,U_{GC}^3\,\frac{\ell_1\ell_2}{U_{R_1}^{\,2}U_{R_2}^{\,2}}\ ,$$

$$\frac{\partial^2 U_{GC}}{\partial U_{R_1}^{\,2}} = 2\,\ell_1\,\frac{U_{GC}^2}{U_{R_1}^{\,3}}\left(\frac{U_{GC}}{U_{R_1}}\,\ell_1 - 1\right)\ , \qquad (4.6)$$

$$\frac{\partial^2 U_{GC}}{\partial U_{R_2}^{\,2}} = 2\,\ell_2\,\frac{U_{GC}^2}{U_{R_2}^{\,3}}\left(\frac{U_{GC}}{U_{R_2}}\,\ell_2 - 1\right)\ .$$

Since the observed values of group velocity in the period range 50 to 350 seconds are in the range 3.0 to 4.5 km/s and since U_{GC} always lies between U_{R_1} and U_{R_2}, assume $U_{R_1} \simeq U_{R_2} \simeq U_{GC}$, then where C is the circumference of the great circle parth and A_{R_i} and $A_{R_{i+2}}$ are the spectral amplitudes for the period T of the Rayleigh phases R_i and R_{i+2}. Maximum amplitudes of Rayleigh phases in narrow-band filtered seismograms (also used for the determination of group velocity) have been used as estimates of the spectral amplitude. Filtered amplitudes and attenuation coefficients for station ADE for the 12 October 1963 event are shown in Figure 4.2(b) and 4.2(d). Attenuation coefficients for other seismograms are shown in Figure 4.2(e) to 4.2(k). The average attenuation for each great circle path shown in Figure 4.1 was calculated by averaging all measurements of attenuation coefficients for all stations within each azimuth window for overlapping 20 second period ranges. Global mean attenuation coefficients (Figure 4.3(c)) were calculated by averaging mean path attenuation coefficients for all paths for each 20 second averaging window, again giving unit weight to each path.

Global mean attenuation coefficients (Figure 4.3(c), Table 4.3) for the complete range of periods from 50 to 600 seconds were calculated by combining data sets for individual paths used in Chapter 3 (Figure 3.9) and this chapter (Figure 4.3(a)) in similar manner to that described in Sec. 4.2.2 for the group velocities.

Figure 4.3 GLOBAL AVERAGE GREAT CIRCLE GROUP VELOCITIES AND ATTENUATION COEFFICIENTS -

Global mean group velocities calculated from mean group velocities for each station averaged over 20 second overlapping windows and weighted equally for each path are shown in (b) for only data reported in this chapter and in (d) for all data from this chapter combined with data from Chapter 3. Global mean attenuation coefficients averaged over the same 20 second averaging windows are shown in (a) for only data reported in this chapter and in (c) for all data from this paper combined with data from Chapter 3.

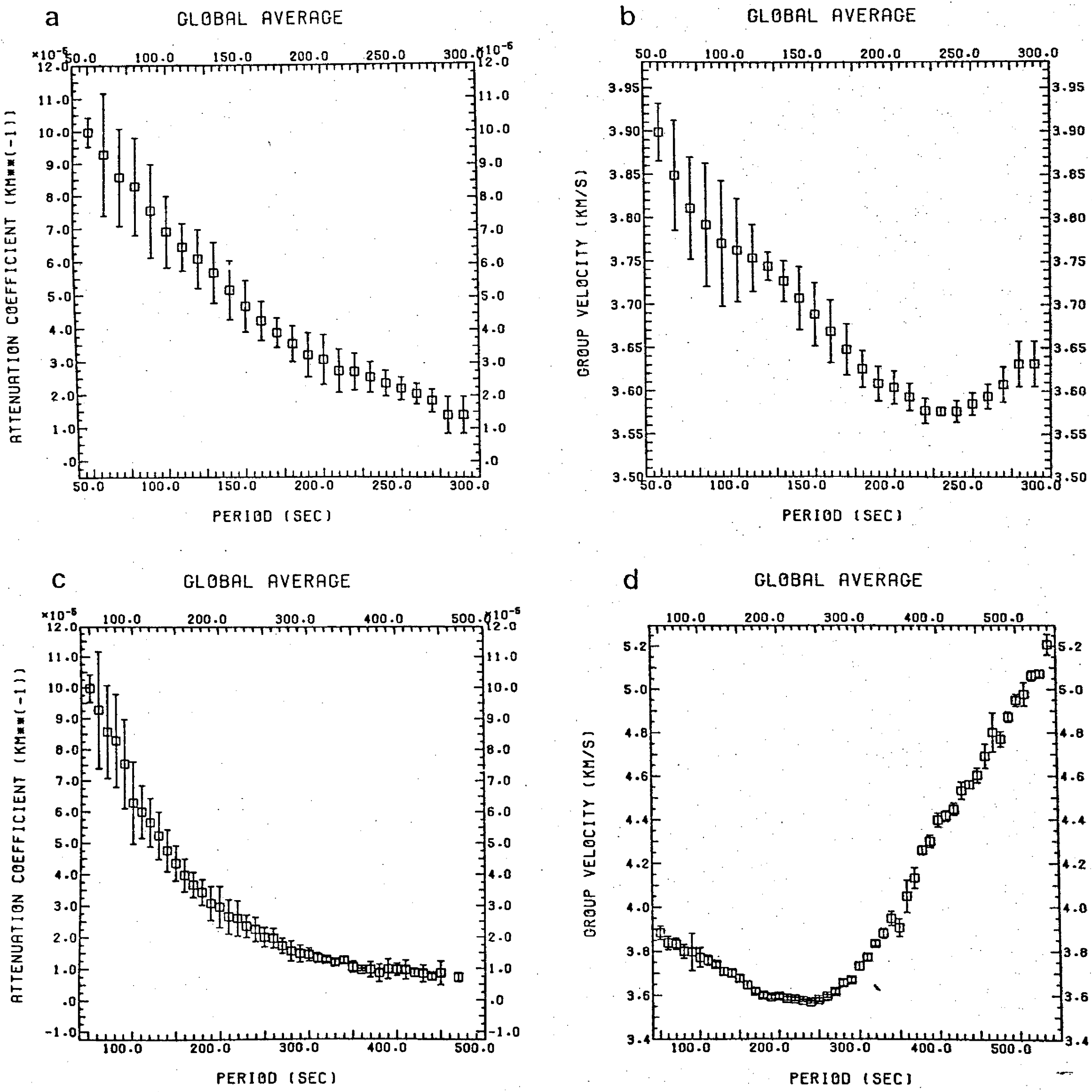
a
GLOBAL AVERAGE
ATTENUATION COEFFICIENT (KM**(-1))
×10⁻⁵
PERIOD (SEC)
b
GLOBAL AVERAGE
GROUP VELOCITY (KM/S)
PERIOD (SEC)
c
GLOBAL AVERAGE
ATTENUATION COEFFICIENT (KM**(-1))
×10⁻⁵
PERIOD (SEC)
d
GLOBAL AVERAGE
GROUP VELOCITY (KM/S)
PERIOD (SEC)

Table 4.3

GLOBAL AVERAGES FOR ALL PATHS - 50 to 550 SECOND PERIODS

T_m (s)	T_{low} (s)	T_{hi} (s)	Group Velocity (km/s)	+/-	No. of Paths	Phase Velocity (km/s) from integration using Simpson's rule*	Trapezoidal** rule	+/-	Attenuation Coefficient (1./km)	+/-	No. of Paths
50	40	60	3.8847	0.0031	6	-	-	-	9.9E-05	4.4E-06	4
60	50	70	3.8383	0.0031	7	3.9724	3.9536	.0298	9.2E-05	1.8E-05	6
70	60	80	3.8024	0.0044	9	3.9931	3.9803	.0287	8.5E-05	1.4E-05	6
80	70	90	3.7998	0.0032	9	4.0211	4.0101	.0265	8.2E-05	1.4E-05	7
90	80	100	3.7974	0.0085	9	4.0512	4.0426	.0211	7.5E-05	1.4E-05	7
100	90	110	3.7720	0.0045	9	4.0840	4.0776	.0151	6.2E-05	1.3E-05	8
110	100	120	3.7588	0.0023	9	4.1233	4.1161	.0124	6.0E-05	8.4E-06	8
120	110	130	3.7399	0.0014	9	4.1597	4.1559	.0106	5.6E-05	7.7E-06	8
130	120	140	3.7079	0.0017	9	4.2043	4.1983	.0099	5.2E-05	7.5E-06	9
140	130	150	3.7004	0.0017	9	4.2453	4.2425	.0092	4.7E-05	6.6E-06	9
150	140	160	3.6761	0.0016	9	4.2936	4.2890	.0086	4.3E-05	5.5E-06	9
160	150	170	3.6464	0.0017	9	4.3409	4.3390	.0079	3.9E-05	5.2E-06	9
170	160	180	3.6176	0.0012	9	4.3965	4.3922	.0074	3.7E-05	3.9E-06	9
180	170	190	3.5987	0.0013	9	4.4491	4.4478	.0071	3.4E-05	4.0E-06	9
190	180	200	3.5908	0.0009	9	4.5100	4.5062	.0070	3.1E-05	5.3E-06	9
200	190	210	3.5943	0.0010	9	4.5684	4.5674	.0067	3.0E-05	6.5E-06	9
210	200	220	3.5836	0.0008	9	4.6349	4.6314	.0064	2.6E-05	5.4E-06	9
220	210	230	3.5805	0.0008	8	4.6986	4.6978	.0062	2.6E-05	5.5E-06	5
230	220	240	3.5736	0.0005	8	4.7695	4.7661	.0062	2.4E-05	3.5E-06	8
240	230	250	3.5667	0.0005	8	4.8371	4.8368	.0063	2.2E-05	3.8E-06	5
250	240	260	3.5772	0.0007	8	4.9131	4.9095	.0064	2.0E-05	3.0E-06	8
260	250	270	3.5937	0.0006	8	4.9833	4.9833	.0064	2.0E-05	3.1E-06	5
270	260	280	3.6142	0.0011	8	5.0616	5.0580	.0061	1.7E-05	2.4E-06	8
280	270	290	3.6540	0.0023	8	5.1325	5.1327	.0056	1.5E-05	3.2E-06	4
290	280	300	3.6665	0.0019	8	5.2113	5.2079	.0049	1.5E-05	2.7E-06	8
300	290	310	3.7301	0.0019	7	5.2829	5.2828	.0041	1.4E-05	2.1E-06	3
310	300	320	3.7696	0.0015	7	5.3589	5.3559	.0032	1.3E-05	1.6E-06	7
320	310	330	3.8329	0.0011	7	5.4278	5.4277	.0025	1.3E-05	7.5E-07	3
330	320	340	3.8787	0.0023	7	5.5008	5.4979	.0016	1.2E-05	1.0E-06	7
340	330	350	3.9459	0.0033	7				1.2E-05	1.0E-06	3
350	340	360	3.9041	0.0040	7				1.0E-05	1.7E-06	7
360	350	370	4.0471	0.0074	7				9.7E-06	4.1E-07	3
370	360	380	4.1307	0.0047	7				9.7E-06	2.4E-06	7
380	370	390	4.2576	0.0020	7				8.6E-06	2.8E-06	5
390	380	400	4.2983	0.0029	7				9.8E-06	3.1E-06	7
400	390	410	4.3966	0.0032	7				9.6E-06	1.9E-06	4
410	400	420	4.4147	0.0025	7				9.5E-06	3.0E-06	7
420	410	430	4.4458	0.0028	7				8.6E-06	1.2E-06	4
430	420	440	4.5312	0.0040	7				8.3E-06	2.7E-06	7
440	430	450	4.5594	0.0019	7				7.4E-06	1.0E-06	2
450	440	460	4.6022	0.0034	7				8.5E-06	3.7E-06	4
460	450	470	4.6900	0.0055	7						-
470	460	480	4.8003	0.0090	7				7.2E-06	1.4E-06	1
480	470	490	4.7688	0.0035	7						
490	480	500	4.8721	0.0024	7						
500	490	510	4.9490	0.0028	7						
510	500	520	4.9766	0.0054	7						
520	510	530	5.0619	0.0023	6						
530	520	540	5.0715	0.0017	5						
540	530	550	5.2073	0.0048	5						
550	540	560	5.3038	0.0081	6						
560	550	570	5.5223	0.0035	5						
570	560	580	5.5774	0.0048	5						
580	570	590	5.5923	0.0020	4						
590	580	600	5.6259	0.0041	3						
600	590	610	5.7295	0.0052	2						

---

* integration by Simpson's rule started at 340 sec and 330 sec with phase velocities of 5.5665 and 5.5008 km/sec.

** integration by trapesoidal rule started at 340 sec with phase velocity of 5.5665 km/sec.

Sec. 4.3 CALCULATION OF PHASE VELOCITIES AND FREE OSCILLATION PERIODS FROM GREAT CIRCLE GROUP VELOCITIES

Observations of free oscillation periods require Fourier analysis of long records containing passages of the same wave train until it has been completely damped in the period range of interest. Since attenuation of fundamental mode wave trains increases with decreasing period in the 50 to 200 second period range, wave trains damp out so rapidly that free oscillation measurements are difficult and accuracy is low. Phase velocities can be calculated by integrating group velocity since

$$C(T) = \left[T \int_{T}^{T_1} \frac{d\tau}{\tau^2 U(\tau)} + \frac{T}{C_1 T_1} \right]^{-1} \tag{4.9}$$

where U(T) is the group velocity measured at period T, and C_1 the phase velocity at period T_1. The equivalent free oscillation periods are roots of the equation

$$C(T) - \frac{2\pi a}{(\ell + 1/2)T} = 0 \tag{4.10}$$

where a is the mean radius of the earth, and ℓ, the angular order number of the spheroidal oscillation ${}_0S_\ell$. Since U(T) is a slowly varying function, integration was performed using both the trapezoidal rule and Simpson's rule. For each period T the difference between phase velocities calculated by these two methods of integration (Table 4.3) was much smaller than the standard deviation of the phase velocity estimate calculated by the method described in the next section.

Sec. 4.3.1 Phase Velocities and their Variances Calculated by Integration of Group Velocities

Consider the observed group velocity $U(T)$ to be the sum of two functions, $u(T)$, the error free group velocity and $\varepsilon(T)$ an error term:

$$U(T) = u(T) + \varepsilon(T). \tag{4.11}$$

The variance of the group velocity at period T is

$$\mathrm{var}[U(T)] = E[\{U(T) - E[U(T)]\}^2], \tag{4.12}$$

and since $E[U(T)] = u(T)$,

$$\mathrm{var}[U(T)] = E[\varepsilon^2(T)]. \tag{4.13}$$

The phase velocity $C(T)$ can be calculated from $U(T)$ by integration

$$C(T) = \left[T \int_T^{T_1} \frac{d\tau}{\tau^2 U(\tau)} + \frac{T}{c_1(T_1)} \right]^{-1} \tag{4.13}$$

where c_1 is the phase velocity at period T_1.

Expanding $1/U(T)$ to the first order

$$\frac{1}{U(T)} = \frac{1}{u(T)} - \frac{\varepsilon(T)}{u^2(T)} \tag{4.15}$$

and substituting into equation 4.14, yields

$$C(T) = \left[T \int_T^{T_1} \frac{d\tau}{\tau^2 u(T)} - T \,{}^{T_1}_{T} \frac{\varepsilon(\tau)d\tau}{\tau^2 u^2(\tau)} \right]^{-1} \tag{4.16}$$

and expanding Equation 4.16 to first order:

$$C(T) = \left[T\int_T^{T_1} \frac{d\tau}{\tau^2 u(\tau)} + \frac{T}{c_1 T_1} \right]^{-1} + T\int_T^{T_1} \frac{\varepsilon(\tau)d\tau}{\tau^2 u^2(\tau)} \cdot \left[T\int_T^{T_1} \frac{d\tau}{\tau^2 u(\tau)} + \frac{T}{c_1 T_1} \right]^{-2} . \tag{4.17}$$

The first term represents an error free estimate of the phase velocity c(T) and is the expectated value of the phase velocity C(T). Equation 4.17 simplifies to

$$C(T) = c(T) + c^2(T) \; . \; T \; . \int_T^{T_1} \frac{\varepsilon(\tau)d\tau}{\tau^2 u^2(\tau)} \quad . \tag{4.18}$$

The variance of the phase velocity C(T) can be calculated from equation 4.18

$$\mathrm{var}[C(T)] = E[\{C(T) - E[C(T)]\}^2] = E[(C(T) = c(T))^2]$$

$$= c^4(T) \; . \; T^2 \; . \int_T^{T_1} \int_T^{T} \frac{E[\varepsilon(\tau)\varepsilon(\eta)] \; d\eta d\tau}{\tau^2 \eta^2 u^2(\tau) u^2(\eta)} \; . \tag{4.19}$$

If ε(τ) represents errors which are uncorrelated, Equation 4.19 simplifies to

$$\mathrm{var}[C(T)] = c^4(T) \; . \; T^2 \; . \left[\int_T^{T_1} \frac{\sqrt{\mathrm{var}[U(\tau)]} \; d\tau}{\tau^2 u^2(\tau)} \right]^2 , \tag{4.20}$$

since var [ε(τ)] is the variance of the group velocity estimate at period τ, var [U(τ)].

Sec. 4.3.2 Calculation of Equivalent Spheroidal Oscillation Period

Spheroidal oscillation periods were derived from the phase velocities by determining the roots of Equation 4.10 with linearly interpolated values for periods between those shown in Table 4.3. The variance of each effective free oscillation period is then

$$\mathrm{var}(T) = \frac{(\ell + 1/2)^2 T^4}{4\pi^2 a^2} \ \mathrm{var}\,(C(T)), \qquad (4.21)$$

where the var (C(T)) is interpolated linearly between values shown in Table 4.3. Spheroidal oscillation periods calculated by this method are listed in Table 4.4 along with observed periods of Derr (1969) and Gilbert and Dziewonski (1975).

Since these periods were calculated from observed group velocities, they must be corrected for anelastic dispersion before inversion can be attempted. The Liu et al. (1976) correction for Rayleigh wave phase velocities was used as a basis for deriving the comparable equation for spheroidal oscillation periods

$$\delta T = \frac{T}{\pi Q_R} \ \ell n(T) \qquad (4.22)$$

for the first order perturbation δT to spheroidal mode periods caused by anelasticity. This expression also appears in Hart et al. (1977a, 1977b). The application of this correction makes free periods directly comparable to body wave travel times at periods of about 1 second.

Sec. 4.4 DISCUSSION

The paths shown in Figure 4.1 traverse all of the major structural features of the earth: stable continental platforms, ocean basins, mid-ocean ridge zones, and island arcs. The Himalayas are also well sampled. The global average group velocities and attenuation coefficients presented in Table 4.3 should therefore represent good areal averages for the whole earth. Selected global average group velocities from Table 4.3 are presented as solid circles in Figure 4.4(a). Group velocities for a path from Mexico to Riverview (RIV) in Sydney, Australia and another from Rat Island in the Aleutians to Charters Towers (CTA) in Queensland, Australia (Landisman et al. 1969) are also shown in Figure 4.4(a). Of these two paths the Rat Island - CTA path traverses the oldest parts of the western Pacific Ocean while the Mexico - RIV path crosses the East Pacific Rise and passes through older portions of the Pacific as well as the northern extension of the New Hebrides Island arc. In addition, group velocities for Forsyth's (1975b) pure path group velocities for ridge zones of 0 - 5 m.y., 5 - 10 m.y. and 10 - 20 m.y. old oceanic crust in the eastern Pacific Ocean are plotted in Figure 4.4(a). All of these, together with the average continental group velocities of Dziewonski et al. (1975) are compared with our global average group velocities (Table 4.3) in Figure 4.4(a). Parametric Earth Models (PEM) for continents and oceans (Dziewonski et al. 1975) are also shown for reference. It is clear that the global average group velocities are well bracketed by both continental and oceanic data in the 70 to 250 second period range.

In Figure 4.4(b) our global average group velocities are contrasted with Rayleigh wave group velocities of several recent earth models: PEM oceanic and continental models (Dziewonski et al. 1975), B1 of Jordan and Anderson (1974), 5.08 M of Kanamori and Press (1970) and HB1 of Haddon and Bullen (1969). Of these models only the PEM models

Figure 4.4 COMPARISON OF GLOBAL AVERAGE GROUP VELOCITIES WITH MODELS AND OTHER DATA -

(a) Selected global average group velocities from Figure 4.3(d) and Table 4.3 are shown as solid dots. For reference, solid and dashed lines indicate group velocities of the Parametric Earth Models (Dziewonski *et al.* 1975) for oceanic and continental structures respectively. Continental Rayleigh wave group velocity data used in devising PEM models are shown as open circles. Group velocities for an old oceanic path (CTA-Rat Is.) and a more average ocean path (RIV-Mex) are shown as dashed lines (both from Landisman *et al.* 1969). "Pure Path" velocities for mid-ocean ridge zones of 0-5, 5-10 and 10-20 m.y. ages (Forsyth 1975b) are shown as triangles and diamonds. The 6 pointed star at a period of about 140 seconds is two superimposed triangles.

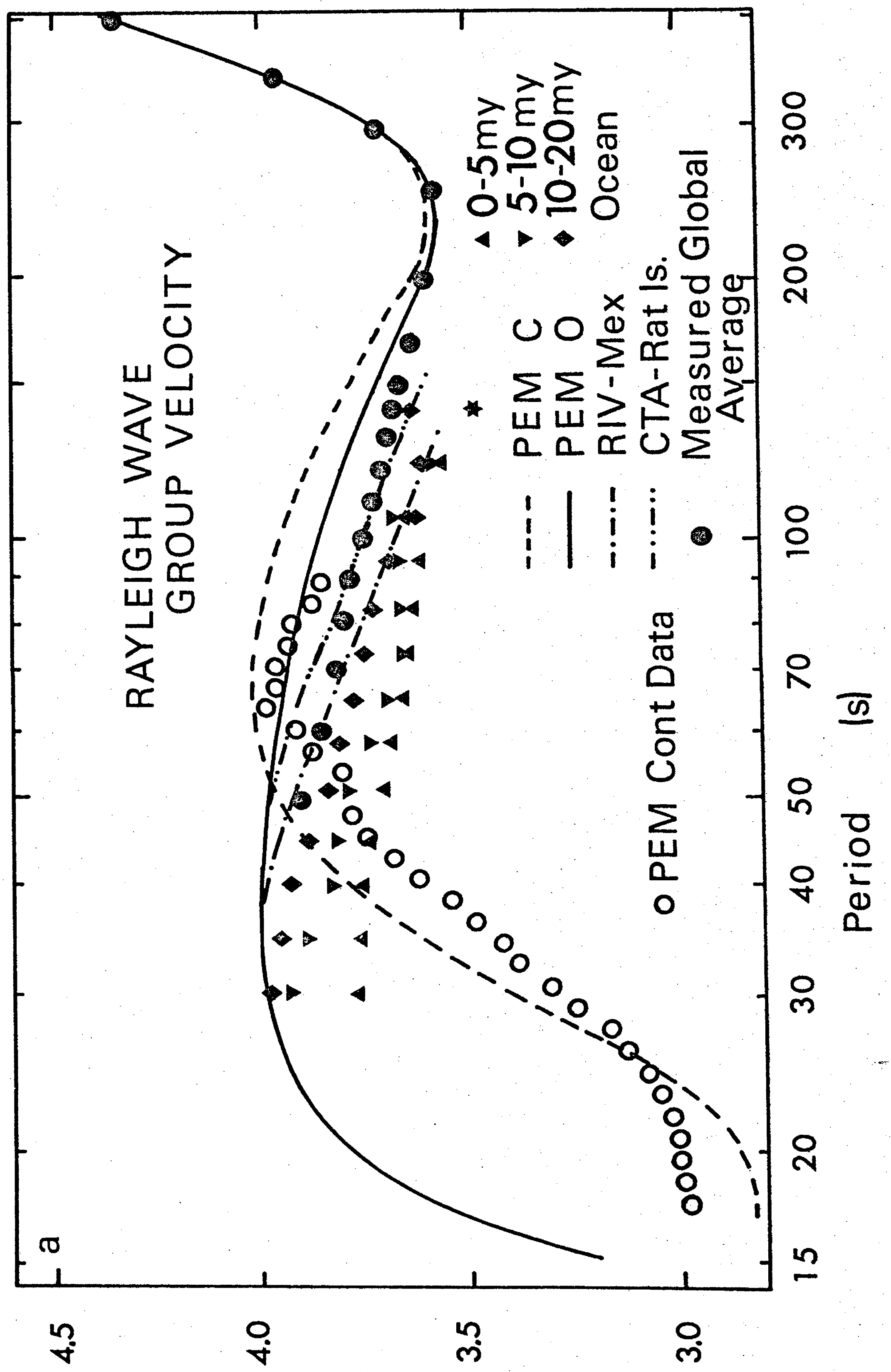
a
RAYLEIGH WAVE
GROUP VELOCITY
PEM C
PEM O
RIV-Mex
CTA-Rat Is.
Measured Global Average
○ PEM Cont Data
▲ 0-5my
▼ 5-10my
◆ 10-20my
Ocean
4.5
4.0
3.5
3.0
Group Velocity (km/s)
15
20
30
40
50
70
100
200
300
Period (s)

Figure 4.4 COMPARISON OF GLOBAL AVERAGE GROUP VELOCITIES WITH MODELS AND OTHER DATA (contd.) -

(b) Selected global average group velocities from Figure 4.3(d) and Table 4.3 are shown as dots with PEM oceanic and continental models again shown as solid and dashed lines. Also shown are models HB1 of Haddon and Bullen (1969), B1 of Jordan and Anderson (1974) and 5.08 M of Kanamori and Press (1970). Note particularly that all of these models lie up to 0.25 km/s above our global average group velocities for periods between 100 and 200 seconds.

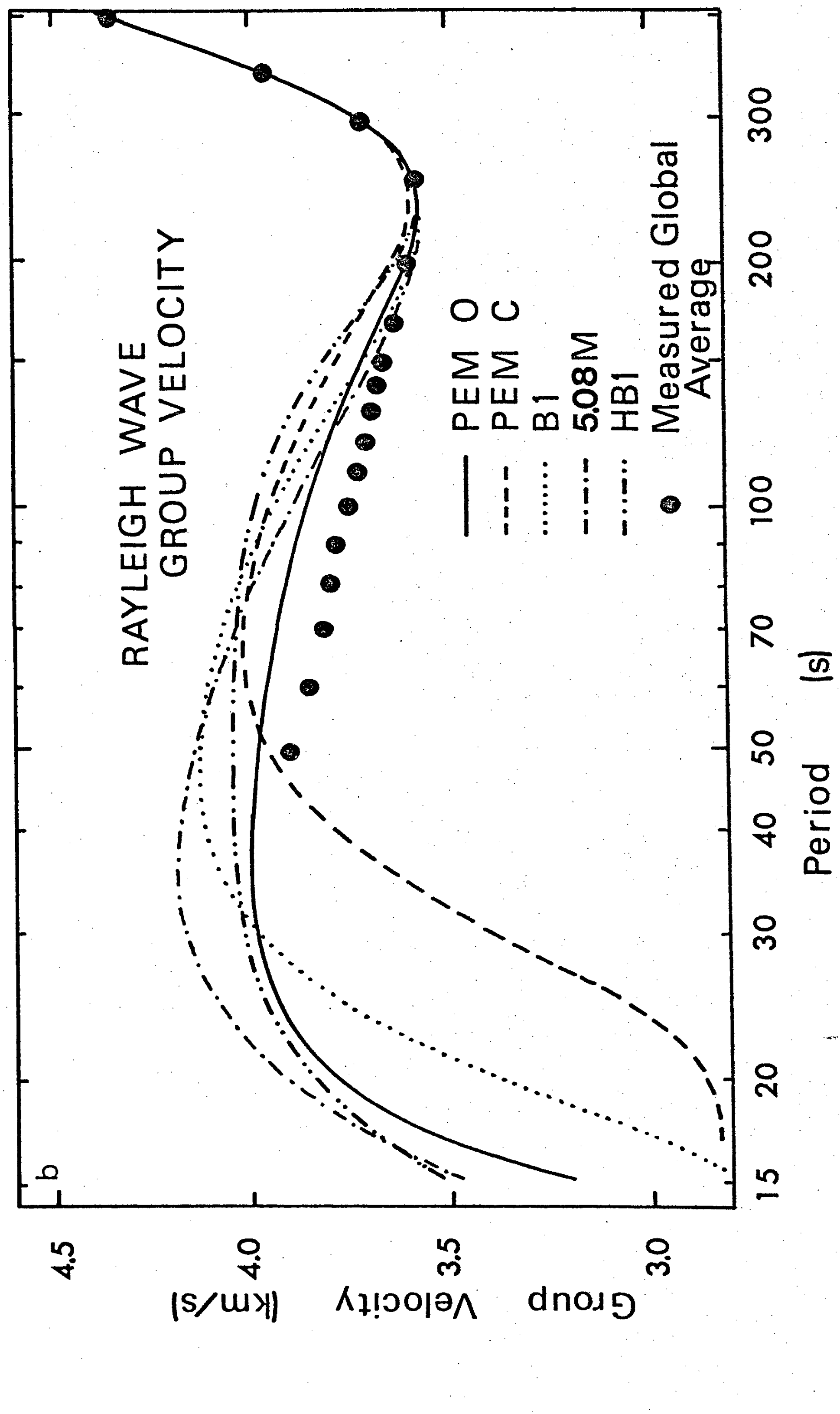
b
RAYLEIGH WAVE
GROUP VELOCITY
PEM O
PEM C
B1
5.08M
HB1
Measured Global Average
Group Velocity (km/s)
4.5
4.0
3.5
3.0
Period (s)
15
20
30
40
50
70
100
200
300

incorporated fundamental mode Rayleigh wave group velocities for the period range 20 to 90 seconds for "typical" continental and oceanic paths. The shortest period fundamental spheroidal mode used in PEM was ${}_0S_{66}$ (141.22 seconds). The inclusion of body wave travel times for epicentral distances greater than 30° and differential travel times does not appear to constrain upper mantle velocities well enough to produce acceptable Rayleigh wave group velocities in the 80 to 250 second period range. All models shown in Figure 4.4(b) exceed the global average group velocities by as much as 0.25 km/s. Both of the PEM oceanic and continental models lie above our global averages. It appears that it will be necessary to fit group velocities of surface waves for periods from a few tens of seconds to at least 250 second periods in order to properly constrain average or regional earth models for the upper mantle.

Global average phase velocities (Table 4.3) derived by intergration of global average group velocities lie between Weidner's (1974) highest and lowest phase velocities for Atlantic Ocean paths for periods between 60 and 120 seconds. Our global average phase velocities coincide with Weidner's phase velocities for oceanic paths which are composed of 40 to 50 percent of mid-ocean ridge zone of less than 40 to 50 m.y. age or which cross the Caribbean. At periods shorter than 150 seconds, mid-ocean ridge zones and island arc regions both seem to cause greater deviations from global average group and phase velocities than do continents and older ocean basins. This inference is also supported by Wu's (1972) pure path dispersion study in which he finds ridge group velocities to be as much as 0.41 km/s lower than continental or oceanic pure path group velocities.

The spheroidal oscillation data (Table 4.4) derived in this study are in good agreement with similar data of Derr (1969) and Gilbert and Dziewonski (1975). Fundamental spheroidal mode periods determined from

TABLE 4.4

	FUNDAMENTAL SPHEROIDAL MODE OBSERVATIONS						COMPARISON WITH MODEL QM2		
Angular Order Number (1)	$t_{int.}$ (2)	SD (3)	t_D (Derr, 1969) (4)	SEM (5)	t_{GD} (Gilbert & Dziewonski, 1975) (6)	SD (7)	$t_{corr.}$ (8)	t_{QM2} (9)	(t_{QM2}- $t_{corr.}$) (10)
34	239.92	.313	239.87	.168	239.70	.120	237.37	237.72	.35
35	234.89	.306	234.51	.090	234.69	.117	232.35	232.71	.36
36	230.09	.299	229.66	.217	229.86	.138	227.55	227.92	.37
37	225.49	.292	224.75	.265	225.22	.113	223.00	223.32	.32
38	221.01	.292	220.08	.218	220.75	.132	218.56	218.90	.34
39	216.75	.289	216.45	.176	216.48	.108	214.34	214.65	.31
40	212.62	.292	212.09	.302	212.41	.127	210.25	210.55	.30
41	208.67	.292	207.88	.359	208.39	.125	206.34	206.60	.26
42	204.84	.294	204.54	.188	204.58	.102	202.54	202.80	.26
43	201.16	.295	201.00	.223	200.93	.100	198.90	199.13	.23
44	197.62	.296	197.51	.150	197.40	.099	195.38	195.58	.20
45	194.15	.295	193.91	.180	194.03	.097	191.93	192.15	.22
46	190.83	.294	190.89	.190	190.62	.095	188.62	188.83	.21
47	187.63	.294	187.48	.057	187.43	.094	185.34	185.62	.17
48	184.49	.291	184.29	.220	184.29	.147	182.34	182.52	.18
49	181.47	.289	181.52		181.30	.109	179.36	179.51	.15
50	178.56	.288	178.63		178.35	.107	176.48	176.59	.11
51	175.71	.287	175.84		175.41	.105	173.65	173.77	.12
52	172.96	.286	173.10		172.56	.104	170.92	171.02	.10
53	170.30	.285	170.41		170.07	.153	168.28	168.36	.08
54	167.72	.283	167.81		167.37	.084	165.72	165.78	.06
55	165.18	.288	165.23		164.84	.082	163.21	163.27	.06
56	162.74	.289	162.73		162.41	.146	160.79	160.83	.04
57	160.38	.290	160.35		160.24	.144	158.45	158.46	.01
58	158.08	.292	158.08		157.69	.142	156.17	156.15	-.02
59	155.81	.295	155.88		155.58	.140	153.92	153.91	-.01
60	153.62	.296	153.74		153.39	.138	151.75	151.72	-.03
61	151.50	.299	151.59		151.19	.136	149.65	149.60	-.05
62	149.43	.300	149.43		149.21	.134	147.60	147.53	-.07
63	147.40	.301	147.28		147.12	.132	145.59	145.51	-.08
64	145.43	.302	145.16		144.96	.130	143.63	143.55	-.08
65	143.51	.303	143.12		142.99	.129	141.73	141.63	-.10
66	141.64	.303	141.15		141.22	.127	139.89	139.77	-.12
67	139.82	.304	139.24				138.09	137.95	-.14
68	138.03	.304	137.38				136.32	136.17	-.15
69	136.29	.305	135.59				134.60	134.44	-.16
70	134.60	.305	133.84				132.93	132.74	-.19
71	132.95	.305	132.15				131.30	131.09	-.21
72	131.33	.306	130.54				129.71	129.48	-.23
73	129.76	.306	128.98				128.15	127.90	-.25

(contd.)

TABLE 4.4 (contd.)

	FUNDAMENTAL SPHEROIDAL MODE OBSERVATIONS						COMPARISON WITH MODEL QM2		
Angular Order Number (1)	$t_{int.}$ (2)	SD (3)	tD (Derr, 1969) (4)	SEM (5)	t_{GD} (Gilbert & Dziewonski 1975) (6)	SD (7)	$t_{corr.}$ (8)	$t_{QM2.}$ (9)	(t_{QM2}- $t_{corr.}$) (10)
74	128.22	.306	127.44				126.63	126.36	-.27
75	126.71	.307	125.96				125.15	124.85	-.30
76	125.24	.307	124.53				123.70	123.38	-.32
77	123.81	.307	123.14				122.28	121.94	-.34
78	122.41	.307	121.79				120.90	120.53	-.37
79	121.03	.307	120.51				119.55	119.15	-.40
80	119.69	.307	119.25				118.22	117.80	-.42
81	118.37	.312	117.98				116.93	116.48	-.45
82	117.08	.315	116.69				115.66	115.19	-.47
83	115.82	.318	115.43				114.40	113.93	-.48
84	114.59	.321	114.23				113.20	112.69	-.51
85	113.38	.324	113.00				112.00	111.47	-.54
86	112.19	.327	111.81				110.84	110.28	-.56
87	111.03	.330	110.67				109.71	109.12	-.59
88	109.89	.332	109.55				108.60	107.97	-.63
89	108.78	.337	108.39				107.51	106.85	-.66
90	107.69	.342	107.30				106.44	105.75	-.69
91	106.62	.346	106.23				105.39	104.68	-.71
92	105.57	.350	105.19				104.35	103.62	-.73
93	104.54	.354	104.16				103.34	102.58	-.76
94	103.53	.358	103.17				102.35	101.56	-.79
95	102.54	.361	102.20				101.39	100.56	-.83
96	101.57	.364	101.25				100.44	99.58	-.86
97	100.62	.368	100.29				99.50	98.62	-.88
98	99.69	.371					98.58	97.68	-.90
99	98.76	.384					97.65	96.75	-.90
100	97.85	.393					96.75	95.83	-.88
101	96.97	.403					95.87	94.94	-.93
102	96.09	.412					94.98	94.06	-.92
103	95.24	.421					94.15	93.19	-.96
104	94.39	.429					93.30	92.34	-.96
105	93.57	.437					92.49	91.51	-.98
106	92.75	.445					91.67	90.68	-.99
107	91.95	.452					90.87	89.88	-.99
108	91.17	.460					90.10	89.08	-1.02
109	90.39	.466					89.34	88.30	-1.04
110	89.64	.473					88.58	87.53	-1.05
111	88.88	.478					87.84	86.78	-1.06
112	88.15	.483					87.12	86.03	-1.09
113	87.42	.487					86.41	85.30	-1.11
114	86.71	.492					85.71	84.58	-1.13
115	86.00	.496					85.02	83.87	-1.15
116	85.31	.501					84.35	83.17	-1.18
117	84.63	.504					83.68	82.48	-1.20

(contd.)

TABLE 4.4 (contd.)

FUNDAMENTAL SPHEROIDAL MODE OBSERVATIONS COMPARISONS WITH MODEL QM2

Angular Order Number (1)	$t_{int.}$ (2)	SD (3)	t_D (Derr, 1969) (4)	SEM (5)	t_{GD} (Gilbert & Dziewonski, 1975) (6)	SD (7)	$t_{corr.}$ (8)	t_{QM2} (9)	(t_{QM2}- $t_{corr.}$) (10)
118	83.97	.508					83.02	81.81	-1.21
119	83.31	.512					82.37	81.14	-1.23
120	82.66	.515					81.73	80.49	-1.24
121	82.02	.519					81.11	79.84	-1.27
122	81.39	.522					80.49	79.20	-1.29
123	80.77	.525					79.88	78.58	-1.30
124	80.17	.528					79.28	77.96	-1.32
125	79.57	.530					78.69	77.35	-1.34
126	78.97	.527					78.10	76.75	-1.35
127	78.38	.525					77.53	76.16	-1.37
128	77.81	.524					76.97	75.58	-1.39
129	77.24	.523					76.41	75.00	-1.41
130	76.68	.522					75.85	74.44	-1.41
131	76.13	.521					75.32	73.88	-1.44
132	75.58	.520					74.78	73.33	-1.45
133	75.05	.518					74.26	72.78	-1.48
134	74.52	.517					73.75	72.25	-1.50
135	74.00	.516					73.24	71.72	-1.52
136	73.48	.515					72.74	71.20	-1.54
137	72.98	.513					72.33	70.69	-1.54
138	72.48	.512					71.76	70.18	-1.58
139	71.98	.511					71.27	69.68	-1.59
140	71.50	.510					70.79	69.19	-1.60
141	71.02	.508					70.32	68.70	-1.62
142	70.55	.507					69.85	68.22	-1.63
143	70.08	.506					69.39	67.76	-1.63
144	69.62	.504					68.94	67.28	-1.66
145	69.16	.501					68.49	66.82	-1.67
146	68.71	.499					68.04	66.36	-1.68
147	68.26	.497					67.61	65.91	-1.70
148	67.82	.494					67.17	65.47	-1.70
149	67.39	.492					66.75	65.03	-1.72
150	66.96	.490					66.32	64.60	-1.72
151	66.54	.488					65.91	64.17	-1.74
152	66.12	.486					65.50	63.75	-1.75
153	65.71	.483					65.09	63.33	-1.76
154	65.30	.481					64.69	62.92	-1.77
155	64.90	.479					64.29	62.51	-1.78
156	64.50	.477					63.90	62.11	-1.79
157	64.11	.475					63.51	61.72	-1.79
158	63.72	.473					63.13	61.32	-1.81
159	63.34	.471					62.75	60.94	-1.81
160	62.96	.469					62.38	60.55	-1.83
161	62.58	.467					62.01	60.18	-1.83

(contd.)

TABLE 4.4 (contd.)

	FUNDAMENTAL SPHEROIDAL MODE OBSERVATIONS						COMPARISONS WITH MODEL QM2		
Angular Order Number (1)	$t_{int.}$ (2)	SD (3)	t_D (Derr, 1969) (4)	SEM (5)	t_{GD} (Gilbert & Dziewonski, 1975) (6)	SD (7)	$t_{corr.}$ (8)	t_{QM2} (9)	(t_{QM2} - $t_{corr.}$) (10)
162	62.21	.465					61.65	59.80	-1.85
163	61.85	.463					61.29	59.43	-1.86
164	61.49	.461					60.93	59.01	-1.86
165	61.13	.459					60.58	58.71	-1.87
166	60.78	.457					60.23	58.35	-1.88
167	60.43	.455					59.89	58.00	-1.89
168	60.08	.453					59.56	57.65	-1.91

NOTE SD = Standard deviation
SEM = Standard error of the mean
$t_{int.}$ = effective spheroidal oscillation periods derived from phase velocities
$t_{corr.}$ = periods in column 2 corrected for dispersion due to anelasticity using Equation 7.

our global average phase velocities corrected for frequency shifts due to anelasticity are presented in column 8 of Table 4.4. There periods can be compared with those of the same modes calculated from model QM2 of Hart et al. (1977b). For periods greater than 155 seconds our estimated periods are slightly greater than those calculated for model QM2 of Hart et al. (1977b). On the other hand, at periods shorter than 155 seconds our estimated periods become progressively smaller than the periods for modes QM2, the differences being 0.21, 0.83, 1.54 and 3.02 per cent at periods of 125, 100, 80 and 60 seconds. These frequency shifts indicate that Rayleigh wave phase velocities for model QM2 are too high compared to the observed global average phase velocities for periods shorter than 125 seconds. Hart et al. (1977b) used the Anderson et al. (1965) model MM8 for anelasticity to compute corrections for their free oscillation data.

In Figure 4.5 values of Q_R^{-1} calculated for model MM8 are compared with Q_R^{-1} calculated from the group velocities and attenuation coefficients listed in Table 4.3. Error bars indicate one standard deviation for each estimate. The values of Q_R^{-1} calculated in this study are lower than those predicted by model MM8. Most estimates of Q_R^{-1} presented by Ben-Menahem (1965) lie between estimates derived in this study and those predicted from model MM8. Attenuation coefficients of Mitchell et al. (1975) for Pacific Ocean paths for the period range 50 to 110 seconds are within a factor of 2 of our global average estimates of attenuation coefficients. Similar estimates for central United States paths by Mitchell (1973a) and Herrmann and Mitchell (1975) indicate that attenuation coefficients at a period of 40 seconds are also within a factor of 2 of our estimate at 50 seconds. A discussion of further implications of these global average group velocities and attenuation coefficients and deviations from them for particular paths will appear in later chapters dealing with regionalization and inversion of the data presented in this chapter and in Chapter 3.

Figure 4.5 Q FOR RAYLEIGH WAVES -

Q's determined from our fundamental mode Rayleigh wave attenuation coefficients and group velocities are contrasted with Q_R's calculated for model MM8 of Anderson, Ben-Menahem and Archambeau (1965). Error bars indicate estimates of 1 standard deviation for each Q_R.

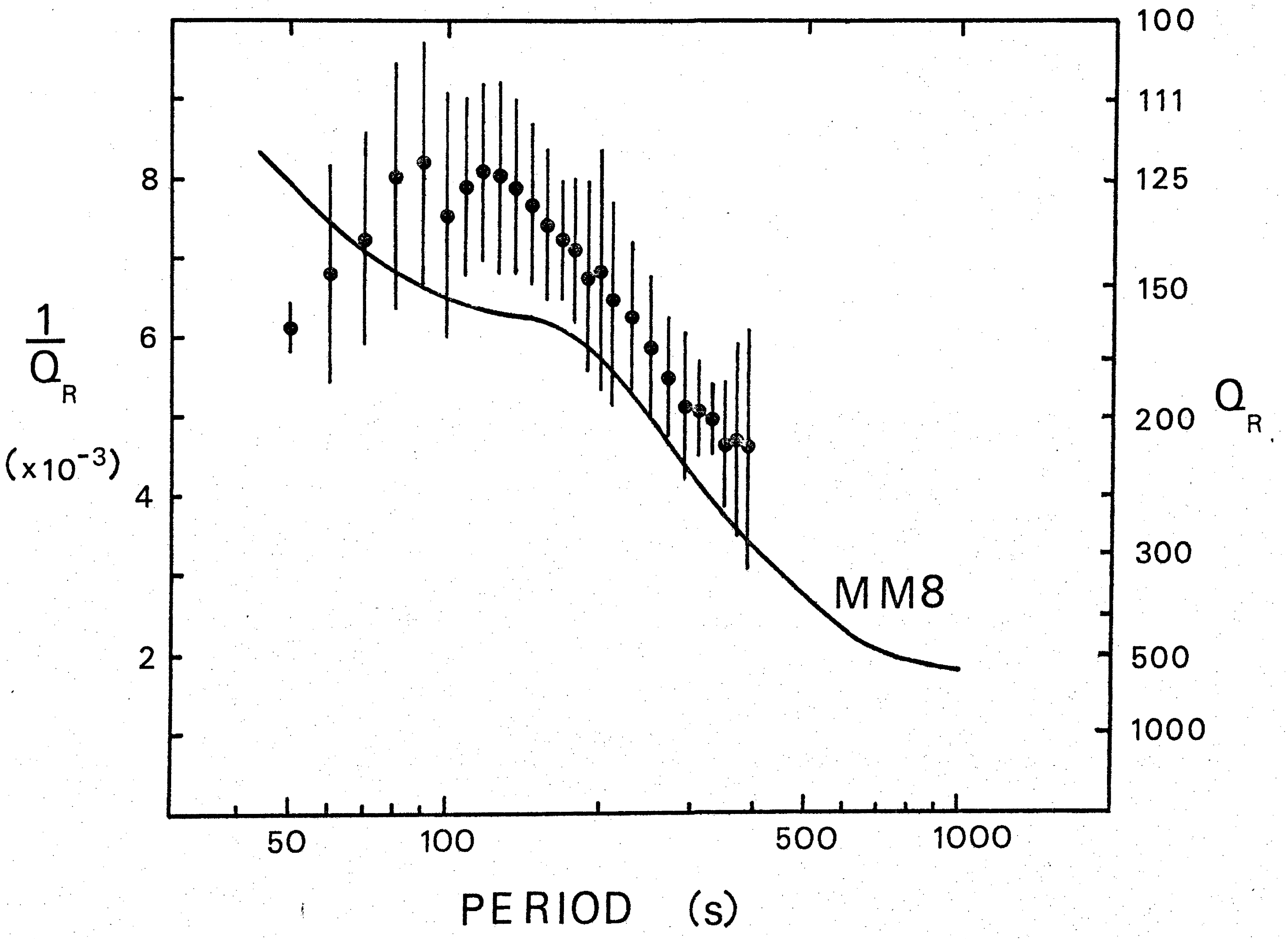
$\frac{1}{Q_R}$
$(\times 10^{-3})$
8
6
4
2
50
100
500
1000
PERIOD (s)
100
111
125
150
200
300
500
1000
Q_R
MM8

Sec. 4.5 SUMMARY

The analysis of Rayleigh waves from several large Kurile Island earthquakes has produced

- global average group and phase velocities for Rayleigh waves for the period range 50 to 600 seconds,
- global average attenuation coefficients for Rayleigh waves for the period range 50 to 450 seconds,
- effective fundamental spheroidal oscillation periods for modes ${}_0S_{34}$ to ${}_0S_{68}$ (60 to 240 seconds).

Recent average earth models derived from free oscillation, travel time, and surface wave dispersion data produce model group velocities which exceed our global average group velocities by as much as 0.25 km/s in the period range 100 to 250 seconds. Spheroidal oscillation periods, when corrected for dispersion due to anelasticity, indicate that shear velocities in the upper mantle are lower than those in model QM2. The global average group velocity data require a more pronounced low velocity layer in the earth than is predicted by recent free oscillation models. Global average Q's for fundamental mode Rayleigh waves are slightly lower (approximately one standard deviation at most periods) than those predicted by model MM8. Attenuation coefficients at short periods (50 to 100 seconds) agree well with similar measurements for shorter paths over oceans and continents.

CHAPTER 5

INVERSION OF GLOBAL AVERAGE GROUP VELOCITIES AND ATTENUATION COEFFICIENTS

Sec. 5.1 INVERSION TECHNIQUES

In recent years the problem of inversion of geophysical data and the uniqueness of models produced from such data has been widely discussed. Several theoretical formalisms have evolved which are commonly in use today. These include:

1. The Backus and Gilbert formalism (Backus and Gilbert 1967, 1968, 1970; Gilbert 1971) which has been used to invert body wave travel times and free oscillation periods (e.g. Gilbert et al. 1973), body wave travel times alone (Johnson and Gilbert 1972), surface wave velocities (Braile and Keller 1975) and electrical conductivity data (Parker 1970, 1972).

2. The stochastic inversion formalism of Franklin (1970), Smith and Franklin (1969) and Jordan and Franklin (1971) has been applied to the inversion of free oscillation periods and body wave travel times (Jordan and Anderson 1974) and the inversion of surface wave attenuation coefficients (Mitchell 1975, 1977).

3. The generalized matrix inversion method of Penrose (1955), later developed by Lanczos (1961), is discussed by Jackson (1972) and Wiggins (1972) and applied to surface wave and free oscillation data by Wiggins (1972).

4. Monte Carlo methods for inversion of seismic data were developed by Keilis-Borok and Yanovskaja (1967) and have been applied to the inversion of free oscillation data by Press (1968, 1969, 1970) and Worthington et al. (1974a). Wiggins (1969) and Worthington et al. (1974b) also applied Monte Carlo techniques to invert body wave travel times.

5. The Hedgehog inversion method also has numerous variations

which have been used by Knopoff (1972) for the inversion of surface wave phase velocities and by Burton (1972, 1977) for the inversion of surface wave attenuation data.

Summaries of the Backus and Gilbert method (1) appear in Parker (1970), the generalized inverse method (3) in Wiggins (1972) and Jackson (1972) and the stochastic method (2) in Wiggins (1972).

The problems of non-uniqueness of models and the effects of linearization on resulting models have been discussed with respect to the inversion of body waves by Johnson and Gilbert (1972), Müller and Alsop (1972) and Wiggins *et al*. (1973). These problems also arise in the inversion of upper mantle shear velocities from surface wave group velocities, which again is a non-linear problem. In this chapter an algorithm is presented which combines the bias-free properties of Monte Carlo inversion with the improved efficiency of refinement modelling (Sec. 5.2). Since no linearization of the problem is involved this technique is also free from any gain introduced by linearization. Corrections for anelastic dispersion in observed group velocities (Sec. 5.3) must be made before group velocities are inverted (Sec. 5.4). Phase velocity partial derivatives for models resulting from the inversion of global average group velocities are necessary in the modelling of attenuation by the method of Anderson *et al*. (1965) (Sec. 5.4). Since the problem of the inversion of attenuation data is a linear problem, a stochastic inversion procedure has been used for the determination of Q_β^{-1} as a function of depth. The amount of attenuation caused by scattering is considerably smaller than attenuation due to anelasticity, and thus the models derived in Sec. 5.5 are representative of the anelastic properties of the mantle.

Sec. 5.2 CONTROLLED MONTE CARLO INVERSION OF RAYLEIGH WAVE GROUP VELOCITIES

An algorithm for a controlled Monte Carlo inversion procedure is block outlined in Figure 5.1. Important features of this algorithm are:

(1) Starting models are randomly generated within predetermined limits.

(2) When predictions from a particular model are acceptably close to observations, in this case group velocities, that model is refined.

(3) Models are refined by applying those random perturbations which produce smaller reduced χ^2 statistics for all models tested.

The computer program using the algorithm described in Figure 5.1 will accept both shear velocities in layers and positions of layer boundaries as parameters and will fit either phase or group velocity observations. Fundamental and first higher mode velocities for Rayleigh and Love waves can be inverted simultaneously using this algorithm. In this chapter, the algorithm has been applied only to fundamental mode Rayleigh wave group velocities. In Chapter 6, however, both fundamental and higher mode Rayleigh and Love wave group velocities have been inverted simultaneously.

The reduced χ^2 statistic ($\chi^2{}_r$) has been used as a "goodness of fit" parameter for listing individual modes of each model generated. Starting models are generated randomly within specified bounds and accepted for refinement or rejected on the basis of the largest initial $\chi^2{}_r$ of all the modes to be tested. This test avoids models which would require many refinements. Each acceptable starting model is refined by generating a random perturbation to the model with the maximum perturbation size controlled by the acceptability of the fit of the current model. A perturbed model which produces an improved (smaller) $\chi^2{}_r$ for all modes is accepted as an improved model, and the perturbation is incorporated into the model. Models which produce acceptable

Figure 5.1 FLOW CHART FOR A CONTROLLED MONTE CARLO INVERSION PROGRAM - for multimode surface wave group or phase velocities.

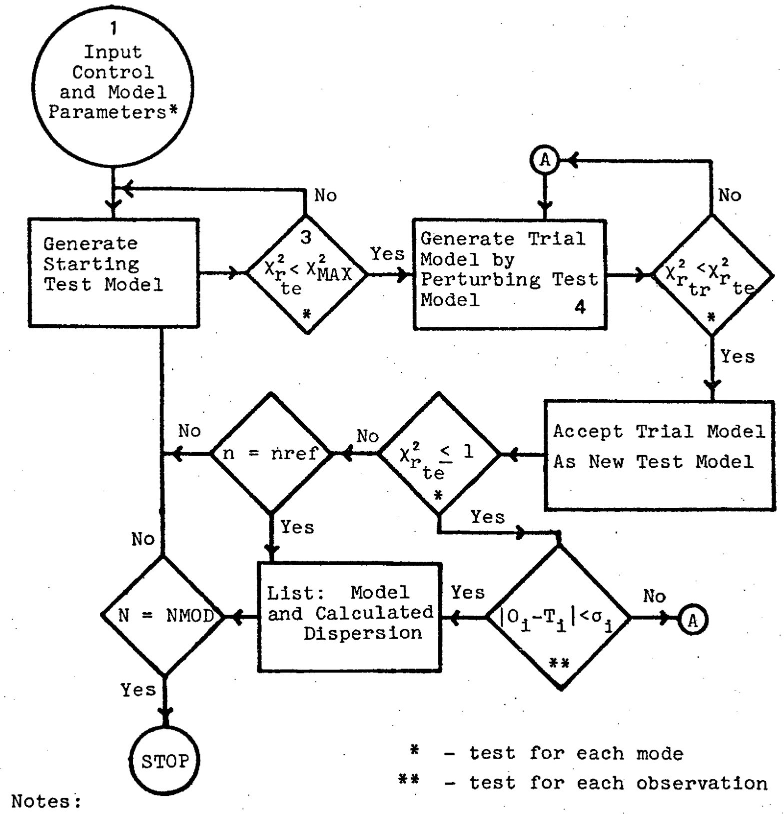

* - test for each mode

** - test for each observation

Notes:

1 Input Data: Fixed model parameters, bounds on variable model parameters, observed velocities O_i with standard deviations σ_i, control parameters: NMOD - number of starting models to generate, nref - number of refinements for each starting model, χ^2_{MAX} - maximum χ^2_r accepted for any mode for all starting models.

3 Reduced χ^2 statistic:

$$\chi^2_r = \frac{1}{(N-1)} \sum_{i=1}^{N} \left[\frac{O_i - T_i}{\sigma_i}\right]^2$$

$\chi^2_{r_{te}}$ - reduced χ^2 statistic for a mode for the test model

$\chi^2_{r_{tr}}$ - reduced χ^2 statistic for a mode for the trial model

4 Method of perturbing test model:

Each trial model parameter, $q_{i_{tr}}$, is generated by perturbing each test model parameter, $q_{i_{te}}$, as follows:

$$q_{i_{tr}} = (1+R*P)*q_{i_{te}}$$

where R is a random number from a uniform distribution over the range (-0.5,+0.5) and P is determined by χ^2_* the largest χ^2_r from the set of χ^2_r for all modes to be tested:

χ^2_*	P
> 10.0	0.04
3.0 to 10.0	0.02
2.0 to 3.0	0.01
1.6 to 2.0	0.0075
1.3 to 1.6	0.005
< 1.3	0.0025

χ^2_r for all modes (depending on the quality of the fit required) are accepted as "successful" models. The refining process is repeated until a successful model is generated or until the maximum number of refinements to the model has been attempted. In either case, parameters for the final refinement are listed along with the calculated dispersion for that model. Models generated by this procedure are not restricted to stay within bounds set for the starting models.

The calculated model dispersion is corrected for the earth's sphericity by the Biswas and Knopoff (1970) correction for Love waves - an exact earth flattening correction - and by either the North and Dziewonski (1976) correction or the Alterman et al. (1961) correction for Rayleigh waves. The North and Dziewonski (1976) correction is an empirical correction for the fundamental mode which corrects calculated phase and group velocities to an accuracy of better than 0.4 per cent for periods shorter than 200 seconds. This correction has been used for correcting group velocities in the inversion of global average group velocities in this chapter and regional group velocities in Chapter 7. The Alterman et al. (1961) correction has been applied to models for calculating fundamental and first higher mode Rayleigh wave group velocities in the inversion in Chapter 6.

TABLE 5.1: KURILE IS. EARTHQUAKES

DATE	ORIGIN TIME (GMT)	LOCATION (USGS)	MS	ABBREVIATION
13 October 1963	5:17:51.2	44°8N 149°5E	8.3	13X63
12 October 1963	11:26:57.9	44°8N 149°0E	7.0	12X63
10 June 1975	13:47:21.7	43°3N 147°0E	7.1	10V175
13 June 1975	18:08:12.8	43°6N 147°4E	6.6	13V175

STATIONS	AZIMUTH AT EVENT AND WINDOW No.	EVENT	EPICENTRAL DISTANCE (km)	GREAT CIRCLE CUMFERENCE (km)	BEGINNING OF DIGITIZATION (GMT)	No. OF SAMPLES	SAMPLE INTERVAL (SEC)	TYPE OF RECORD
ALQ	124°4(1)	13V175	8549.7	40031.0	17:58:13.1	22440	1	HGLP
ZLP	119°5(1)	10V175	15565.2	40034.0	13:32:01.6	23100	1	HGLP
		13V175	15493.7	40033.8	17:50:46.4	22440	1	HGLP
DUG	124°9(1)	13X63	7528.3	40030.7	9:14:00	11216	4	WWSSN
CHG	104°8(2)	10V175	5232.2	40040.9	13:37:43.0	24420	1	HGLP
		13V175	5272.4	40040.6	17:52:43.0	22440	1	HGLP
BUL	83°4(3)	13X63	13993.1	40041.3	8:34:00	12751	4	WWSSN
NDI	79°6(3)	12X63	6440.4	40040.7	11:31:00	17665	1	WWSSN
NAI	74°6(3)	12X63	11837.3	40039.4	11:40:00	13685	1	WWSSN
KIP	79°4(3)	10V175	5595.9	40043.0	13:34:25.3	12766	1	HGLP
		13V175	5568.2	40042.5	18:03:37.8	22440	1	HGLP
AFI	22°4(4)	13X63	7586.3	40022.4	8:12:00	10440	4	WWSSN
EIL	54°2(4)	10V175	9385.8	40031.3	13:35:55.9	23100	1	HGLP
		13V175	9392.3	40031.0	17:57:12.1	8580	1	HGLP
IST	22°8(4)	13X63	8806.6	40041.5	9:06:00	12089	4	WWSSN
STU	25°4(5)	12X63	8926.9	40014.2	11:36:00	17889	1	WWSSN
AQU	31°1(5)	13X63	9414.0	40016.9	9:48:00	17002	4	WWSSN
VAL	12°5(6)	12X63	9102.7	40009.5	11:37:00	15990	1	WWSSN
HNR	12°7(6)	13X63	6096.7	40009.6	8:50:00	13183	4	WWSSN
PTO	16°4(6)	12X63	9702.2	40010.6	11:35:00	15422	1	WWSSN
TOL	20°1(6)	13X63	10209.9	40011.9	9:34:00	14670	4	WWSSN
KON	20°3(6)	10V175	7947.4	40012.6	13:37:41.3	23100	1	HGLP
		13V175	7928.0	40012.5	17:56:26.3	22440	1	HGLP
SBA	4°3(7)	13X63	13716.0	40008.2	8:21:00	11816	4	WWSSN
CTA	176°6(7)	10V175	7018.3	40008.0	13:38:16.6	23430	1	HGLP
		13V175	7052.2	40008.0	17:53:33.6	22440	1	HGLP
		13X63	7189.9	40008.1	9:16:00	13195	4	WWSSN
TAU	178°4(7)	12X63	9716.4	40008.0	11:35:00	16915	1	WWSSN
RAB	3°5(7)	12X63	5435.3	40008.1	11:27:00	20629	1	WWSSN
ADE	171°0(8)	12X63	8894.2	40008.8	11:38:00	15168	1	WWSSN
		13X63	8900.2	40008.8	8:34:00	11763	4	WWSSN
MUN	151°9(9)	12X63	9127.8	40015.4	11:35:00	14886	1	WWSSN
OGD*	148°2(9)	10V175	9775.3	40016.9	13:38:39.6	23100	1	HGLP
		13V175	9730.2	40016.9	17:56:01.0	22770	1	HGLP

* DATA NOT INCLUDED DUE TO DIGITIZER MALFUNCTION.

Sec. 5.3 THE CORRECTION OF OBSERVED GROUP VELOCITIES FOR ANELASTIC DISPERSION

As described in Section 4.3.2, the presence of anelasticity in the earth causes free oscillation periods to be shifted to periods longer than would be observed in a perfectly elastic earth. The effect of anelasticity on phase velocities causes phase velocities to be shifted to slower velocities. In each case the shift is of the order of 1 per cent for periods of several hundred seconds. Since group velocity is related to the first derivative of the phase velocity, the correction is slightly more complex.

Let us consider the phase velocity correction for anelasticity (Liu et al. 1976, Equations 40 and 41). In the case of both Rayleigh and Love waves, the correction is of the form

$$\frac{\Delta c}{c} = \frac{Q^{-1}}{\pi} \ln \frac{\omega}{2\pi} \tag{5.1}$$

where c is the phase velocity, Δc is the correction to the phase velocity and Q^{-1} is the specific attenuation of the appropriate mode at angular frequency ω. The group velocity u, expressed in terms of the phase velocity and its derivative with respect to period T, is

$$u = \frac{c}{1 + \frac{T}{c}\frac{dc}{dT}} \quad . \tag{5.2}$$

Similar expressions relate phase and group velocities for group and phase velocities corrected for anelasticity, u and c, and group and phase velocities which are not corrected for anelasticity (observed velocities), **U** and **C**. The phase velocity corrected for anelastic dispersion, is thus

$$c = C - \Delta c$$

$$= C + \frac{c}{\pi Q} \ln(T) \; . \qquad (5.3)$$

The group velocity, corrected for anelastic dispersion, can be expressed in terms of the observed phase velocity using Equation 5.3:

$$u = \frac{C - \Delta c}{1 + \frac{T}{(C-\Delta c)} \frac{dc}{dT}} \qquad (5.4)$$

Consider the problem of evaluating $\frac{dc}{dT}$. Upon differentiating Equation 5.3 with respect to time, a second $\frac{dc}{dT}$ term arises from the differentiation of Δc (Equation 5.1). When all $\frac{dc}{dT}$ terms are collected, the remaining terms contain only the uncorrected phase velocity C and the correction term Δc

$$\frac{dc}{dT} = \left(1 - \frac{\ln T}{\pi Q}\right)^{-1} \left[\frac{dC}{dT} - \frac{(C-\Delta c)\Delta c}{Q} \frac{dQ}{dT} + \frac{(C-\Delta c)}{\pi Q T} \right]. \qquad (5.5)$$

Only the derivatives $\frac{dC}{dT}$ and $\frac{dQ}{dT}$ provide computational problems. The derivative $\frac{dC}{dT}$ can be evaluated directly in terms of observed phase and group velocities by solving Equation 5.2 (written for uncorrected phase and group velocities) for the derivative of the phase velocity:

$$\frac{dC}{dT} = \frac{C}{T} \left(\frac{C}{U} - 1 \right). \qquad (5.6)$$

The derivative $\frac{dQ}{dT}$ was determined by differentiating a fourth degree polynomial which was fitted to Q as a function of period (data in Figure 4.5). Equations 5.4, 5.5, and 5.6 in conjunction with the polynomial fitting Q as a function of period provide a straight forward and accurate method for correcting observed group velocities for anelastic dispersion. In practice C has been taken as the phase velocity calculated by trapezoidal rule integration of the observed group velocities described in Sec. 4.3 and listed in Table 4.3 for the global average data. The correction Δc has been calculated with the uncorrected phase velocity calculated by integrating group velocities. All group velocities used in modelling in this chapter and in Chapter 7 have been corrected for anelastic dispersion in this manner. The corrected global average group velocities are given in Table 5.2.

TABLE 5.2 GLOBAL AVERAGE GROUP VELOCITIES CORRECTED FOR ANELASTIC DISPERSION

PERIOD (S)	UNCORRECTED GROUP VELOCITY (km/s)	CORRECTED GROUP VELOCITY (km/s)
60	3.8545	3.8648
70	3.8351	3.8488
80	3.7937	3.8121
90	3.7952	3.8193
100	3.7460	3.7761
110	3.7464	3.7825
120	3.7278	3.7691
130	3.7065	3.7518
140	3.7088	3.7573
150	3.6752	3.7253
160	3.6510	3.7019
170	3.6320	3.6830
180	3.6237	3.6746
190	3.5988	3.6491
200	3.5928	3.6428
210	3.5726	3.6222
220	3.5775	3.6275
230	3.5728	3.6234
240	3.5665	3.6183
250	3.5774	3.6312
260	3.5950	3.6516
270	3.6135	3.6735
280	3.6539	3.7181
290	3.6602	3.7279
300	3.7301	3.8029
310	3.7696	3.8461
320	3.8329	3.9129
330	3.8787	3.9605

Sec. 5.4 SHEAR VELOCITY MODELS FOR THE UPPER MANTLE

In this section, models are presented which fit the global average Rayleigh wave group velocities presented in Table 5.2. As Dziewonski (1971b) pointed out, an averaging of dispersion curves approximately corresponds to an averaging of velocity and density distributions. As a consequence, global average and pure-path dispersion curves, and the corresponding models derived for them, may not represent actual upper mantle structure. Several recent studies of upper mantle structure derived from surface wave dispersion data have indicated that the average thickness of the lithosphere (taken as the depth of the top of the low velocity zone) is about 70 km beneath the oceans (Kanamori and Press 1970, Forsyth 1975b). Other studies (Press 1970, Dziewonski 1971b) have found that the average lithospheric thickness beneath the continents is approximately twice as great as beneath the oceans. Since about 2/3 of the earth's surface is covered by ocean, global average surface wave dispersion data should be weighted towards representation of the oceanic upper mantle structure. For this reason two sets of shear velocity model bounds have been used for generating average earth models:

(1) models with layer boundaries similar to oceanic models of Dziewonski (1971b) (100 km lithospheric lid),

and

(2) models with layer boundaries similar to 5.08 M of Kanamori and Press (1970) (70 km lithospheric lid).

These two types of shear velocity bounds are presented in Table 5.3 and will be referred to as type 1 and type 2 bounds in the ensuing discussion. Densities were assumed to be constant in both types of upper mantle models, since this study did not produce a data set from which density could be determined simultaneously with shear velocities. Several successful models, i.e. models which fit within one standard deviation for periods between 50 and 300 seconds are shown, in Figures 5.2 and 5.3. All successful models

TABLE 5.3 STARTING MODEL BOUND ON SHEAR VELOCITY MODELS DERIVED BY CONTROLLED MONTE CARLO INVERSION OF GLOBAL AVERAGE GROUP VELOCITIES

TYPE 1 - BASED ON DZIEWONSKI (1971b) OCEANIC MODELS

Depth to Top of Layer (km)	Compressional Velocity (km/s)	Range of Shear Velocities (km/s)		Density (g/cc)
		Low	High	
0.0	1.44	0.0		1.02
3.0	6.50	3.72		2.79
21.0	8.37	4.30	4.50	3.40
100.0	8.37	4.20	4.30	3.40
200.0	8.37	4.60	4.60	3.40
412.5	9.50	5.20		3.80
658.5	10.26	5.64		4.05
671.0	10.67	5.91		4.35
703.5	10.93	6.07		4.40
719.5	10.97	6.09		4.41
737.0	10.97	6.10		4.42
757.5	10.98	6.14		4.46
783.5	11.05	6.18		4.49
809.5	11.10	6.24		4.51
846.0	11.19	6.32		4.54
908.5	11.33	6.37		4.57
983.5	11.47	6.38		4.61
1058.5	11.60	6.39		4.64
1133.5	11.72	6.46		4.68
1208.5	11.85	6.52		4.71

TABLE 5.3 STARTING MODEL BOUND ON SHEAR VELOCITY MODELS DERIVED BY CONTROLLED MONTE CARLO INVERSION OF GLOBAL AVERAGE GROUP VELOCITIES

TYPE 2 - BASED ON KANAMORI (1970a) 5.08 M

Depth to Top of Layer (km)	Compressional Velocity (km/s)	Range of Shear Velocities (km/s)		Density (g/cc)
		Low	High	
0.0	1.44	0.00		1.02
3.0	6.50	3.72		2.79
21.0	8.37	4.500	4.575	3.40
70.0	8.37	4.300	4.350	3.40
150.0	8.37	4.250	4.350	3.40
220.0	8.37	4.600	4.600	3.40
412.5	9.50	5.20		3.80
658.5	10.26	5.64		4.05
671.0	10.67	5.91		4.35
703.5	10.93	6.67		4.40
719.5	10.97	6.09		4.41
737.0	10.97	6.10		4.42
757.5	10.98	6.14		4.46
783.5	11.05	6.18		4.49
809.5	11.10	6.24		4.51
846.0	11.19	6.32		4.54
908.5	11.33	6.37		4.57
983.5	11.47	6.38		4.61
1058.5	11.60	6.39		4.64
1133.5	11.72	6.46		4.68
1208.5	11.85	6.52		4.71

Figure 5.2 SHEAR VELOCITY MODELS FROM TYPE 1 BOUNDS - have been determined by controlled Monte Carlo inversion of global average Rayleigh wave group velocities for periods between 50 and 300 seconds. Type 1 bounds for shear velocities of starting models are listed in Table 5.3(a). All models have lithospheric thicknesses of 100 km and are listed in Table 5.4(a).

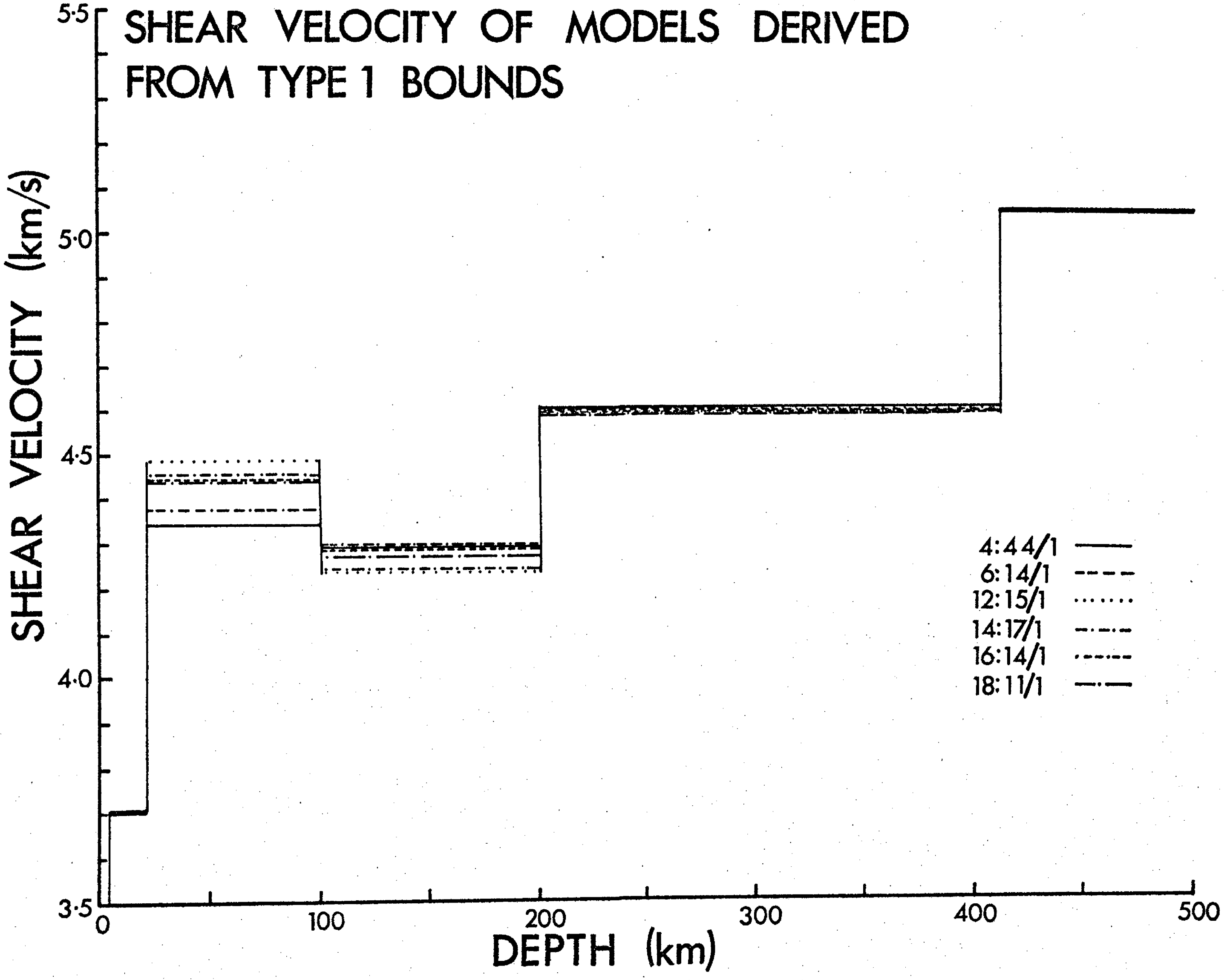

SHEAR VELOCITY OF MODELS DERIVED FROM TYPE 1 BOUNDS

Table 5.3 SHEAR VELOCITY MODELS FROM TYPE 2 BOUNDS - have been determined by controlled Monte Carlo inversion of global average Rayleigh wave group velocities for periods between 50 and 300 seconds. Type 2 bounds for shear velocities of starting models are listed in Table 5.3(b). All models have lithospheric thicknesses of 70 km and are listed in Table 5.4(b).

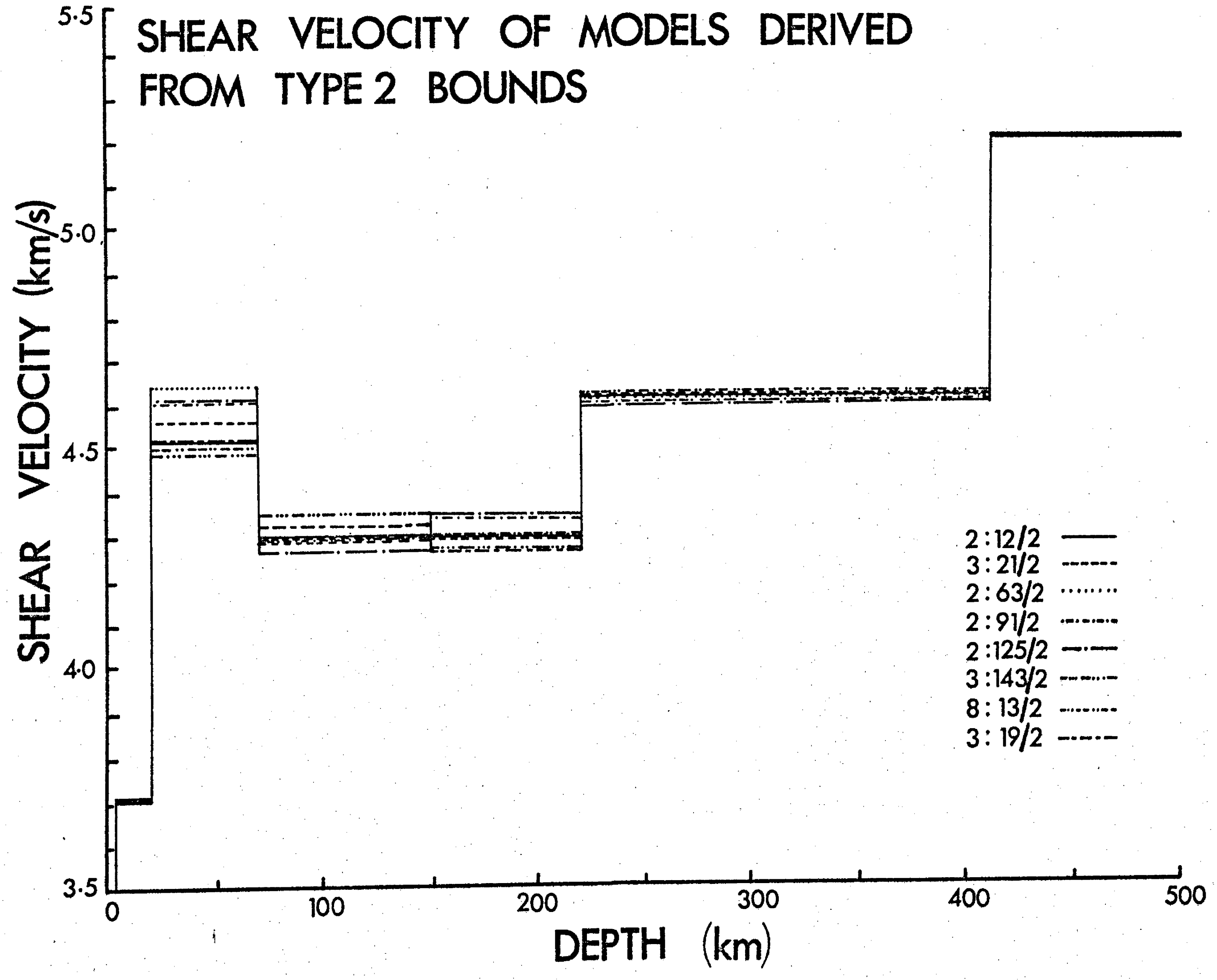
SHEAR VELOCITY OF MODELS DERIVED FROM TYPE 2 BOUNDS
SHEAR VELOCITY (km/s)
5·5
5·0
4·5
4·0
3·5
0
100
200
300
400
500
DEPTH (km)
2 : 12/2
3 : 21/2
2 : 63/2
2 : 91/2
2 : 125/2
3 : 143/2
8 : 13/2
3 : 19/2

are listed in Table 5.4.

It is evident from Figures 5.2 and 5.3 that Rayleigh wave group velocities alone, for periods between 50 and 300 seconds, do not constrain the range of average lithospheric shear velocities or thicknesses within close limits. Shorter period data are required in the 20 to 50 second period range for the determination of bounds on average shear velocity and thickness of the lithosphere. This is also apparent from the partial derivatives of phase and group velocity with respect to shear velocity for models presented in Figures 5.6 and 5.7. Average shear velocities for the low velocity zone are better determined - the range of shear velocities derived for type 1 bounds is about 0.1 km/s wide. For type 2 bounds the two low velocity layers are slightly more variable. Average velocities for the region between the low velocity zone and the 412 km discontinuity are less variable than any of the other layers and cluster tightly about an average of 4.6 km/s. This is not an artifact of the narrow bounds on starting model velocities for this layer since other models were produced from wider bounds which resulted in no more scatter than that shown in Figure 5.2 and 5.5.

As a test of whether a low velocity zone was required by the global average data set, several models were refined from a constant velocity upper mantle starting model. The starting model and resulting successful models for layer thicknesses chosen from type 1 and type 2 bounds are shown in Figures 5.4 and 5.5 and Table 5.4 parts (c) and (d). Since the starting model was a constant velocity model, the resulting models have low-contrast low velocity zones with low lid velocities, but all fall approximately within the ranges of shear velocities described by models derived from type 1 and type 2 bounds.

Recently Burkhard and Jackson (1976) pointed out that the "standardized" partial derivatives of phase velocity with respect to density are not small compared to partials with respect to shear velocity

TABLE 5.4 SHEAR VELOCITY MODELS DERIVED FROM A CONSTANT VELOCITY UPPER MANTLE -

with a lithospheric thickness of 100 km show that a low zone is required by global average Rayleigh wave group velocities for periods between 50 and 30 km. Models are listed in Table 5.4(c).

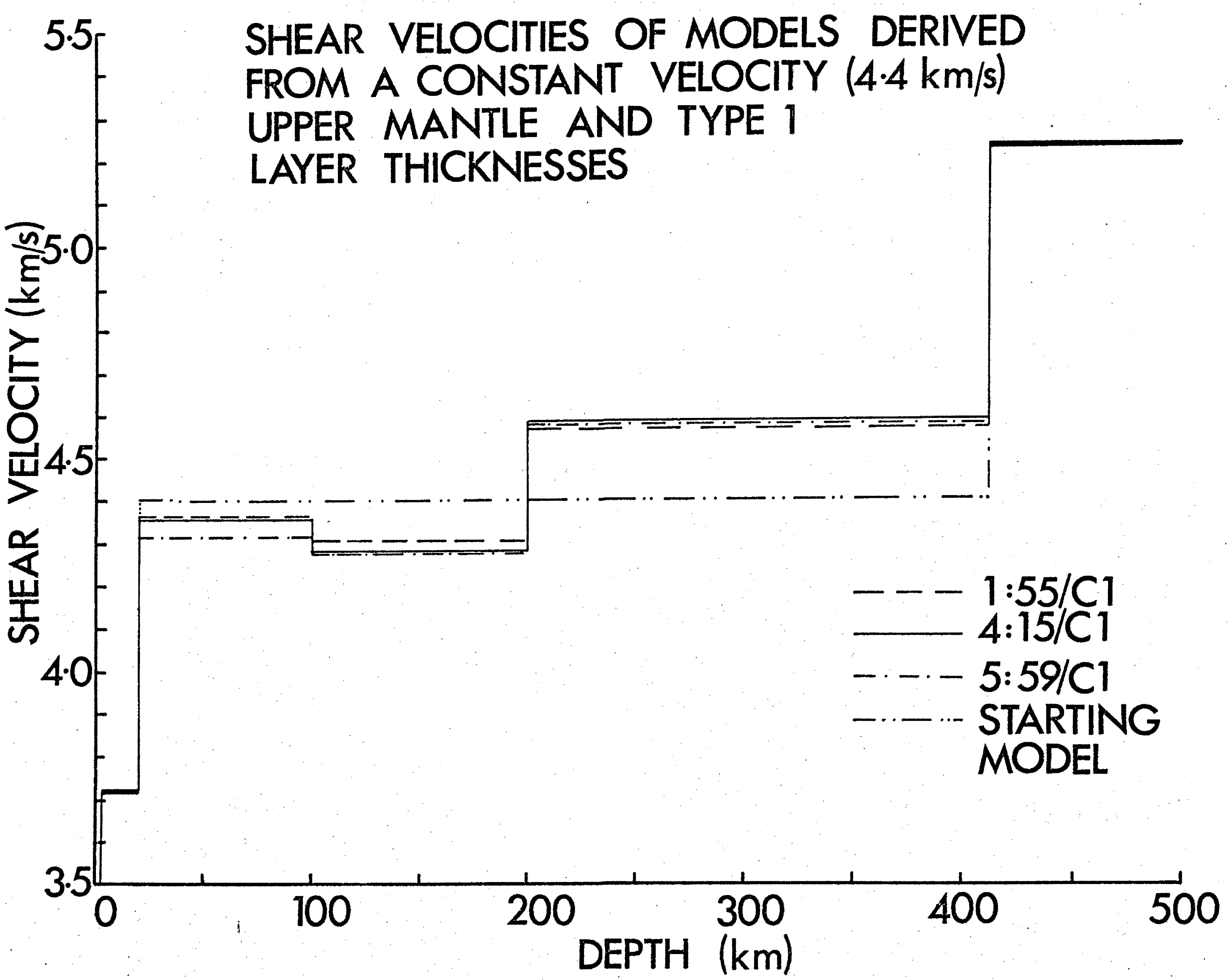

SHEAR VELOCITIES OF MODELS DERIVED FROM A CONSTANT VELOCITY (4·4 km/s) UPPER MANTLE AND TYPE 1 LAYER THICKNESSES

Figure 5.5 SHEAR VELOCITY MODELS DERIVED FROM A CONSTANT VELOCITY UPPER MANTLE -

with a lithospheric thickness of 70 km show that a low velocity zone is required by global average Rayleigh wave group velocities for periods between 50 and 300 km. Models are listed in Table 5.4(d).

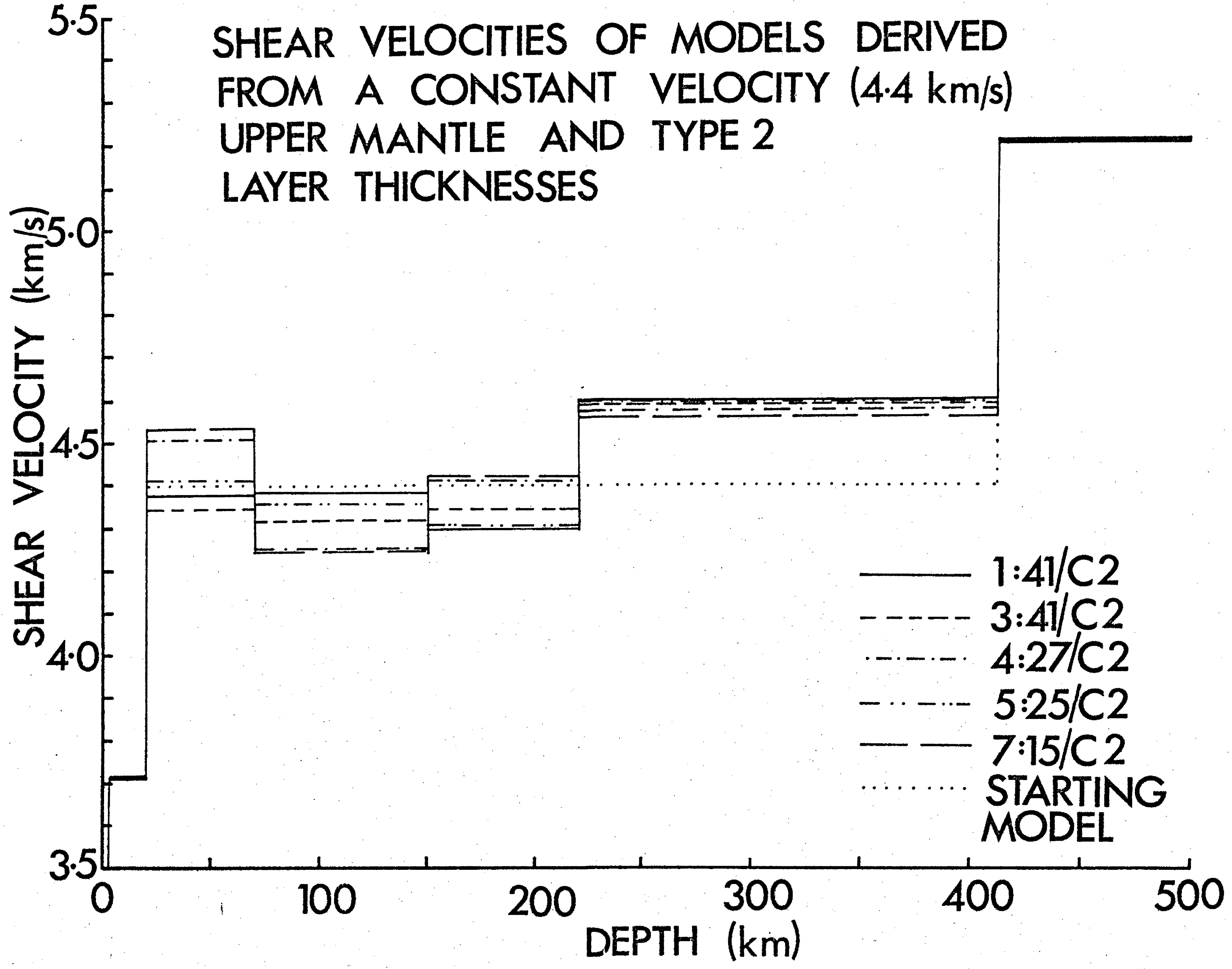
SHEAR VELOCITIES OF MODELS DERIVED FROM A CONSTANT VELOCITY (4·4 km/s) UPPER MANTLE AND TYPE 2 LAYER THICKNESSES
SHEAR VELOCITY (km/s)
5·5
5·0
4·5
4·0
3·5
0
100
200
300
400
500
DEPTH (km)
1:41/C2
3:41/C2
4:27/C2
5:25/C2
7:15/C2
STARTING MODEL

TABLE 5.4(a) AVERAGE EARTH MODELS FOR SHEAR VELOCITY DERIVED BY CONTROLLED MONTE CARLO INVERSION OF GLOBAL AVERAGE GROUP VELOCITIES

TYPE 1 MODELS:

Depth to Top of Layer (km)	Compressional Velocity (km/s)	Density (g/cc)	Shear Velocity (km/s) for Models: 4:44/1	6:14/1	12:15/1	14:17/1	16:14/1	18:11/1
0.0	1.44	1.02	0.0	0.0	0.0	0.0	0.0	0.0
3.0	6.50	2.79	3.720	3.720	3.720	3.720	3.720	3.720
2.10	8.37	3.40	4.346	4.443	4.478	4.452	4.375	4.432
100.	8.37	3.40	4.278	4.276	4.236	4.245	4.294	4.273
200.	8.37	3.40	4.592	4.578	4.584	4.583	4.579	4.580
412.5	9.50	3.80	5.200	5.200	5.200	5.200	5.200	5.200
χ^2_r			.2446	.3165	.3371	.3108	.2595	.2686

TABLE 5.4(b) AVERAGE EARTH MODELS FOR SHEAR VELOCITY DERIVED BY CONTROLLED MONTE CARLO INVERSION OF GLOBAL AVERAGE GROUP VELOCITIES

TYPE 2 MODELS:

Depth to Top of Layer (km)	Compressional Velocity (km/s)	Density (g/cc)	Shear Velocity (km/s) for Models: 2:12/2	3:21/2	2:63/2	2:91/2	2:125/2	3:143/2	8:13/2	3:19/2
0.0	1.44	1.02	0.0	0.0	0.0	0.0	0.0	0.0	0.0	0.0
3.0	6.50	2.79	3.720	3.720	3.720	3.720	3.720	3.720	3.720	3.720
21.0	8.37	3.40	4.510	4.556	4.634	4.600	4.612	4.477	4.487	4.518
70.0	8.37	3.40	4.296	4.296	4.279	4.275	4.262	4.348	4.289	4.313
150.0	8.37	3.40	4.281	4.276	4.290	4.320	4.340	4.267	4.295	4.255
220.0	8.37	3.40	4.610	4.614	4.605	4.591	4.582	4.607	4.619	4.619
412.5	9.50	3.80	5.20	5.200	5.200	5.200	5.200	5.200	5.200	5.200
χ^2_r			.3371	.3587	.3166	.2747	.3161	.2691	.3335	.3825

TABLE 5.4(c)

MODELS DERIVED FROM A CONSTANT VELOCITY (4.4 km/s) UPPER MANTLE WITH LAYER BOUNDARIES FROM TYPE 1 BOUNDS

Depth to Top of Layer (km)	Compressional Velocity (km/s)	Density (g/cc)	Shear Velocity (km/s) for Models: 1:55/CD	4:15/CD	5:59/CD
0.0	1.44	1.02	0.0	0.0	0.0
3.0	6.50	2.79	3.72	3.72	3.72
21.0	8.37	3.40	4.367	4.364	4.325
100.0	8.37	3.40	4.305	4.280	4.303
200.0	8.37	3.40	4.572	4.583	4.578
412.5	9.50	3.80	5.200	5.200	5.200
χ^2_r			.2388	.1885	.1568

TABLE 5.4(d)

MODELS DERIVED FROM A CONSTANT VELOCITY (4.4 km/s) UPPER MANTLE WITH LAYER BOUNDARIES FROM TYPE 2 BOUNDS

Depth to Top of Layer (km)	Compressional Velocity (km/s)	Density (g/cc)	Shear Velocity (km/s) for Models: 1:41/CK	3:41/CK	4:27/CK	5:25/CK	7:15/CK	9:42/CK	13:41/CK
0.0	1.44	1.02	0.0	0.0	0.0	0.0	0.0	0.0	0.0
3.0	6.50	2.79	3.72	3.72	3.72	3.72	3.72	3.72	3.72
21.0	8.37	3.40	4.375	4.347	4.512	4.415	4.538	4.500	4.533
70.0	8.37	3.40	4.377	4.323	4.250	4.361	4.244	4.368	4.259
150.0	8.37	3.40	4.295	4.348	4.414	4.310	4.420	4.334	4.394
220.0	8.37	3.40	4.598	4.590	4.572	4.596	4.564	4.586	4.577
412.5	9.50	3.80	5.200	5.200	5.200	5.200	5.200	5.200	5.200
χ^2_r			.2576	.2026	.2961	.2902	.2531	.2750	.2334

for layers at lithospheric lid depths. Partial derivatives of both phase and group velocity with respect to compressional velocity, shear velocity and density are shown in Figures 5.6 and 5.7 for two successful models - 2:91/2 and 4;44/1. These two models represent extremes in terms of average shear velocities in the lithospheric lid. They also provide a basis of comparison between the resolving power of layers in each of the two layering schemes. Partials for these two models shown in Figures 5.6 and 5.7 are normalized to constant layer thickness. From these figures it is apparent that density partials are appreciable only for the first layer (omitting the water layer) ~ 21 km thick in both models. No independent information on density is available from this study since only Rayleigh wave velocities were measured. Phase velocity partials with respect to shear and compressional velocities for these two models will be used to derive models for Q^{-1} in the next section.

Figure 5.6 PARTIAL DERIVATIVES OF PHASE AND GROUP VELOCITY WITH RESPECT TO COMPRESSIONAL VELOCITY, SHEAR VELOCITY AND DENSITY - for model 2:91/2 are shown for periods between 50 and 400 seconds. Layer numbers are the same as those in Table 5.4(b) for this model. All partial derivatives are normalized to constant layer thickness. Phase velocity partial derivatives with respect to compressional and shear velocities were used in the inversion of global average attenuation data.

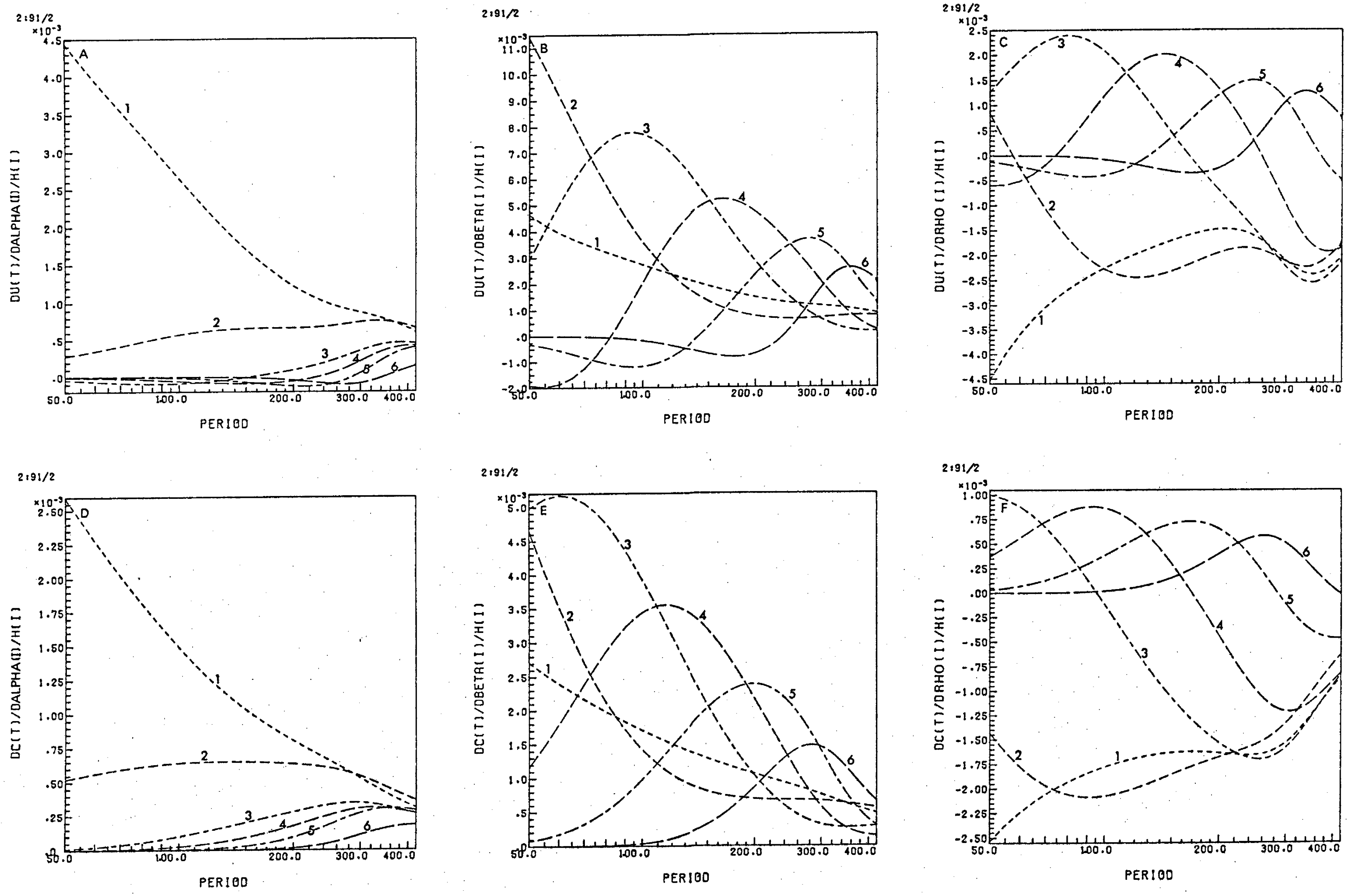
2:91/2
A
DU(T)/DALPHA(I)/H(I)
×10⁻³
4.5
4.0
3.5
3.0
2.5
2.0
1.5
1.0
.5
.0
50.0
100.0
200.0
300.0
400.0
PERIOD
1
2
3
4
5
6
2:91/2
B
DU(T)/DBETA(I)/H(I)
×10⁻³
11.0
10.0
9.0
8.0
7.0
6.0
5.0
4.0
3.0
2.0
1.0
.0
-1.0
-2.0
50.0
100.0
200.0
300.0
400.0
PERIOD
1
2
3
4
5
6
2:91/2
C
DU(T)/DRHO(I)/H(I)
×10⁻³
2.5
2.0
1.5
1.0
.5
.0
-.5
-1.0
-1.5
-2.0
-2.5
-3.0
-3.5
-4.0
-4.5
50.0
100.0
200.0
300.0
400.0
PERIOD
1
2
3
4
5
6
2:91/2
D
DC(T)/DALPHA(I)/H(I)
×10⁻³
2.50
2.25
2.00
1.75
1.50
1.25
1.00
.75
.50
.25
0
50.0
100.0
200.0
300.0
400.0
PERIOD
1
2
3
4
5
6
2:91/2
E
DC(T)/DBETA(I)/H(I)
×10⁻³
5.0
4.5
4.0
3.5
3.0
2.5
2.0
1.5
1.0
.5
0
50.0
100.0
200.0
300.0
400.0
PERIOD
1
2
3
4
5
6
2:91/2
F
DC(T)/DRHO(I)/H(I)
×10⁻³
1.00
.75
.50
.25
.00
-.25
-.50
-.75
-1.00
-1.25
-1.50
-1.75
-2.00
-2.25
-2.50
50.0
100.0
200.0
300.0
400.0
PERIOD
1
2
3
4
5
6

Figure 5.7 PARTIAL DERIVATIVES OF PHASE AND GROUP VELOCITY WITH RESPECT TO COMPRESSIONAL VELOCITY, SHEAR VELOCITY AND DENSITY - for model 4:44/1 are shown for periods between 50 and 400 seconds. Layer numbers are the same as those in Table 5.4(a) for this model. All partial derivatives are normalized to constant layer thickness. Phase velocity partial derivatives with respect to compressional and shear velocities were used in the inversion of global average attenuation data.

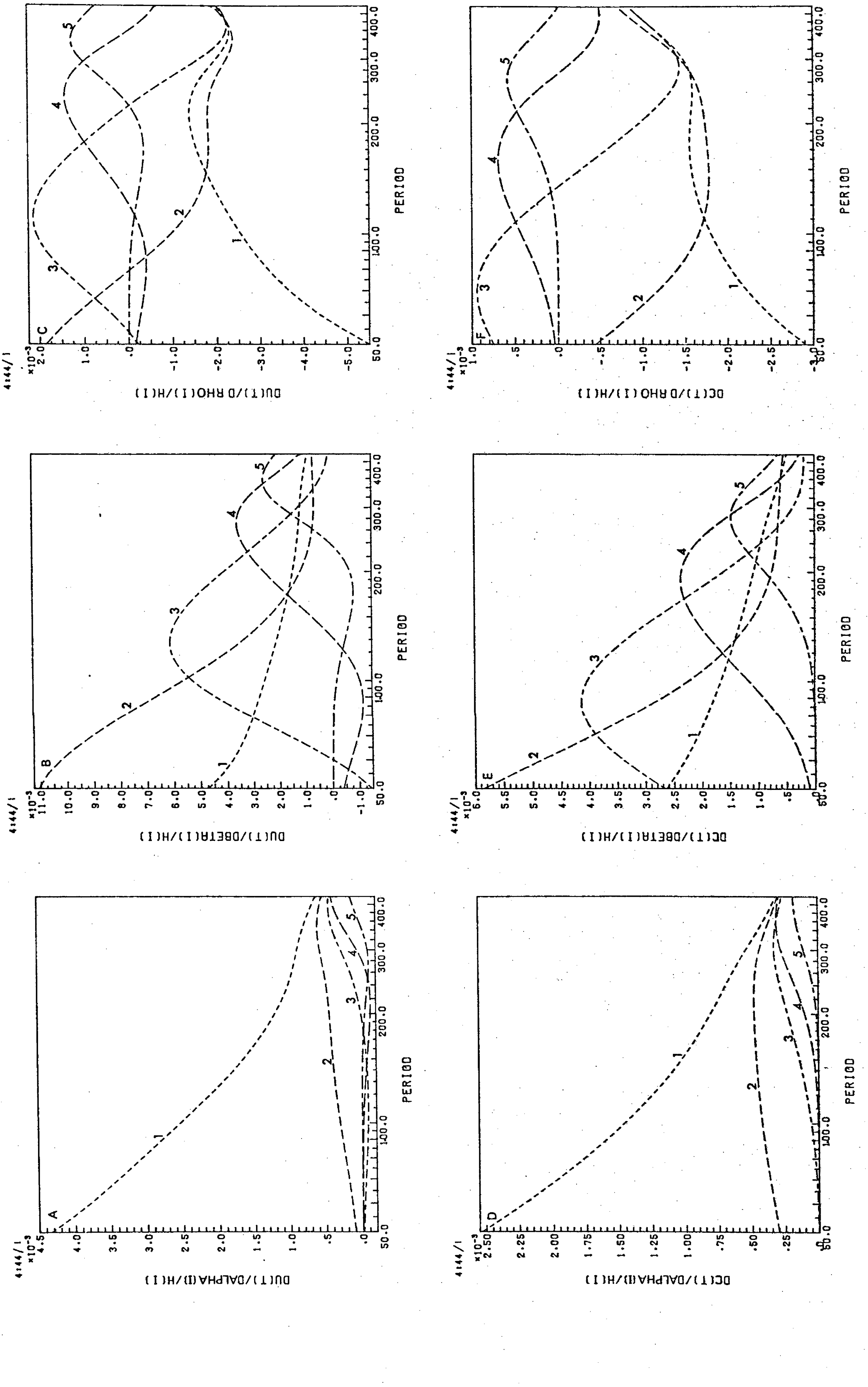
A
DU(T)/DALPHA(I)/H(I)
×10^-3
4.5
4.0
3.5
3.0
2.5
2.0
1.5
1.0
.5
.0
50.0
100.0
200.0
300.0
400.0
PERIOD
1
2
3
4
5
4:44/1
B
DU(T)/DBETA(I)/H(I)
×10^-3
11.0
10.0
9.0
8.0
7.0
6.0
5.0
4.0
3.0
2.0
1.0
.0
-1.0
C
DU(T)/D RHO(I)/H(I)
×10^-3
2.0
1.0
.0
-1.0
-2.0
-3.0
-4.0
-5.0
D
DC(T)/DALPHA(I)/H(I)
×10^-3
2.50
2.25
2.00
1.75
1.50
1.25
1.00
.75
.50
.25
0
E
DC(T)/DBETA(I)/H(I)
×10^-3
6.0
5.5
5.0
4.5
4.0
3.5
3.0
2.5
2.0
1.5
1.0
.5
0
F
DC(T)/D RHO(I)/H(I)
×10^-3
1.0
.5
.0
-.5
-1.0
-1.5
-2.0
-2.5
-3.0

Sec. 5.5 Q^{-1} MODELS

Anderson and Archambeau (1964) and Anderson, et al. (1965) have presented a theory for calculating Q^{-1} for surface wave modes from the specific attenuation of compressional waves, Q^{-1}_{α}, and shear waves, Q^{-1}_{β}, in a layered medium. Methods of inversion of Q^{-1} data based on the major inversion techniques mentioned in the introduction to this chapter have been briefly discussed by Lee and Solomon (1975). A stochastic inversion program described by Mitchell (1977) has been used in this study to estimate Q^{-1}_{β} as a function of depth from the observed attenuation coefficients of Rayleigh waves. Q^{-1}_{α} has been assumed to be one half of Q^{-1}_{β} in this analysis. This differs only slightly from the ideal ratio of 0.44 for a Poisson solid.

Models 2:91/2 and 4:44/1 were selected from the two classes of shear velocity models discussed in Sec. 5.4. Partial derivatives of phase velocity with respect to compressional and shear velocities for models 2:91/2 and 4:44/1 are shown in Figure 5.6 and 5.7. These partials and model phase and group velocities are necessary for the calculation of Q^{-1}_{α}, Q^{-1}_{β}, γ_R and Q^{-1}_{R} for attenuation models. The partials and phase and group velocities were calculated using a surface wave dispersion program with the North and Dziewonski (1976) correction for the earth's sphericity. Since this earth flattening correction begins to break down for periods in excess of 250 seconds and since fewer data are incorporated in the global averages for attenuation coefficients at these long periods, data and partials were restricted to periods from 50 to 300 seconds. Some preliminary attempts at inversion of longer period data produced models with unusually low Q's in the deepest layers of these models. It also appeared that error estimates for the global average attenuation coefficients for periods greater than 300 seconds were too conservative.

Several models fitting Q_R^{-1} calculated from observed group velocities and attenuation coefficients periods between 50 and 300 seconds are shown in Figure 5.8 and 5.9. These models are characterized by a high attenuation layer in the 100 to 220 km depth range. It is evident from the varieties of successful models for shear velocity described in Sec. 5.3 that a range of depths and velocities for the low velocity zone could produce acceptable fits to observed group velocity data. This also appears to be true of Q^{-1} models for this part of the upper mantle. Measurements for periods between 50 and 100 seconds are critical in determining some features of these models - notably the thickness, shear velocity and Q^{-1} of the lithosphere. Since the 50 second attenuation coefficient represents the average of attenuation for only 4 great circle paths (Table 4.3), a test was made to see how much this data influenced the character of Q^{-1} models derived for the average earth. The 50 second data for group velocity and attenuation coefficients were omitted in the inversion of models shown in Figure 5.10. The resulting models are of lower contrast in Q^{-1} between layer 4 and the adjacent layers. This is mainly caused by the loss of resolution in shallower layers and the resulting effect on average Q^{-1} in deeper layers. However, models derived from this restricted data set still show that on a global scale, the greatest attenuation is present at depths between 100 and 200 km. Resolution kernels for models 3/50 and 3/T both indicate that attenuation in the low velocity zone is well resolved (Figure 5.11). Since models produced with and without the 50 second data are substantially in agreement, the group velocity and attenuation coefficient derived for this period are thought to be a reasonable estimate of the global average. The 50 to 100 second attenuation coefficients are also in good agreement with attenuation coefficients measured for Pacific Ocean paths by Mitchell et al. (1976) for similar periods.

Figure 5.8 MODELS FOR SPECIFIC ATTENUATION FOR SHEAR WAVES - as a function of depth are shown for models 2/50, 3/50, 35/50 and 4/50 which assume problem variances of 2×10^{-3}, 10^{-3}, 3×10^{-4} and 2×10^{-4} respectively. All models fit global average attenuation coefficients or periods between 50 and 300 seconds. All models were devised using phase velocity partial derivatives generated from model 2:91/2 (Figure 5.6). All models show that a zone of high attenuation exists for depths between 100 and 200 km. Model MM8 of Anderson *et al* (1965) is shown for comparison. Resolution kernels for model 3/50 are shown in Figure 5.11.

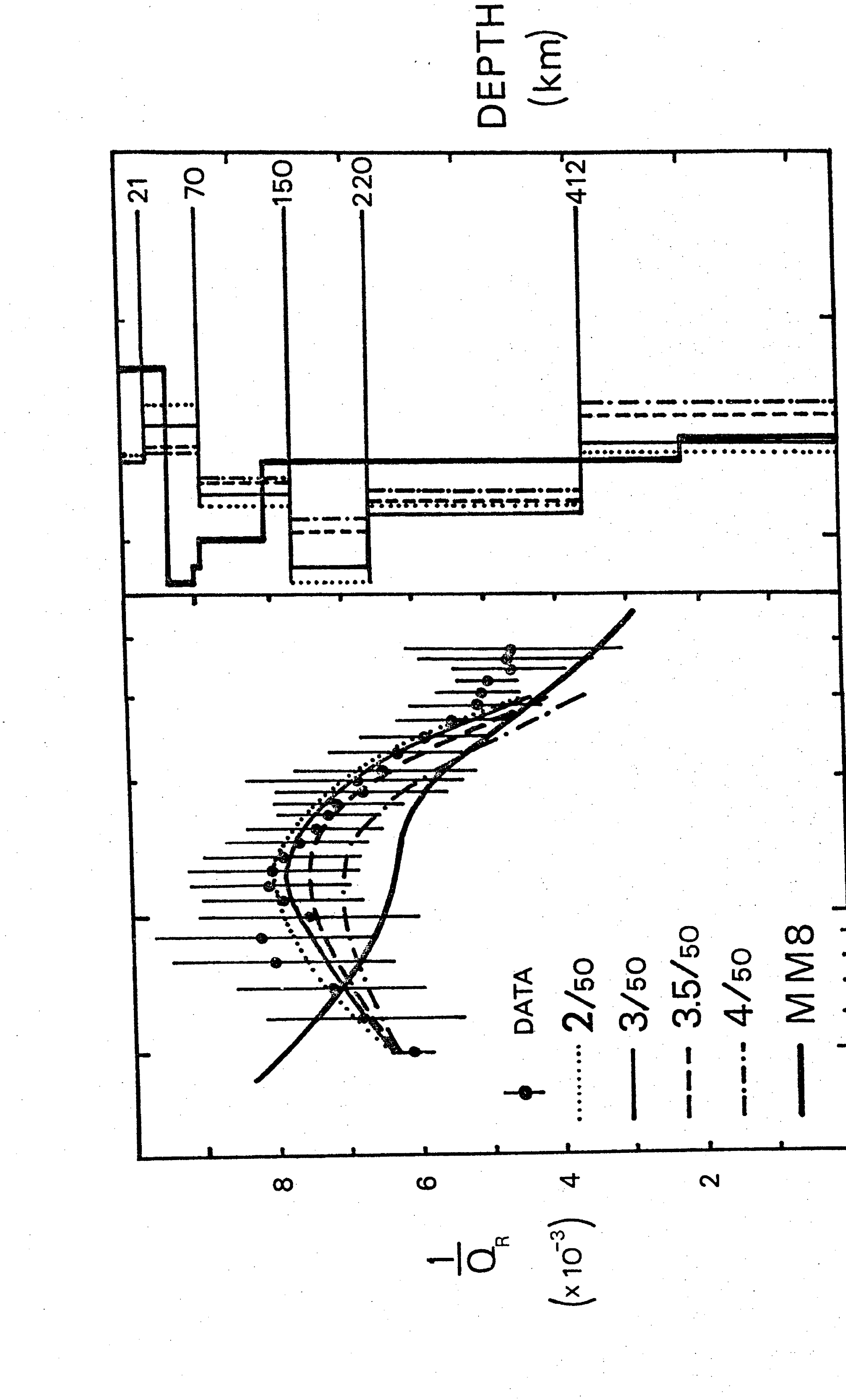
DEPTH (km)
21
70
150
220
412
$\frac{1}{Q_\beta}$
10^{-2}
10^{-3}
$\frac{1}{Q_R}$ ($\times 10^{-3}$)
8
6
4
2
PERIOD (s)
50
100
300
DATA
2/50
3/50
3.5/50
4/50
MM8

Figure 5.9 MODELS FOR SPECIFIC ATTENUATION FOR SHEAR WAVES - as a function of depth are shown for models 2/T, 3/T and 3.6/T which assume problem variances of 2×10^{-3}, 10^{-3} and 5×10^{-4} respectively. All models fit global average attenuation coefficients for periods between 50 and 300 seconds. All models were devised using phase velocity partial derivatives generated from model 4:44/1 (Figure 5.7). These models show that a zone of high attenuation exists for depths between 100 and 200 km. Resolution kernels for model 3/T are shown in Figure 5.11.

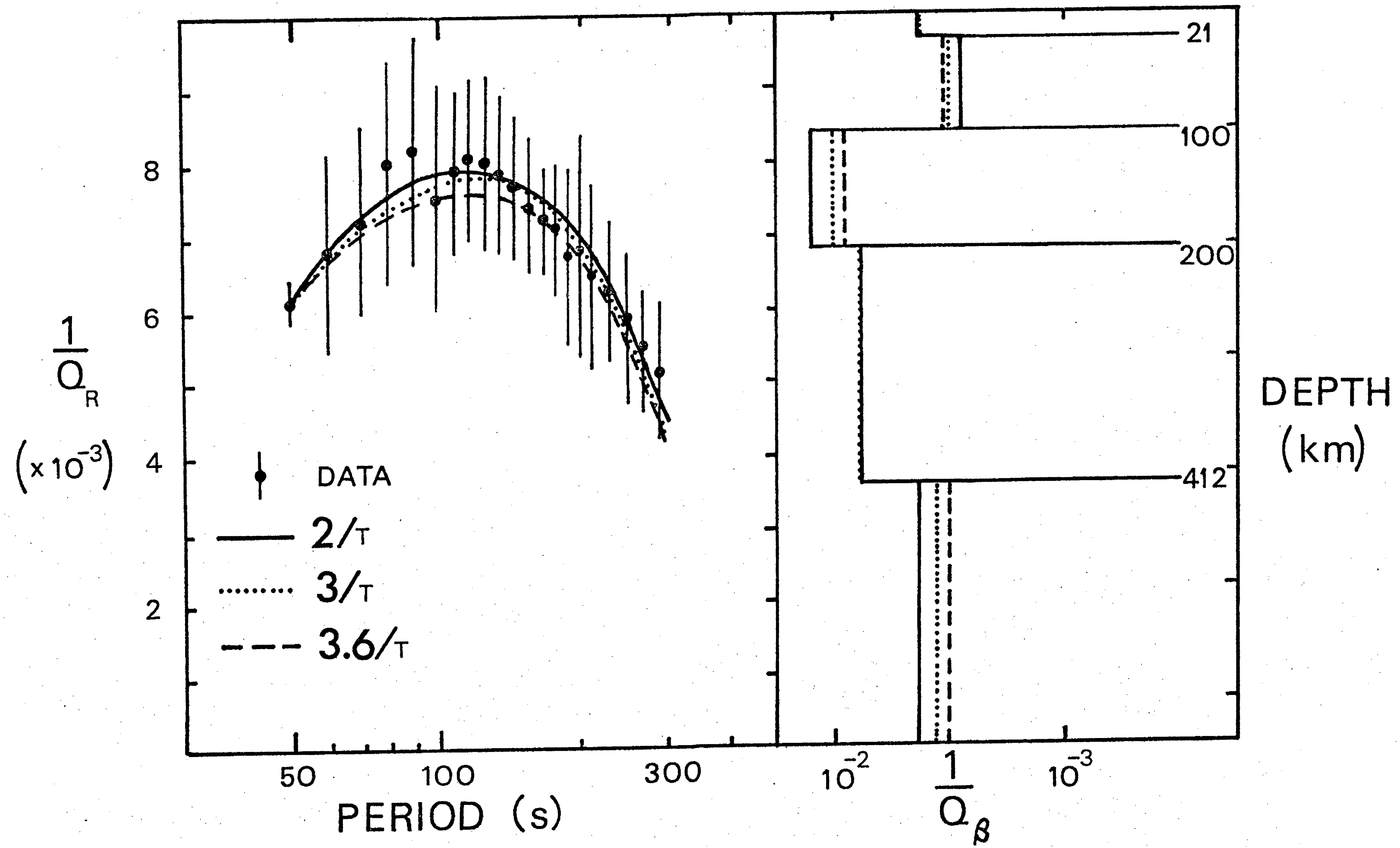
$\frac{1}{Q_R}$
$(\times 10^{-3})$
8
6
4
2
DATA
2/T
3/T
3.6/T
50
100
300
PERIOD (s)
21
100
200
412
DEPTH
(km)
10^{-2}
$\frac{1}{Q_\beta}$
10^{-3}

Figure 5.10 MODELS FOR SPECIFIC ATTENUATION FOR SHEAR WAVES - as a function of depth are shown for models 3/60, 3.5/60 and 4/60 which assume problem variances of 10^{-3}, 3×10^{-4} and 2×10^{-4}. All models fit global average attenuation coefficients for periods between 60 and 300 seconds. All models were devised using phase velocity partial derivatives generated from model 2:91/2 (Figure 5.6). These models were derived in order to test whether the 50 second attenuation coefficient was consistent with the rest of the data.

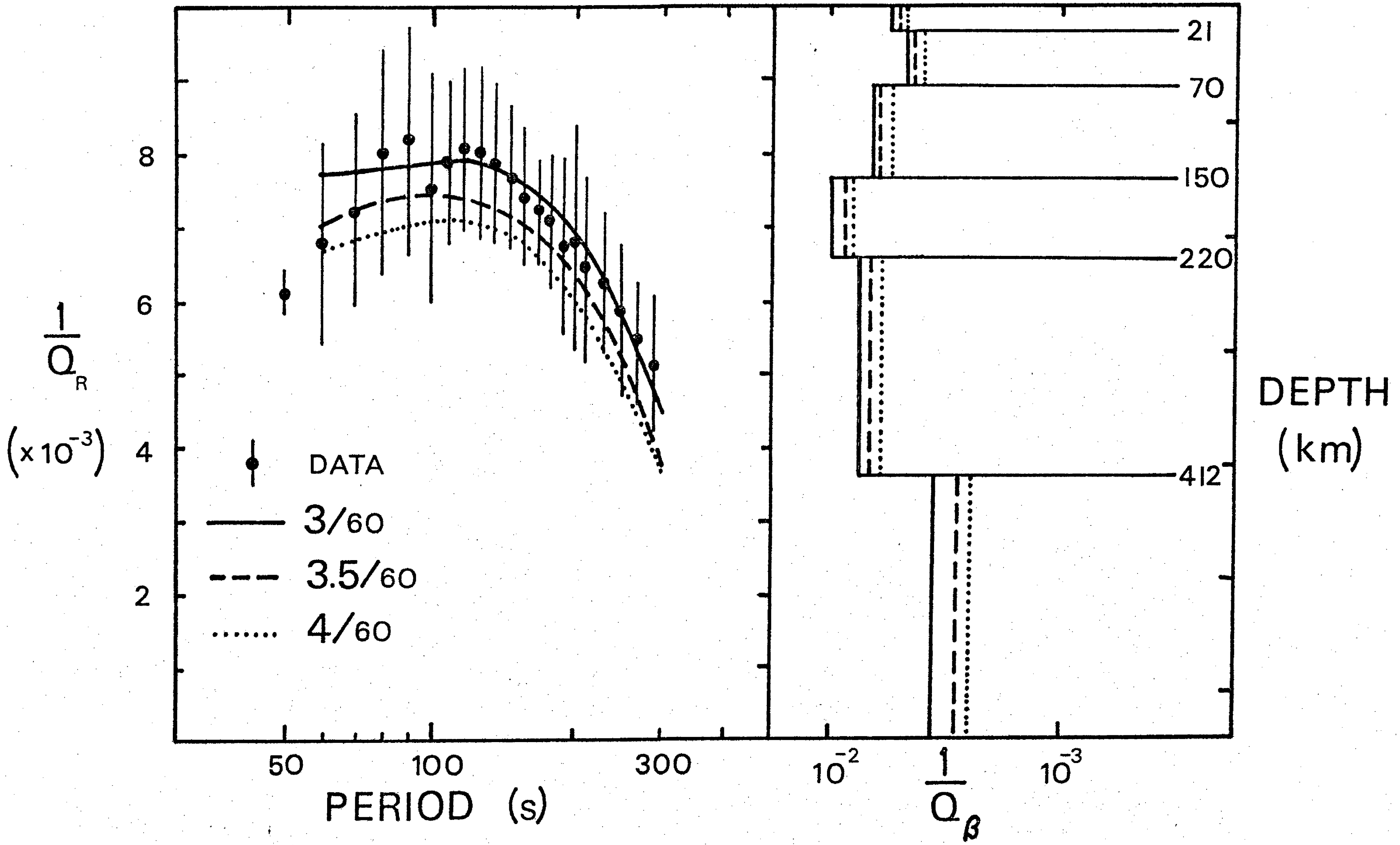
$\frac{1}{Q_R}$ ($\times 10^{-3}$)
8
6
4
2
50
100
300
PERIOD (s)
DATA
3/60
3.5/60
4/60
10^{-2}
$\frac{1}{Q_\beta}$
10^{-3}
21
70
150
220
412
DEPTH (km)

TABLE 5.5(a) Q MODELS DERIVED FROM 2:91

Depth to Top of Layer (km)	V_P (km/s)	V_S (km/s)	Attenuation $1/Q_\beta$ $(\times 10^{-2})$ 2/5	3/5	3.5/5	4/5	3/6	3.5/6	4/6
0	6.50	3.720	.605	.639	.665	.663	.748	.708	.676
21	8.37	4.600	.378	.472	.574	.593	.676	.645	.615
70	8.37	4.275	.837	.784	.737	.727	.822	.768	.738
150	8.37	4.320	1.176	1.099	.966	.907	1.009	.941	.901
220	8.37	4.591	.854	.888	.834	.780	.871	.822	.776
415	9.50	5.300	.644	.560	.436	.392	.557	.435	.392
$\sigma^2_{\text{problem}}$			2×10^{-3}	10^{-3}	3×10^{-4}	2×10^{-4}	10^{-3}	3×10^{-4}	2×10^{-4}

TABLE 5.5(b) Q MODELS DERIVED FROM 4:44

Depth to Top of Layer (km)	V_P (km/s)	V_S (km/s)	Attenuation ($1/Q_\beta$ in units of 10^{-}) 2/T	3/T	3.6/T
0	6.5	3.72	.630	.647	.654
21	8.37	4.346	.449	.495	.525
100	8.37	4.278	1.091	1.005	.953
200	8.37	4.592	.882	.910	.904
415	9.50	5.20	.642	.563	.510
$\sigma^2_{\text{problem}}$			2×10^{-3}	10^{-3}	6×10^{-4}

Model MM8 of Anderson *et al*. (1965) is contrasted with models 2/50 to 4/50 in Figure 5.8. MM8 does not fit the attenuation data presented in this thesis.

Each suite of models shown in Figures 5.8 to 5.10 contains models generated for different problem variances. The problem variance is a parameter which adjusts the trade-off between resolution and precision of estimates within each model. The higher values of the problem variance increase resolution but produce larger standard deviations for model parameters (Mitchell 1977). By trial and error, a problem variance of 10^{-3} was found to produce the most reasonable trade-off. Models 3/T and 3/50 correspond to this value of the problem variance. These models and the other models shown in Figures 5.8 and 5.10 are listed in Table 5.5. The models are characterized by a lithospheric lid with average Q of about 200 overlying a low velocity, high attenuation zone of average Q of 85 - 110. Q's of 170 to 200 are found for the 400 to 600 km depth range but resolution kernels for 3/50 and 3/T show that resolution is poor at these depths.

Figure 5.11 RESOLUTION KERNELS -

for models 3/T and 3/50 show that the specific attenuation at depths of 100 to 200 km - the depth of the low velocity/high attenuation zone - are well resolved in model 3/T and 3/50.

NORMALIZED RESOLUTION KERNELS

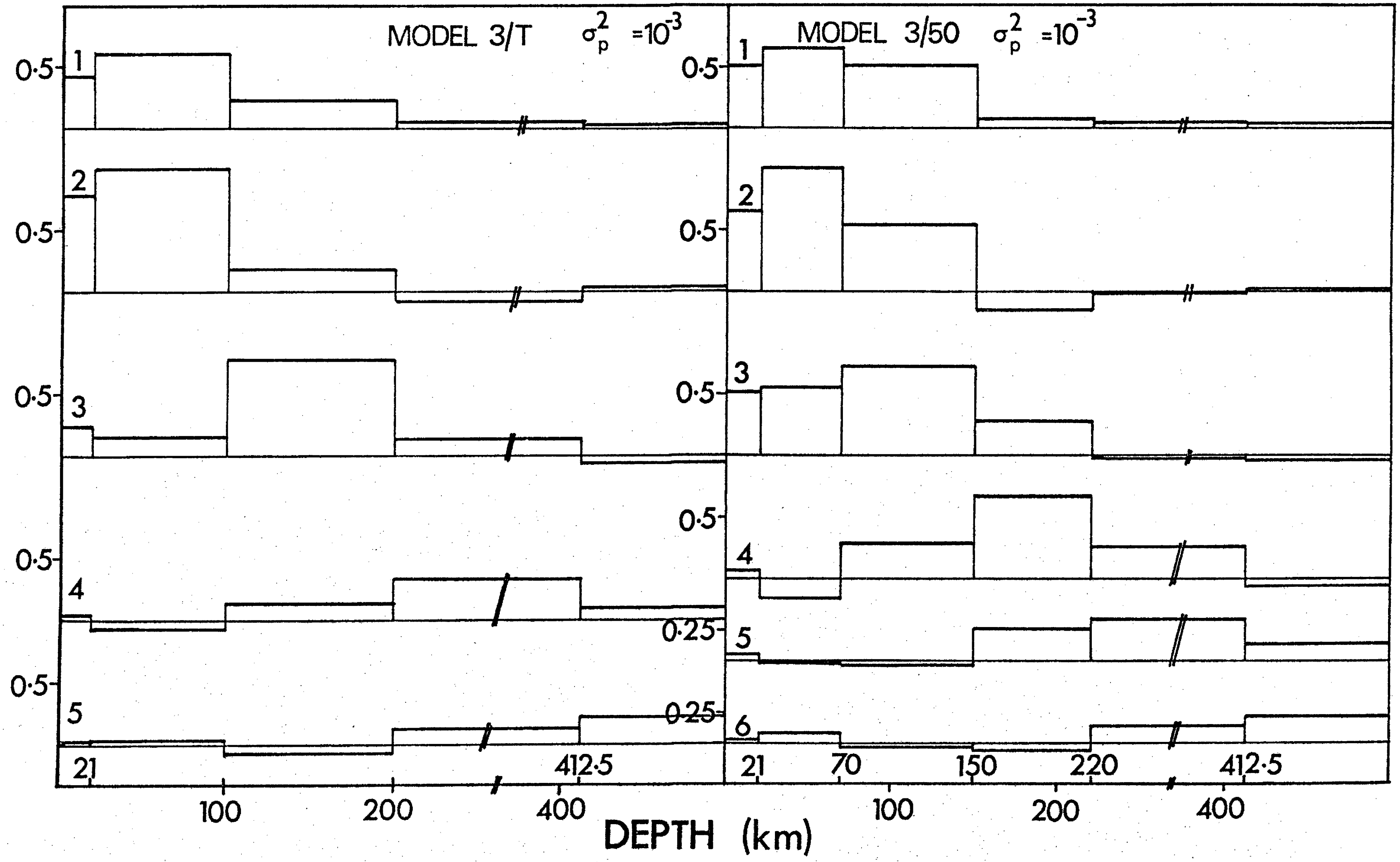

Sec. 5.6 ERRORS IN ESTIMATES OF ATTENUATION AND THEIR EFFECTS ON Q^{-1} MODELS

Reduction in surface wave amplitudes due to scattering caused by lateral heterogeniety has been a topic of deep concern for at least the last ten years. McGarr and Alsop (1967), McGarr (1969a), Drake (1972a, 1972b) and others have recently dealt with the problem of transmission and reflection of short period Rayleigh waves at continental margins. McGarr (1969b) has studied the effects of focusing and defocusing at short periods. Capon (1970, 1971) and Hamada (1972) have shown that Rayleigh waves for periods as great as 50 seconds are laterally refracted by mid-ocean ridges. Hamada (1972) also shows that island arc chains cause serious multipathing problems at periods as great as 140 seconds.

Few attempts have been made to estimate the amount of scattering and multipathing which occurs at periods greater than 100 seconds. Reiter (1973) has estimated that energy losses for spheroidal modes ${}_0S_{19}$ to ${}_0S_{24}$ (300 to 360 seconds) due to a single scattering event in each great circle passage are of the order of 1 to 5 per cent. If at worst 5 such scattering events occurred along a great circle path, a decrement in amplitude of less than 12 per cent should occur. This decrement is small compared to the decrement in amplitude of 82 to 98 per cent actually measured at 150 seconds and 50 seconds respectively. Focusing may occasionally cause more serious problems than losses caused by reflection and mode conversion.

The errors introduced by not considering losses caused by reflection, refraction, and mode conversion are systematic but small compared to the estimates of standard deviations for the attenuation coefficient measurements listed in Table 4.3. If these losses were taken into account the anelastic Q^{-1}_R would be smaller than the values of Q^{-1}_R shown in Figure 4.5 and reproduced in Figures 5.8, 5.9 and 5.10.

Thus, the models shown in Figures 5.8 to 5.10, which have problem variances of less than 10^{-3}, would be in better agreement with these data corrected for scattering losses of 1 to 5 per cent.

CHAPTER 6

THRUST FAULTING AND CRUST-UPPER MANTLE STRUCTURE IN EASTERN AUSTRALIA

Sec. 6.1 INTRODUCTION

Since 1958 the Australian National University (ANU) in cooperation with the Sydney Water Board and the Snowy Mountains Authority has monitored earthquake activity in southeastern Australia (Jaeger and Read 1969). Of the hundreds of crustal earthquakes recorded, only the Picton earthquake of 9 March, 1973 ($m_b \simeq 5.5$) is well enough recorded to provide definitive information on the state of stress in the crust, mode of crustal deformation, and average crust and upper mantle shear wave velocities. Figure 6.1 gives locations of the southeast Australian seismic stations used for locating the Picton earthquake and its aftershocks, as well as locations (stippled areas) of other concentrations of activity within this part of Australia. Similar concentrations may exist north along the coast and off-shore but station coverage is too sparse to locate such activity accurately, if it exists.

The crustal structure in southeastern Australia is inferred from two primary sources: large-scale refraction experiments (Cleary 1973, Underwood 1969, 1970, Doyle et al. 1959, 1966) with shot points in the Bass Strait and off-shore New South Wales and surface wave studies (Thomas 1969, Goncz 1974). Large-scale refraction experiments in Victoria and southern New South Wales are consistent with a two-layer crust thickening from 25 km at the eastern continental margin to 42 km beneath the Snowy Mountains. P-velocities found for the crustal layers and upper-most mantle are 6.0, 6.6 and 7.9 km/s respectively (Cleary 1973). Further north, another crustal refraction profile was recorded from 230 to 605 km SSE of Charters Towers, Queensland by the Bureau of Mineral Resources (BMR) and University of

Figure 6.1 SOUTHEASTERN AUSTRALIA -

Seismic stations used to locate the main shock and its aftershocks are identified by 3 letter codes. Regions known for high levels of shallow focus activity are stippled. Of these regions Talbingo and Eucumbene are also major reservoirs.

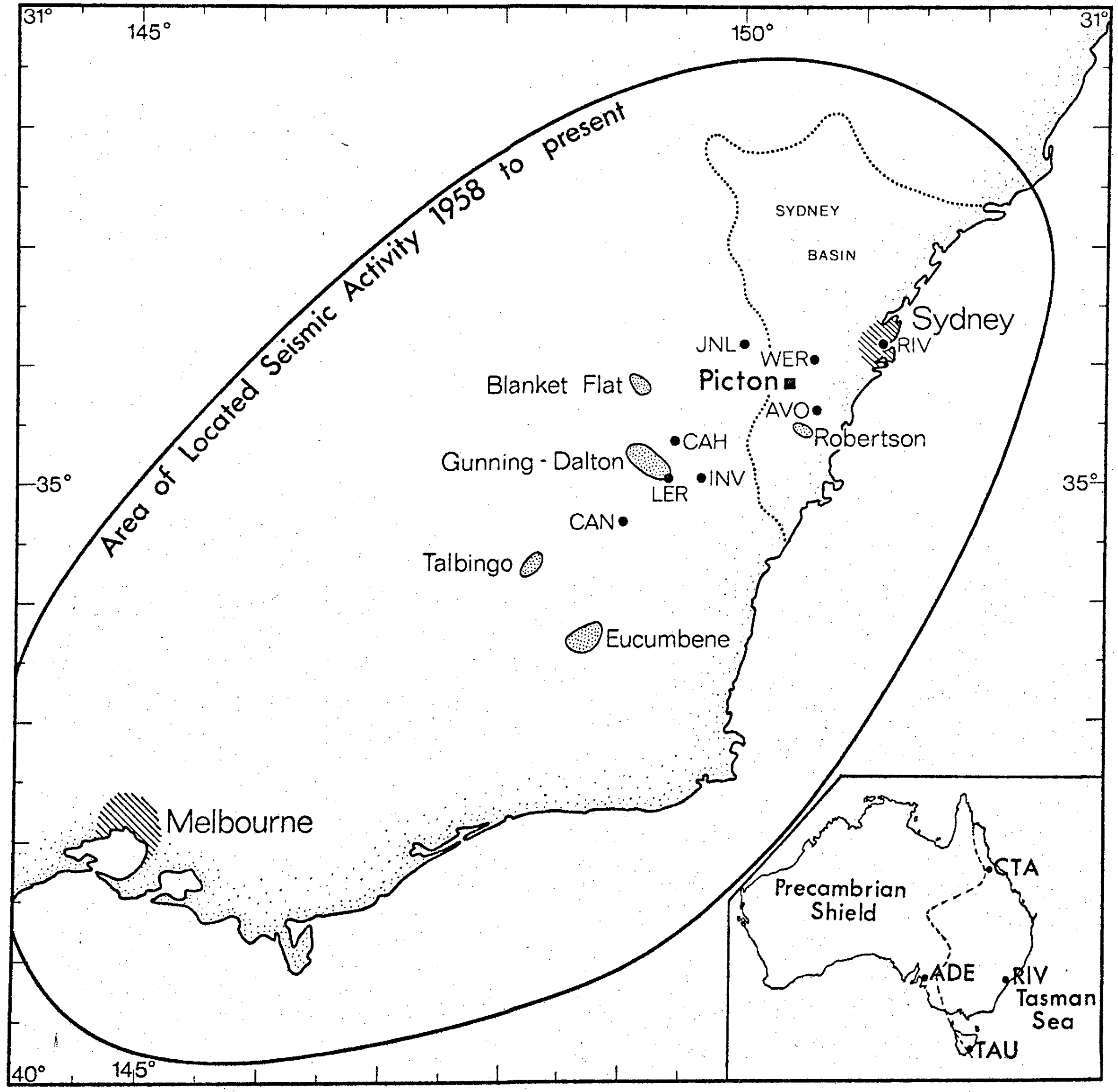
31°
145°
150°
31°
35°
35°
40°
145°
Area of Located Seismic Activity 1958 to present
SYDNEY
BASIN
Sydney
RIV
JNL
WER
Picton
AVO
Robertson
Blanket Flat
CAH
Gunning - Dalton
INV
LER
CAN
Talbingo
Eucumbene
Melbourne
Precambrian
Shield
CTA
ADE
RIV
Tasman
Sea
TAU

Queensland (Connelly and Collins 1973). Collins (personal communication 1975) finds that a 36 to 39 km thick multi-layer crust overlies an upper mantle with a P-velocity of 8.13 km/s. This profile is about 100 km to the east and nearly parallel to the path between the Picton earthquake and Charters Towers and provides a starting model for surface wave inversions to be discussed later.

Thomas (1969) and Goncz (1974) used distant earthquakes of moderate magnitude for measurements of fundamental mode surface wave dispersions between WWSSN stations in Australia. Because they used distant events, they were unable to obtain reliable measurements at periods shorter than 10 to 15 seconds thus limiting resolution at crustal depths. Goncz and Cleary (1976) inverted fundamental mode Rayleigh wave phase velocities from 10 to 90 seconds for eastern and western Australian paths using a 'raw' Monte Carlo method. Four models fitting their data from eastern Australia have low velocity zones in the upper mantle which lead them to conclude that a low velocity zone is required by their data. Other estimates of surface wave dispersion across the Australian continent have been made by Bolt and Niazi (1964) and Landisman _et al_. (1969). Group velocities measured by Landisman _et al_. (1969) for periods of 10 to 120 seconds for the Adelaide to Charters Towers path and By Goncz (1974) for the Riverview-Charters Towers path are in substantial agreement with group velocities measured in this study.

The southeastern continental margin has been a tectonically active region during the last 80 m.y. (Weissel and Hayes 1971). Wellman and McDougall (1974) describe an igneous episode lasting from 80 to 10 m.y. ago that supplied alkaline and tholeiitic basaltic lavas to a 300 km wide coastal region. The older of these lava fields were extruded concurrently with the opening of the Central Tasman basin, formation of the Dampier ridge (Hayes and Ringis 1973) and initial stages of separation of Australia from

Antarctica (Weissel and Hayes 1971). The central volcano provinces show a southward migration of eruptive centres with time which is a good agreement with Australia's rate of drift northward from Antarctica. Wellman and McDougall suggest that the triggering mechanism for this volcanism is related to a tensional stress field and that cessation of volcanic activity 10 to 15 m.y. ago coincides with a change to a predominantly compressive stress field. This change accounts for the upwarping of the eastern Highlands in the Kosciusko uplift.

Evidence for contemporary compressive stress in this region comes from in situ measurements at depths of 1200 and 1800 feet in a mine near Cobar, N.S.W. (Stephenson and Murray 1970). Heat flow values for southeastern Australia reported by Sass (1964) and Jaeger (1970) are 2.0 and 2.9 HFU, which is higher than the average 1.6 HFU for continents. Consequently, the subcrust beneath this part of Australia may be hotter and more mobile than the subcrust beneath stable parts of continents.

The Picton earthquake occurred beneath the back end of the Warragamba Reservoir, one of the Sydney reservoirs, 11 years and 4 months after it was first filled.

In this chapter, measurements of surface wave dispersion at Adelaide, South Australia, Hobart, Tasmania, and Charters Towers, Queensland will be considered first. Earth models for the crust and upper mantle consistent with dispersion of surface waves are discussed in Section 6.3. Finally synthetic surface wave seismograms derived from the best models are used along with aftershock locations and P-wave first-motion focal mechanism to determine fault orientation, moment and stress drop for the Picton earthquake.

Sec. 6.2 SURFACE WAVE DISPERSION

Surface waves were recorded on long period instruments at the three stations shown in the insert in Figure 6.1. Of these, TAU in Hobart, Tasmania, and ADE in Adelaide, South Australia, are World Wide Standard Seismograph Network (WWSSN) stations. CTA at Charters Towers, Queensland, is a high-gain, wide-band, long-period seismograph station recording analogue and digital seismograms. For each station, group velocities and spectral amplitudes were determined separately for both Rayleigh and Love waves. In this analysis, the single station method, instrumental corrections are included in estimates of group arrival times.

Sec. 6.2.1 Instrumental Response

Phase and amplitude response for the WWSSN instruments at ADE and TAU and the high and low gain instruments at CTA (Rynn 1971) were estimated from theoretical expressions derived by Hagiwara (1958) and compared with the response derived from calibration pulses recorded on each seismogram. Each calibration pulse was Fourier analyzed and compared with the Fourier transform of a step function in acceleration. Instrumental amplitude response and instrumental phase delay were calculated from the differences of these spectra. Good agreement was found between amplitude response and phase delay derived by this method and the theoretical quantities predicted from Hagiwara's formulae. Microseismic noise superimposed on the calibration pulses lead to an apparent increase in magnification between 8 and 20 seconds and caused an apparent shift in amplitude response maximum to shorter periods. Other methods of instrument response analysis (e.g. Mitchell and Landismam 1969) are also very susceptible to microseism contamination.

At CTA calibration tests of the high and low gain systems carried out by Jack Millican in the month following the Picton earthquake (April 1973) produced amplitude responses essentially similar to the theoretical responses for the high system. The amplitude response of the high gain photographic and digital records peaks sharply at a period of 40 seconds and falls off at 18db/oct at shorter periods; the low gain photographic record peaks at about 30 seconds and falls off much more gradually at 3 db/oct for shorter periods. This difference in frequency response causes high and low gain records to look radically different (compare seismograms in Figures 6.2 to 6.5). Phase and group delays used for high and low gain records were those predicted for an ideal system consisting of a seismometer and galvonometer with free periods of 30 and 100 seconds.

The seismograms from WWSSN stations ADE and TAU are included In Figures 6.6 and 6.12. These seismograms and the low gain seismograms at CTA were digitized on a DMAC digitizer at the Commonwealth Scientific and Industrial Research Organization, Division of Computing Research, Canberra. The digitized records were interpolated to one sample per half second, low-pass filtered, decimated to one sample per second and linear trends were removed. The high gain digital records, sampled at one per second, were demultiplexed and horizontal components combined to separate radial and transverse components; then remaining linear trends were removed.

Sec. 6.2.2 Group Velocity Dispersion

Group velocities and relative spectral amplitudes were determined using the Direct Filtering Method (DFM) discussed in Chapter 2. DFM locates maxima in the envelope of a narrow-band filtered seismogram and estimates group velocities by least-squares fitting of a parabola to each envelope maximum. Standard errors of group velocities are estimated from the uncertainty of arrival maxima calculated from regression statistics for the best fitting parabola for each maximum and are compared with the half-amplitude width of that parabola. Figures 6.7 to 6.12 show group velocities and

Figure 6.2 CTA LOW-GAIN VERTICAL SEISMOGRAM AND SYNTHETICS - The Charters Towers low-gain vertical seismogram (top) was recorded at a magnification of 6,800. Synthetic seismograms are shown generated from models E1 (middle) and CTA1F2 (bottom) with fault orientation parameters of station azimuth relative to fault strike, fault dip, direction of slip measured downward from the horizontal, and source depth (see Ben-Menahem 1961).

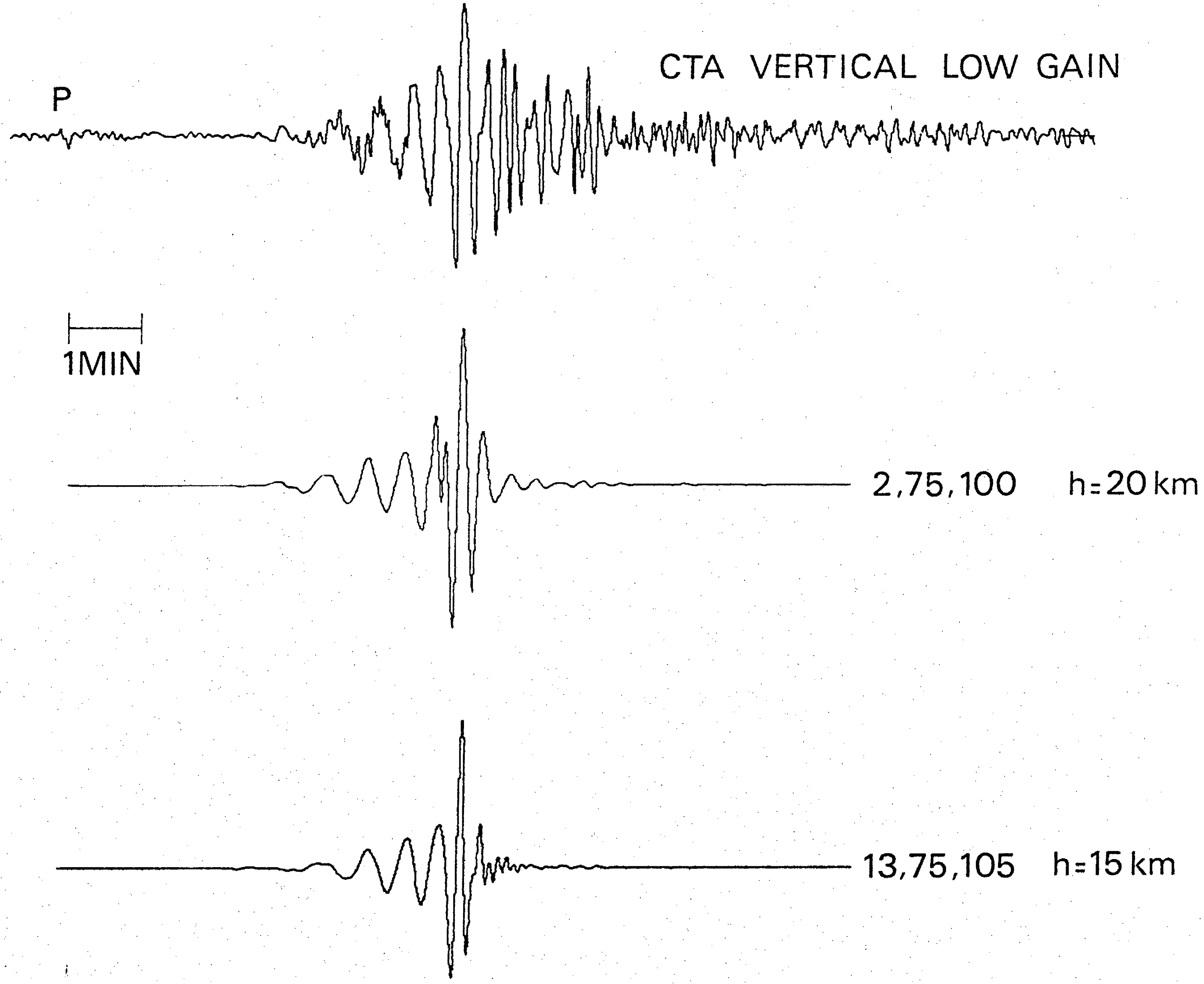
CTA VERTICAL LOW GAIN
P
1MIN
2,75,100 h=20 km
13,75,105 h=15 km

Figure 6.3 CTA LOW-GAIN RADIAL SEISMOGRAM AND SYNTHETICS - The Charters Towers low-gain radial seismogram (top) synthesized from N-S (magnification 5,400) and E-W (magnification 5,300) low-gain seismograms. Synthetic seismograms for models E1 (middle) and CTA1F2 (bottom) are also shown. Fault orientation parameters are as described in the caption to Figure 6.2.

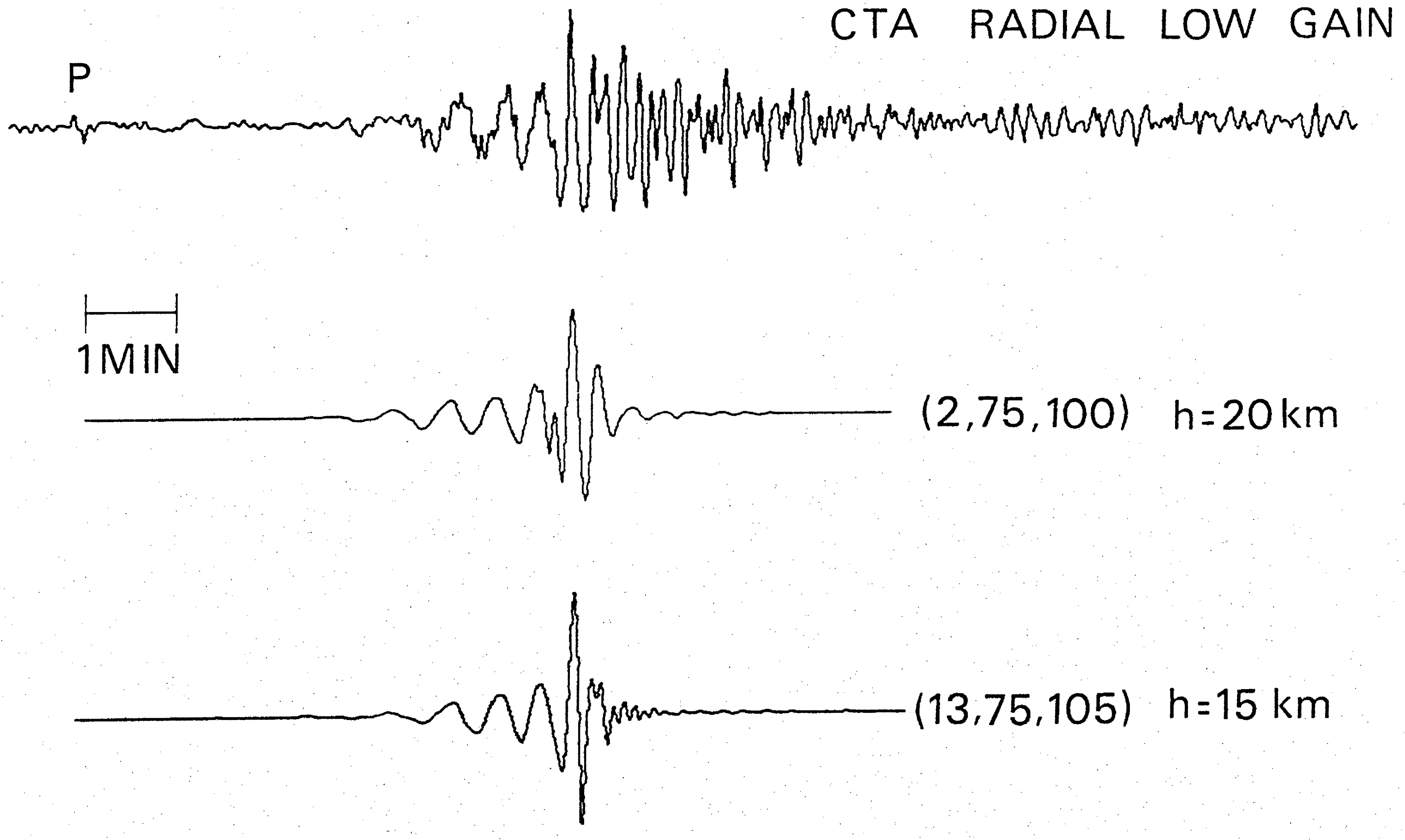
CTA RADIAL LOW GAIN
P
1MIN
(2,75,100) h=20km
(13,75,105) h=15 km

Figure 6.4 CTA LOW-GAIN TRANSVERSE SEISMOGRAM AND SYNTHETICS - The Charters Towers low-gain transverse seismogram (top) synthesized from N-S and E-W low-gain seismogram. Synthetic seismograms for models E1 (middle) and CTA1F2 (bottom) are also shown. Fault orientation parameters are as described in the caption to Figure 6.2.

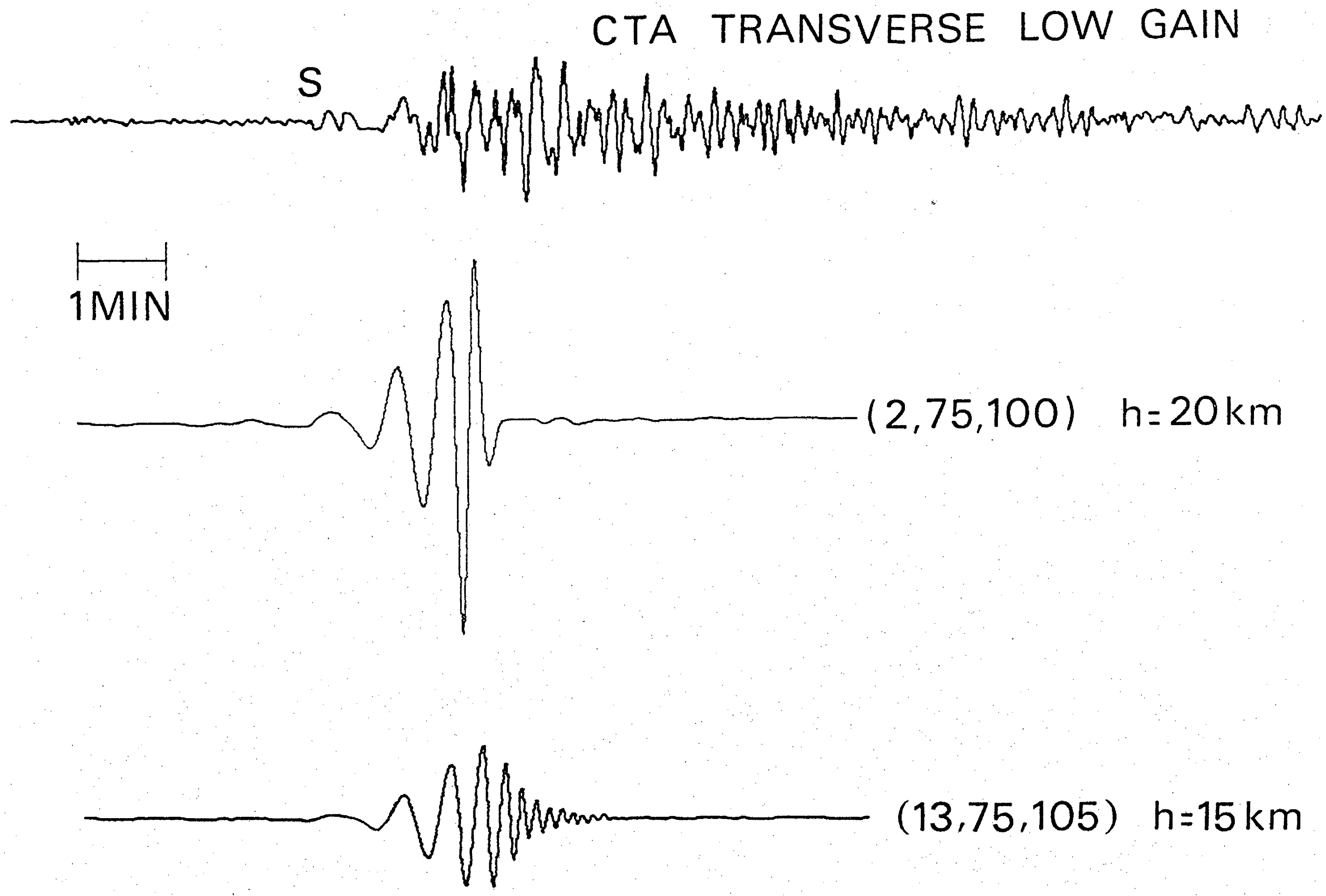
CTA TRANSVERSE LOW GAIN
S
1MIN
(2,75,100) h=20km
(13,75,105) h=15km

Figure 6.5 DIGITAL HIGH GAIN SEISMOGRAMS -

of the Picton earthquake recorded at CTA are shown for vertical (top), radial (middle) and transverse (bottom) components. The maximum amplitudes of all traces have been equalized.

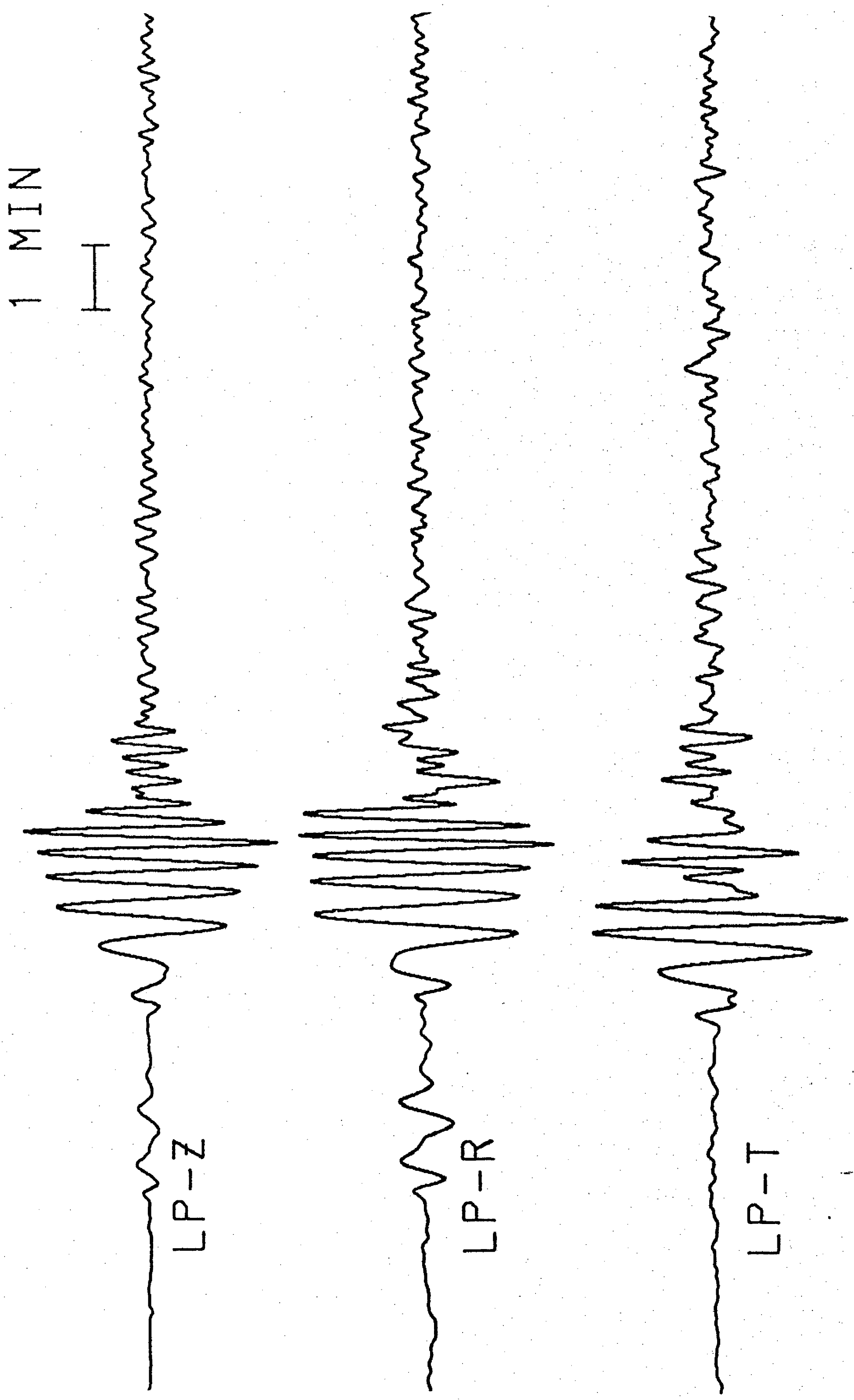
1 MIN
LP-Z
LP-R
LP-T

Figure 6.6 ADE SEISMOGRAMS AND SYNTHETIC SEISMOGRAMS - for the Picton earthquake as recorded at Adelaide, South Australia, are shown as vertical columns, E-W (radial) and N-S (transverse) respectively. In each column are the WWSSN seismograms of magnification 750 (top) and synthetic seismogram generated from model E1 (middle) and model ADEF2 (bottom).

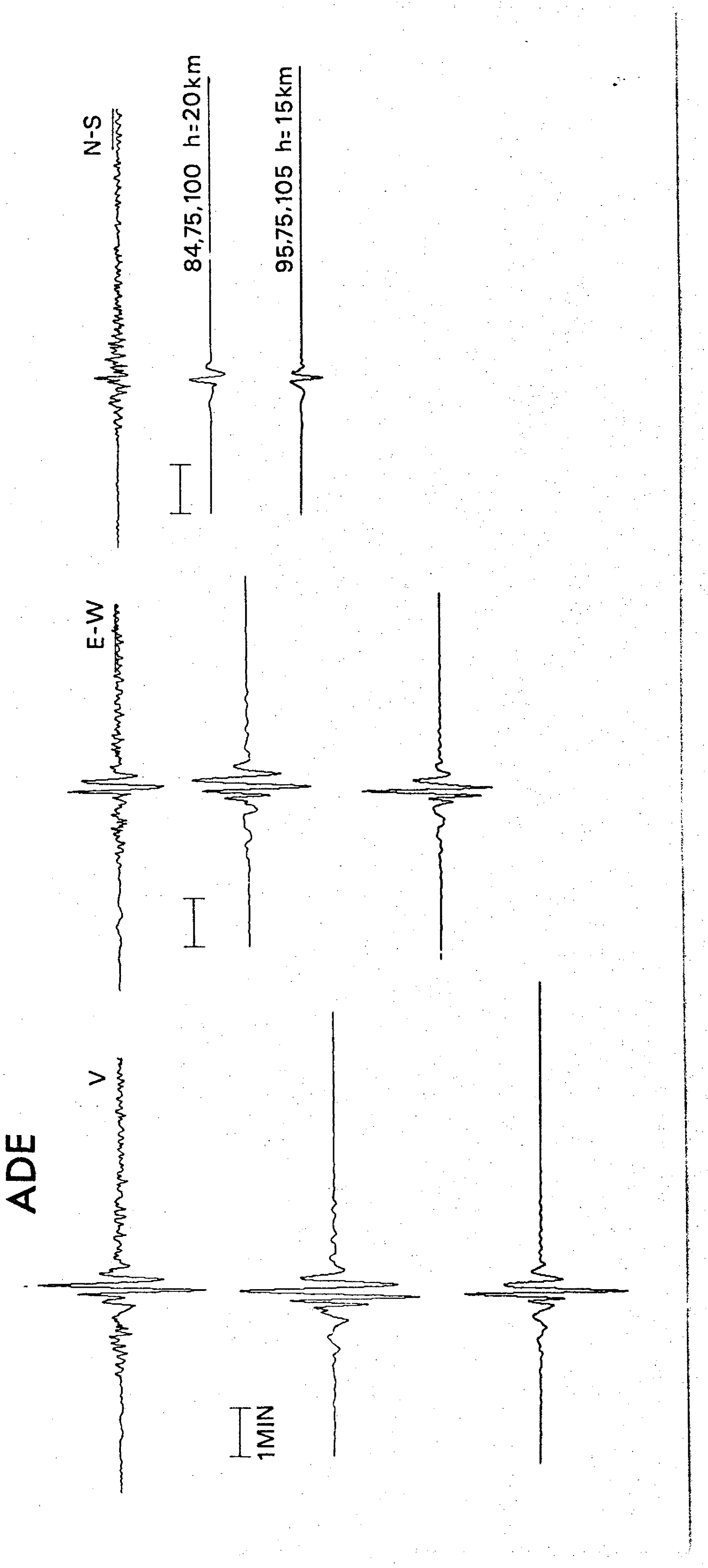
ADE
V
E-W
N-S
84,75,100 h=20km
95,75,105 h=15km
1MIN

relative spectral amplitude estimates (filtered amplitudes) for Rayleigh and Love waves recorded at each station.

For comparison, group velocities and spectral amplitudes for model E1, a Goncz and Cleary (1976) model for eastern Australia, are shown as a solid line in each figure. Also, included in each figure is the group velocity dispersion for two models, CTA1F2 and CTA2S1, and the amplitude spectrum for a synthetic seismogram generated from model CTA1F2. Both CTA1F2 and CTA2S1 were derived by controlled Monte Carlo inversion of the CTA group velocity data and are discussed in Section 6.3. The amplitude spectrum of the fundamental mode for the CTA1F2 synthetic is plotted as a dashed line with the filtered amplitudes for each seismogram.

Disparities between the digitized and synthetic seismograms arise from two sources; higher modes which are not included in the synthetic, and late arrivals due to surface waves laterally refracted at the continental margin. Laterally refracted Rayleigh arrivals at CTA (open triangles in Figure 6.7 and 6.8) are of larger amplitude than the direct fundamental mode arrivals in the period range 7 to 17 seconds. They arrive approximately 100 seconds later than fundamental mode arrivals; this delay is the time difference required to traverse a 300 km longer path than the direct path of 1600 km from Picton to CTA. The longer path length is consistent with waves reflected from the continental margin near Maryborough, Queensland. Love waves observed at CTA are affected more acutely by laterally refracted arrivals which follow fundamental mode arrivals so closely that at periods shorter than 25 seconds fundamental mode arrivals are biased toward slower group velocities. Uncontaminated first higher modes are observed for Rayleigh and Love waves in the period range 5 to 15 and 10 to 20 seconds respectively. The first higher Rayleigh mode begins to be biased to lower group velocities by the much higher amplitude fundamental mode arrivals beyond periods of 15 seconds.

Figure 6.7 RAYLEIGH WAVE GROUP VELOCITY DISPERSION FROM THE VERTICAL CTA HIGH-GAIN DIGITAL SEISMOGRAM - of the Picton earthquake. Circles indicate observations of the fundamental mode, squares, the first higher Rayleigh mode, upward pointing triangles the second higher Rayleigh mode and downward pointing triangles the later refracted arrivals. Open symbols for the fundamental and first higher modes and refracted arrivals indicate that the fundamental mode arrivals are of smaller amplitude than the refracted arrivals or that first higher mode arrivals (diamonds) interfere with fundamental mode arrivals. The solid line indicates group velocities and amplitudes of Goncz and Cleary (1976) model E1 and the dashed curve, velocities and amplitudes of model CTA1F2. CTA2S1 group velocities are shown as a dot-dash where they differ from those of CTA1F2. Model spectral amplitudes have floating vertical scale but are presumed to fit near the maximum. Standard errors of observations are inferred from least squares determinations of group arrival times. Lack of error bars indicates errors smaller than symbol sizes.

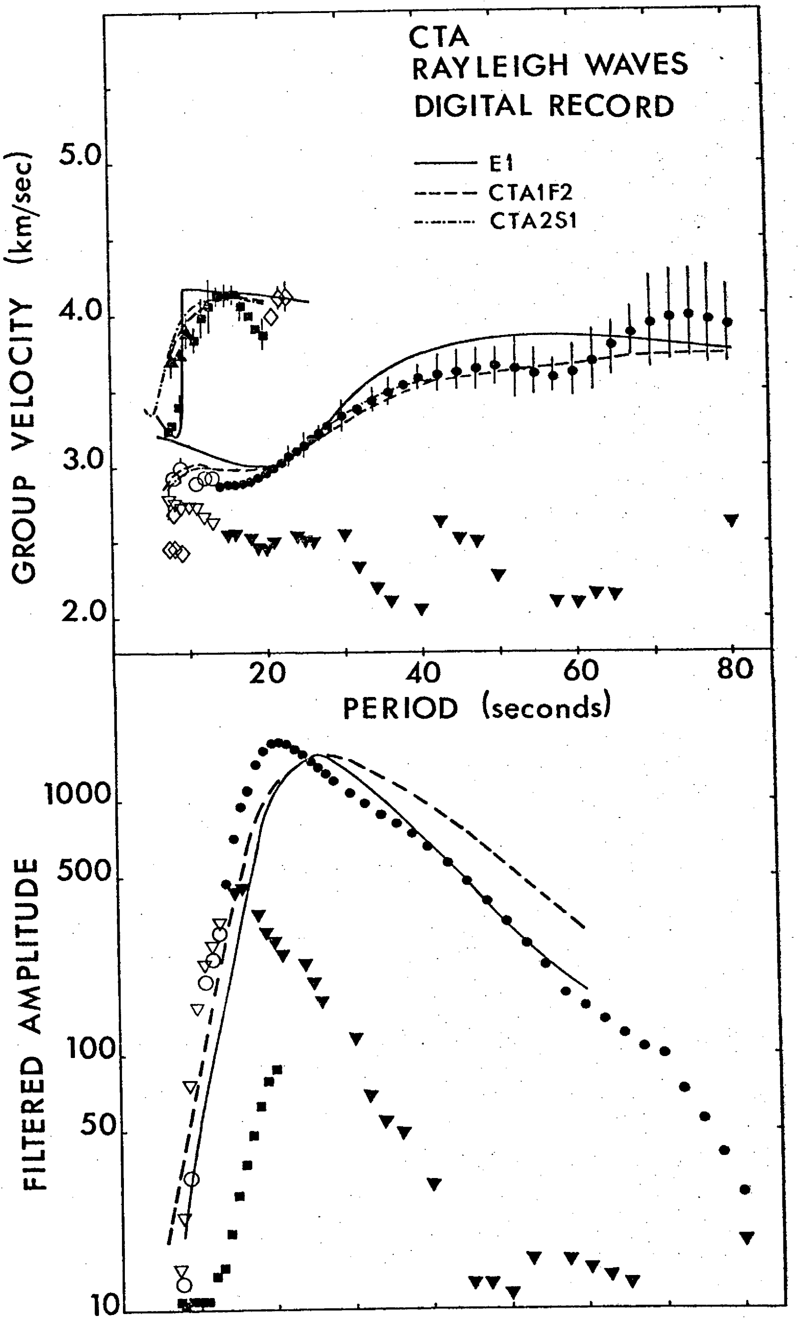
CTA
RAYLEIGH WAVES
DIGITAL RECORD
——— E1
– – – – CTA1F2
–·–·–·– CTA2S1
GROUP VELOCITY (km/sec)
5.0
4.0
3.0
2.0
20
40
60
80
PERIOD (seconds)
FILTERED AMPLITUDE
1000
500
100
50
10

Figure 6.8 RAYLEIGH WAVE GROUP VELOCITY DISPERSION FROM THE VERTICAL CTA LOW-GAIN ANALOGUE SEISMOGRAM - of the Picton earthquake. For explanation of symbols, see Figure 6.7.

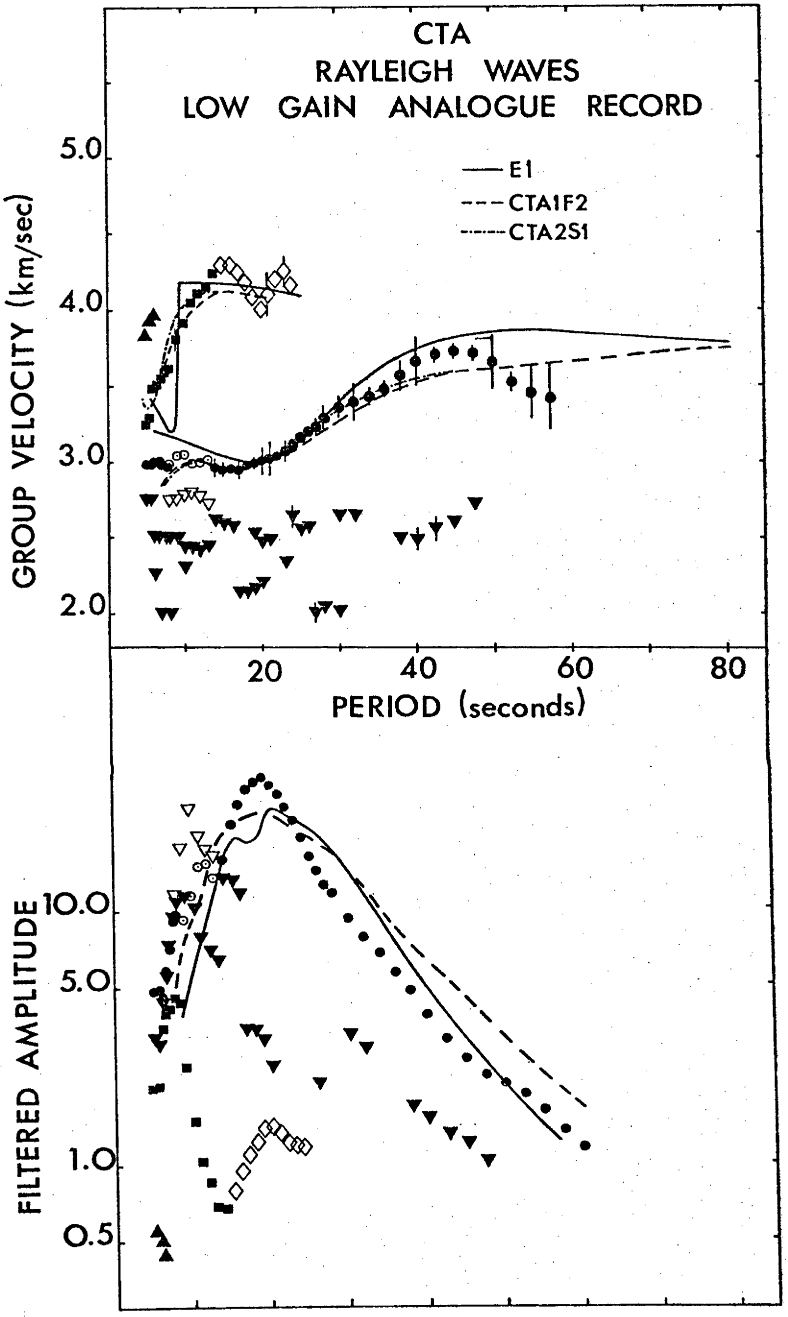
CTA
RAYLEIGH WAVES
LOW GAIN ANALOGUE RECORD
E1
CTA1F2
CTA2S1
GROUP VELOCITY (km/sec)
5.0
4.0
3.0
2.0
20
40
60
80
PERIOD (seconds)
FILTERED AMPLITUDE
10.0
5.0
1.0
0.5

Figure 6.9 LOVE WAVE GROUP VELOCITY DISPERSION FROM THE CTA HIGH-GAIN SEISMOGRAM - of the Picton earthquake. Squares indicate observations of the fundamental mode, triangles the first higher Love mode, open diamonds, later refracted arrivals. Solid and dashed lines represent models E1 and CTA1F2 respectively.

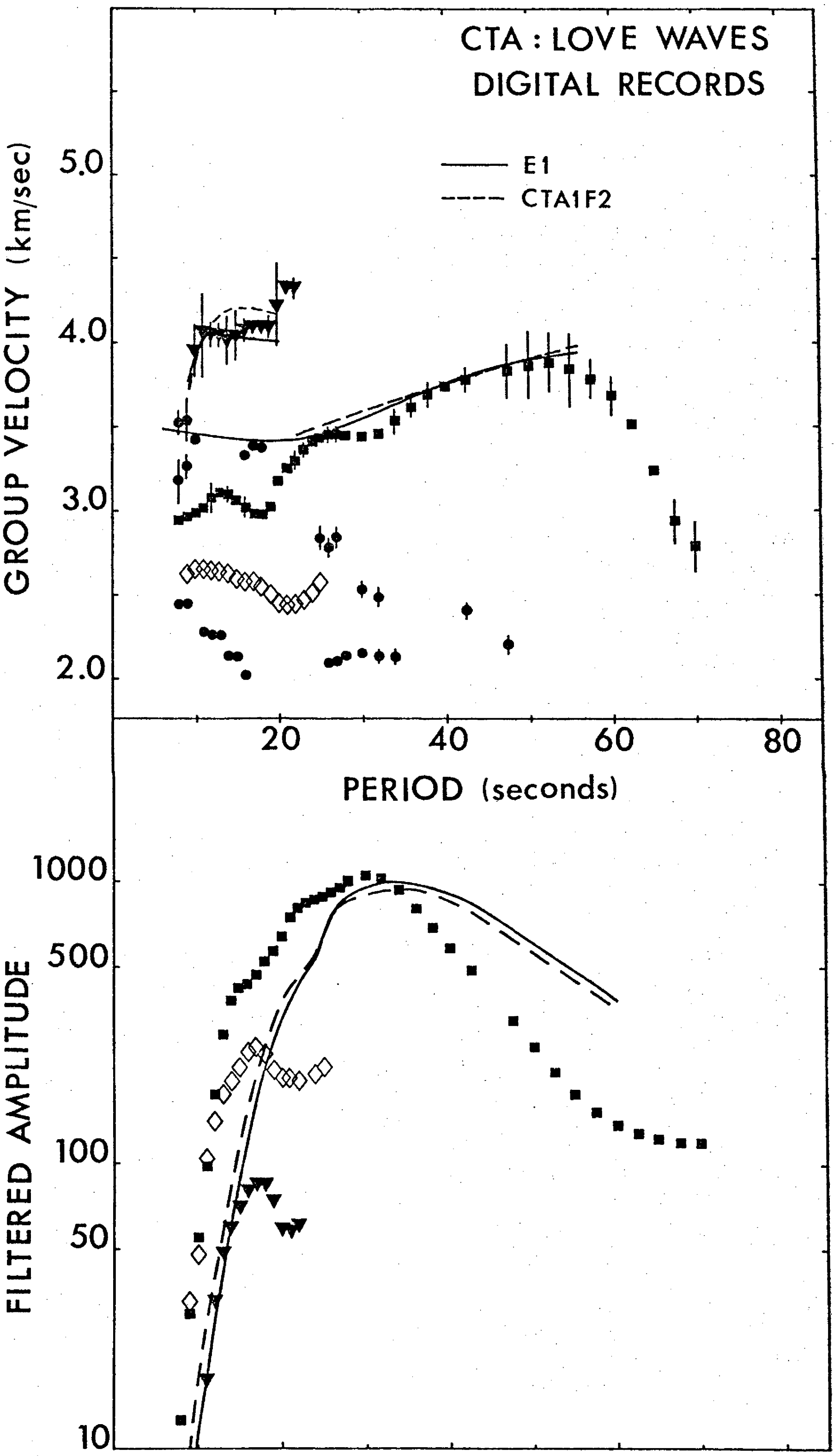
CTA : LOVE WAVES
DIGITAL RECORDS
E1
CTA1F2
GROUP VELOCITY (km/sec)
5.0
4.0
3.0
2.0
20
40
60
80
PERIOD (seconds)
FILTERED AMPLITUDE
1000
500
100
50
10

Figure 6.10 RAYLEIGH WAVE GROUP VELOCITY DISPERSION FROM THE ADE LONG PERIOD VERTICAL SEISMOGRAM -

Circles indicate Rayleigh wave fundamental mode, squares, the first higher mode and triangles the second higher mode. Amplitudes of later refracted arrivals are plotted as open diamonds in the lower half of the figure.

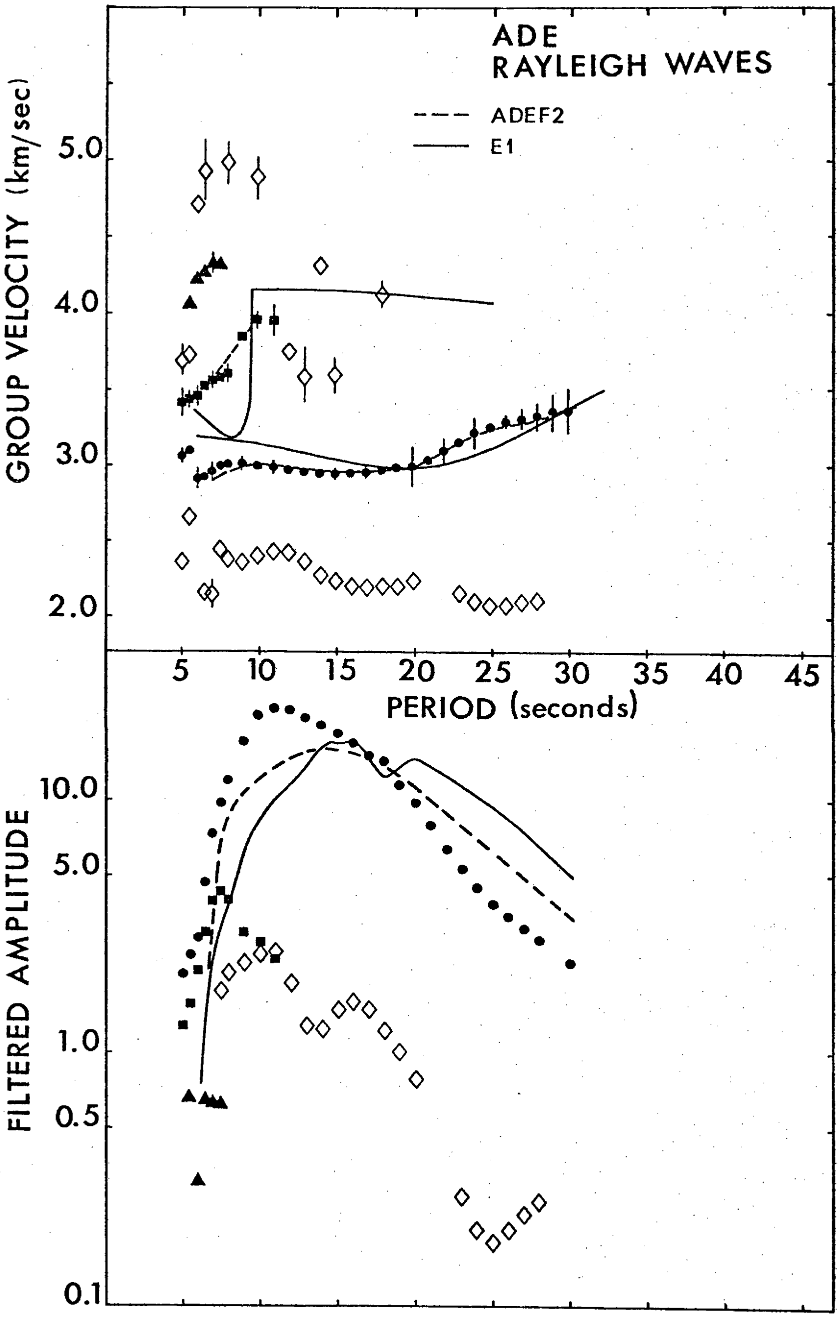
ADE
RAYLEIGH WAVES
ADEF2
E1
GROUP VELOCITY (km/sec)
5.0
4.0
3.0
2.0
5
10
15
20
25
30
35
40
45
PERIOD (seconds)
FILTERED AMPLITUDE
10.0
5.0
1.0
0.5
0.1

Figure 6.11 LOVE WAVE GROUP VELOCITY DISPERSION FROM THE ADE LONG PERIOD N-S SEISMOGRAM -

of the Picton earthquake. Squares represent fundamental mode arrivals and triangles the first higher Love mode. Open squares indicate the group velocities of interfering fundamental and first higher mode arrivals at periods between 5 and 15 seconds. Solid and dashed lines are used for models E1 and ADEF2 respectively.

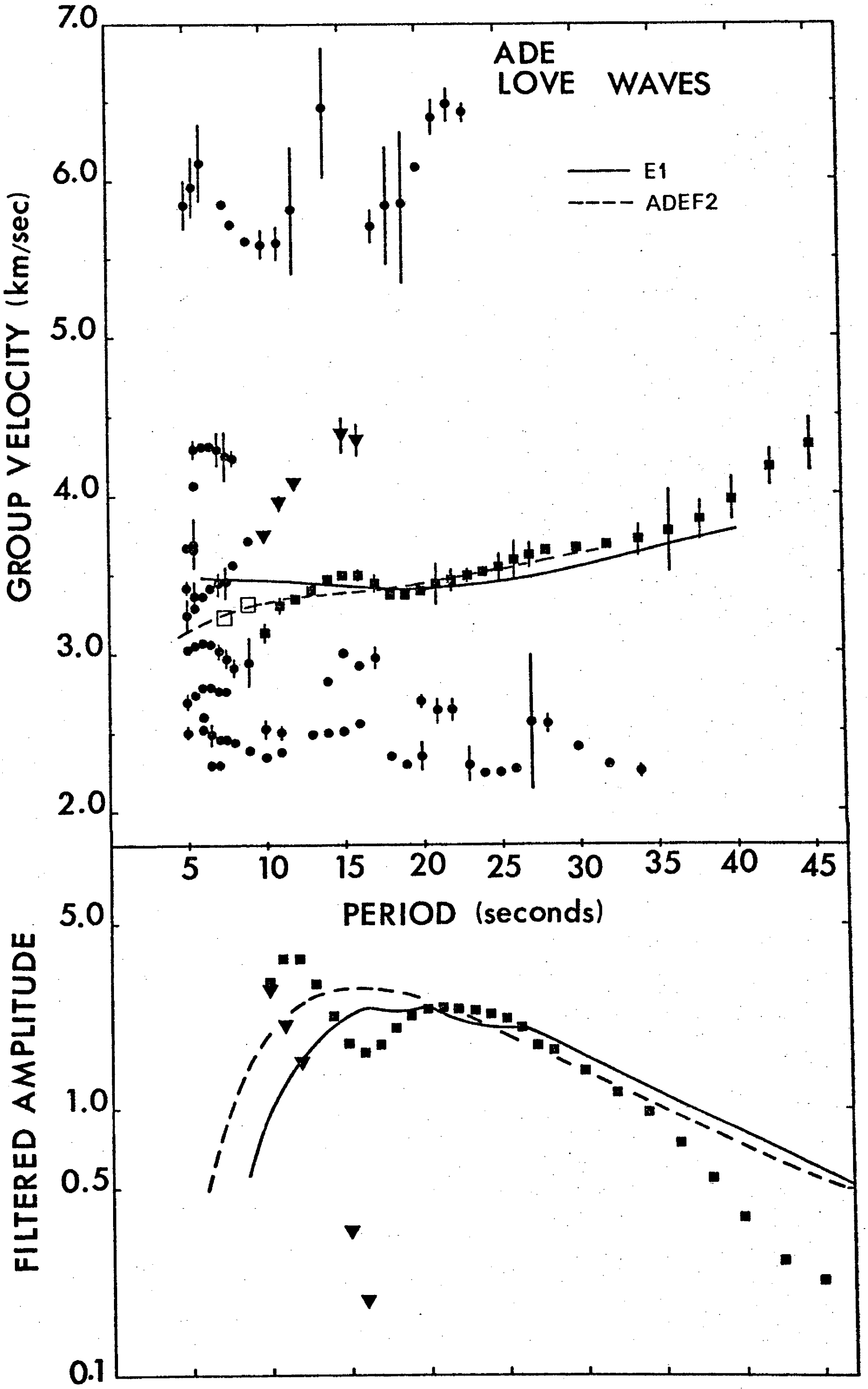
ADE
LOVE WAVES
E1
ADEF2
GROUP VELOCITY (km/sec)
7.0
6.0
5.0
4.0
3.0
2.0
5
10
15
20
25
30
35
40
45
PERIOD (seconds)
FILTERED AMPLITUDE
5.0
1.0
0.5
0.1

Figure 6.12 RAYLEIGH WAVE GROUP VELOCITY DISPERSION FROM THE TAU LONG PERIOD VERTICAL SEISMOGRAM -

of the Picton earthquake. Circles indicate group velocities and amplitudes of the fundamental mode, and squares, the first higher Rayleigh mode. The solid line represents model E1 dispersion. The recorded seismogram (top) and a synthetic seismogram (bottom) from model E1 are shown with source parameters of the synthetic as described in the caption to Figure 6.2.

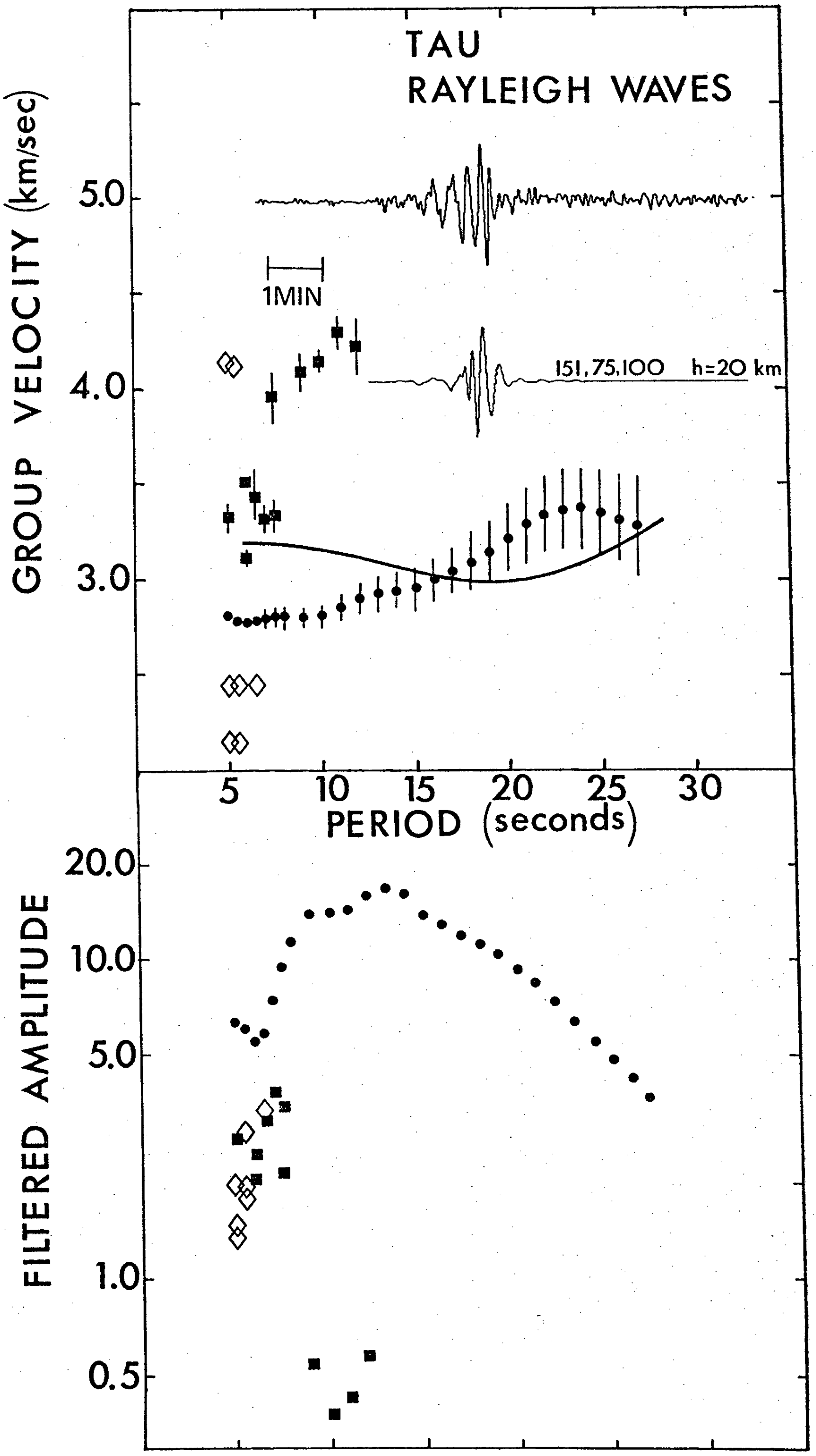
TAU
RAYLEIGH WAVES
1MIN
151,75,100 h=20 km
GROUP VELOCITY (km/sec)
5.0
4.0
3.0
5
10
15
20
25
30
PERIOD (seconds)
FILTERED AMPLITUDE
20.0
10.0
5.0
1.0
0.5

At ADE lateral refraction is not serious since these arrivals are approximately one-tenth the amplitude of fundamental mode arrivals. The only modal interference problem arises from fundamental and first higher mode Love waves between 7 and 13 seconds. Approximate group velocities of interfering group arrivals are indicated by the open squares in Figure 6.11.

Dissimilarity between modelled and observed seismograms in Figure 6.12 indicates that the nature of the Picton-TAU path is markedly different from either of the other two which we have successfully modelled. The transition from continent to ocean is abrupt in eastern Australia as the 400 m isobath is within 100 km of the coastline. The Picton-TAU path crosses east of the Bass Strait where water depths exceed 2 km; this contrasts sharply with the Bass Strait proper which is less than 200 m deep. The close proximity of this path to the continental margin causes reflections and refractions of surface waves from the margin resulting in extension of the surface wave coda to later times than reasonable models allow as seen in the TAU vertical seismogram. An attempt was made to model this path but no model was found which adequately reproduced the observed group velocity dispersion.

It is also interesting to compare dispersion from the digital and analogue vertical seismograms at CTA. Although the analogue record was digitized and a plot of the digitized record compared with the original photographic record used for digitizing, it appears that some of the differences are real and may be due to the analogue recording system, but most are probably caused by very small digitizing errors. The most prominent differences are in the increased smoothness of group velocities and filtered amplitudes of the laterally refracted arrivals in the digitally recorded seismogram, and the increased scatter in the fundamental mode group velocities of Rayleigh waves at periods of 20 to 60 seconds in the digitized analogue record. Agreement between first higher mode group velocities and the fundamental mode from 10 to 25 seconds of the two sets of digital data is excellent.

Sec. 6.3 CONTROLLED MONTE CARLO INVERSION OF GROUP VELOCITIES

Crust and upper mantle models presented in Table 6.2 fit group velocities within 95% confidence limits and show compatibility between fundamental mode dispersion of Love and Rayleigh waves. Group velocities of the first higher modes extend the resolution of shear velocities to depths of about 140 to 180 km. The models were computed by a variation of the Monte Carlo method in which random perturbations that "improve" the fit are incorporated in a new model.

Sec. 6.3.1 Monte Carlo Inversion of Surface Wave Group Velocities

The same algorithm described in Chapter 5 (Figure 5.1) was used to simultaneously invert fundamental and higher mode group velocities for both Rayleigh and Love waves. Since this technique combines the bias-free properties of Monte Carlo modelling with the increased efficiency of refinement modelling, apparent conflicts in information provided by Rayleigh and Love waves, either due to mode contamination or inadequacy of the Rayleigh wave earth flattening approximation, are minimized. The version of program used for inversion of the group velocities presented in Section 6.2 could vary both layer thickness and shear velocity. Choice of layer parameters to be varied during a run were based on the sensitivity of group velocities calculated from a model to changes in model parameters (thickness of layer or shear velocity) and other information on crustal structure along each path provided by refraction profiles.

P-velocities, densities, and bounds on layer thicknesses for an average model of the Picton-CTA path were derived from a refraction profile in the Bowen basin in south central Queensland (Conelly and Collins 1973) and continental upper mantle models based on long period surface wave and free oscillation data (Dziewonski 1971, Dziewonski et al. 1975). Initial upper and lower bounds on shear velocity were derived from P-velocities by allowing Poisson's ratio to range from 0.25 to 0.28 for crustal layers and from 0.25 to 0.30 for upper mantle layers. In one series of models these bounds were relaxed for mantle layers to encourage formation of low velocity zones in starting models. Bounds for all models are listed in Table 6.3.

Love wave group velocities for periods of 10 to 22 seconds were systematically slower than model group velocities for all models generated. As noted earlier examination of Love wave arrivals showed that high amplitude refracted arrivals biased fundamental mode group velocities to unreasonably slow velocities for periods shorter than 25 seconds. For this reason, only fundamental mode Love wave dispersion for periods exceeding 22 seconds was used in subsequent inversions.

Higher mode group and phase velocity calculations require earth structures extending to depths of 400 km or greater. For calculations to these depths the earth's sphericity has been taken into account. This was accomplished by applying earth flattening approximations to earth models before calculating surface wave dispersion. These approximations correct dispersion calculated for a flat layered earth by adjustments to the elastic constants and layer thicknesses of the model. The corrections to Love waves are exact (Biswas and Knopoff 1970), but those applied to Rayleigh waves (Alterman _et al._ 1961) tend to over-correct earth models thereby giving phase and group velocities which are too high (Anderson 1966). These discrepancies are greater for models containing low velocity zones. Empirical corrections (e.g. Bolt and Dorman 1961, North and Dziewonski 1976) which apply only to the fundamental mode were not used.

The reduced χ^2 statistic (see Figure 5.1) was used to judge the "goodness" of fit of each mode. A reduced χ^2 of less than 1.0 represents an "acceptable" fit for a mode. The largest of the χ^2's for each mode was taken as the best indication of the acceptability of each model. Of all models produced only the best fitting ones are listed in Table 6.2. The largest χ^2 for each model is also listed in this table. Two different sets

TABLE 6.1

CTA GROUP VELOCITIES

DATA SET #1

Period	Fundamental Rayleigh Mode	First Higher Rayleigh Mode	Fundamental Love Mode	First Higher Love Mode
7.5	2.98 ± .07	3.58 ± .10		
10	2.96 ± .07	3.93 ± .10		3.96 ± .15
12.5	2.95 ± .07	4.14 ± .10		4.05 ± .10
15	2.92 ± .07	4.29 ± .10		4.06 ± .10
17.5	2.91 ± .07	4.24 ± .10		4.12 ± .10
20	2.96 ± .07	4.04 ± .10		4.25 ± .10
22.5	3.05 ± .07		3.32 ± .07	4.34 ± .15
25	3.15 ± .09		3.45 ± .07	
27.5	3.25 ± .10		3.465 ± .10	
30	3.35 ± .10		3.445 ± .10	
32.5	3.42 ± .10		3.48 ± .10	
35	3.47 ± .10		3.58 ± .08	
37.5	3.52 ± .10		3.70 ± .10	
40	3.60 ± .10		3.76 ± .10	
42.5	3.62 ± .15		3.80 ± .10	
45	3.63 ± .15		3.82 ± .10	
47.5	3.66 ± .15		3.84 ± .10	
50	3.67 ± .15		3.88 ± .20	
52.5	3.65 ± .20		3.89 ± .20	
55	3.62 ± .15		3.86 ± .20	
57.5	3.60 ± .15			
60	3.63 ± .20			
62.5	3.71 ± .20			
65	3.80 ± .20			
67.5	3.89 ± .25			
70	3.96 ± .30			
72.5	3.98 ± .30			
75	4.00 ± .30			
77.5	3.98 ± .30			
80	3.93 ± .35			

TABLE 6.1 (contd.)

CTA GROUP VELOCITIES

DATA SET #2

Period	Fundamental Rayleigh Mode	First Higher Rayleigh Mode	Fundamental Love Mode	First Higher Love Mode
6	2.800 ± .07			
8	2.985 ± .07	3.600 ± .10		
10	2.960 ± .07	3.930 ± .10		3.960 ± .15
12	2.950 ± .07	4.120 ± .10		4.050 ± .12
14	2.920 ± .07	4.240 ± .10		4.060 ± .10
16	2.900 ± .07	4.285 ± .15		4.080 ± .10
18	2.920 ± .07	4.190 ± .17		4.110 ± .10
20	2.960 ± .07	4.040 ± .20		4.180 ± .12
22	3.040 ± .07		3.320 ± .10	
24	3.120 ± .07		3.420 ± .08	
26	3.190 ± .08		3.460 ± .08	
28	3.280 ± .09		3.460 ± .09	
30	3.350 ± .10		3.450 ± .10	
32	3.400 ± .10		3.470 ± .10	
34	3.440 ± .10		3.545 ± .09	
36	3.500 ± .10		3.625 ± .10	
38	3.550 ± .10		3.710 ± .10	
40	3.590 ± .10		3.760 ± .10	
42	3.620 ± .12		3.790 ± .10	
44	3.630 ± .15		3.810 ± .12	
46	3.650 ± .15		3.830 ± .15	
48	3.660 ± .15		3.840 ± .15	
50	3.670 ± .15		3.880 ± .17	
52	3.660 ± .20		3.890 ± .20	
54	3.640 ± .15		3.870 ± .20	
56	3.630 ± .15			
58	3.600 ± .15			
60	3.630 ± .20			

TABLE 6.1 (contd.)

ADE GROUP VELOCITIES

DATA SET #3

Period	Fundamental Rayleigh Mode	First Higher Rayleigh Mode	Fundamental Love Mode
5.0			3.00 ± .15
7.5	3.00 ± .07	3.60 ± .10	3.10 ± .15
10	3.00 ± .07	3.95 ± .10	3.25 ± .15
12.5	2.96 ± .07		3.37 ± .20
15	2.95 ± .08		3.50 ± .20
17.5	2.97 ± .09		3.50 ± .15
20	3.00 ± .09		3.40 ± .10
22.5	3.15 ± .10		3.50 ± .10
25	3.25 ± .10		3.55 ± .10
27.5	3.30 ± .12		3.63 ± .10
30	3.35 ± .12		3.66 ± .15

TABLE 6.2 SHEAR VELOCITY MODELS DERIVED BY CONTROLLED MONTE CARLO INVERSIONS

TABLE 6.2(a) CTA MODELS - DATA SET #1

FLAT LAYERED EARTH MODELS (NO CORRECTION FOR SPHERICITY)

			CTA1F1		CTA1F2	
Layer No.	V_p(km/s)	(g/cc)	Z(km)	V_S(km/s)	Z(km)	V_S(km/s)
1	4.0	2.4	0.53	2.277	1.36	2.320
2	5.5	2.67	5.78	3.085	5.43	3.124
3	6.4	2.85	29.0	3.672	29.0	3.689
4	7.1	2.95	37.1	3.910	37.5	3.953
5	8.13	3.33	84.0	4.276	67.0	4.241
6	8.2	3.335	180.0	4.381	180.0	4.346
7	8.6	3.35	420.0	4.639	420.0	4.687
largest χ^2_r			1.05		0.99	

TABLE 6.2(a)(contd.) CTA MODELS - DATA SET #1

SPHERICALLY CORRECTED EARTH MODELS

			CTA1S1		CTA1S2	
Layer No.	V_p(km/s)	(g/cc)	Z(km)	V_S(Km/s)	Z(km)	V_S(km/s)
1	4.0	2.4	0.63	2.276	1.35	2.385
2	5.5	2.67	6.67	3.151	4.89	3.027
3	6.4	2.85	29.0	3.668	29.0	3.655
4	7.1	2.95	39.6	4.085	37.9	4.077
5	8.13	3.33	98.0	4.289	80.0	4.241
6	8.2	3.335	180.0	4.380	180.0	4.278
7	8.6	3.35	420.0	4.614	420.0	4.700
largest χ^2_r			1.140		1.252	

TABLE 6.2(a)(contd.) CTA MODELS - DATA SET #1

FLAT LAYERED EARTH RAYLEIGH WAVES

SPHERICAL EARTH LOVE WAVES

			CTA1FS1		CTA1FS2	
Layer No.	V_p(km/s)	(g/cc)	Z(km)	V_S(km/s)	Z(km)	V_S(km/s)
1	4.0	2.4	0.73	2.200	0.71	2.384
2	5.5	2.67	5.73	3.086	5.78	3.220
3	6.4	2.85	29.0	3.629	29.0	3.676
4	7.1	2.95	34.5	4.251	40.1	4.051
5	8.13	3.33	85.0	4.293	82.0	4.353
6	8.2	3.335	180.0	4.384	180.0	4.567
7	8.6	3.35	420.0	4.722	420.0	4.792
largest χ^2_r			1.63		1.61	

TABLE 6.2(b) CTA MODELS - DATA SET #2

FLAT EARTH MODELS (NO CORRECTION FOR SPHERICITY)

			CTA2F1		CTA2F2	
Layer No.	V_p(km/s)	ρ(g/cc)	Z(km)	V_S(km/s)	Z(km)	V_S(km/s)
1	4.0	2.4	1.232	2.296	0.554	2.239
2	5.5	2.67	5.402	3.043	5.77	3.065
3	6.4	2.85	29.0	3.694	29.0	3.647
4	7.1	2.95	35.3	3.957	39.1	4.194
5	8.13	3.33	55.0	4.172	64.0	4.226
6	8.2	3.335	180.0	4.319	180.0	4.382
7	8.6	3.35	420.0	4.582	420.0	4.679
largest χ^2_r			1.083		1.233	

TABLE 6.2(b)(contd) CTA MODELS - DATA SET #2

SPHERICAL EARTH MODELS

CTA2S1		CTA2S2	
Z(km)	V_S(km/s)	Z(km)	V_S(km/s)
1.05	2.412	0.72	2.460
6.58	3.233	5.42	3.025
29.0	3.634	29.0	3.699
39.3	4.115	42.5	4.065
89.0	4.233	73.0	4.291
180.0	4.271	180.0	4.435
420.0	4.582	420.0	4.973
largest χ^2_r 1.097		1.328	

TABLE 6.2(c) CTA MODELS - DATA SET #2

FLAT LAYERED EARTH RAYLEIGH WAVES

SPHERICAL EARTH LOVE WAVES

CTA2F1					CTA2FS2				
Layer No.	Z(km)	V_P(km/s)	V_S(km/s)	ρ(g/cc)	Layer No.	Z(km)	V_P(km/s)	V_S(km/s)	ρ(g/cc)
1	0.59	4.0	2.328	2.40	1	1.04	4.0	2.237	2.40
2	5.76	5.5	3.240	2.67	2	4.75	5.5	3.303	2.67
3	29.1	6.4	3.640	2.85	3	26.9	6.4	3.611	2.85
4	37.3	7.1	3.818	2.95	4	35.7	7.1	3.928	2.95
5	161.0	8.13	4.205	3.335	5	70.0	8.13	4.331	3.335
6	218.0	8.2	4.301	3.402	6	120.0	8.13	4.461	3.335
7	420.0	8.6	4.545	3.430	7	191.0	8.13	4.425	3.335
8	670.0	9.5	5.280	3.768	8	227.0	8.2	3.921	3.402
					9	420.0	8.6	4.631	3.430
					10	670.0	9.5	5.280	3.763
largest χ^2_r		1.04					1.24		

TABLE 6.2(d) ADE MODELS - DATA SET #3

FLAT EARTH MODELS (NO CORRECTION FOR SPHERICITY)

			ADEF1		ADEF2		ADEF3	
Layer No.	V_p(km/s)	ρ(g/cc)	Z(km)	V_S(km/s)	Z(km)	V_S(km/s	Z(km)	V_S(km/s)
1	4.0	2.40	0.82	2.253	0.70	2.346	0.81	2.399
2	5.5	2.67	6.79	3.450	6.13	3.261	6.56	3.196
3	6.4	2.85	29.0	3.591	29.0	3.659	29.0	3.662
4	7.1	2.95	31.2	4.266	33.4	3.988	40.2	4.102
5	8.13	3.33	62.0	4.278	70.0	4.290	99.0	4.196
largest χ^2_r			0.970		0.982		0.927	

of models were produced using data sets listed in Table 6.1 for CTA and ADE and model bounds listed in Table 6.3. Of the two data sets shown for CTA in Table 6.1 data set #1, was used for some of the first models produced. Since group arrivals at periods of 60 seconds and greater have small amplitudes, a second data set (#2) was used to test whether more consistent models could be devised by excluding this low amplitude data. Data set #2 was used for later models when we also found that changes in some layers significantly changed fundamental mode dispersion in the period range 20 to 40 seconds. A closer spacing of measurements in this period range improved ability of the χ^2 test to reject models which fit poorly.

Sec. 6.3.2 Models Generated by controlled Monte Carlo Inversions

Regardless of what earth flattening approximation was applied, models were found which fit all modes with reduced χ^2 statistics all less than 1.10. The worst fitting mode was always either the Love or Rayleigh first higher mode with the other 3 modes producing acceptable reduced χ^2 statistics. Models generated without either earth flattening approximation were used only for generating synthetic seismograms for fundamental mode arrivals. All of these models also produce fundamental mode group velocity dispersion which fits acceptably when calculated with the earth flattening approximations. Four additional models fit all data with reduced χ^2 statistics of 1.25 or less; three of these have been calculated using the Love wave earth flattening approximation and two of these also with the Rayleigh wave earth flattening approximation.

Of all spherical earth models with reduced χ^2 statistics of 1.25 or less calculated with at least one earth flattening approximation, all have subcrustal S-velocities ranging from 4.20 to 4.32 km/s. In each of these models the subcrustal P-velocity of 8.13 km/sec was taken from the BMR refraction profile in the Bowen basin. This combination leads to Poisson's ratios ranging from 0.30 to 0.32. These ratios are unrealistically high for subcrustal rocks which suggests that the subcrustal P-velocity beneath the Bowen basin is higher than the average velocity for the Picton-CTA path. A more acceptable sub-crustal P-velocity would be 7.6 to 7.8 km/sec.

Low contrast low velocity zone models fit observed fundamental and higher mode dispersion almost as well as the models presented in Table 6.2; however, no thick high S-velocity lid (4.6 to 4.7 km/s) at depths shallower than 160 to 180 km produces satisfactory fundamental mode Rayleigh wave dispersion (Figure 3.13). Many of the high contrast low velocity zone models produce acceptable fundamental mode dispersion, but higher modes generated from these models were not acceptably close to observed data. Model CTA2FS2 does not have a pronounced low velocity zone above a depth of 220 km. Dispersion for all modes could be fit almost as well by replacing the two layers between 70 and 191 km depth in CTA2FS2 by a layer with an S-velocity of 4.445 km/s.

Partial derivations of group velocity with respect to shear velocity for model CTA2S1, shown in Figure 6.14, indicate that fundamental mode Rayleigh and Love waves in the period range 5 to 60 seconds are sensitive to changes in shear velocity in subcrustal layers shallower than 100 km. Extending the period range to 100 seconds increases sensitivity to changes as deep as 150 km. The first higher mode Rayleigh and Love waves in the period range 10 to 20 seconds are sensitive to changes in shear velocity at depths between 90 and 180 km. The addition of higher mode data to fundamental mode data places additional constraints on deeper structure within models. A decrease in S-velocity between 140 and 180 km will increase the first higher mode group velocity and produce better agreement with observed dispersion (Figures 6.7 and 6.8). As a test, layer 6 in CTA2S1 (Table 6.2b) was replaced with two layers with shear velocities of 4.35 and 4.22 km/s, producing a 41 km thick low velocity zone with a 0.13 km/s contrast. The introduction of this low velocity zone raised first higher Rayleigh mode group velocities by 0.035 km/s at 20 seconds and less at

Figure 6.13 GROUP VELOCITIES - (dotted lines) are shown for a number of different models (dashed lines) at the top of each graph. The bounds for group velocities observed for the Picton - CTA path are shown as solid lines in each figure. Group velocities and period scales appear on the left and bottom side of each graph, shear velocity and depth appear at the right and top side of each graph. Note that no model with a thick high shear velocity lid produces Rayleigh wave group velocities which fall within acceptable bounds for the Picton CTA path.

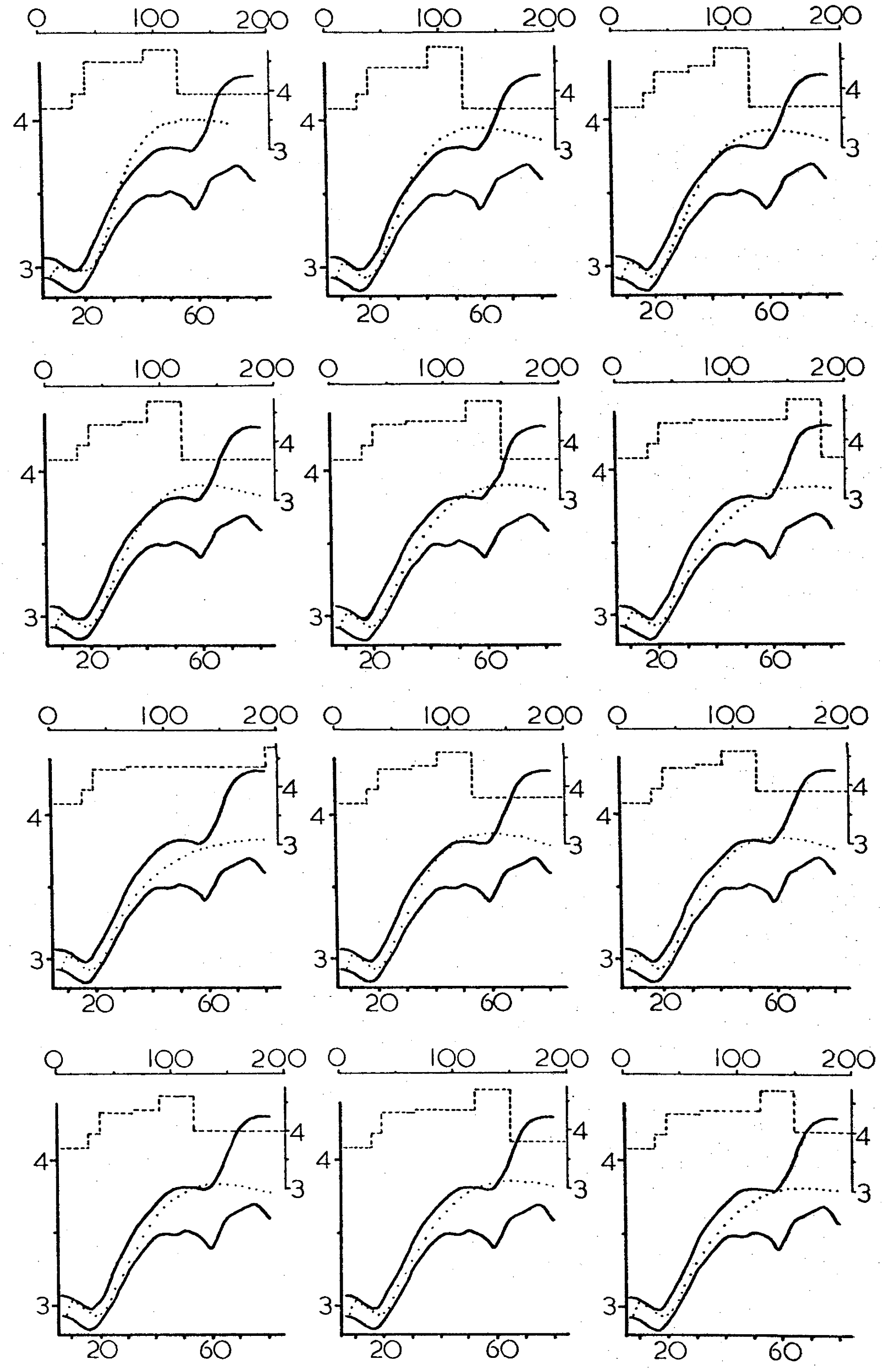
0
100
200
4
3
4
3
20
60
0
100
200
4
3
4
3
20
60
0
100
200
4
3
4
3
20
60
0
100
200
4
3
4
3
20
60
0
100
200
4
3
4
3
20
60
0
100
200
4
3
4
3
20
60
0
100
200
4
3
4
3
20
60
0
100
200
4
3
4
3
20
60
0
100
200
4
3
4
3
20
60
0
100
200
4
3
4
3
20
60
0
100
200
4
3
4
3
20
60
0
100
200
4
3
4
3
20
60

Figure 6.14 PARTIAL DERIVATIVES OF GROUP VELOCITY WITH RESPECT TO SHEAR VELOCITY -

in model CTA2S1 normalized by layer thickness.

CTA2S1 MODEL + PEM CONTINENTAL MODEL**FUNDAMENTAL RAYLEIGH**

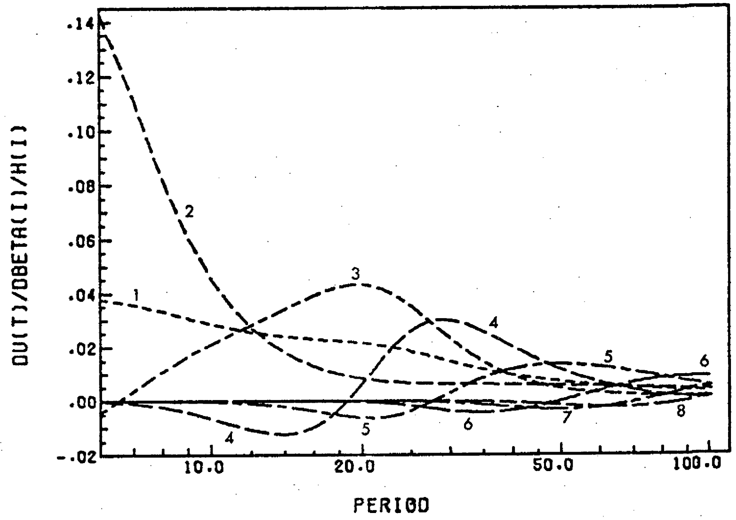

CTA2S1 MODEL + PEM CONTINENTAL MODEL**LOVE FUNDAMENTAL MODE**

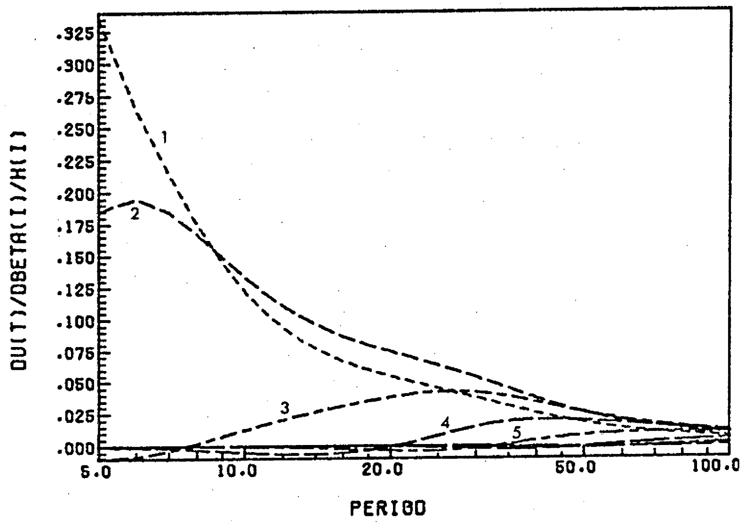

CTA2S1 MODEL + PEM CONTINENTAL MODEL**FIRST HIGHER RAYLEIGH MODE**

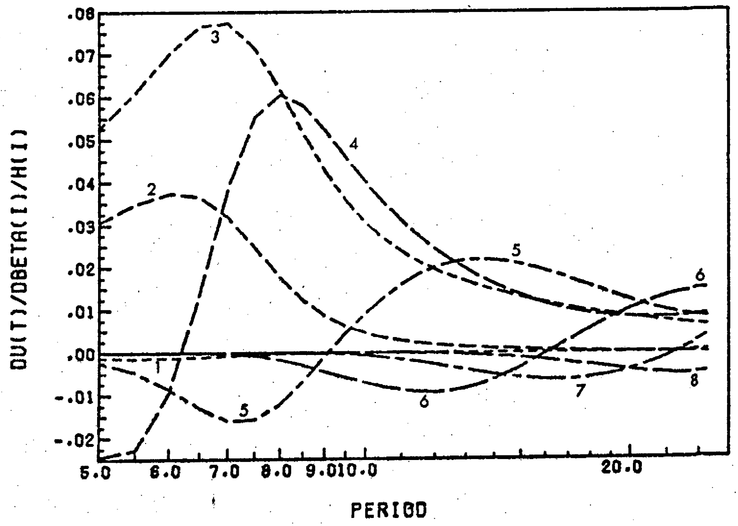

CTA2S1 MODEL + PEM CONTINENTAL MODEL**FIRST HIGHER LOVE MODE**

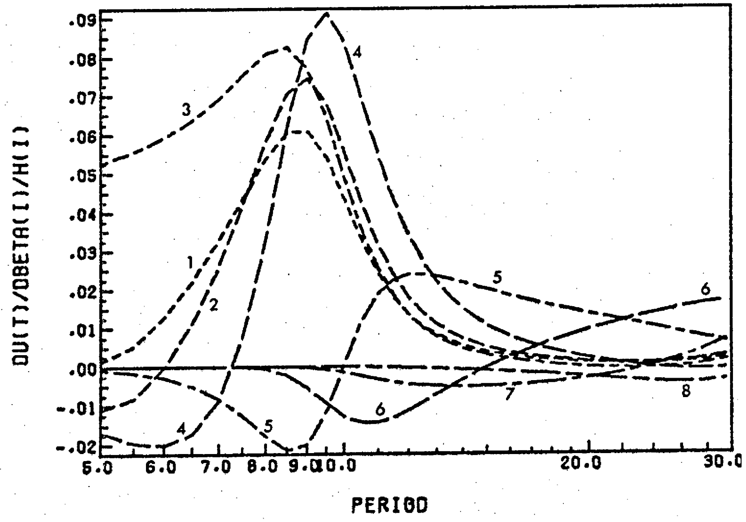

shorter periods. This change in CTA2S1 increased the reduced χ^2 statistic for the first higher Rayleigh mode from 1.0954 to 1.1187. The addition of such low-contrast, low-velocity zones to many of the models increases reduced χ^2 statistics only slightly.

Models were also generated for the Picton-Adelaide path using the ADE dispersion data listed in Table 6.1 and model bounds in Table 6.3. Models were easily found which fit all three observed modes with reduced χ^2 statistics less than 1.0. It is evident that dispersion data for ADE extended only to periods long enough to resolve crustal structure. Shear velocities in subcrustal layers were not well controlled.

No inversion of TAU dispersion data was successful in producing crustal models. The TAU path complexity violates assumptions of lateral homogeneity which are necessary for modelling surface wave dispersion.

Sec. 6.3.3 Comparison of Observed and Modelled Shear Wave Travel Times

As a final constraint on surface wave models S-wave travel times were calculated and compared with observed travel times. These are summarized in Table 6.4 for models CTA1F2, CTA2FS2 and CTA2S1. Travel times were also calculated for Goncz and Cleary (1976) model E1, a low-contrast low-velocity zone model for eastern Australia, and for the continental Parametric Earth Model (PEM) of Dziewonski et al. (1975). Of these models only CTA1F2 produced acceptable S-wave times for CTA and ADE. CTA2S1 produced S-travel times which were 4 to 6 seconds late for both CTA and ADE.

All S-wave ray paths to CTA for models except CTA2FS1 bottom at a depth of 180 to 190 km and at 50 to 60 km for ADE ray paths. Agreement between calculated travel times with observed travel times are indicative of accuracy of model velocities near these depths.

ScS times for all models were also calculated by extending each model using PEM S-velocities for depths greater than 420 km. ScS times

TABLE 6.3(a) STARTING MODEL BOUNDS SET 1

Layer No.	Range of Depths (km)		Range of Shear Velocity in Layer (km/s)		Compressional Velocity (km/s)	Density (g/cc)
1	0.5	1.5	2.29	2.35	4.0	2.40
2	5.0	7.0	3.12	3.18	5.5	2.67
3	29.0	29.0	3.60	3.70	6.4	2.85
4	32.0	40.0	4.05	4.10	9.1	2.95
5	45.0	100.0	4.25	4.70	8.13	3.33
6	180.0	180.0	4.00	4.60	8.2	3.335
7	420.0	420.0	4.50	4.70	8.6	3.35

TABLE 6.3(b) STARTING MODEL BOUNDS SET 2

Layer No.	Range of Depths (km)		Range of Shear Velocity in Layer (km/s)		Compressional Velocity (km/s)	Density (g/cc)
1	0.5	1.5	2.29	2.35	4.0	2.40
2	5.0	7.0	3.12	3.16	5.5	2.67
3	29.0	29.0	3.60	3.70	6.4	2.850
4	32.0	40.0	4.00	4.10	7.1	2.950
5	150.0	180.0	4.55	4.75	8.13	3.335
6	200.0	220.0	4.40	4.60	8.2	3.402
7	420.0	420.0	4.50	4.75	8.6	3.430
8	670.0	670.0	5.28	5.28	9.5	3.763

TABLE 6.3(c) STARTING MODEL BOUNDS SET 3

Layer No.	Range of Depths (km)		Range of Shear Velocity in Layer (km/s)		Compressional Velocity (km/s)	Density (g/cc)
1	0.5	1.5	2.290	2.350	4.0	2.400
2	5.0	7.0	3.120	3.180	5.50	2.670
3	28.6	30.0	3.600	3.700	6.40	2.850
4	32.0	40.0	4.000	4.100	7.10	2.950
5	150.0	180.0	4.250	4.750	8.13	3.335
6	200.0	220.0	4.000	4.600	8.2	3.402
7	420.0	420.0	4.500	4.750	8.6	3.430
8	670.0	670.0	5.280	5.280	9.5	3.768

TABLE 6.4 CTA SHEAR WAVE TRAVEL TIMES

Phase	CTANS WWSSN short period seismogram	CTA EW low gain analogue seismogram	CTA transverse high gain digital seismogram	Model travel times (sec)++						
				t_{JB}	PEM+	E1+++	CTA1F2	CTA2FS1	CTA2FS2	CTA2S1
S_n	340.7±1									
S	-	369.9±4	368.4±4	370.10	348.77	367.43	370.00	386.85	383.31	376.34
Lg	395.1±1									
ScS	-	960.6±4	**	954.15	950.57	952.93	953.41	959.30	958.21	956.61
ScS-S	-	590.70	608*	584.05	601.80	585.50	583.41	572.45	574.90	580.27

ADE SHEAR WAVE TRAVEL TIMES

Phase	ADE-LP-Z	ADE-LP-NS	t_{JB}	PEM+	E1+++	CTA1F2	CTA2FS1	CTA2FS2	CTA2S1
S	250.2±4	253.4±4	252.6	235.00	239.30	254.77	259.98	252.60	257.80

* From cross-correlation of ScS with high gain transverse digital record
** Onset of pulse hidden in noise
\+ Dziewonski, Hales and Lapwood (1975) Parametric Earth Model with continental upper mantle.
\++ All CTA models to 420 km depth over PEM mantle.
\+++ Goncz and Cleary (1975) model E1 to 400 km over PEM mantle

provide an additional check on higher mode information. Since the observed ScS time for CTA was greater than any ScS time calculated from the models, the presence of a low velocity zone is inferred at depths below those resolved by observed surface wave modes, probably below a depth of 140 km.

Of the spherical earth models generated in this study CTA2S1 is the best representative of average S-wave velocities along the Picton-CTA path. Several of the best fitting models are compared with models of shields and island arc regions in Figure 6.15.

Figure 6.15 MODELS -

CTA1S1, CTA2S1 and CTA2FS1 are shown in contrast with CANSD (Brune and Dorman 1963), ARC-1 (Kanamori and Abe 1968) and E1 (Goncz and Cleary 1976).

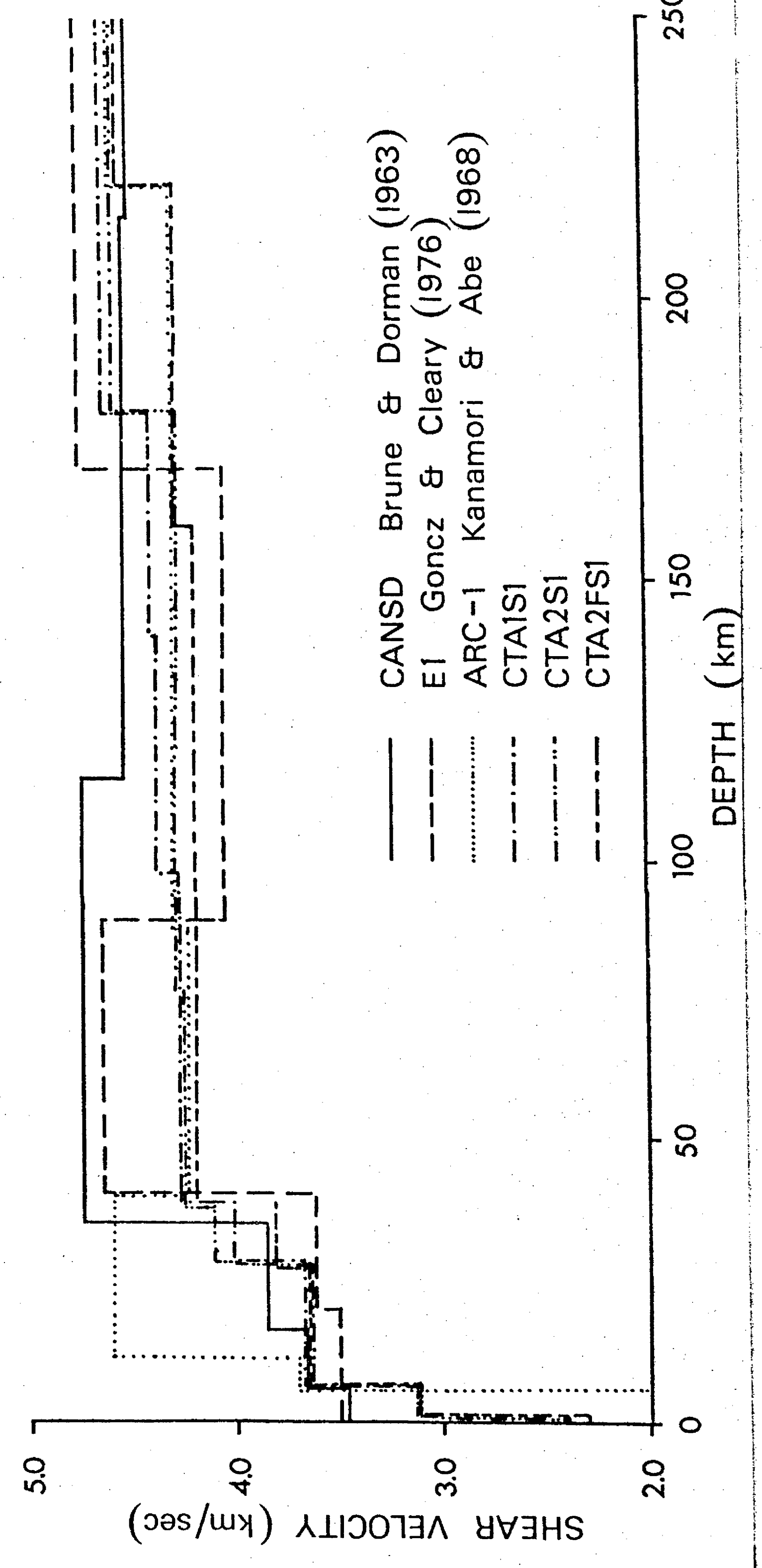
CANSD Brune & Dorman (1963)
E1 Goncz & Cleary (1976)
ARC-1 Kanamori & Abe (1968)
CTA1S1
CTA2S1
CTA2FS1
SHEAR VELOCITY (km/sec)
5.0
4.0
3.0
2.0
DEPTH (km)
0
50
100
150
200
250

Sec. 6.4 SOURCE PARAMETERS

P-wave first motions, aftershock locations and amplitudes of fundamental mode Rayleigh and Love waves are definitive in regard to certain average properties of the Picton earthquake: orientation and size of the fault, sense and amount of slip on that surface, seismic moment and stress drop. These source parameters are inferred from first motions of P-wave arrivals which give the sense of motion at the source, relative locations of aftershocks which define the orientation and size of the fault surface, and comparison of observed and synthetic surface waves which define the source moment, orientation and depth, stress released, and amount of slip.

Sec. 6.4.1 P-wave First Motions

Figure 6.16 shows first motions of P-waves projected onto the focal sphere. Take off angles at the source were computed assuming a uniform crust with a compressional velocity of 6.0 km/s overlying a Jeffreys-Bullen (J-B) upper mantle.

P-wave first motions (Fitch 1976) are consistent with thrust faulting on one of two possible surfaces represented by the solid nodal planes in Figure 6.7. From this evidence alone, strike-slip faulting can not be excluded. Such a solution would have a pair of nearly vertical nodal planes; one with a E-W strike and the other with a N-S strike.

Sec. 6.4.2 Source Parameters from Synthesis of Surface Waves

The nodal plane ambiguity is firmly resolved in favour of thrust faulting by the strong excitation of fundamental mode Rayleigh waves relative to that of Love waves along the path to ADE. To quantitative this argument and estimate the seismic moment (Aki 1966), fundamental

Figure 6.16 FOCAL MECHANISM SOLUTIONS -

First motions of P-waves are plotted on an equal area projection of the lower hemisphere of the focal sphere. Compressional and dilatational first motions are given by solid and open circles respectively. X's represent first motions of indeterminant polarity. Large symbols are used for data read from long period records and small symbols represent data read from short period records. Nodal surfaces for the solutions by Fitch (1976) are shown by solid curves. The refined solutions based on surface wave amplitudes are shown by the dashed curves. P and T identify axes of maximum and minimum compressive stress respectively. The orientation of these axes, strike and dip is given for the solution by Fitch (1976). In the southwestern quadrant projections are given for rays at take-off angles varying from 80° to 50°.

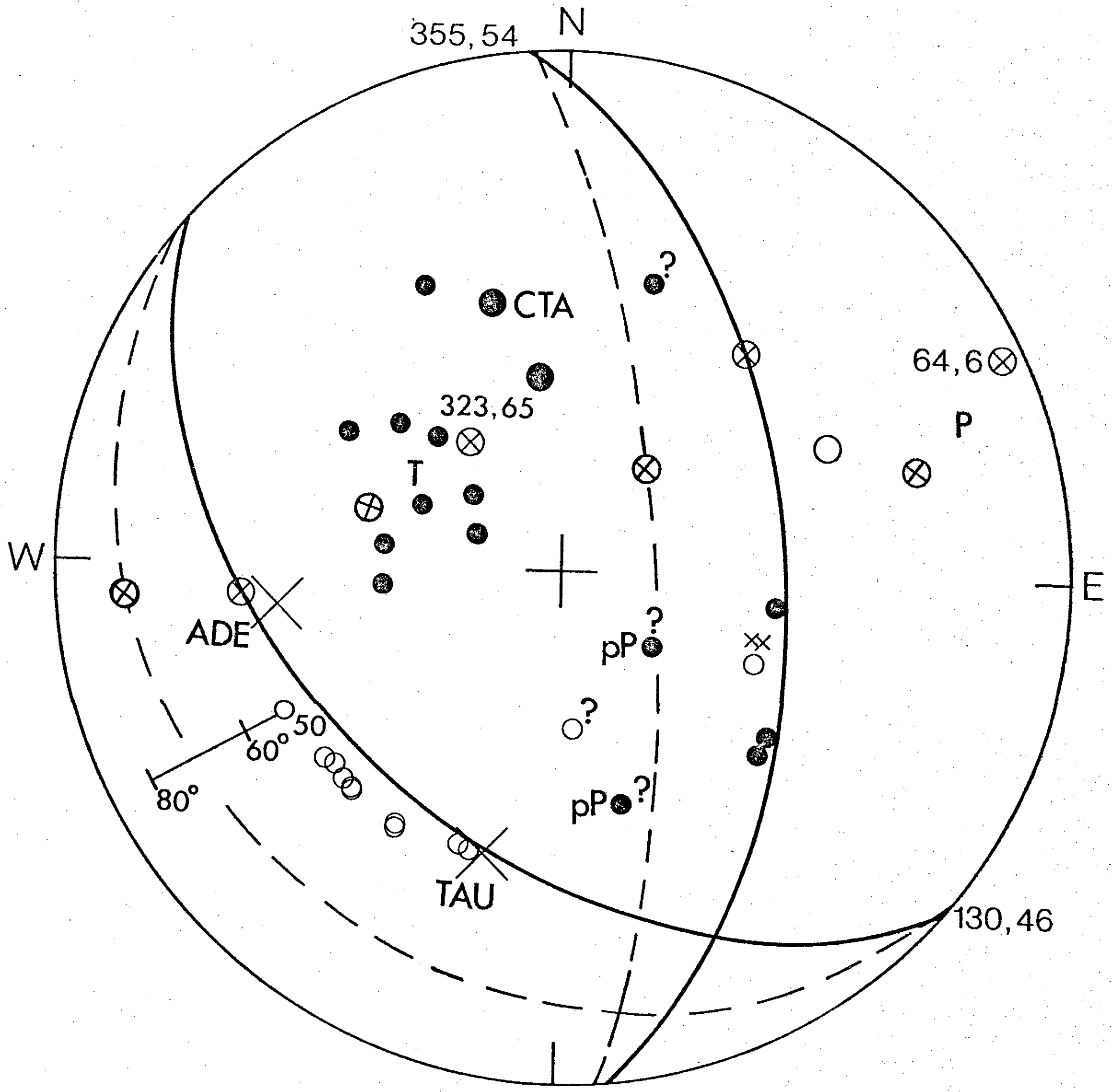

MAR 9 1973 34·17S 150·32E 21 Km
PICTON

mode surface waves at ADE, CTA and TAU were synthesized using computer programs written by D. Harkrider (1964, 1970). Included in these synthetics are the effects of the recording system and propagation from source to receiver. The propagation effects include geometric spreading, attenuation, and dispersion. The TAU records are not included in the source study because the observed dispersion (Figure 6.12) was not closely approximated by the models derived for eastern Australia or those taken from other studies (see discussion in Section 6.2).

Sec. 6.4.2.1 Attenuation

Anelastic properties of the crust and upper mantle of eastern Australia are poorly known and cannot be accurately measured from the Picton data. Consequently, these properties must be assumed from other studies. Attenuation coefficients for both Love and Rayleigh waves are taken from Mitchell's results for central North America (1972, 1973b). At longer periods than 25 seconds these coefficients may be underestimated by at most a factor of 2, if Solomon's (1972) results for the western United States are taken as an extreme example of anelasticity in a tectonically active zone. The effect of such a zone on surface wave amplitudes is dependent on its depth. Goncz and Cleary (1976) show that a low velocity zone in the depth interval from 90 to 150 km beneath eastern Australia (Model E1) satisfies their group velocities for Rayleigh waves of the fundamental mode. Inversions presented in Section 6.3 suggest that such a zone is located at some depth greater than 120 to 150 km.

Attenuation of the fundamental modes is strongly dependent on crustal properties at periods less than 20 seconds. The shape of the Rayleigh wave train is particularly sensitive to the anelastic properties of the crust because the highest amplitudes, the Airy phase, propagate in the crust. In eastern Australia the crust includes an unexposed basement overlain by a Paleozoic geosyncline (Oversby 1971, Scheibner 1973, and Harrington

1974), which, in the south, is uplifted and penetrated by numerous basaltic flows that range in age from Cretaceous to late Tertiary (Wellman and McDougall 1974).

Attenuation is enhanced at periods less than 10 seconds by propagation through sedimentary basins. The path from Picton to CTA traverses the Sydney basin in the source region (Figure 6.1) and the Drummond basin (Olgers 1972) extending south from CTA. The path to ADE crosses the mountainous regions of New South Wales and the Murray basin east of Adelaide (e.g. Harrington 1974).

The synthetic seismograms in Figures 6.2 to 6.4 and 6.6 were generated using either attenuation coefficients from Mitchell (1973a, 1973b) or a modification of these coefficients in which attenuation was doubled for periods less than 23 seconds. The modified coefficients were used with excitation functions derived from Model E1 of Goncz and Cleary (1976). Attenuation was not increased at the longer periods, 24 to 60 seconds, in spite of the presence of a low velocity zone in this model, because the spectral amplitudes at these periods are more sensitive to the shear velocity in the deep crust and uppermost mantle.

Sec. 6.4.2.2 Synthetic Surface Waves

After assigning attenuation coefficients, computing instruments responses and producing a crust-upper mantle model, synthetic seismograms can be computed given, in addition, a description of the source, its depth and its strength. The radiation pattern has been approximated by a stationary double couple which is completely defined by three parameters, two of which correspond to the strike and dip of a fault surface, while the third defines the direction of slip on that surface (Ben-Menahem and Harkrider 1964). There is a fundamental ambiguity associated with such a source, in that slip on either of two orthogonal planes yields the same far field radiation pattern. For the Picton earthquake this ambiguity is resolved by the distribution in depth of the aftershocks.

The size of the source, the characteristic dimension of which is about 8 km (Figure 6.17), and the kinematics of the source, dip-slip, ensure that surface waves with periods greater than 15 seconds "see" a stationary point source. The component of the synthetic wave trains with the shortest period, 6 seconds, corresponds to a wave length that is about 3 to 4 times longer than the source size.

Since the dip of the aftershock plane is steep consider the vertical Rayleigh wave displacement generated by a line of rupture of length b moving vertically with velocity ν from depth h_1 to h_2 in an istropic half-space (Ben-Menahem 1961, eq. 1-53):

$$u_z^R = \frac{LC'_4}{\mu\sqrt{r_o}}\sqrt{K_\beta}\left[\frac{\sin Y_R}{Y_R}\right]\left\{\left[\frac{\sin \Theta_2}{\Theta_2}\right]\exp(i\Theta_2 - h_2K_nd_2) - E_1\left[\frac{\sin\Theta_1}{\Theta_1}\right]\exp(i\Theta_1 - h_1K_nd_1)\right\}\bullet$$

$$\bullet\ \exp(i\psi_R + \frac{3\pi i}{4})$$

where

$$Y_R = \frac{\omega b}{2C_R}\cos\Theta_o,\quad \psi_R = \omega(t - \frac{r_o}{C_R}) + Y_R\ ,$$

$$\Theta_1 = \frac{h_1 - h_2}{2C_R}\,\omega\left(id_1 - \frac{C_R}{\nu}\right),\quad \Theta_2 = \frac{h_2 - h_1}{2C_R}\,\omega\left(id - \frac{C_R}{\nu}\right),$$

$$\gamma = \tfrac{1}{2}\sqrt{3+\sqrt{3}} = 1.0876,\quad d_1 = \frac{\sqrt{\gamma^2-1}}{\gamma},\quad d_2 = \frac{\sqrt{\gamma^2-\tfrac{1}{3}}}{\gamma},$$

$$E_1 = \frac{2\gamma^2}{2\gamma^2-1}\ .$$

Figure 6.17 AFTERSHOCK LOCATIONS -

map view and vertical section. All locations are relative to the master earthquake (Table 6.5). The only control of absolute depth is the depth of 15 km for the master earthquake. This depth may be overestimated because seismic velocities for sediments in the Sydney basin are expected to be less than the velocities of 6.0 km/sec and 3.6 km/sec assumed for crustal P- and S- phases respectively. Furthermore, the refined take-off angles (Table 6.5) suggest that these velocities are too high to be representative of the entire crust in this region. These angles are shallower than angles consistent with straight rays from a depth of 15 km. Error bars are projections of error ellipses onto vertical and horizontal planes and are approximately 95% confidence limits.

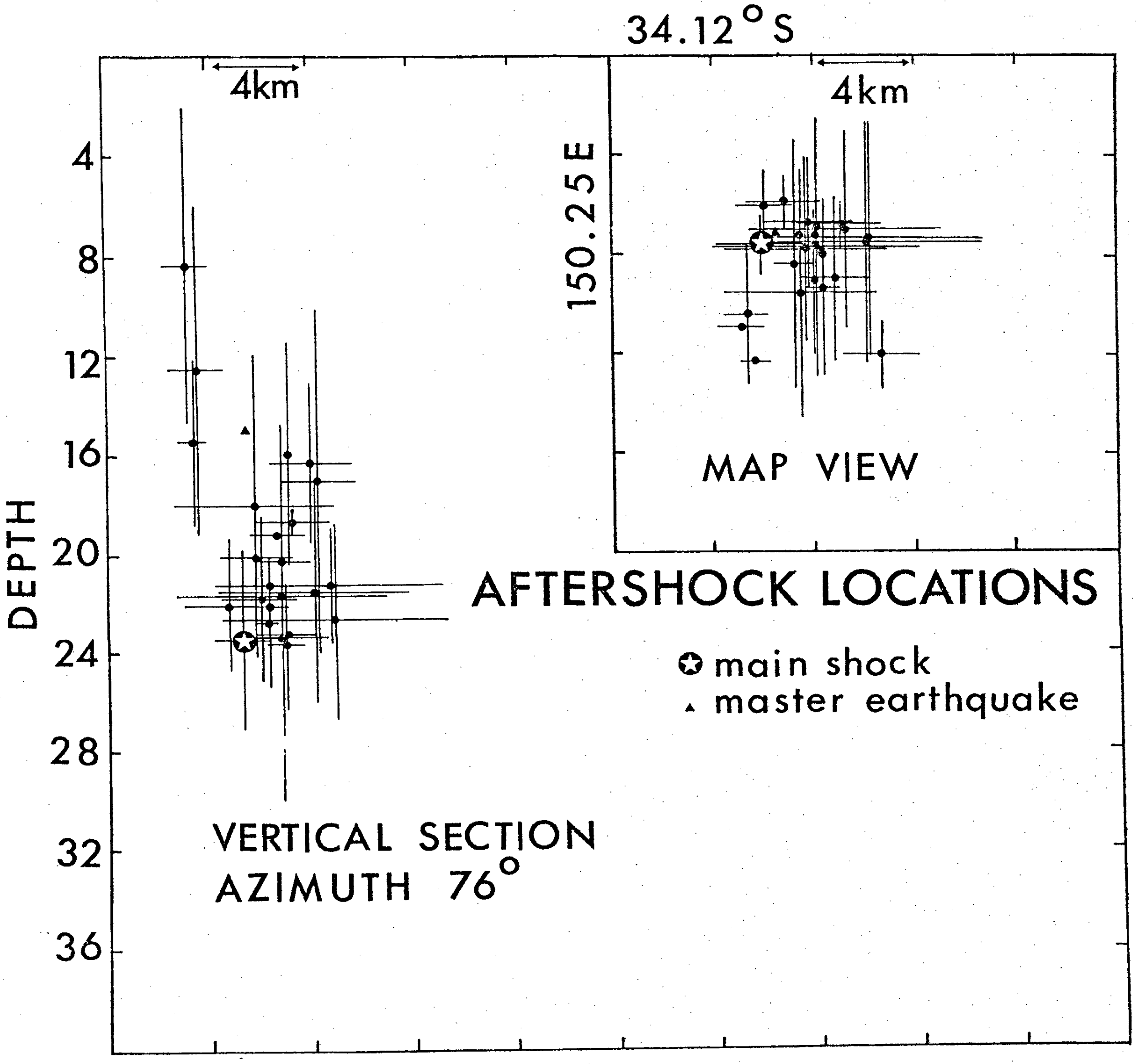
34.12° S
4km
4km
150.25 E
MAP VIEW
DEPTH
4
8
12
16
20
24
28
32
36
AFTERSHOCK LOCATIONS
main shock
master earthquake
VERTICAL SECTION
AZIMUTH 76°

and K_n is the nth root of the Rayleigh wave characteristic equation, K_β is the wave number in half-space of shear modulus μ, L is the magnitude of the source function, and C'_4 is a positive real constant. The azimuthal dependence of the displacement appears in the $\frac{\sin Y_R}{Y_R}$ and $\exp(i\psi_R + \frac{3\pi i}{4})$ factors. Although rupture velocity effects the amplitude of the Rayleigh wave, this effect does not change as a function of azimuth for vertical dip slip faults. For faults with near vertical dip the rupture velocity has a slight though small effect on the radiation pattern.

Cusps in the excitation function, shown in Figure 6.18, control the amplitudes of Love waves at ADE and of Rayleigh waves at CTA. In terms of the mechanism solution these cusps constrain the direction of slip on the fault and the dip of the fault respectively. Apparent uncertainty in these angles is 5 to 10 degrees. The remaining fault parameters, strike and seismic moment, were less constrained by the data. The strike is uncertain by no more than 20% provided that the estimate is based on a fit to the long period part of the surface wave trains.

The most obvious discrepancy between the observed wave trains and the synthetic wave trains derived from model El is an overestimate of the excitation of the fundamental mode Love wave at CTA (Figures 6.4 and 6.9). When the synthetic and observed wave trains are superimposed, phase differences are apparent that can be attributed to disparities between predicted and measured group velocities (Figures 6.2 and 6.3). It should be noted that the short period oscillations seen in the early part of the observed seismograms are higher mode arrivals. The higher modes are not included in the synthetic seismograms. A comparison of filtered and predicted spectral amplitudes (Figures 6.7 to 6.11) reveals good agreement at CTA but a gross overestimate of the long period amplitudes of the fundamental Rayleigh mode at ADE.

For these computations the source depth was taken to be 20 km; this depth, computed from arrival times of P- and S- waves from the main

Figure 6.18 SOURCE AMPLITUDE AND PHASE SPECTRA -

The top and bottom figures are the phase and modulus respectively of the complex radiation pattern function, $\chi(\theta, h)$ (Harkrider 1970). θ is the azimuth from the strike of the fault to the recording stations. Angles θ, δ, and λ are defined by Ben-Menahem and Harkrider (1964). Uncertainty in θ is given by width of bars (the bars themselves are only used to guide the reader to the appropriate parts of the curves).

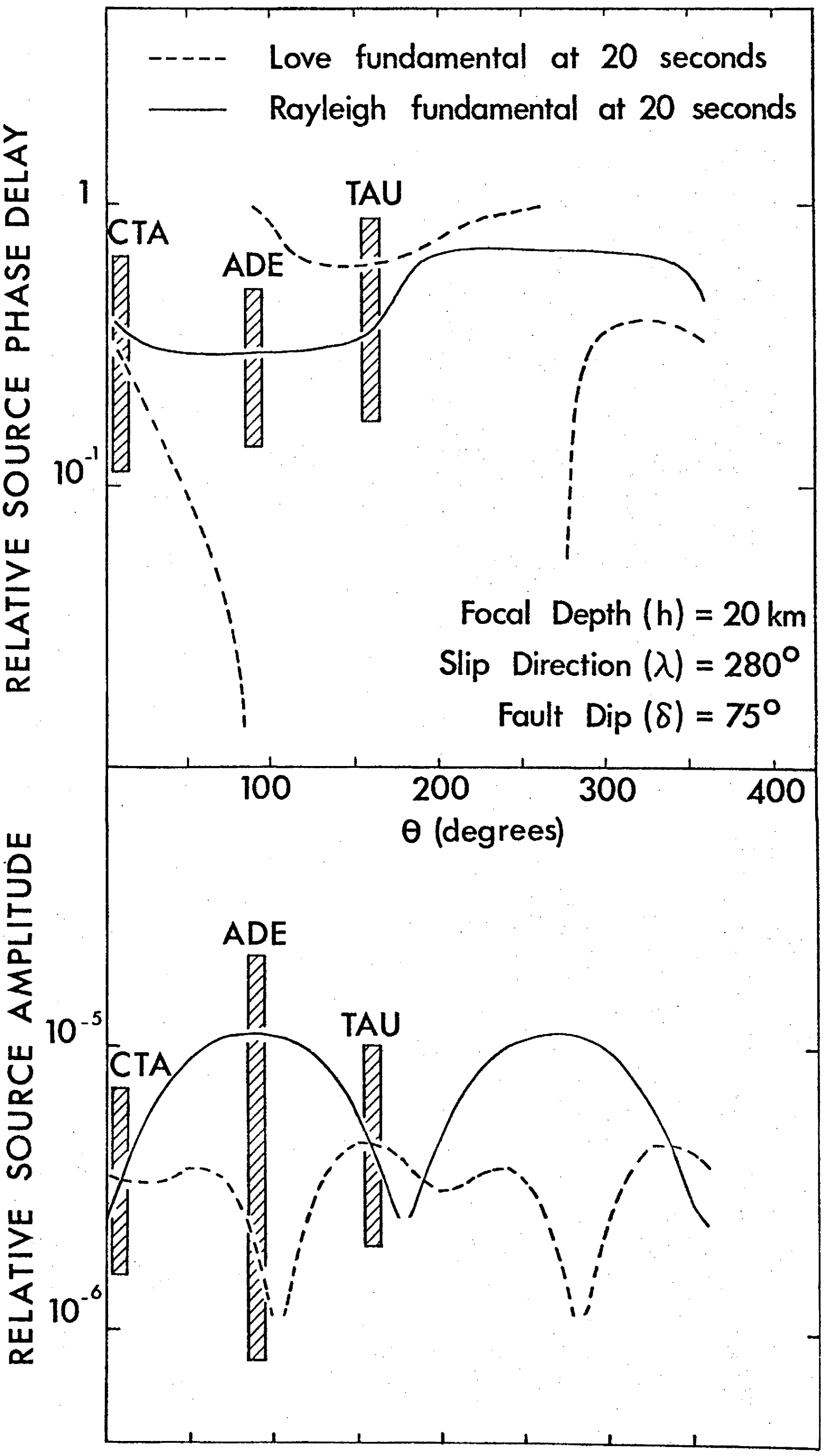
----- Love fundamental at 20 seconds
—— Rayleigh fundamental at 20 seconds
RELATIVE SOURCE PHASE DELAY
1
10^{-1}
CTA
ADE
TAU
Focal Depth (h) = 20 km
Slip Direction (λ) = 280°
Fault Dip (δ) = 75°
100
200
300
400
θ (degrees)
RELATIVE SOURCE AMPLITUDE
10^{-5}
10^{-6}
ADE
TAU
CTA

shock recorded at local stations is uncertain by ± 5 km. It is consistent with pP-P times of 5 to 6 seconds read from records taken at WWSSN stations CTA, POO, SBA, and CHG, if the crust is assumed to have an average P-wave velocity of about 6 km/s.

A refined set of synthetics was computed with excitation functions derived from flat earth models ADEF2 and CTA1F2 (Table 6.2). The dispersion predicted from these models fits nearly all the observations within the error-bounds in Table 6.1. These models were computed from group velocities of the fundamental and first higher modes. The Love waves recorded at CTA were sucessfully modelled by reducing the seismic moment from 1.10 x 10^{24} to 0.57 x 10^{24} dyne-cm, rotating the fault 10° in the clockwise direction and replacing the modified attenuation coefficients for the ADE path by Mitchell's values.

Rayleigh waves at ADE are more sensitive to small changes in source depth than are the other surface waves. For example, Rayleigh wave excitation at long periods is reduced by 17% at ADE and 8% at CTA by raising the source depth from 20 to 15 km. These percentages come from the ratio of the peak spectral amplitudes to those at the longest periods, which are 50 and 60 seconds for synthetics of the ADE and CTA surface waves respectively. The refined source depth for surface wave excitation is taken to be 15 km because of the improved agreement between the observed and synthetic amplitude spectra for Rayleigh waves at ADE (Figure 6.10). Shallower excitation depths were not considered because such depths approach the depth of the shallowest aftershocks (Figure 6.17).

The overall agreement between synthetic and observed wave forms is improved by these changes; however, long period excitation of Love and Rayleigh waves is also overestimated by the refined model. This is particularly apparent for the fundamental mode Love wave at CTA (Figure 6.9). This disparity is too large to be explained as an effect of increased attenuation even with a well-developed low velocity zone within 100 km of the surface, which appears not to be the case in this region. This bias to some extent can be seen in all the amplitude spectra. Furthermore, the synthetic spectra generally are more rounded than the observed ones. A simple explanation for these discrepancies has not been found; however, uncertainty in the attenuation coefficients and deviations from a laterally homogeneous earth may jointly account for them. Focusing and diffraction effects may also greatly influence amplitudes at periods shorter than 28 seconds (McGarr 1969). Otherwise the source spectra may be peaked in the manner suggested by elasto-dynamic theory of Archambeau (1968). In any case, these data by themselves do not permit a definitive explanation.

Sec. 6.4.3 Comparison of Body and Surface Wave Mechanism

In Figure 6.16 the surface wave solutions are superimposed the solution from first motions. The most striking disparity between these solutions is shown by the band of dilatational first motions in the SW quadrant of this figure. These dilations were recorded in a distance range from 1° to 9° which includes stations of the ANU and Snowy Mountains network, TOO, (operated by the Bureau of Mineral Resources near Melbourne), and stations operated by the University of Tasmania (Figure 6.1). Some and possibly all of this disparity can be explained by errors in projecting the ray paths to these stations onto the focal sphere. Uncertainty in the crustal structure of southeastern Australia is sufficiently great to allow errors of at least 20° in the take-off angles required for this projection. In Figure 6.16, take-off angles were computed for an earth model consisting of a Jeffreys-Bullen (J-B) sub-crust overlain by a crust with a uniform compressional velocity of 6.0 km/sec. This model yields take-off angles near 50° for the closest stations of the ANU network, INV, CAH and LER. These stations are about 1° from the source.

In contrast, the routine earthquake locations, computed by the seismology group at the ANU, use travel times consistent with the assumption of straight ray paths for crustal phases recorded at distances less than about 1.5°. For the abovementioned stations the corresponding take-off angles from the Picton earthquake would be slightly greater than 90° (where an angle of 0° refers to the downward vertical). These ray paths pass through the upper hemisphere of the focal sphere which in Figure 6.16 corresponds to positions near the rim of the NE quadrant. Model CTA1F2 predicts take-off angles of about 78° for these rays. The corresponding open circles in Figure 6.16 would plot closer to the rim of the SW quadrant. Both J-B and CTA1F2 have crustal models bring the ANU data into agreement with the mechanism solution from surface waves.

Sec. 6.4.4 Aftershocks, Slip and Stress Drop

The Picton earthquake left no surface trace nor did it occur within a mapped fault zone; consequently, all information as to the size and orientation of that rupture must be seismological inference. Focal mechanism solutions (Figure 6.16) suggest that the orientation of the rupture coincides with one of a pair of nodal planes for each solution. From locations of the main shock and 23 aftershocks (Figure 6.17), relative to a master earthquake (chosen from among the better recorded aftershocks) the fault surface appears to dip steeply, possibly toward the east. The nodal plane that most closely coincides with the distribution of locations is the more steeply dipping of the planes determined from the surface wave analysis (Figure 6.16). The inferred strike of the fault is nearly north-south.

Accurate estimates of fault slip and stress drop depend on an accurate estimate of the size of the fault at the time of the main shock. Inferring fault size from aftershocks, yields minimum values of both average slip and average stress drop. Uncertainty in the size of the aftershock zone for this earthquake is due mainly to uncertainty in the crustal structure in the region enclosed by the network of local recording stations. The closest stations in this network, WER and AVO, are about 30 km from the source region i.e. at a greater distance than the depth for most of the activity. Consequently, the distribution in depth of this activity is very sensitive to crustal structure. In contrast both the distribution of epicenters and the horizontal distribution of relative locations are stable for a wide range of crustal models.

To minimize uncertainty in the dimensions of the aftershock zone, an attempt, partially successful, was made to invert arrival times of crustal P and S phases for relative locations (Figure 6.17) and take-off angles for ray paths between the master earthquake and the eight stations shown in Figure 6.1. The inversion scheme is the same as the one used by Fitch and Rynn (1976) to compute near-source estimates of V_P/V_S. This scheme is a generalization of a master earthquake scheme used by Fukao (1972) to locate aftershocks of a Brazilian deep earthquake. Restrictions imposed by the station coverage meant that neither near-source velocities, V_P/V_S, nor all the take-off angles could be refined. In the joint-relative-locations tabulated in Table 6.5 the take-off angles to the four more distant stations are assigned a fixed value of 65°. RIV is 65 km from the source region and the three western stations, INV, LER and CAH are about 100 km from the source. Compressional and shear velocities in the source region are assigned values of 6.0 and 3.6 km/sec. These are crustal velocities consistent with travel-times from local earthquakes in southeastern Australia. The take-off angles for ray paths to the three closest stations, AVO, WER and JNL are refined along with the parameters giving the relative locations.

The resulting angles (Table 6.5) were used in individual relative locations of about 90 aftershocks recorded in the month of March 1973. The better-determined of these locations are plotted in Figure 6.17. If steeper take-off angles were assumed for the outer stations, the separations between

TABLE 6.5 JOINT RELATIVE LOCATIONS

MASTER Earthquake 15 Mar 1973 11.30 GMT 34.15S 150.32E 15.0 km deep

Event #	Date (March 1973)	Time GMT	Polar Angle (degrees)	Azimuth (degrees)	Length (degrees)	Standard Errors** NS (km)	EW (km)	Z (km)	#Data Points
1	09	19:53	9.4	119.8	10.0	4.1	1.3	3.6	8
2	09	20:41	8.2	338.1	8.5	2.8	1.7	3.8	7
3	12	14:42	39.0	127.7	4.7	3.4	1.4	0.7	8
4	12	17:03	34.6	139.5	5.1	3.7	0.8	0.3	9
5	14	06:06	88.7	188.8	5.2	0.3	0.6	3.4	8
6	15	16:38	16.4	95.0	5.7	5.1	0.0	5.3	12
7	15	21:48	7.0	96.0	7.7	2.8	0.8	3.0	11
8	23	17:06	122.5	198.9	3.9	3.3	1.2	6.5	12
9	24	10:43	28.4	92.1	7.9	5.5	4.7	3.6	11

TABLE 6.5 (contd)

Station	Initial* take-off angle (P and S waves) degrees		Final* take-off angle (P and S waves) degrees
WER	115.0)	from assumption	97.2 ± 8.7
AVO	111.7)	of straight ray	80.5 ± 10.9
JNL	108.3)	paths	87.9 ± 11.1
IUN	65.0		65.0
LER	65.0		65.0
CAH	65.0		65.0
RIV	65.0		65.0

RMS Residuals for Differential Arrival Times

P waves 0.105 from 55 data points

S waves 0.117 from 31 data points

All data 0.109 from 86 data points

*take-off angle of 0° is downward vertical.

** A χ^2 test on residuals shows that standard errors are approximately 95% confidence limits.

master and secondary events would increase and the apparent dip of the fault would also increase. The gap between the master earthquake and the secondary events, shown in Figure 6.17, is probably more apparent than real. The locations of activity closer to the master earthquake are difficult to resolve given reading errors of about ± 0.1 second for both P and S arrival times.

The down-dip length of the fault surface is about 16 km; however, the down-dip length at the time of the main shock is probably less. The down-dip length is set at 10 km, which is twice the difference between the depth of the main shock and the nominal depth of 15 km used in computing the refined synthetics. As with most well-located earthquake sequences, particularly those associated with thrust faulting (e.g. Whitcomb et al. 1973), the main shock occurs near the base of the activity. The width of the fault surface, taken from the horizontal distribution of activity, is about 8 km. Substitution of a fault size, S, of 80 km^2 into the equation:

$$M_o = \mu \overline{D} S$$

(Aki 1966), where M_o is seismic moment, $0.57 \times 10^{24} \pm 20\%$ dyne-cm from the refined synthetics and μ is shear modulus, in this case assumed to be 3.3×10^{11} dyne/cm^2, yields an estimate of 2 cm for average slip, $\overline{D}$. The corresponding estimate of stress drop, $\overline{\Delta\sigma}$, is about 1 bar, when the appropriate substitutions are made in the equation:

$$\Delta\sigma = \eta\mu \frac{\overline{D}}{w}$$

(Brune and Allen 1967, Kanamori and Anderson 1975). η is a factor that depends on the geometry of the fault and w is the down-dip length of the fault. For pure strike-slip Knopoff (1958) estimates a value of about 2/3 for η and for pure dip-slip, Starr (1928) estimates $\eta = 1$. For rupture in which the horizontal and vertical dimensions are approximately equal, which is the case for the Picton earthquake, η is about 4/3.

Sec. 6.5 CONCLUSIONS

Shallow earthquakes are one of the more obvious manifestations of continuing deformation of the continental margin of southeastern Australia. Conventionally, the P axis is defined as the center of the dilatational quadrant of the focal sphere (Hodgson 1957, Honda 1962) and is coincident with the axis of maximum compressive stress. It has been pointed out by McKenzie (1969a) and others that this conventional estimate of the direction of maximum stress is valid only in a medium that was homogeneous prior to the earthquake. In the case of the Picton earthquake the P axis is inclined toward the east. It is probable that the Picton earthquake occurred in a zone of weakness i.e. a previously active fault zone. In this case, the orientation of the P axis is strongly dependent on the strength of material in the zone and may not therefore be oriented in the direction of maximum compressive stress.

In situ stress measurements provide independent information on the orientation and strength of crustal stress fields. In this region high quality measurements of this kind have been made in a mine near Cobar, New South Wales, 540 km WNW of the epicenter. Measurements at the 1200 and 1800 foot levels reveal a nearly horizontal axis of maximum compressive stress trending EW (Stephenson and Murray 1970). If this stress measurement at the 1200 foot level are taken to be representative of the crust in the entire New South Wales region then the resolved shear stress on the fault plane is about 40 bars. A resolved shear stress of about 80 bars results from similar analysis using the measurements at the 1800 foot level. If the estimated stress drop of 1 bar is a large fraction of the strength of the fault zone, then this zone must be extremely weak by comparison with the strength of unfractured rock. At confining pressures corresponding to mid-crustal depths, dry unfractured rock will have a fracture strength of kilobars (Griggs and Handin 1960).

The *in situ* stress measurements and the focal mechanism for the

Picton earthquake could be consistent with a regional stress field that is dominated by uni-axial compression along an east-west trend. However, more information of both kinds is needed to firmly establish such a trend. Filling of the Warragamba reservoir probably had negligible effect on the source region of the Picton earthquake. The long time lapse between the first filling and the earthquake, 11 years, and the mid-crustal depth to the main shock argue against a reservoir effect (Rothe 1969, Gough and Gough 1970).

Models produced by a controlled Monte Carlo inversion of surface wave dispersion represent the average structure for the paths from Picton to Adelaide and Charters Towers. Four spherical earth models presented in Table 6.2 fit all observed fundamental and higher mode dispersion with reduced χ^2 statistics of 1.25 or less. Although no layer above a depth of 180 km in any of these models contains a shear velocity as high as 4.7 km/s, the apparent velocity of the S_n phase recorded at Charters Towers, these models represent averages of shear wave velocities in the real earth. The interpretation of this observation as a long distance S_n phase (Molnar and Oliver 1969) requires a layer with a velocity of 4.7 km/s at some depth between Moho and 200 km. Models produced in this study indicate that this layer must be as thin as 30 km at a depth of 180 km or much thinner at shallower depths. The apparent velocity of S calculated from S times at ADE and CTA is only 4.5 km/s. Subcrustal S-velocities for these models range from 4.20 to 4.32 km/s which is 0.4 to 0.5 km/s slower than CANSD subcrustal velocities. Kanamori and Abe (1968) and Fix (1975) have found models for the Philippine Sea and central Mexico with upper mantle shear velocities of 3.6 to 4.2 km/s at depths shallower than 100 km. The prejudice that continental plates slide on a low velocity zone is partially supported by the ScS travel time for Charters Towers. S-wave travel times and higher mode group velocities tend to preclude the presence of any <u>pronounced</u> low velocity zone at depths of less than 180 km. Below this depth, low velocity zones have little effect on observed higher mode dispersion and observed fundamental mode amplitude and dispersion.

The vertical one way travel time for S-waves from the core-mantle boundary to the earth's surface inferred from ScS is 474.4 seconds. The presence of a high contrast, low velocity zone in the models is precluded only by poor fitting of higher modes and is not excluded by the fundamental mode data. It is likely, as suggested by ScS times (Table 6.4), that a low velocity zone or zone of lower than average velocity does exist below a depth of 140 km for the CTA-Picton path.

In comparing the partial derivatives of group velocity with respect to shear velocities in layers for CTA2S1 (Figure 6.14) it is evident that shear velocities at depths greater than 100 km contribute significantly to the first higher Rayleigh mode for periods greater than 9 seconds. The higher mode data used for inversion (Table 6.1 data set #2) is of good quality to 15 second periods and becomes questionable for greater periods. Since first higher Rayleigh modes produced by the preferred models have slightly slower group velocities than the observations, it is possible that either lateral refractions not well separated from the fundamental Rayleigh mode at periods greater than 40 seconds bias observed fundamental mode group velocities to slower values than those actually present along the path or that the Alterman, Jarosch, and Pekeris (1961) earth flattening approximation does not adequately approximate higher mode group velocities. Either of these possibilities could cause a conflict between observed and computed Rayleigh modes. For this reason any inversion procedure may not adequately model low velocity zones at depths greater than 140 km. Only low contrast low velocity zones without high velocity lids are able to reasonably fit the group velocity data presented in Section 6.2.

CHAPTER 7

REGIONALIZATION AND PURE PATH MODELS FOR SHEAR VELOCITY AND ATTENUATION

Sec. 7.1 INTRODUCTION

Differences in the dispersion of long period surface waves which transverse paths through different upper mantle provinces or regions were first pointed out by Brune (1960). Since that time the dispersion of great circle surface waves has been used by Toksöz and Anderson (1966) to show that the upper mantle is laterally heterogeneous. Toksöz, Chinnery and Anderson (1967) determined velocity structures for the upper mantle which produced the observed phase velocity dispersion. Their models indicated the presence of a pronounced shear wave low velocity zone beneath the oceans and a more pronounced low velocity zone beneath tectonic regions. Kanamori (1970a) and Dziewonski (1971a) measured phase and group velocities for great circle Rayleigh waves for 150 to 360 second periods and determined pure path velocities for shield, oceanic and tectonic regions. Kanamori (1970a) also measured velocities for Love waves and Q's for both Rayleigh and Love waves in this period range. These regionalized surface wave velocities have been modelled by Kanamori and Press (1970), Press (1970) and, Dziewonski (1971b) A more recent regionalization by Wu (1972) employs 4 types of upper mantle provinces; continent, ocean basin, island arc, and mid-ocean ridge zones. Using these 4 types of regions Wu (1972) calculated pure path phase velocities for periods between 160 and 300 seconds from Kanamori's (1970a) phase velocities for the Kurile Island earthquake of 13 October 1963, in conjunction with his own phase velocity data from the Rat Island earthquake of 4 February 1965. Wu's (1972) pure path phase velocities show distinct differences in the dispersion of Rayleigh waves in his four regions .

Although both Kanamori (1970a) and Wu (1972) calculated Q for Rayleigh waves (Q_R), neither has modelled regional Q_R or Q^{-1}_R satisfactorily. The methods used for separating pure path group velocities and Q^{-1}_R are described in Section 7.2 of this chapter and pure path group velocities calculated from the group velocity data of Chapter 3 and Chapter 4 are presented in Section 7.3. The pure path group velocities for continental and oceanic regions are inverted in Section 7.4 to give shear velocity models for continents and oceans. Pure path separation of Q^{-1}_R for periods between 50 and 300 seconds shows that most of the dissipation of Rayleigh waves energy takes place beneath the oceans (Sec. 7.5). Models for oceanic attenuation indicate that the sub-oceanic mantle has an average Q of less than 80 in the upper most 200 km (Sec. 7.6).

Sec. 7.2 REGIONALIZATION OF MIXED PATH GROUP VELOCITIES AND ATTENUATION COEFFICIENTS

Two regionalization schemes have been used in determining pure path group velocity and Q^{-1}_R in this study. Rather than use the threefold regionalization scheme of Kanamori (1970a) and Dziewonski (1971a) which was based on Umbgrove's (1947, Plate V) classification of provinces of Cenozoic folding, two fourfold regionalization schemes of four crust-upper mantle province types: continent, deep ocean basin, island arc and mid-ocean ridge zones were used. Although more provinces have been recognized as having different surface wave dispersion characteristics (Knopoff 1972), because of the limitations imposed by the precision with which group velocities can be determined, more elaborate regionalization schemes were not justified.

The first regionalization scheme (Figure 7.1), hereafter called the original regionalization scheme, is a modification of the scheme based on Umbgrove (1947). Umbgrove's belts of cenozoic folding are interpreted in this regionalization as either island arc or mid-ocean ridge zones with the addition of

(1) the mid-ocean ridges zones taken as strips of approximately 1000 km widths centered on the major mid-ocean ridges,

(2) the Mariana's and Aleutian island arcs,

(3) the Columbia River Plateau and Colorado Plateau - taken as parts of the Basin and Range island arc zone in the western United States,

and

(4) the Red Sea - taken as a mid-ocean ridge zone.

Continental margins as well as shore-lines are shown in Figure 7.1.

Figure 7.1 AN ORIGINAL REGIONALIZATION BASED ON 4 UPPER MANTLE PROVINCES - is a modification of Umbgrove's (1947) classification of provinces of Cenozoic folding. Important differences between this regionalization and other regionalizations based on Umbgrove's classification system are described in Sec. 7.2. Pure path group velocities derived using this regionalization are shown in Figure 7.5.

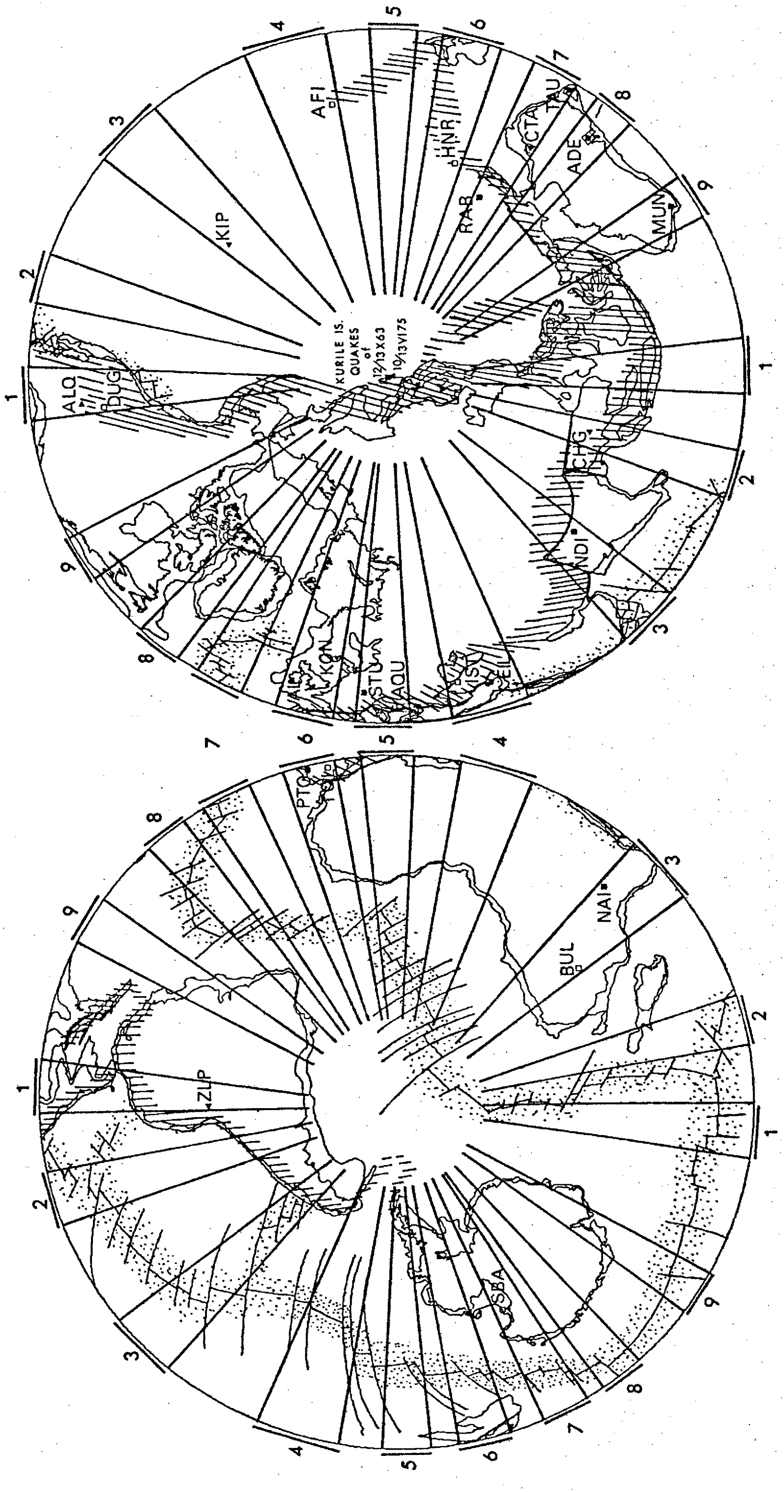
KURILE IS.
QUAKES
of
12/13X63
10/13VI75
KIP
AFI
HNR
RAB
CTA
TAU
ADE
MUN
CHG
NDI
ALQ
DUG
KON
VAL
STU
AQU
MSH
EIL
PTO
SJG
ZLP
BUL
NAI
SBA
1
2
3
4
5
6
7
8
9

The second regionalization scheme used in this study was devised by Wu(1972) and will be called the Wu regionalization. Figure 1 from Wu's (1972) paper on regionalization of Rayleigh wave phase velocities is shown in Figure 7.2. This scheme differs from the original scheme in that Wu (1972)

(1) considers the western United States to be a mid-ocean ridge zone, rather than island arc,

and

(2) includes the East African Rift as a mid-ocean ridge zone.

Other differences are primarily in the interpretation of the widths of island arc and ridge zones and in small differences in interpretation as for Central America. The differences between these two regionalization schemes cause differences of up to 14 per cent in path composition for similar great circle paths (Table 7.1(c) and (d)). These differences are mainly due to estimation of path lengths which cross ridge or arc regions obliquely and for which actual path compositions may be widely at variance with those shown if horizontal refraction occurs. It is possible that these difficulties could be overcome by computing phase velocities for each of the regions used in this study, calculating path deflections at the region boundaries, deriving revised paths from the calculated deflections, and finally arriving at a revised set of path compositions. Such an iterative process is possible but such a refinement would only be justified for a much larger data set.

Group velocities and attenuation coefficients for individual paths determined by combining group velocities measured at each station on a path and averaging over 20 second windows (Sec. 4.2.2) are shown in Figure 7.3. The deviations from global average group velocities and attenuation coefficients are shown in Figure 7.4. Averaging windows for attenuation which contain only one sample have been assigned standard deviations which are 100 per cent of the estimated value (e.g. Figure

Figure 7.2 A REGIONALIZATION PROPOSED BY WU (1972) - is based on global tectonic theory and the USCGS world seismicity map. Four distinct regions province types are used: ocean, continent, arc and ridge. Pure path group velocities and specific attenuation calculated using this regionalization are shown in Figures 7.6 and 7.9.

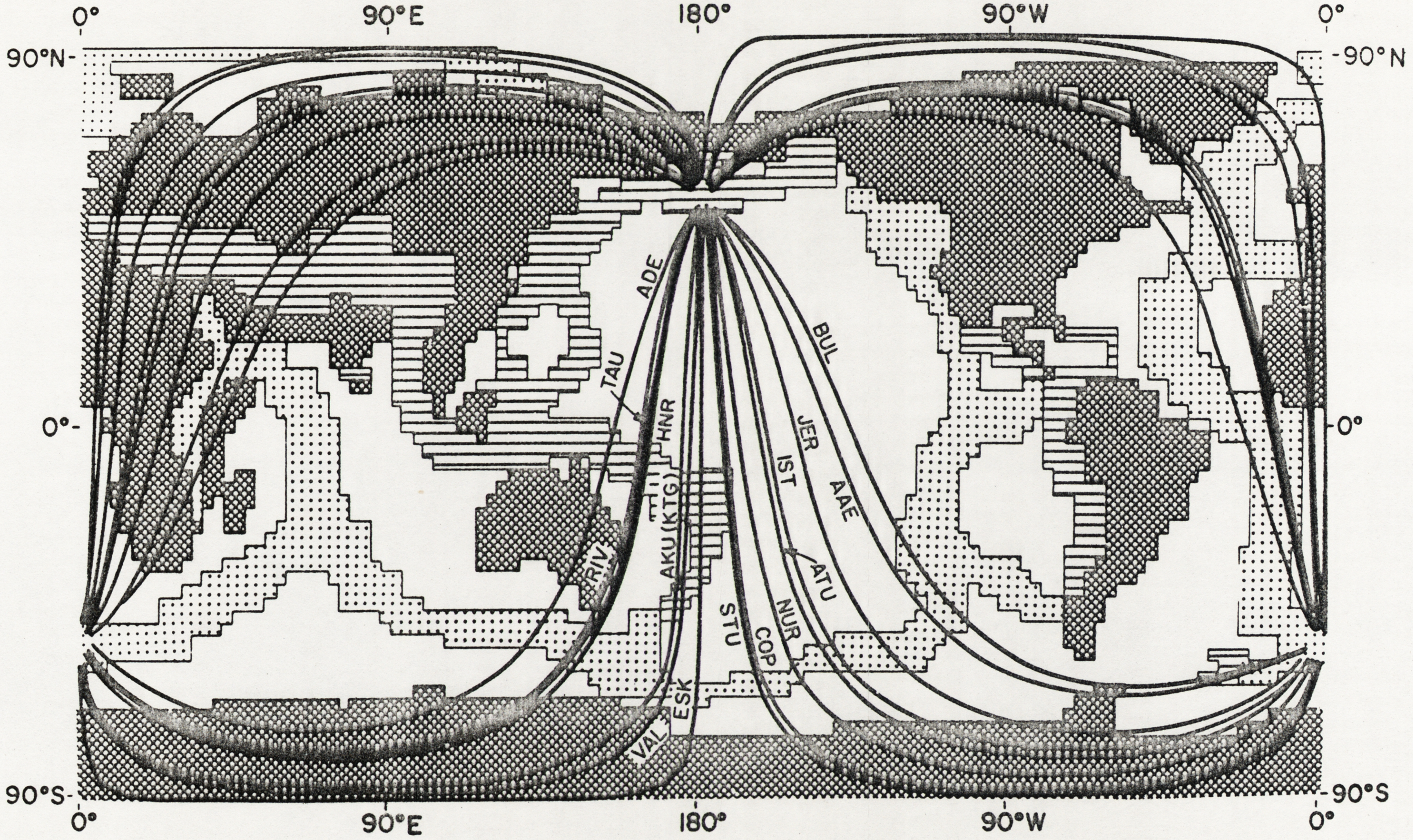

Fig. 1. Great-circle paths of Rat Island earthquake data. Shadings indicate the regionalization used in this paper: white, ocean; cross hatching, continent; horizontal lines, arc; dots, ridge.

TABLE 7.1 (a) PURE PATH COMPOSITION FOR INDIVIDUAL STATIONS AND PATHS

ORIGINAL REGIONALIZATION - INDIVIDUAL STATIONS

Sta Ident.	R_1 Ocean	Continent	Arc	Ridge	R_2 Ocean	Continent	Arc	Ridge
KIP	1.00	.00	.00	.00	.50	.25	.12	.14
KON	.00	.82	.18	.00	.63	.23	.069	.076
CHG	.00	.42	.58	.00	.80	.083	.016	.100
ALQ	.40	.067	.40	.13	.42	.27	.18	.13
ZLP	.33	.28	.34	.05	.40	.17	.22	.21
EIL	.00	.76	.24	.00	.69	.16	.054	.098
CTA	.79	.13	.079	.00	.46	.32	.13	.094
NAI	.11	.50	.33	.057	.62	.16	.016	.20
PTO	.00	.85	.15	.00	.66	.18	.073	.081
TAU	.63	.31	.057	.00	.48	.28	.14	.10
RAB	1.00	.00	.00	.00	.44	.33	.14	.090
ADE	.24	.36	.40	.00	.41	.40	.064	.13
VAL	.00	.83	.17	.00	.65	.21	.072	.078
STU	.00	.84	.16	.00	.63	.15	.089	.140
NDI	.00	.40	.60	.00	.71	.19	.013	.093
MUN	.34	.30	.35	.00	.56	.30	.097	.043

GREAT CIRCLE DATA

IST	.55	.28	.083	.089
AQU	.48	.30	.11	.11
CTA	.52	.29	.12	.078
DUG	.41	.23	.22	.14
ADE	.37	.39	.14	.097
BUL	.60	.23	.11	.089
AFI	.55	.28	.083	.089
HNR	.50	.35	.092	.058
TOL	.50	.35	.092	.058
SBA	.52	.29	.12	.078

TABLE 7.1(b) PURE PATH COMPOSITION FOR INDIVIDUAL STATIONS AND PATHS

WU (1972) - REGIONALIZATION - INDIVIDUAL STATIONS

Sta Ident.	R_1 Ocean	Continent	Arc	Ridge	R_2 Ocean	Continent	Arc	Ridge
KIP	1.00	.00	.00	.00	.44	.279	.134	.147
KON	.00	.79	.21	.00	.73	.11	.040	.12
CHG	.00	.58	.42	.00	.72	.064	.058	.16
ALQ	.40	.00	.27	.33	.33	.32	.22	.18
ZLP	.27	.29	.22	.22	.36	.22	.22	.20
EIL	.00	.88	.12	.00	.665	.123	.049	.163
CTA	.83	.063	.11	.00	.43	.22	.079	.27
NAI	.090	.53	.28	.094	.70	.12	.045	.138
PTO	.00	.83	.17	.00	.765	.059	.044	.132
TAU	.64	.28	.080	.00	.45	.160	.086	.290
RAB	1.00	.00	.00	.00	.42	.22	.098	.25
ADE	.73	.19	.088	.00	.31	.35	.17	.17
VAL	.00	.82	.18	.00	.75	.076	.043	.129
STU	.00	.88	.12	.00	.49	.20	.093	.22
NDI	.00	.40	.60	.00	.71	.19	.013	.093
MUN	.27	.30	.12	.30	.43	.47	.065	.035

GREAT CIRCLE DATA

IST	.64	.30	.06	.24
AQU	.55	.35	.10	.34
CTA	.72	.19	.085	.44
DUG	.53	.25	.22	.38
ADE	.53	.31	.15	.26
BUL	.66	.22	.12	.22
AFI	.629	.30	.071	.258
HNR	.775	.17	.051	.21
TOL	.585	.32	.098	.19
SBA	.72	.19	.085	.44

TABLE 7.1(c) PURE PATH COMPOSITION FOR INDIVIDUAL STATIONS AND PATHS

PATH COMPOSITIONS - ORIGINAL REGIONALIZATION

Path Number	Ocean	Continent	Arc	Ridge
1	.41	.23	.22	.14
2	.69	.13	.092	.088
3	.60	.23	.11	.089
4	.55	.28	.081	.089
5	.48	.30	.11	.11
6	.50	.35	.092	.058
7	.52	.29	.12	.078
8	.37	.39	.14	.097
9	.53	.30	.14	.033

TABLE 7.1(d) PURE PATH COMPOSITION FOR INDIVIDUAL STATIONS AND PATHS

PATH COMPOSITIONS - WU (1972) REGIONALIZATION

Path Number	Ocean	Continent	Arc	Ridge
1	.34	.25	.22	.19
2	.62	.13	.11	.14
3	.52	.24	.115	.125
4	.51	.30	.065	.125
5	.38	.35	.10	.17
6	.58	.245	.075	.10
7	.50	.19	.085	.22
8	.40	.31	.15	.14
9	.39	.43	.078	.097

Figure 7.3.1 GROUP VELOCITIES AND ATTENUATION COEFFICIENTS ARE SHOWN FOR PATHS 1, 2 AND 3 -

Calculation of these averages described in Sec. 4.2.

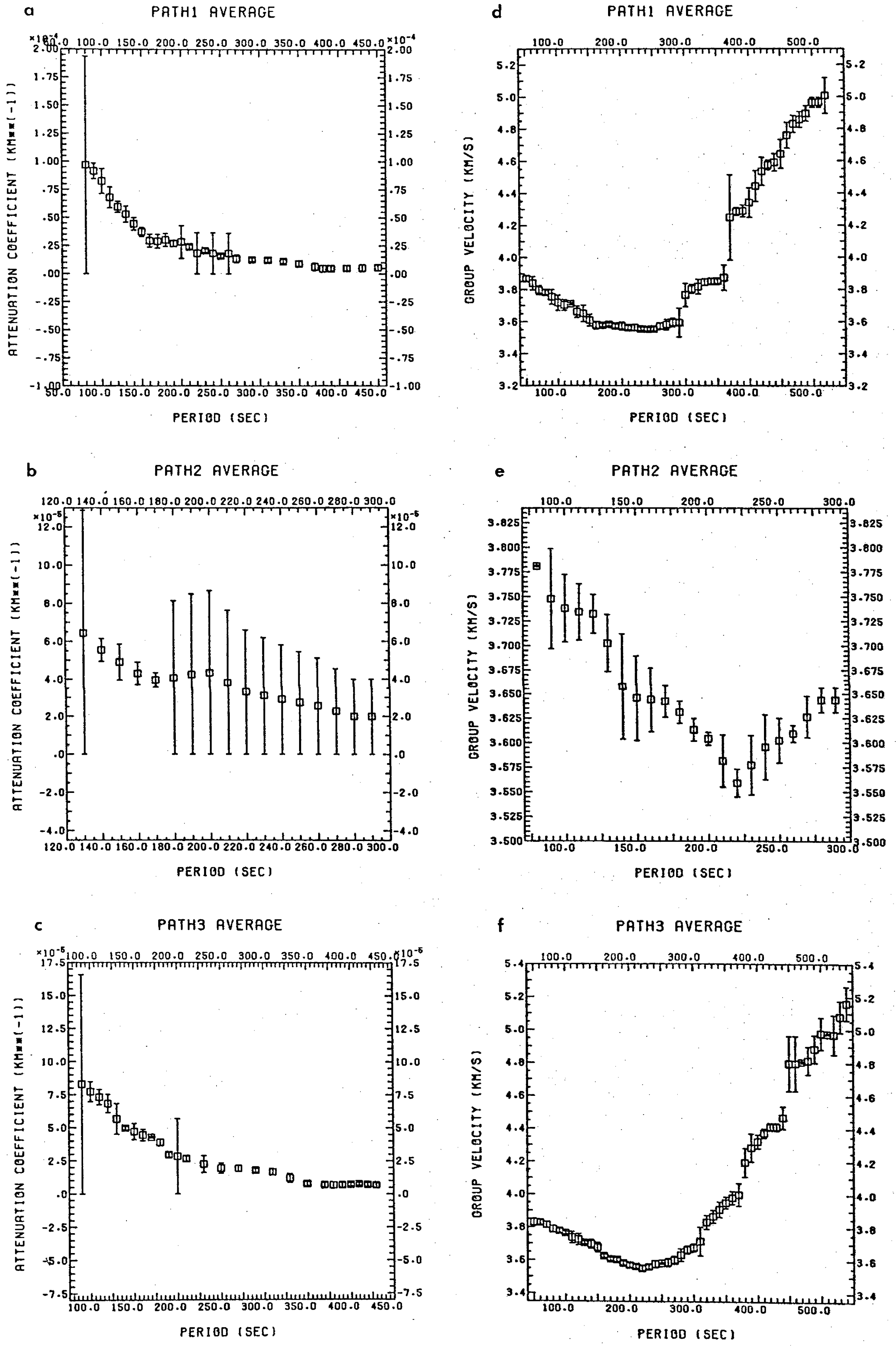
a
PATH1 AVERAGE
ATTENUATION COEFFICIENT (KM**(-1))
×10⁻⁴
2.00
1.75
1.50
1.25
1.00
.75
.50
.25
.00
-.25
-.50
-.75
-1.00
50.0 100.0 150.0 200.0 250.0 300.0 350.0 400.0 450.0
PERIOD (SEC)
d
PATH1 AVERAGE
GROUP VELOCITY (KM/S)
5.2
5.0
4.8
4.6
4.4
4.2
4.0
3.8
3.6
3.4
3.2
100.0 200.0 300.0 400.0 500.0
PERIOD (SEC)
b
PATH2 AVERAGE
ATTENUATION COEFFICIENT (KM**(-1))
×10⁻⁵
12.0
10.0
8.0
6.0
4.0
2.0
.0
-2.0
-4.0
120.0 140.0 160.0 180.0 200.0 220.0 240.0 260.0 280.0 300.0
PERIOD (SEC)
e
PATH2 AVERAGE
GROUP VELOCITY (KM/S)
3.825
3.800
3.775
3.750
3.725
3.700
3.675
3.650
3.625
3.600
3.575
3.550
3.525
3.500
100.0 150.0 200.0 250.0 300.0
PERIOD (SEC)
c
PATH3 AVERAGE
ATTENUATION COEFFICIENT (KM**(-1))
×10⁻⁵
17.5
15.0
12.5
10.0
7.5
5.0
2.5
.0
-2.5
-5.0
-7.5
100.0 150.0 200.0 250.0 300.0 350.0 400.0 450.0
PERIOD (SEC)
f
PATH3 AVERAGE
GROUP VELOCITY (KM/S)
5.4
5.2
5.0
4.8
4.6
4.4
4.2
4.0
3.8
3.6
3.4
100.0 200.0 300.0 400.0 500.0
PERIOD (SEC)

Figure 7.3.2 GROUP VELOCITIES AND ATTENUATION COEFFICIENTS AVERAGED BY PATH ARE SHOWN FOR PATHS 4, 5 AND 6 - Calculation of these averages is described in Sec. 4.2.

a

PATH4 AVERAGE

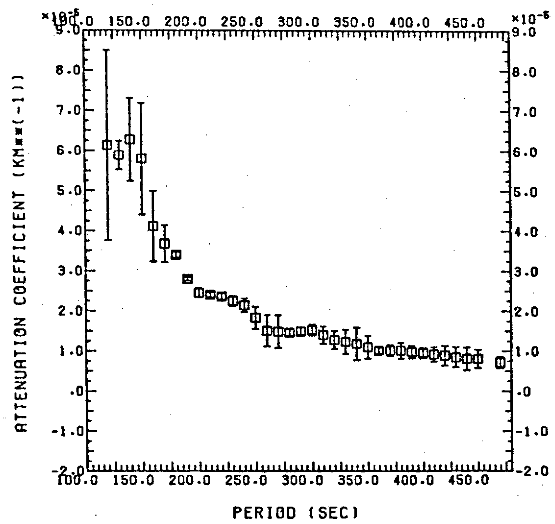

d

PATH4 AVERAGE

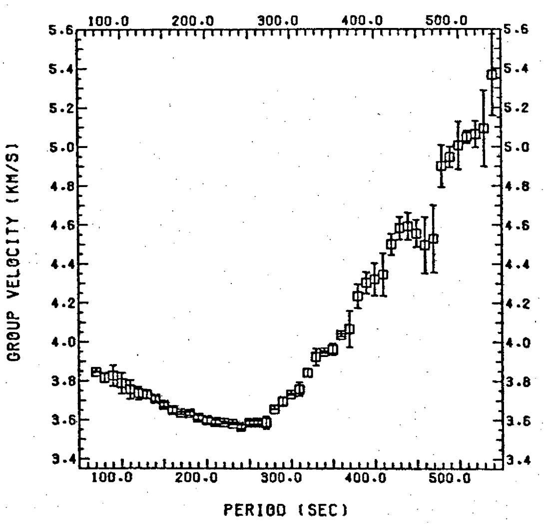

b

PATH5 AVERAGE

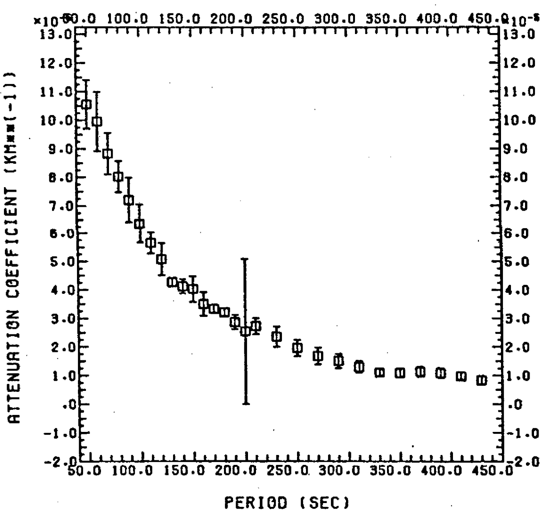

e

PATH5 AVERAGE

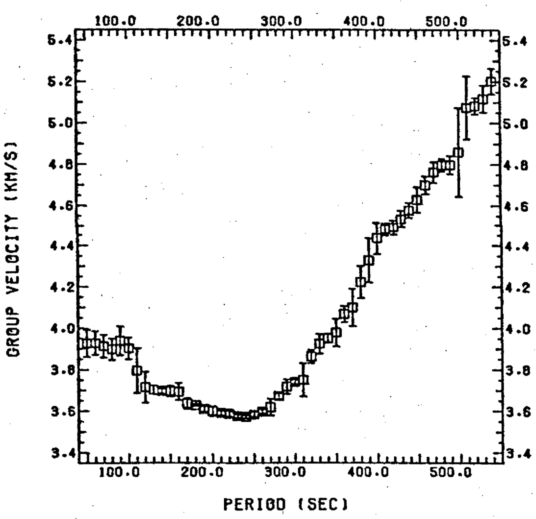

c

PATH6 AVERAGE

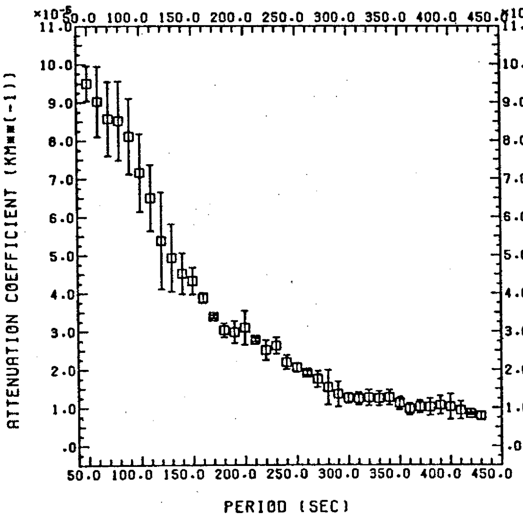

f

PATH6 AVERAGE

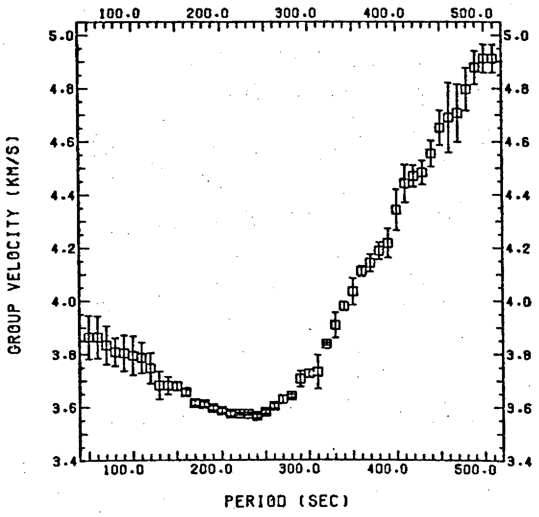

Figure 7.3.3 GROUP VELOCITIES AND ATTENUATION COEFFICIENTS AVERAGED BY PATH ARE SHOWN FOR PATHS 7, 8 AND 9 -

Calculation of these averages is described in Sec. 4.2.

a PATH7 AVERAGE

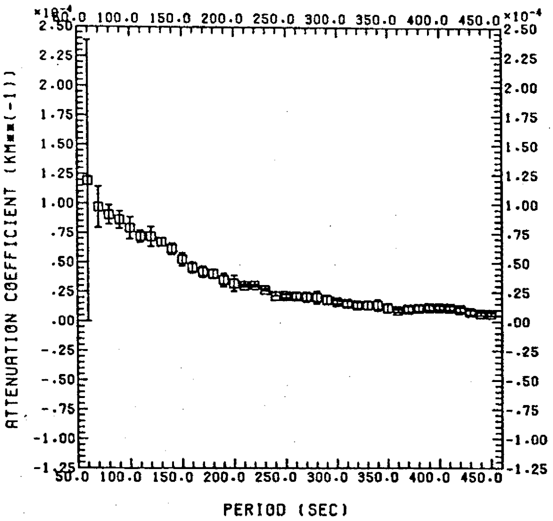

d PATH7 AVERAGE

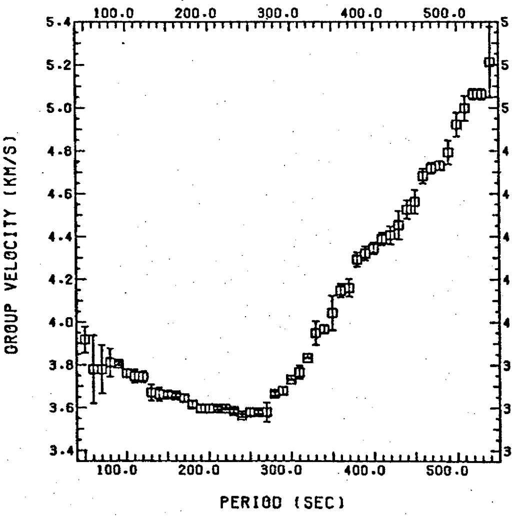

b PATH8 AVERAGE

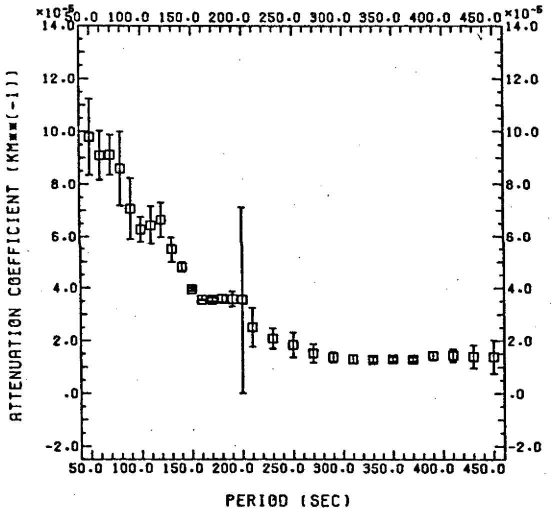

e PATH8 AVERAGE

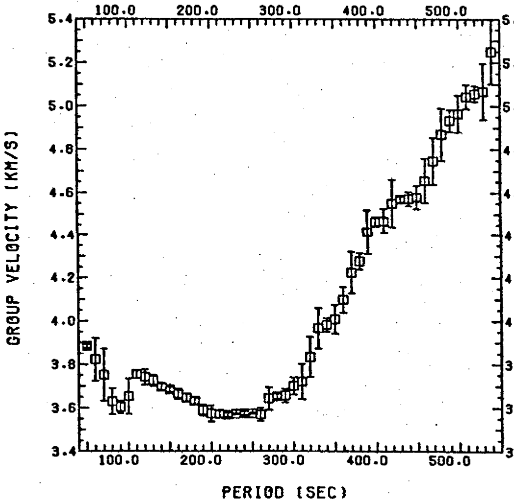

c PATH9 AVERAGE

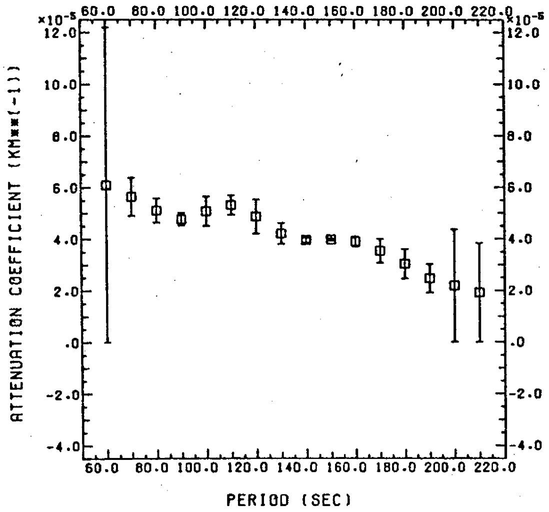

f PATH9 AVERAGE

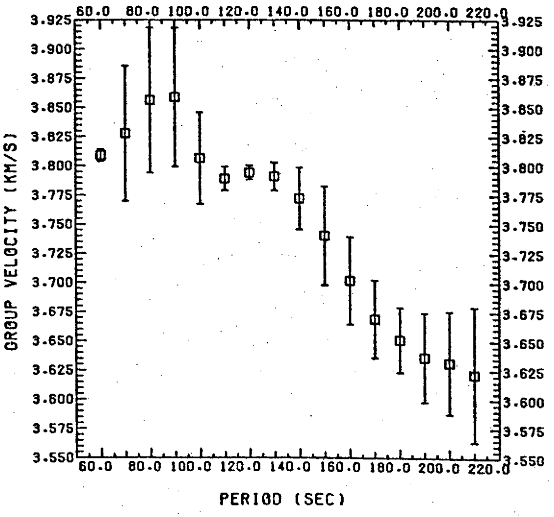

Figure 7.4 RESIDUAL ATTENUATION AND GROUP VELOCITY DISPERSION - Residual attenuation coefficients, calculated as the difference between path average attenuation coefficients and global average attenuation coefficients, are shown in (a), (b) and (c) for paths 1 - 3, 4 - 6 and 7 - 9 respectively. Residual group velocity dispersion, calculated as the difference between path average group velocities and global average group velocities, are shown in (d), (e) and (f) for paths 1 - 3, 4 - 6 and 7 - 9 respectively.

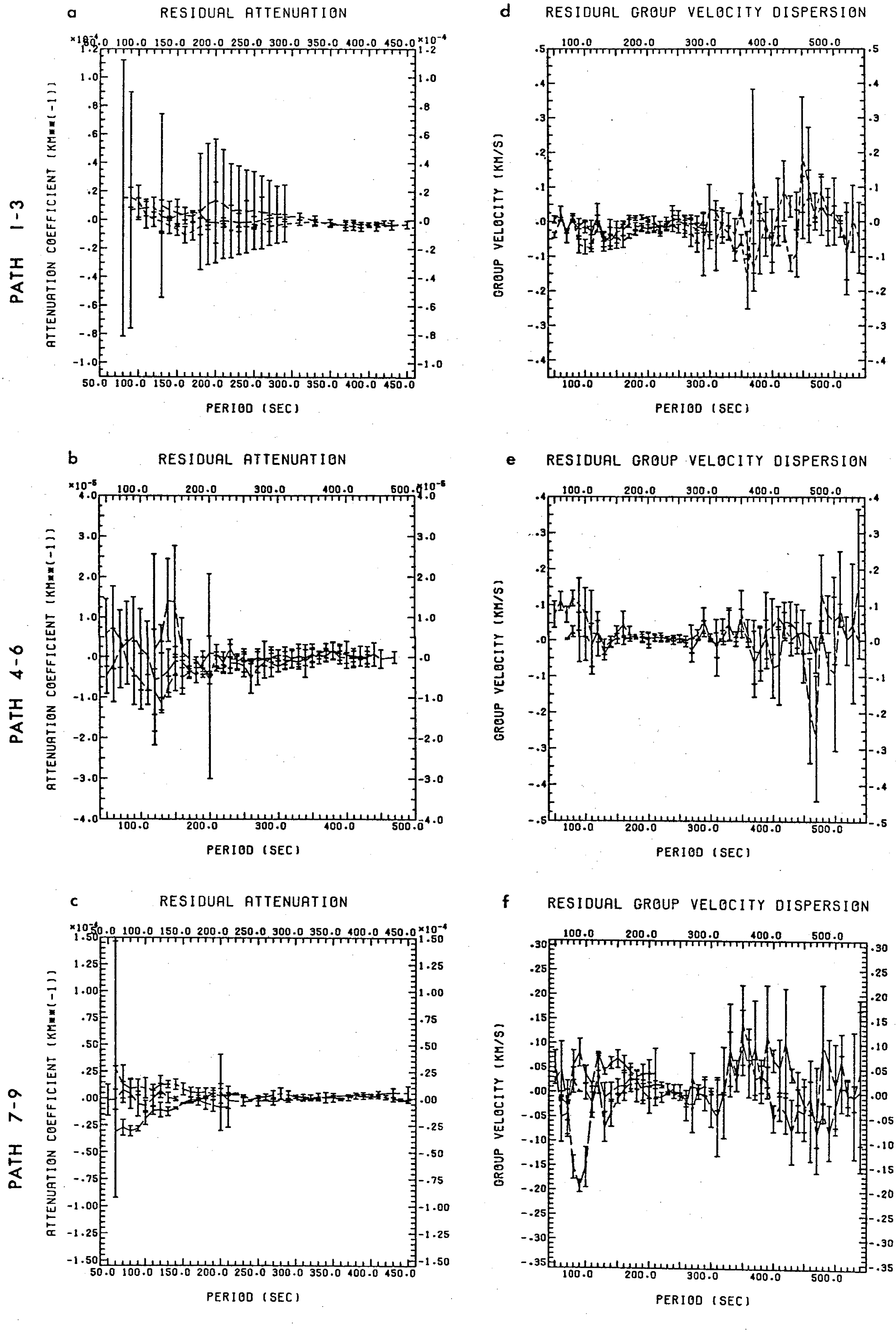
PATH 1-3
PATH 4-6
PATH 7-9
a
RESIDUAL ATTENUATION
ATTENUATION COEFFICIENT (KM**(-1))
×10⁻⁴
1.2
1.0
.8
.6
.4
.2
.0
-.2
-.4
-.6
-.8
-1.0
50.0 100.0 150.0 200.0 250.0 300.0 350.0 400.0 450.0
PERIOD (SEC)
b
RESIDUAL ATTENUATION
ATTENUATION COEFFICIENT (KM**(-1))
×10⁻⁵
4.0
3.0
2.0
1.0
.0
-1.0
-2.0
-3.0
-4.0
100.0 200.0 300.0 400.0 500.0
PERIOD (SEC)
c
RESIDUAL ATTENUATION
ATTENUATION COEFFICIENT (KM**(-1))
×10⁻⁴
1.50
1.25
1.00
.75
.50
.25
.00
-.25
-.50
-.75
-1.00
-1.25
-1.50
50.0 100.0 150.0 200.0 250.0 300.0 350.0 400.0 450.0
PERIOD (SEC)
d
RESIDUAL GROUP VELOCITY DISPERSION
GROUP VELOCITY (KM/S)
.5
.4
.3
.2
.1
.0
-.1
-.2
-.3
-.4
100.0 200.0 300.0 400.0 500.0
PERIOD (SEC)
e
RESIDUAL GROUP VELOCITY DISPERSION
GROUP VELOCITY (KM/S)
.4
.3
.2
.1
.0
-.1
-.2
-.3
-.4
-.5
100.0 200.0 300.0 400.0 500.0
PERIOD (SEC)
f
RESIDUAL GROUP VELOCITY DISPERSION
GROUP VELOCITY (KM/S)
.30
.25
.20
.15
.10
.05
.00
-.05
-.10
-.15
-.20
-.25
-.30
-.35
100.0 200.0 300.0 400.0 500.0
PERIOD (SEC)

7.3.1(b)). Path average group velocities have been calculated with each observation assigned unit weight.

The pure path regional group velocities observations have in the past been calculated from great circle measurements (with the exception of Hamada (1972) who calculated pure path velocities from individual velocity estimates for R_1 and R_2 paths). Kanamori's (1970a) regional group velocities were calculated as if each station defined a different path and each path was given equal weight in his analysis. Dziewonski (1971a) summed autocorrelograms of observations at stations within an azimuth window and calculated great circle group velocities from the autocorrelogram sum for each path. Dziewonski required phase velocities calculated from seismograms for stations within each azimuth window (path) to be consistent at all periods. Path averages defined in this way are areal averages for paths. In either of these methods pure path group and/or phase velocities at each period, T, are calculated by a multiple linear regression analysis of great circle travel times derived from a set of equations of the form

$$\frac{1}{\overline{V}_j(T)} = \sum_{i=1}^{N} \frac{\ell_{ij}}{V_i(T)} \quad , \qquad (7.1)$$

where V_i is the pure path phase or group velocity for the i^{th} type region, $\overline{V}_j$ is the phase or group velocity measured at the j^{th} station, and ℓ_{ij} is the fraction of the j^{th} great circle path which is comprised of the i^{th} type of pure path region of the N regions.

Since group velocity measurements for Rayleigh phases from R_1 to R_4 have been made from the smaller 3 events used in this study and since many of the R_1 and R_2 paths are 1 or 2 region composite paths, another method of weighting group velocities was also attempted in which individual measurements of group velocity were weighted equally in the multiple linear analysis. For this purpose Equation 7.1 can be rewritten

$$\frac{\ell_j}{\overline{U}_j(T)} = \sum_{i=1}^{N_s} \frac{\ell_{ij}}{U_i(T)} \qquad (7.2)$$

where

$$\ell_j = \sum_{i=j}^{N_s} \ell_{ij} \qquad (7.3)$$

is the fraction of a great circle path over which the group velocity measurement is made and N_s is the number of measurements of the group velocity U at period T. In Equations 7.1, 7.2 and 7.3 each term represents the group or phase travel time of a Rayleigh phase. Similar equations can be written in terms of the energy dissipated along each path. In that case only single station measurements have been used in order to avoid differences between seismic stations. In the equivalent equations for dissipation, Q_R replaces velocity, since Q^{-1}_R is the specific attenuation along the path, so that at period T,

$$\overline{Q}^{-1}_R(T) = \sum_{i=1}^{N} \ell_{ij} \; Q^{-1}_{R_i}(T) \qquad (7.4)$$

where Q^{-1}_R is the pure path attenuation for the i^{th} region, and $\overline{Q}^{-1}_R$ is the measured attenuation for the great circle path. Equations 7.2 and 7.3 reduce to equations like 7.1 when only great circle data are used. As remarked earlier in the discussion of the Kanamori and Dziewonski studies there are two methods of weighting which can be used when calculating pure path group velocities or attenuation coefficients. In the first method measurements are weighted by individual measurements, in the second measurements are weighted by path. The second method suffers more from noisy or

Sec. 7.3 GROUP VELOCITY REGIONALIZATION

Pure path group velocities have been derived from path averages for both the Wu (1972) and original regionalization schemes and are shown for 4, 3 and 2 regional separations in Figures 7.5(a) and 7.6(a). Pure path group velocities were also derived by weighting all observations equally rather than by giving paths equal weight (Figures 7.5(b) and 7.6(b)). Important differences between the pure path group velocities derived in these pure path separations are that

(1) equal weighting of individual observations produces greater standard errors in pure path group velocities than equal weighting of paths,

(2) continental group velocities for periods between 50 and 150 seconds produced by the original regionalization are unacceptably low compared with the normal continental group velocities,

(3) island arc group velocities are not well separated from continental and oceanic velocities in any of the original regionalization separations (Figure 7.5(a) and (b)),

(4) mid-ocean ridge group velocities are not well resolved in any of these pure path separations,

and

(5) separation of pure path group velocities is poor for all combinations of regions at periods greater than about 300 seconds.

Of the two regionalization schemes the Wu scheme produces pure path group velocities which agree with observed group velocities for all regions for periods shorter than 100 seconds and which also agree with results of other long period regionalization studies (e.g. Dziewonski 1971a). Group velocities for oceans and continents are similar for periods between

Figure 7.5(a) PURE PATH GROUP VELOCITIES DERIVED USING THE ORIGINAL REGIONALIZATION -

Pure path group velocities, calcualted using the original regionalization with path average group velocities weighted equally, are shown for

4 regions: ocean, continent, arc and ridge provinces (upper left panel),

3 regions: ocean-ridge, continent and arc provinces (upper right panel), and

2 regions: ocean-ridge and continent-arc provinces (lower right panel).

Continental and oceanic group velocity determined in the 4 region regression adnalysis are shown without arc and ridge group velocities in the lower left panel. Of the 4 region types group velocities for continents are shown as triangles, oceans as circles, arcs as X's and ridges as diamonds. When ocean and ridge provinces are combined in 2 and 3 region regression analyses, the ocean-ridge group velocities are shown as circles. In the 2 region regression analysis the continent-arc group velocities are shown as triangles.

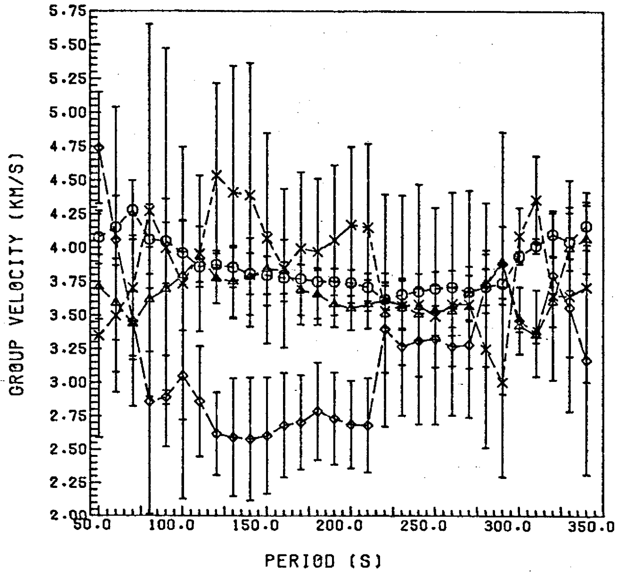
PATH AVERAGE U FOR 4 REGIONS - ORIGINAL REGIONS

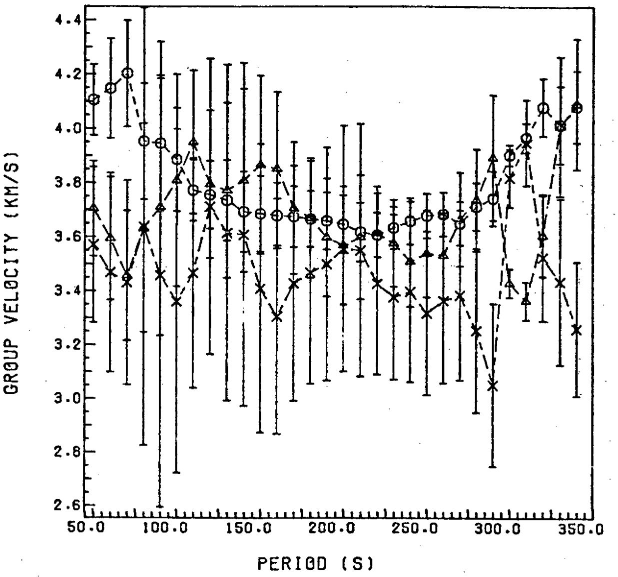
ORIGINAL REGIONALIZATION - PATH AVERAGE GROUP VELOCITIES - 3 REGIONS

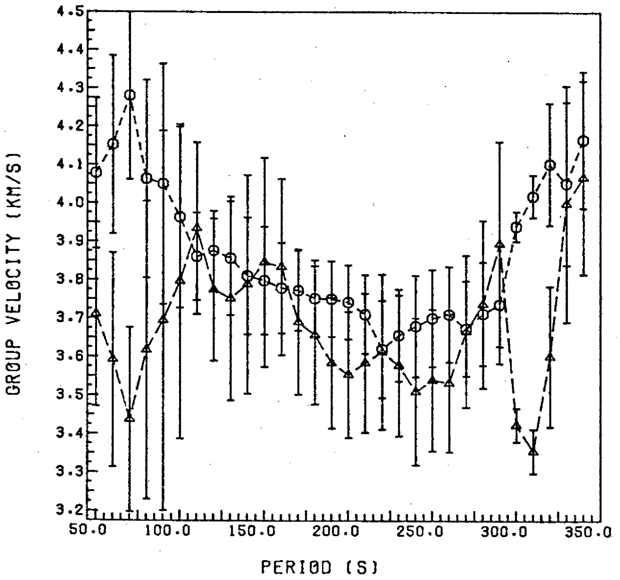
PATH AVERAGE U FOR 4 REGIONS - ORIGINAL REGIONS O & C

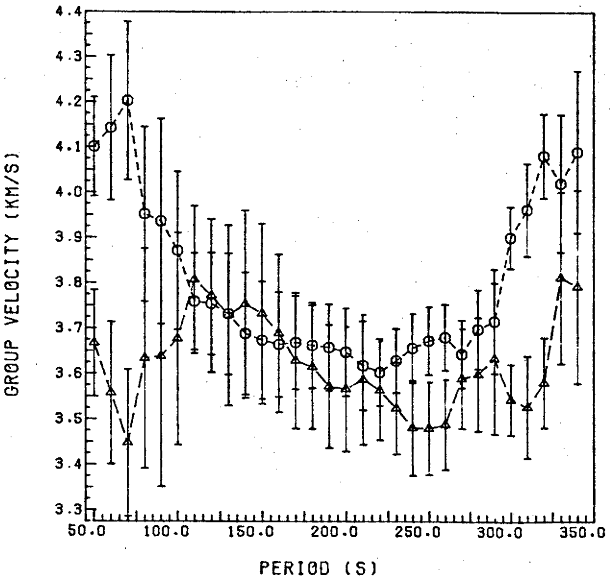
ORIGINAL REGIONALIZATION - PATH AVERAGE U - 2 REGIONS

Figure 7.5(b) PURE PATH GROUP VELOCITIES DERIVED USING THE ORIGINAL REGIONALIZATION -

Pure path group velocities, calculated using the original regionalization with individual group velocity observations weighted equally, are shown for

4 regions: ocean, continent, arc and ridge provinces (upper left panel),

3 regions: ocean-ridge, continent and arc provinces (upper right panel), and

2 regions: ocean-ridge and continent-arc provinces (lower right panel).

Continental and oceanic group velocities determined in the 4 region regression analysis are shown without arc and ridge group velocities in the lower left panel. Symbols used for regions are the same as those described in the caption to Figure 7.5(a).

INDIVIDUALLY AVERAGED U FOR 4 REGIONS - ORIGINAL REGIONS

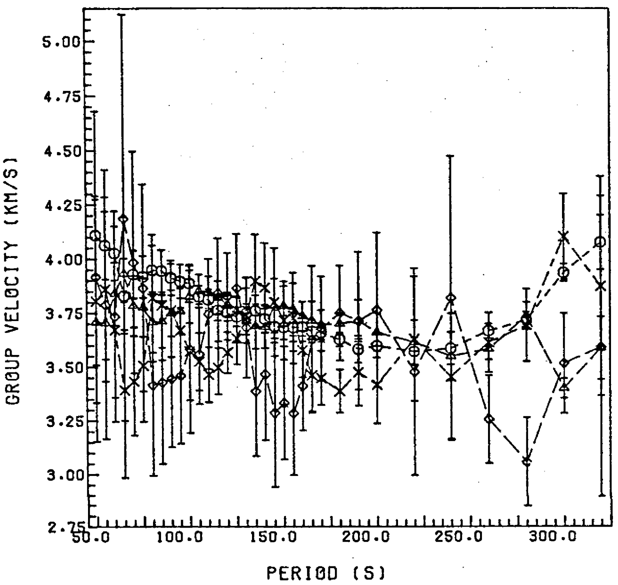

INDIVIDUALLY AVERAGED U FOR 3 REGIONS - ORIGINAL REGIONS

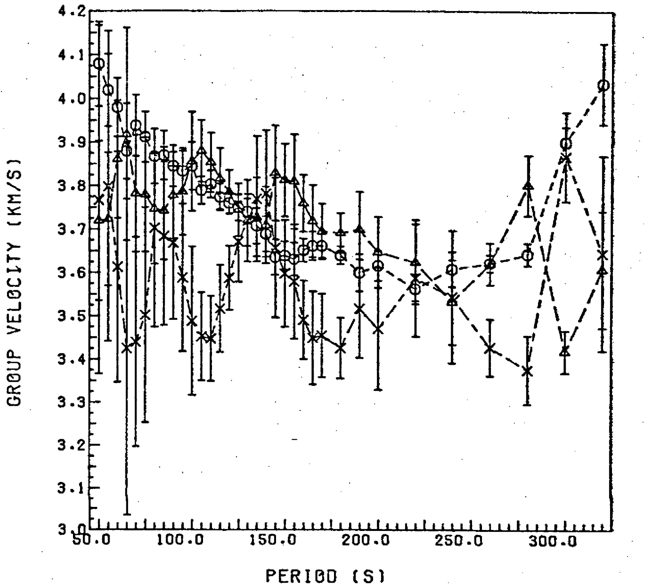

INDIVIDUALLY AVERAGED U FOR 4 REGIONS - ORIGINAL REGIONS B + C

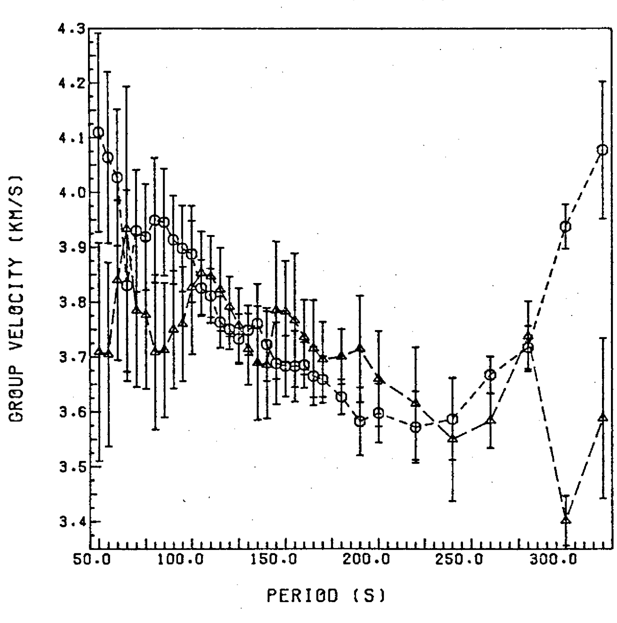

INDIVIDUALLY AVERAGED U FOR 2 REGIONS - ORIGINAL REGIONS

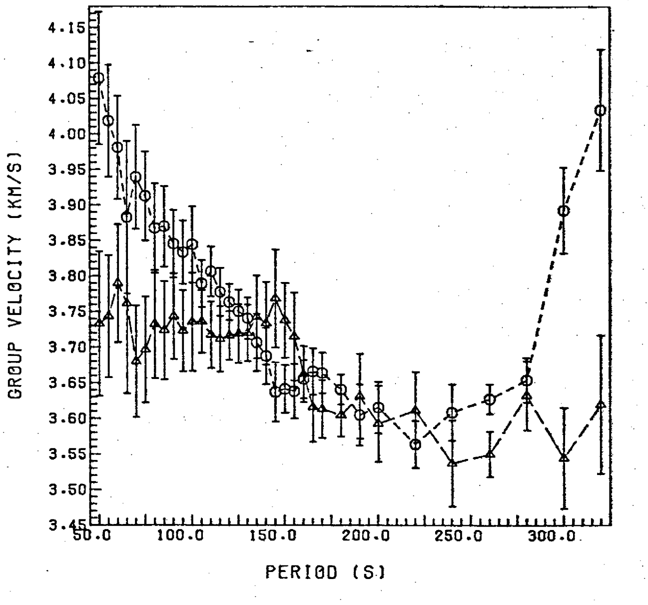

Figure 7.6(a) PURE PATH GROUP VELOCITIES DERIVED USING THE WU (1972) REGIONALIZATION -

Pure path group velocities, calculated using the Wu (1972) regionalization with path average group velocities weighted equally, are shown for

4 regions: ocean, continent, arc and ridge provinces (upper left panel),

3 regions: ocean-ridge, continent and arc provinces (lower left panel), and

2 regions: ocean-ridge and continent-arc provinces (lower right panel).

Continental and oceanic group velocities determined in the 4 region regression analysis are shown in the upper right panel. Symbols used for regions are the same as those described in the caption to Figure 7.5(a). Also shown are pure path group velocities for shield, ocean and tectonic regions as determined by Hamada (1972) (shown as solid symbols) in the lower left panel). Dziewonski's (1971a) pure path group velocities for shields (solid line) and oceans (dashed line) are also shown in the lower two panels.

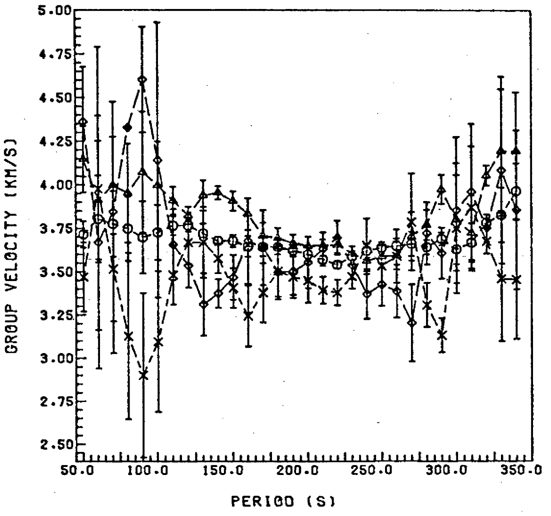

PATH AVERAGE GROUP VELOCITIES FOR 4 REGIONS - WU (1972)

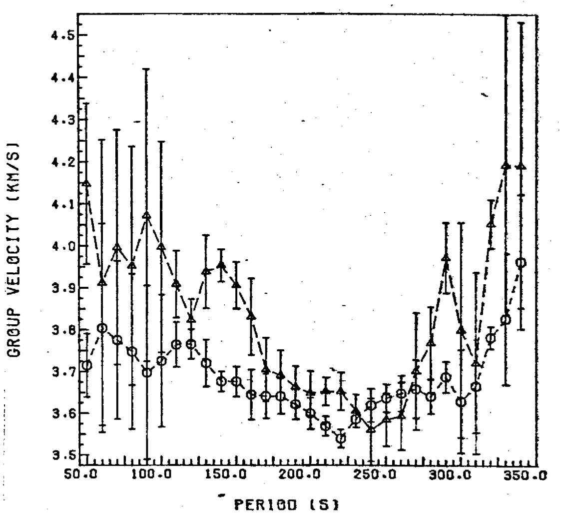

WU(1972) - PATH AVERAGE GROUP VELOCITY - 4 REGIONS O & C

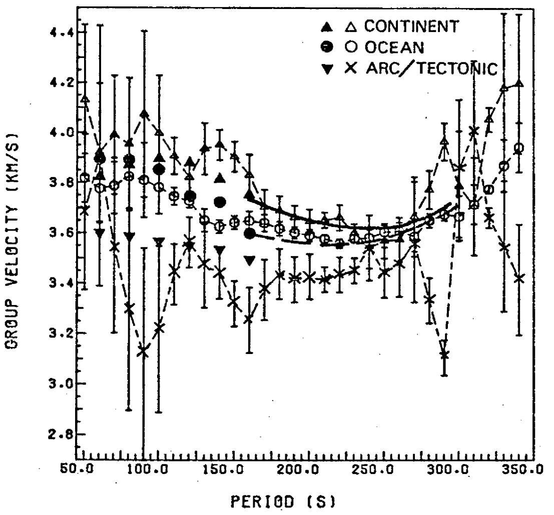

PATH AVERAGE GROUP VELOCITIES FOR 3 REGIONS - WU (1972)

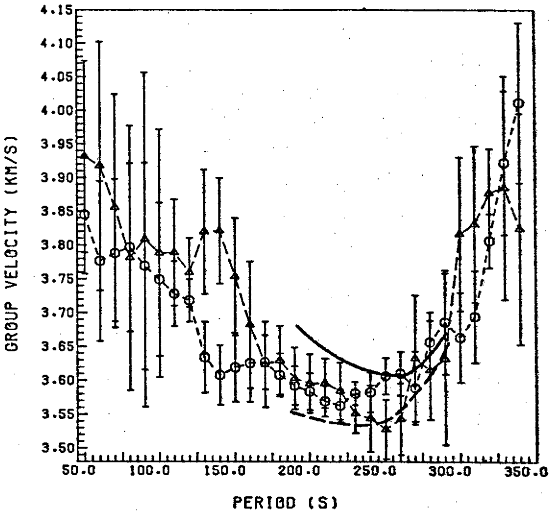

PATH AVERAGE GROUP VELOCITIES FOR 2 REGIONS - WU (1972)

Figure 7.6(b) PURE PATH GROUP VELOCITIES DERIVED USING THE WU (1972) REGIONALIZATION -

Pure path group velocities calculated using the Wu (1972) regionalization with individual group velocity observations weighted equally, are shown for

4 regions: ocean, continent, arc and ridge provinces (upper left panel),

3 regions: ocean-ridge, continent and arc provinces (lower left panel), and

2 regions: ocean-ridge and continent-arc provinces (lower right panel).

Continental and oceanic group velocities determined in the 4 region regression analysis are shown in the upper right panel. Symbols used for regions are the same as those described in the caption to Figure 7.5(a).

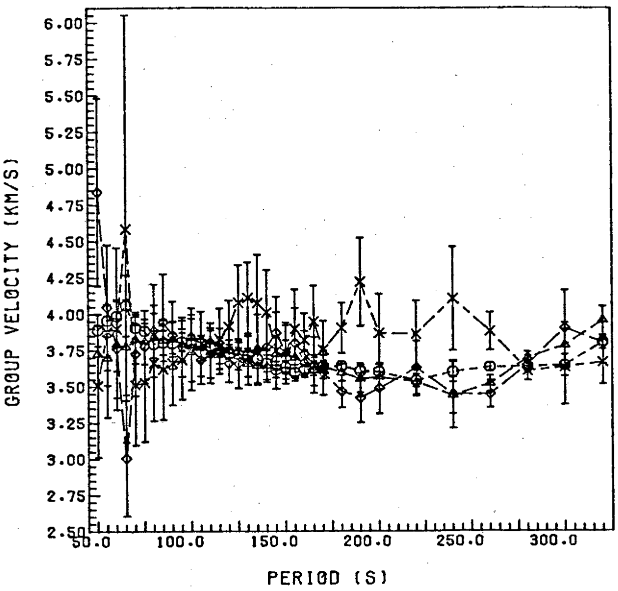
INDIVIDUALLY AVERAGED GROUP VELOCITIES FOR 4 REGIONS - WU (1972)

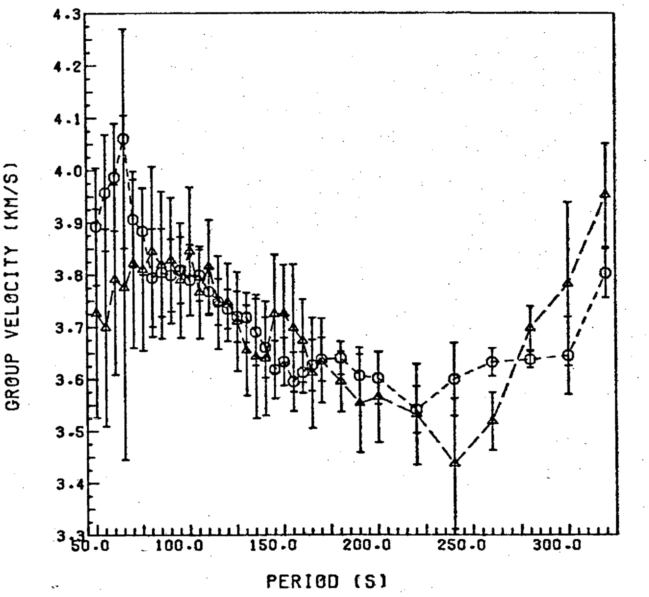
INDIVIDUAL O + C GROUP VELOCITIES FOR 4 REGIONS - WU (1972)

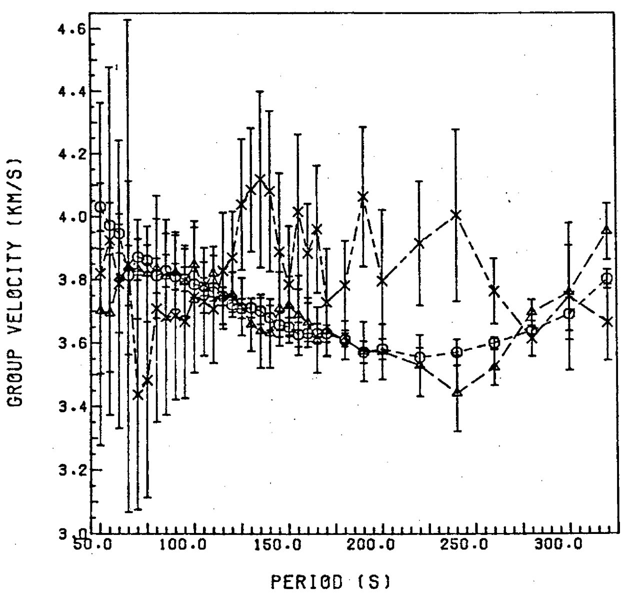
WU(1972) - INDIVIDUAL OBS - GROUP VELOCITY - 3 REGIONS

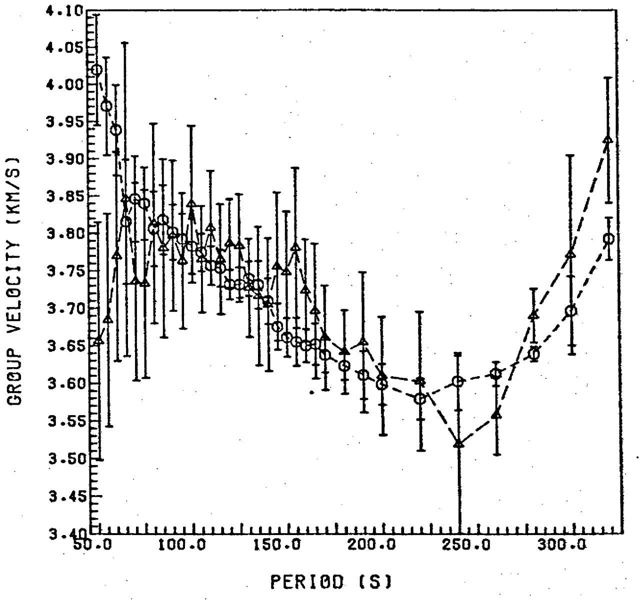
INDIVIDUALLY AVERAGED GROUP VELOCITIES FOR 2 REGIONS - WU (1972)

Figure 7.6(c) PURE PATH GROUP VELOCITIES DERIVED USING THE WU (1972) REGIONALIZATION -

Pure path group velocities calculated using the Wu (1972) regionalization with individual R_1, R_2 and great circle observations weighted equally, are shown for 4 (top panel) 3 (middle panel) and 2 (bottom panel) region combinations as described in the caption to Figure 7.6(b). Symbols used for regions are the same as those described in the caption to Figure 7.5(a).

INDIVIDUALLY AVERAGED U(R1.R2)FOR 4 REGIONS - WU (1972)

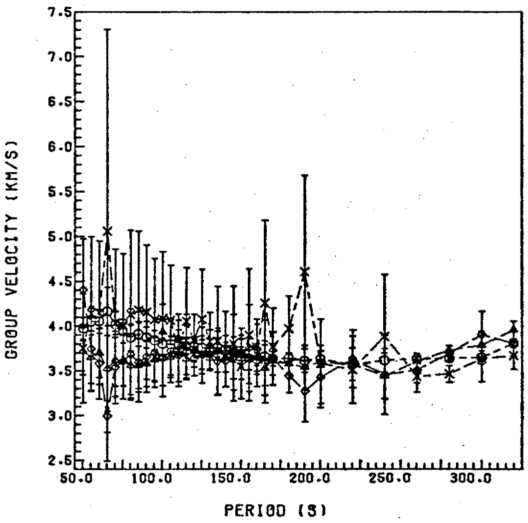

INDIVIDUALLY AVERAGED U(R1.R2) FOR 3 REGIONS - WU (1972)

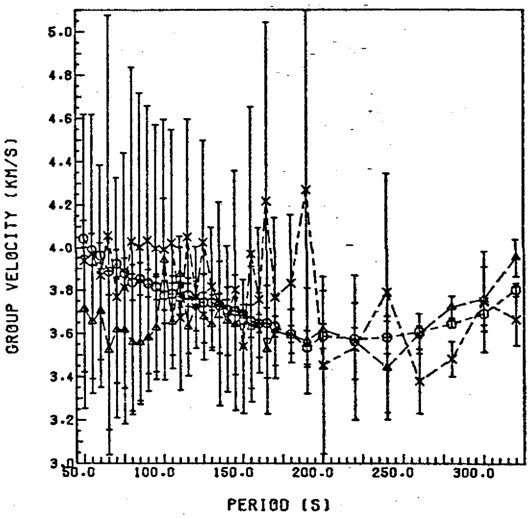

WU(1972) REGIONALIZATION - INDIVIDUAL R1 & R2 U - 2 REGIONS

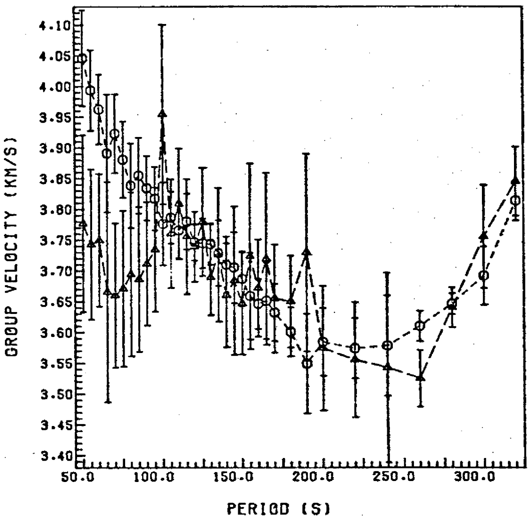

100 and 150 seconds although continental group velocities are slightly higher than the oceanic velocities throughout this period range. This similarity between continental and oceanic phase velocities of Rayleigh waves for these periods has also been noted by Wu (1972). The pure path separations with equally weighted observations based on the Wu scheme (Figure 7.6(b) for 3 and 4 regions) show that continental velocities begin to decrease at periods shorter than 80 seconds, a characteristic feature of continental group velocity dispersion. However, the Wu scheme with equal weighting of paths (Figure 7.6(a) for 3 and 4 regions) obscures this feature. When 2 pure path regions are used, continent-island arc and ocean-ridge provinces, the resulting continent-arc group velocities are lower than pure continental group velocities derived for 3 and 4 regions and ocean-ridge group velocities are lower than pure oceanic group velocities from 4 region separations. These combined 2 and 3 region pure path group velocities as well as the 4 region group velocities agree with pure path group velocities determined by Dziewonski (1971a) for 3 regions and Wu(1972) for 4 regions. Dziewonski's pure path group velocities for shields are less than one standard error higher than the 4 region continental group velocities (Figure 7.6(a)). Dziewonski's oceanic region (corresponding to the combined ocean-ridge province in this study) velocities lie slightly more than one standard error below the ocean ridge group velocities. These disparities may in part be caused by the differences in the regionalization schemes as described earlier in the discussion of the modification of the Umbgrove scheme used in this study.

However, the Wu scheme does produce group velocities for periods shorter than 100 seconds for all regions which are in good agreement with measurements for short paths within such regions.

The two regions which do not produce smooth or reasonable group velocities in this study are the mid-ocean ridge and island arc provinces. At periods shorter than 100 seconds the mid-ocean ridge group velocities determined from path averages (Figure 7.6(a)) are higher than other regional velocities. This is probably caused by lateral refraction at these short periods. The pure path island arc group velocities for both individually weighted and path weighted pure path separations for the 4 region analysis show that island arc group velocities are very low for periods shorter than 120 seconds. At longer periods the island arc velocities are extremely erratic. Since path 1, the path which contains a larger proportion of island arc than the other 8 paths, traverses the western Pacific Ocean circle of island arcs as far south as the Sunda Arc as well as the Aleutian island arc, the western United States and portions of the central and South American island arcs, all of which are extremely complex regions, it is not surprising that multipathing should cause difficulties on this path at long periods. Nevertheless, it is probably that at least on some parts of this path the velocity structure differs from that in other regions down to at least 600 km.

Pure path separation of the individual group velocity observations was also attempted using only R_1 and R_2 group velocities and great circle group velocities. The results of regression analysis for 3 and 4 regions are shown in Figure 7.6(c). These regional group velocities show the effect of lower precision in R_1 and R_2 group velocity estimates due to short path lengths. Standard errors for the pure path group velocities derived in this way are much larger than those derived using the whole data set and demonstrate the importance of the more precise R_3 and R_4 group velocity estimates.

The Wu (1972) regionalization scheme (Figure 7.2) has been shown to produce pure path group velocities which are consistent with other short and long period Rayleigh wave studies and will be used in Sec. 7.4 for the regionalization of Q^{-1}_R.

In the next section models for 2, 3 and 4 region continental and oceanic structure are presented which have been derived from regression analyses based on equal weighting of individual group velocity observations (Figure 7.6(b)). Group velocities and their standard errors for pure path separations shown in Figure 7.6(a) and (b) are listed in Table 7.2.

Table 7.2(a) REGIONAL GROUP VELOCITIES AFTER WU (1972) - 4 REGIONS

Period	Standard Deviation	Number of Observations	Ocean		Continent		Arc		Ridge	
			u	±	u	±	u	±	u	±
50	.7548E-02	31	3.8928	.1123	3.7264	.2002	3.5073	.4934	4.8393	.6437
60	.6776E-02	32	3.9872	.1028	3.7912	.1824	3.8999	.5578	3.7641	.3394
70	.6594E-02	37	3.9065	.0919	3.8217	.1616	3.5118	.4153	3.7266	.2890
80	.7911E-02	46	3.7945	.0940	3.8443	.1631	3.6633	.3992	3.8873	.3187
90	.6060E-02	49	3.7993	.0696	3.8277	.1204	3.6621	.2899	3.8551	.2324
100	.7017E-02	63	3.7903	.0679	3.8456	.1227	3.7585	.2833	3.7662	.2304
110	.5227E-02	64	3.7685	.0453	3.8159	.0897	3.7313	.2080	3.7239	.1643
120	.4583E-02	67	3.7349	.0376	3.7479	.0746	3.9136	.1808	3.6598	.1308
130	.5881E-02	69	3.7186	.0477	3.6554	.0867	4.1115	.2449	3.6811	.1686
140	.7583E-02	72	3.6613	.0582	3.6399	.1096	4.0118	.2911	3.7736	.2252
150	.6432E-02	74	3.6338	.0461	3.7261	.0936	3.7302	.2108	3.7377	.1858
160	.5601E-02	74	3.6132	.0393	3.6736	.0797	3.8199	.1855	3.7237	.1606
170	.5669E-02	69	3.6381	.0420	3.6360	.0813	3.7534	.1994	3.5938	.1536
180	.4090E-02	62	3.6409	.0319	3.5956	.0581	3.9031	.1734	3.4656	.1116
190	.5790E-02	47	3.6068	.0540	3.5534	.0944	4.2213	.3034	3.4232	.1706
200	.5853E-02	50	3.6019	.0500	3.5657	.0874	3.8682	.2693	3.4878	.1752
220	.4429E-02	26	3.5416	.0451	3.5325	.0970	3.8615	.2305	3.6301	.1840
240	.6065E-02	25	3.5999	.0701	3.4374	.1258	4.1049	.3568	3.4457	.2338
260	.2495E-02	25	3.6333	.0268	3.5194	.0555	3.8800	.1312	3.4468	.0939
280	.1390E-02	22	3.6377	.0155	3.6978	.0423	3.6080	.0669	3.6532	.0593
300	.2650E-02	10	3.6457	.0745	3.7828	.1566	3.6329	.2581	3.9011	.2615
320	.1531E-02	10	3.8037	.0469	3.9528	.0988	3.6670	.1519	3.8003	.1433
340	.1732E-02	10	3.9333	.0567	4.2231	.1276	3.4249	.1499	3.8873	.1696
360	.4356E-02	10	4.1129	.1559	4.1254	.3062	3.0540	.2997	4.7828	.6459
380	.3728E-02	10	4.0049	.1265	4.5016	.3120	4.0808	.4580	4.5985	.5110
400	.4164E-02	10	4.0683	.1458	4.7344	.3855	4.5340	.6315	4.4584	.5365

contd.

TABLE 7.2(a) REGIONAL GROUP VELOCITIES AFTER WU (1972) - 4 REGIONS (contd)

Period	Standard Deviation	Number of Observations	Ocean		Continent		Arc		Ridge	
			u	±	u	±	u	±	u	±
420	.3556E-02	10	4.4084	.1462	4.7245	.3278	4.9499	.6427	3.9226	.3546
440	.2741E-02	10	4.4897	.1169	4.7454	.2549	4.7350	.4533	4.3472	.3357
460	.6319E-02	10	4.5048	.2714	4.6172	.5564	5.9040	1.6250	4.5201	.8369
480	.2209E-02	10	4.8049	.1079	5.0730	.2348	5.2609	.4511	4.1540	.2471
500	.2338E-02	10	5.1047	.1289	4.8930	.2312	5.3090	.4861	4.2982	.2799
520	.1459E-02	10	4.8074	.0714	5.2272	.1647	4.7137	.2392	5.6576	.3028
540	.2837E-02	10	5.0827	.1551	5.5816	.3650	4.9424	.5112	5.1019	.4786
560	.3164E-02	10	5.6683	.2151	5.3691	.3767	5.5473	.7183	5.4099	.6002
580	.5425E-02	10	5.4888	.0346	5.6287	.0710	5.8922	.1390	5.4235	.1034
600	.6447E-02	7	5.5819	.0525	5.6990	.1218	6.3419	.2456	5.4910	.1698

From individual observations

± indicates standard deviations

TABLE 7.2(b) REGIONAL GROUP VELOCITIES AFTER WU (1972) - 3 REGIONS

INDIVIDUAL OBSERVATIONS ARE EQUALLY WEIGHTED

Period (Seconds)	Standard Deviation	Number of Observations	Ocean + Ridge u	±	Continent u	±	Island Arc u	±
50	.8163E-02	31	3.9356	.1134	3.7428	.2208	3.5001	.5551
60	.6786E-02	32	3.9860	.0920	3.7807	.1838	3.9528	.5937
70	.6627E-02	37	3.8975	.0781	3.8304	.1614	3.5042	.4091
80	.8022E-02	46	3.7848	.0763	3.8533	.1658	3.5825	.4115
90	.6057E-02	49	3.7841	.0553	3.8359	.1205	3.5792	.2915
100	.6430E-02	63	3.7105	.0470	3.8709	.1122	3.4767	.2152
110	.5110E-02	64	3.7588	.0341	3.8201	.0867	3.6973	.1943
120	.4723E-02	67	3.7392	.0303	3.7483	.0762	3.9701	.1897
130	.5952E-02	69	3.7201	.0376	3.6548	.0864	4.1415	.2495
140	.7767E-02	72	3.6823	.0464	3.6305	.1103	4.0948	.3075
150	.6478E-02	74	3.6457	.0354	3.7206	.0930	3.7540	.2132
160	.5646E-02	74	3.6366	.0306	3.6636	.0791	3.9196	.1936
170	.5626E-02	69	3.6439	.0319	3.6351	.0797	3.8063	.2011
180	.3953E-02	62	3.6365	.0232	3.5995	.0555	3.9776	.1716
190	.5630E-02	47	3.5906	.0416	3.5550	.0923	4.2495	.3454
200	.5706E-02	50	3.6010	.0369	3.5699	.0844	3.9161	.2616
220	.4692E-02	26	3.5611	.0352	3.5349	.1038	3.9579	.2463
240	.6397E-02	25	3.5979	.0532	3.4627	.1358	4.1819	.3750
260	.2336E-02	25	3.6213	.0813	3.5471	.0534	3.9168	.1202
280	.1388E-02	22	3.6394	.0117	3.6949	.0446	3.6109	.0625
300	.2650E-02	10	3.6457	.0745	3.7828	.1566	3.6329	.2581
320	.1531E-02	10	3.8037	.0469	3.9528	.0988	3.6670	.1519
340	.1732E-02	10	3.9333	.0567	4.2231	.1276	3.4249	.1499
360	.4356E-02	10	4.1129	.1559	4.1254	.3062	3.0540	.2997
380	.3728E-02	10	4.0049	.1265	4.5016	.3120	4.0808	.4580
400	.4164E-02	10	4.0683	.1458	4.7344	.3855	4.5340	.6315

contd.

TABLE 7.2(b) REGIONAL GROUP VELOCITIES AFTER WU (1972) - 3 REGIONS INDIVIDUAL OBSERVATIONS ARE EQUALLY WEIGHTED (contd)

Period (Seconds)	Standard Deviation	Number of Observations	Ocean + Ridge		Continent		Island Arc	
			u	±	u	±	u	±
420	.3556E-02	10	4.4084	.1462	4.7245	.3278	4.9499	.6427
440	.2741E-02	10	4.4887	.1169	4.7454	.2549	4.7350	.4533
460	.6319E-02	10	4.5048	.2714	4.6172	.5564	5.9040	1.6250
480	.2209E-02	10	4.8049	.1079	5.0730	.2348	5.2609	.4511
500	.2338E-02	10	5.1047	.1289	4.8930	.2312	5.3090	.4861
520	.1459E-02	10	4.8074	.0714	5.2272	.1647	4.7137	.2392
540	.2837E-02	10	5.0827	.1551	5.5816	.3650	4.9424	.5112
560	.3164E-02	10	5.6683	.2151	5.3691	.3767	5.5473	.7183
580	.5425E-03	10	5.4888	.0346	5.6287	.0710	5.8922	.1390
600	.6447E-03	7	5.5819	.0525	5.6990	.1218	6.3419	.2456

From individual observations weighted equally

± indicates standard deviations

TABLE 7.2(c) REGIONAL GROUP VELOCITIES AFTER WU (1972) - 2 REGIONS

Period	Standard Deviation	Number of Observations	Ocean + Ridge		Continent + Arc	
			u	±	u	±
50	.7194E-02	31	4.0328	.0718	3.7298	.1031
60	.6332E-02	32	3.9467	.0608	3.8005	.0928
70	.6832E-02	37	3.8635	.0590	3.7361	.0894
80	.7963E-02	46	3.8108	.0553	3.8031	.0937
90	.6092E-02	49	3.8075	.0411	3.7880	.0705
100	.6934E-02	63	3.7846	.0416	3.8188	.0725
110	.5179E-02	64	3.7599	.0287	3.7868	.0522
120	.4298E-02	67	3.7217	.0230	3.7883	.0420
130	.5277E-02	69	3.7130	.0280	3.7797	.0503
140	.7143E-02	72	3.6805	.0364	3.7599	.0669
150	.6426E-02	74	3.6513	.0301	3.7389	.0567
160	.5553E-02	74	3.6313	.0254	3.7338	.0471
170	.5568E-02	69	3.6310	.0265	3.6651	.0485
180	.4447E-02	62	3.6125	.0218	3.6556	.0407
190	.6465E-02	47	3.5717	.0380	3.7132	.0709
200	.5851E-02	50	3.5864	.0317	3.6282	.0583
220	.5104E-02	26	3.5520	.0341	3.6532	.0720
240	.6868E-02	25	3.5683	.0488	3.6132	.0965
260	.2488E-02	25	3.5983	.0173	3.6044	.0349
280	.1372E-02	22	3.6421	.0106	3.6653	.0216
300	.2403E-02	10	3.6927	.0473	3.7564	.0838
320	.1532E-02	10	3.8145	.0322	3.8461	.0560
340	.2775E-02	10	3.9595	.0627	3.8954	.1040
360	.4872E-02	10	4.2744	.1284	3.7208	.1666
380	.3521E-02	10	4.1103	.0858	4.4119	.1693
400	.3671E-02	10	4.1362	.0906	4.7142	.2015
420	.3307E-02	10	4.3101	.0886	4.7306	.1828
440	.2351E-02	10	4.4651	.0676	4.7234	.1295
460	.5693E-02	10	4.4696	.1640	5.0063	.3524
480	.2487E-02	10	4.6737	.0784	0434	.1563
500	.2664E-02	10	4.9310	.0934	4.9308	.1600
520	.1956E-02	10	4.9540	.0693	5.1230	.1268
540	.2576E-02	10	5.1099	.0970	5.3391	.1814
560	.2705E-02	10	5.6150	.1230	5.4033	.1951
580	.5466E-02	10	5.4681	.0236	5.7114	.0440
600	.8284E-02	7	5.5358	.0418	5.9352	.0818

From individual observations.

± indicates standard deviations.

TABLE 7.2(d) REGIONAL GROUP VELOCITIES AFTER WU (1972) - 4 REGIONS

DERIVED FROM PATH AVERAGE GROUP VELOCITIES

Period	Standard Deviation	Number of Paths	Ocean		Continent		Island Arc		Ridge	
			u	±	u	±	u	±	u	±
50	.1820E-02	6	3.7146	.0759	4.1473	.1908	3.4692	.1991	4.3618	.3157
60	.6083E-02	7	3.8038	.2497	3.9116	.3408	3.9764	.8135	3.6681	.7285
70	.4802E-02	8	3.7751	.1892	3.9961	.2795	3.5157	.4873	3.8446	.6317
80	.6166E-02	9	3.7475	.1856	3.9519	.2844	3.1269	.4816	4.3273	1.0007
90	.7094E-02	9	3.6972	.2078	4.0717	.3473	2.8997	.4765	4.6019	1.3022
100	.5318E-02	9	3.7250	.1581	3.9965	.2508	3.0950	.4069	4.1400	.7900
110	.1769E-02	9	3.7641	.0537	3.9083	.0798	3.4802	.1711	3.6547	.2048
120	.1164E-02	9	3.7656	.0354	3.8231	.0503	3.6679	.1251	3.5338	.1260
130	.1897E-02	9	3.7199	.0563	3.9380	.0869	3.6686	.2040	3.3106	.1802
140	.8390E-03	9	3.6764	.0243	3.9530	.0387	3.5770	.0858	3.3740	.0828
150	.1240E-02	9	3.6759	.0359	3.9057	.0558	3.4055	.1149	3.4663	.1291
160	.2108E-02	9	3.6450	.0600	3.8313	.0914	3.2439	.1772	3.6749	.2468
170	.1884E-02	9	3.6413	.0535	3.7047	.0764	3.3769	.1716	3.6370	.2160
180	.1488E-02	9	3.6410	.0423	3.6914	.0599	3.5013	.1457	3.4968	.1577
190	.1265E-02	9	3.6214	.0356	3.6632	.0501	3.4680	.1215	3.5002	.1343
200	.1352E-02	9	3.5996	.0375	3.6483	.0531	3.4484	.1284	3.5528	.1479
210	.8494E-03	9	3.5696	.0232	3.6523	.0335	3.3927	.0781	3.6289	.0970
220	.8013E-03	8	3.5395	.0218	3.6527	.0453	3.3790	.0740	3.6948	.0986
230	.7219E-03	8	3.5860	.0201	3.6058	.0398	3.4712	.0704	3.5375	.0814
240	.1406E-02	8	3.6194	.0400	3.5603	.0755	3.6532	.1518	3.3699	.1439
250	.1169E-02	8	3.6362	.0335	3.5848	.0636	3.5308	.1178	3.4237	.1235
260	.1480E-02	8	3.6478	.0427	3.5933	.0810	3.5883	.1542	3.3860	.1530
270	.2412E-02	8	3.6588	.0700	3.7012	.1400	3.7844	.2794	3.2022	.2229
280	.1439E-02	8	3.6411	.0414	3.7689	.0866	3.3069	.1273	3.7203	.1795
290	.1257E-02	8	3.6877	.0371	3.9724	.0840	3.1310	.0996	3.6054	.1472
300	.3123E-02	7	3.6291	.1240	3.7994	.2569	3.7500	.3746	3.8533	.4209
310	.2755E-02	7	3.6662	.1117	3.7211	.2174	3.8690	.3518	3.9582	.3918
320	.6196E-03	7	3.7821	.0267	4.0534	.0580	3.6755	.0714	3.7517	.0791

(contd.)

TABLE 7.2(d) (contd.)

Period	Standard Deviation	Number of Paths	Ocean		Continent		Island Arc		Ridge	
			u	±	u	±	u	±	u	±
330	.3552E-02	7	3.8270	.1568	4.1934	.3559	3.4590	.3625	4.0833	.5375
340	.3387E-02	7	3.9638	.1605	4.1925	.3392	3.4545	.3448	3.8555	.4570
350	.4502E-02	7	4.0873	.2267	4.0459	.4199	3.3245	.4244	4.0919	.6841
360	.6353E-02	7	4.0932	.3209	4.2702	.6601	3.0601	.5074	4.5292	1.1828
370	.6589E-02	7	3.9464	.3094	4.0374	.6120	5.0490	1.4327	4.3131	1.1125
380	.2225E-02	7	4.0968	.1126	4.1884	.2224	4.3797	.3641	4.7151	.4490
390	.4091E-02	7	4.0415	.2015	4.7501	.5260	4.2184	.6210	4.5133	.7564
400	.3371E-02	7	4.0930	.1703	5.0309	.4861	4.2592	.5215	4.2975	.5650
410	.3463E-02	7	4.2310	.1869	4.7833	.4515	4.6841	.6481	4.2212	.5600
420	.2563E-02	7	4.2765	.1414	5.0120	.3669	5.0134	.5495	3.9677	.3663
430	.4010E-02	7	4.2335	.2167	5.1953	.6168	4.7017	.7561	4.2381	.6538
440	.2994E-02	7	4.3696	.1724	4.9751	.4223	4.5584	.5307	4.4315	.5337
450	.5511E-02	7	4.8746	.3948	4.4225	.6142	5.7007	1.5275	3.8069	.7249
460	.6080E-02	7	4.7628	.4159	4.2272	.6191	6.1809	1.9812	4.4524	1.0940
470	.5540E-02	7	4.6450	.3604	4.4240	.6178	6.4100	1.9413	4.5878	1.0582
480	.2765E-02	7	4.7531	.1883	5.2721	.4379	5.4117	.6906	4.0428	.4101
490	.2861E-02	7	4.9856	.2144	5.0362	.4135	5.7334	.8022	3.9259	.4003
500	.2994E-02	7	5.0748	.2325	4.8348	.3988	5.5488	.7862	4.3907	.5238
510	.1742E-02	7	4.6810	.1151	5.7816	.3319	4.4718	.2972	5.2884	.4423
520	.1518E-02	6	4.8000	.1407	5.4923	.2677	4.5154	.2674	5.4797	.4816

TABLE 7.2(e) REGIONAL GROUP VELOCITIES AFTER WU (1972) - 3 REGIONS

DERIVED FROM PATH AVERAGE GROUP VELOCITIES

Period	Standard Deviation	Number of Paths	Ocean + Mid-Ocean Ridge		Continent		Island Arc	
			u	±	u	±	u	±
50	.2913E-02	6	3.8185	.0969	4.1302	.3025	3.6833	.3112
60	.4994E-02	7	3.7768	.1374	3.9211	.2761	3.9085	.5294
70	.4164E-02	8	3.7881	.1115	3.9910	.2370	3.5434	.3409
80	.5739E-02	9	3.8251	.1266	3.9539	.2649	3.2961	.4064
90	.6771E-02	9	3.8106	.1482	4.0747	.3320	3.1206	.4298
100	.4904E-02	9	3.7824	.1058	3.9980	.2315	3.2181	.3311
110	.1621E-02	9	3.7471	.0343	3.9079	.0731	3.4365	.1248
120	.1298E-02	9	3.7286	.0272	3.8223	.0560	3.5634	.1074
130	.2250E-02	9	3.6516	.0452	3.9363	.1030	3.4741	.1770
140	.1318E-02	9	3.6272	.0261	3.9517	.0608	3.4384	.1016
150	.1328E-02	9	3.6425	.0266	3.9048	.0598	3.3201	.0954
160	.1888E-02	9	3.6495	.0379	3.8314	.0818	3.2548	.1304
170	.1685E-02	9	3.6406	.0337	3.7047	.0683	3.3752	.1252
180	.1423E-02	9	3.6184	.0281	3.6908	.0572	3.4387	.1096
190	.1209E-02	9	3.6025	.0236	3.6628	.0479	3.4160	.0919
200	.1220E-02	9	3.5925	.0237	3.6481	.0479	3.4286	.0935
210	.7865E-03	9	3.5785	.0152	3.6525	.0310	3.4170	.0599
220	.9026E-03	8	3.5602	.0188	3.6630	.0507	3.4360	.0733
230	.6523E-03	8	3.5793	.0137	3.6026	.0354	3.4522	.0535
240	.1572E-02	8	3.5827	.0331	3.5436	.0826	3.5437	.1358
250	.1309E-02	8	3.6053	.0279	3.5706	.0698	3.4449	.1069
260	.1645E-02	8	3.6093	.0351	3.5757	.0880	3.4789	.1369
270	.2820E-02	8	3.5882	.0596	3.6670	.1587	3.5667	.2468
280	.1278E-02	8	3.6518	.0280	3.7743	.0762	3.3336	.0977
290	.1129E-02	8	3.6761	.0250	3.9661	.0743	3.1061	.0749
300	.2691E-02	7	3.6682	.0826	3.7891	.2194	3.8547	.2803

(contd.)

TABLE 7.2(e) (contd.)

Period	Standard Deviation	Number of Paths	Ocean + Mid-Ocean Ridge		Continent		Island Arc	
			u	±	u	±	u	±
310	.2495E-02	7	3.7164	.0786	3.7086	.1949	4.0101	.2812
320	.5188E-03	7	3.7765	.0169	4.0550	.0484	3.6625	.0488
330	.3031E-02	7	3.8715	.1036	4.1804	.3007	3.5500	.2677
340	.2792E-02	7	3.9435	.0990	4.1981	.2793	3.4167	.2284
350	.3676E-02	7	4.0882	.1401	4.0457	.3416	3.3259	.2849
360	.5339E-92	7	4.1668	.2114	4.2510	.5478	3.1629	.3743
370	.5503E-02	7	4.0089	.2017	4.0216	.5053	5.3100	1.0875
380	.2501E-02	7	4.1977	.1005	4.1633	.2461	4.6760	.3832
390	.3617E-02	7	4.1205	.1401	4.7240	.4583	4.4372	.4992
400	.2822E-02	7	4.1290	.1097	5.0177	.4034	4.3567	.3754
410	.2828E-02	7	4.2292	.1153	4.7838	.3674	4.6786	.4338
420	.2310E-02	7	4.2164	.0936	5.0326	.3321	4.8149	.3753
430	.3274E-02	7	4.2343	.1339	5.1950	.5017	4.7043	.5079
440	.2451E-02	7	4.3808	.1073	4.9716	.3439	4.5886	.3617
450	.5457E-02	7	4.6362	.2675	4.4737	.6201	4.9648	.9428
460	.5026E-02	7	4.7027	.2535	4.2389	.5128	5.9381	1.2421
470	.4525E-02	7	4.6344	.2217	4.4263	.5034	6.3605	1.2831
480	.3005E-02	7	4.6047	.1453	5.3187	.4827	4.9631	.5188
490	.3729E-02	7	4.7505	.1919	5.0987	.5504	5.0280	.6607
500	.2948E-02	7	4.9338	.1637	4.8673	.3965	5.1521	.5484
510	.1939E-02	7	4.7816	.1011	5.7450	.3633	4.7050	.3008
520	.1713E-02	6	4.9449	.1045	5.4250	.2918	4.7082	.2777
530	.1053E-02	5	4.9909	.0675	5.4324	.1991	4.7502	.3528
540	.4565E-02	5	5.1841	.3157	5.8888	1.0141	4.2019	1.1964

TABLE 7.2(f) REGIONAL GROUP VELOCITIES AFTER WU (1972) - 2 REGIONS

DERIVED FROM PATH AVERAGE GROUP VELOCITIES

Period	Standard Deviations	Number of Paths	Ocean + Mid-Ocean Ridge		Continent + Island Arc	
			u	±	u	±
50	.2754E-02	6	3.8450	.0877	3.9316	.1426
60	.4325E-02	7	3.7766	.1186	3.9178	.1848
70	.4107E-02	8	3.7882	.1100	3.8558	.1686
80	.5855E-02	9	3.7970	.1247	3.7816	.1961
90	.7301E-02	9	3.7693	.1532	3.8090	.2480
100	.5468E-02	9	3.7495	.1135	3.7885	.1838
110	.2344E-02	9	3.7283	.0481	3.7893	.0788
120	.1541E-02	9	3.7185	.0315	3.7599	.0510
130	.2699E-02	9	3.6344	.0526	3.8203	.0922
140	.2293E-02	9	3.6083	.0441	3.8217	.0784
150	.2632E-02	9	3.6197	.0509	3.7539	.0868
160	.2951E-02	9	3.6260	.0573	3.6825	.0937
170	.2057E-02	9	3.6273	.0400	3.6240	.0633
180	.1657E-02	9	3.6084	.0319	3.6301	.0511
190	.1504E-02	9	3.5927	.0287	3.6034	.0457
200	.1438E-02	9	3.5838	.0273	3.5956	.0435
210	.1213E-02	9	3.5693	.0228	3.5959	.0367
220	.1177E-02	8	3.5627	.0244	3.5843	.0420
230	.8183E-03	8	3.5809	.0172	3.5512	.0287
240	.1406E-02	8	3.5827	.0296	3.5437	.0491
250	.1267E-02	8	3.6067	.0270	3.5279	.0438
260	.1517E-02	8	3.6103	.0324	3.5430	.0529
270	.2549E-02	8	3.5892	.0538	3.6331	.0934
280	.2018E-02	8	3.6569	.0442	3.6156	.0733
290	.3463E-02	8	3.6863	.0770	3.6321	.1269
300	.2340E-02	7	3.6635	.0664	3.8168	.1139
310	.2358E-02	7	3.6944	.0681	3.8316	.1157
320	.1309E-02	7	3.8066	.0401	3.8776	.0658
330	.3285E-02	7	3.9227	.1069	3.8858	.1657
340	.3502E-02	7	4.0118	.1192	3.8246	.1712
350	.4040E-02	7	4.1603	.1479	3.7035	.1851
360	.5962E-02	7	4.2812	.2311	3.7066	.2737
370	.5530E-02	7	3.9335	.1810	4.4864	.3719
380	.2488E-02	7	4.1612	.0911	4.3678	.1586
390	.3197E-02	7	4.1390	.1159	4.5971	.2257
400	.2820E-02	7	4.1703	.1037	4.7124	.2092
410	.2459E-02	7	4.2359	.0933	4.7383	.1844
420	.2044E-02	7	4.2291	.0773	4.9373	.1664
420	.2986E-02	7	4.2630	.1148	4.9735	.2468
440	.2262E-02	7	4.4065	.0929	4.8005	.1741
450	.4837E-02	7	4.5988	.2164	4.6710	.3526
460	.5367E-02	7	4.5873	.2389	4.8289	.4182
470	.5056E-02	7	4.5203	.2186	5.0868	.4372
480	.2677E-02	7	4.6275	.1213	5.1608	.2382
490	.3232E-02	7	4.7554	.1546	5.0683	.2774
500	.2607E-02	7	4.9120	.1331	4.9850	.2165
510	.2454E-02	7	4.8524	.1222	5.2496	.2259
520	.2061E-02	6	4.9934	.1208	5.1018	.1905
530	.1227E-02	5	4.9850	.0783	5.2399	.1390
540	.4092E-02	5	5.1678	.2806	5.3403	.4813

Sec. 7.4 REGIONAL SHEAR VELOCITY MODELS FOR OCEANS AND CONTINENTS

Models for upper mantle shear velocities have been derived by controlled Monte Carlo inversion of pure path continental and oceanic group velocities. Group velocities for periods between 50 and 300 seconds for each continental or oceanic region in Table 7.2(a), (b) and (c) were integrated to give phase velocities which were used in conjunction with the group velocities to calculate group velocities corrected for anelastic dispersion as described in Section 5.2. The corrected group velocities were used in each inversion. Starting model bounds for oceanic models were taken from the type 2 bounds described in Chapter 5 (Table 5.3) with shear velocity limits of the 220 to 412 km layer extending from 4.5 to 4.6 km/s. Starting model bounds for continental models are shown in Figure 7.8(c).

Models resulting from inversions of oceanic group velocities are shown in Figure 7.7. These models all have high velocity lids (beginning at a depth of 70 km) in which shear velocities are not well controlled but range from 4.4 to 4.65 km/s. The shear velocities in the low velocity zone in 2, 3, and 4 region oceanic models (Figures 7.7(a) to (c)) vary from 4.2 to 4.4 km/s. Models generated from a constant velocity starting model (4.4 km/s for upper mantle layers) produced several models with low velocity layers ranging from 4.2 to 4.4 km/s in which two of the layers had approximately the same velocity. Two such models are shown in Figure 7.7 (e). This indicates that the 2 regions data do not closely constrain the depth of the low velocity zone. A series of models derived from the type 1 bounds used in Chapter 5 (Table 5.3) are also shown in Figure 7.7(d). These models have 100 km thick high velocity lids with shear velocities which range from 4.4 to 5.4 km/s. No oceanic model was produced which did not contain a low velocity zone.

Models produced from continental data sets are shown in Figure 7.8. These models have been derived from starting model bounds which

Figure 7.7(a) SHEAR VELOCITY MODELS DERIVED FROM PURE PATH OCEANIC GROUP VELOCITIES FROM A 4 REGION PURE PATH SEPARATION -

Models have been produced by controlled Monte Carlo inversion of pure path oceanic group velocities listed in Table 7.2(a). These models are listed in Table 7.3(a). The thickness of the lithospheres of these models is 70 km.

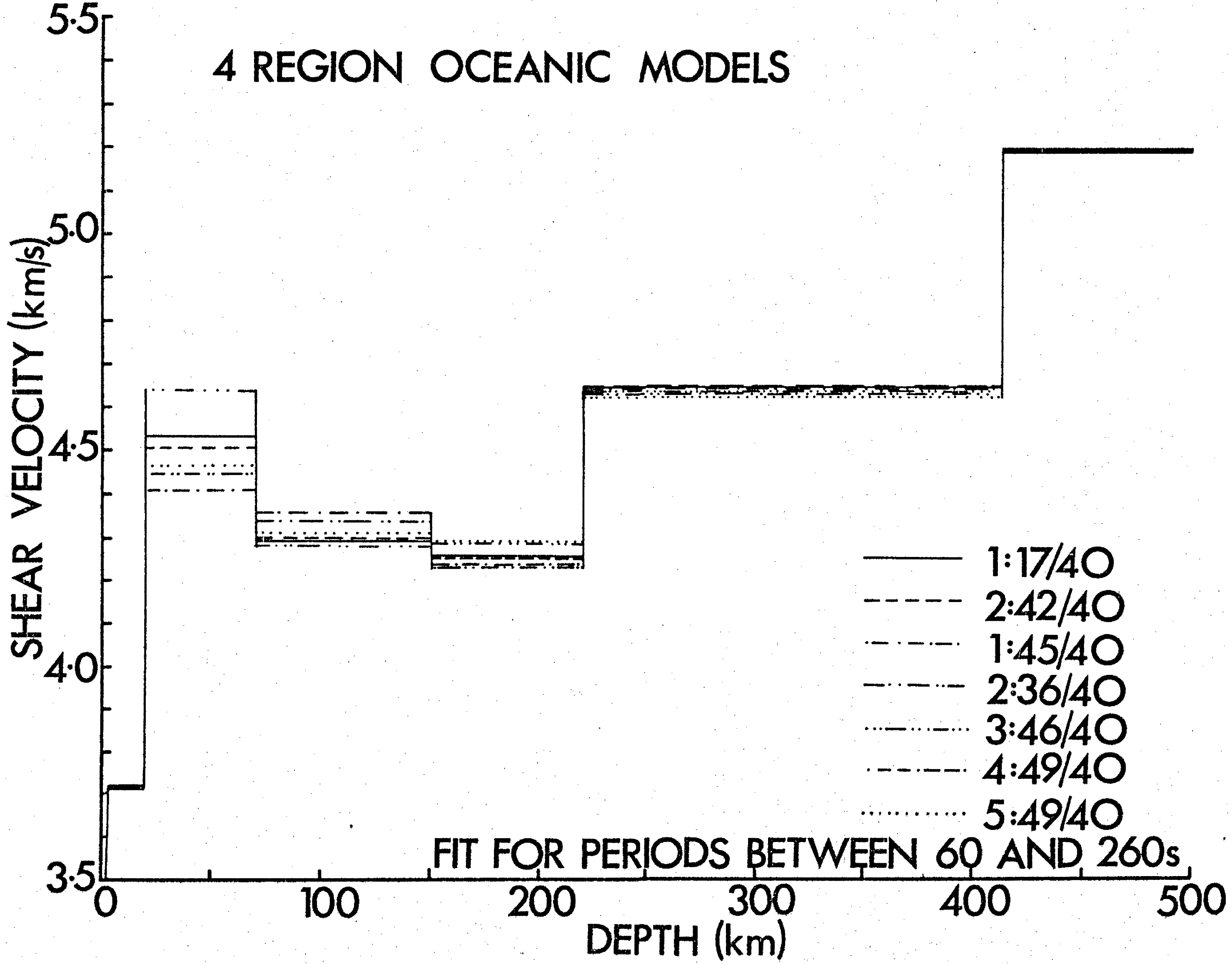
4 REGION OCEANIC MODELS
SHEAR VELOCITY (km/s)
5·5
5·0
4·5
4·0
3·5
0
100
200
300
400
500
DEPTH (km)
1:17/4O
2:42/4O
1:45/4O
2:36/4O
3:46/4O
4:49/4O
5:49/4O
FIT FOR PERIODS BETWEEN 60 AND 260s

Figure 7.7(b) SHEAR VELOCITY MODELS DERIVED FROM PURE PATH OCEANIC-RIDGE GROUP VELOCITIES FROM A 3 REGION PURE PATH SEPARATION -

Models have been produced by controlled Monte Carlo inversion of pure path ocean-ridge group velocities listed in Table 7.2(b). These models are listed in Table 7.3(b).

The thickness of the lithosphere of these models is 70 km.

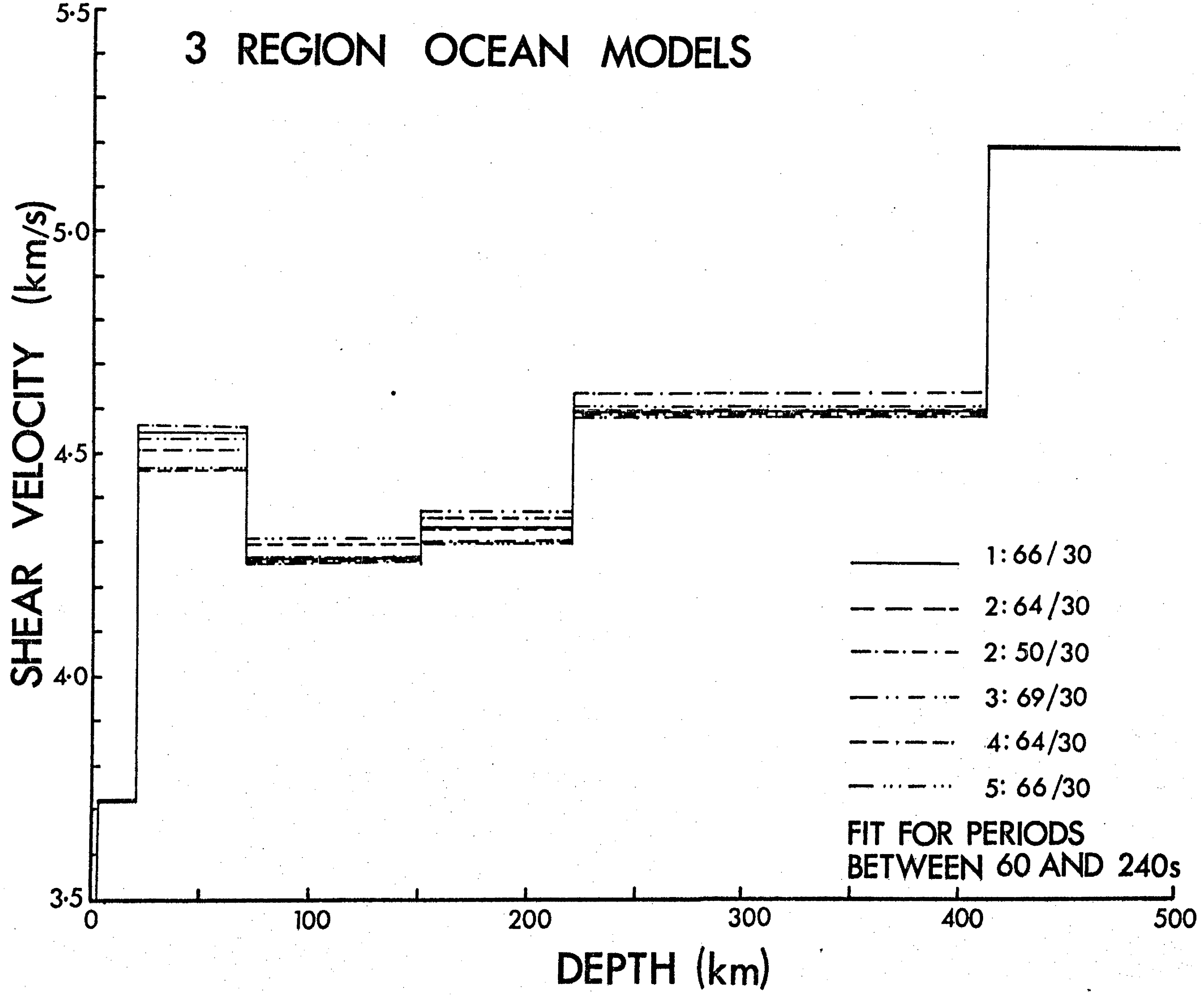
3 REGION OCEAN MODELS
SHEAR VELOCITY (km/s)
5·5
5·0
4·5
4·0
3·5
0
100
200
300
400
500
DEPTH (km)
1: 66/30
2: 64/30
2: 50/30
3: 69/30
4: 64/30
5: 66/30
FIT FOR PERIODS
BETWEEN 60 AND 240s

Figure 7.7(c) SHEAR VELOCITY MODELS DERIVED FROM PURE PATH OCEANIC-RIDGE GROUP VELOCITIES FROM A 2 REGION PURE PATH SEPARATION - Models have been produced by controlled Monte Carlo inversion of pure path ocean-ridge group velocities listed in Table 7.2(c). These models are listed in Table 7.3(c). The thickness of the lithosphere os these models is 70 km.

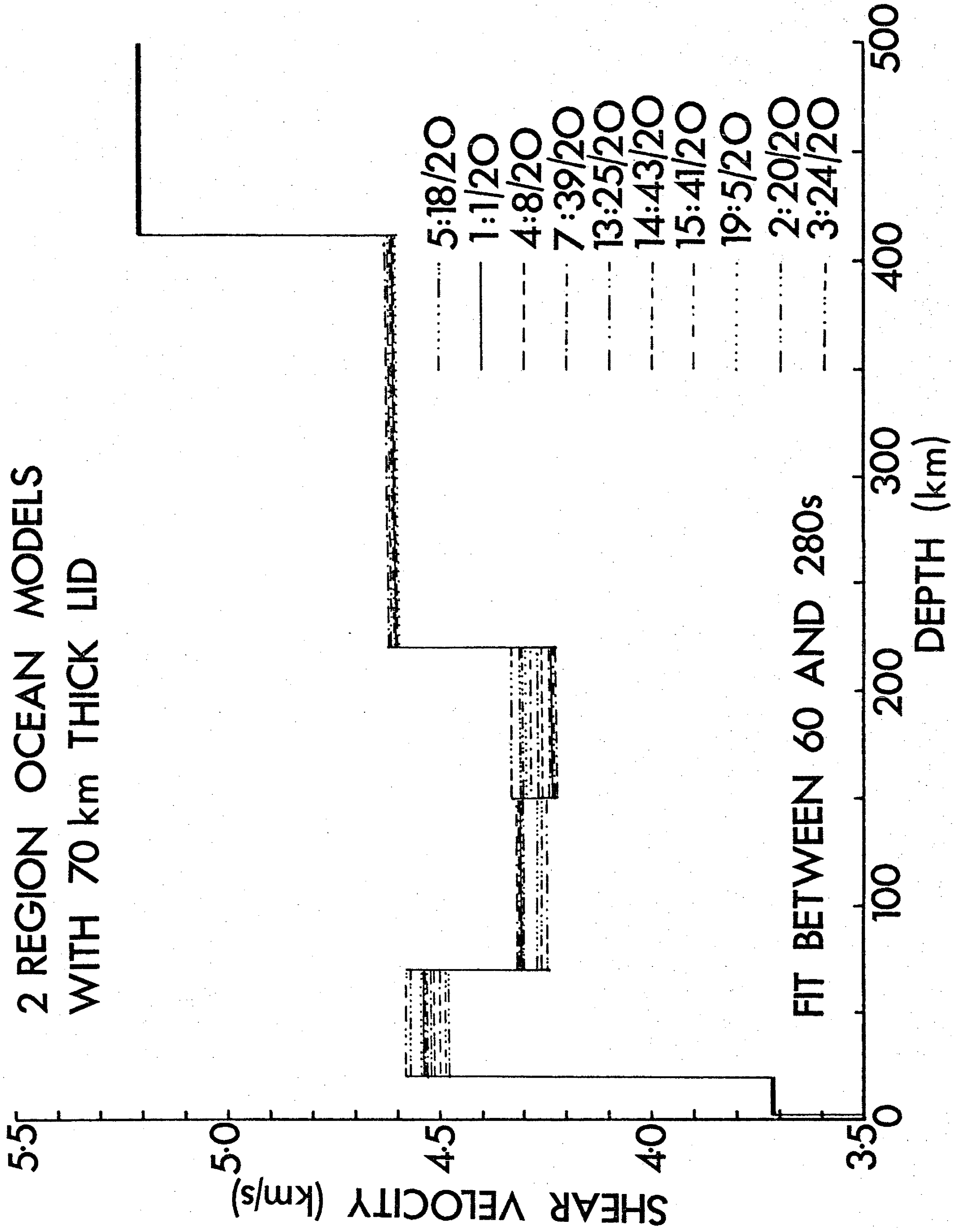
2 REGION OCEAN MODELS
WITH 70 km THICK LID
FIT BETWEEN 60 AND 280s
5:18/20
1:1/20
4:8/20
7:39/20
13:25/20
14:43/20
15:41/20
19:5/20
2:20/20
3:24/20
SHEAR VELOCITY (km/s)
5·5
5·0
4·5
4·0
3·5
DEPTH (km)
0
100
200
300
400
500

Figure 7.7(d) SHEAR VELOCITY MODELS WITH 100 KM THICK LITHOSPHERE LIDS DERIVED FROM PURE PATH OCEANIC-RIDGE GROUP VELOCITIES FROM A 2 REGION PURE PATH SEPARATION -

Models have been produced by controlled Monte Carlo inversion of pure path ocean-ridge group velocities listed in Table 7.2(c). Models are listed in Table 7.3(d).

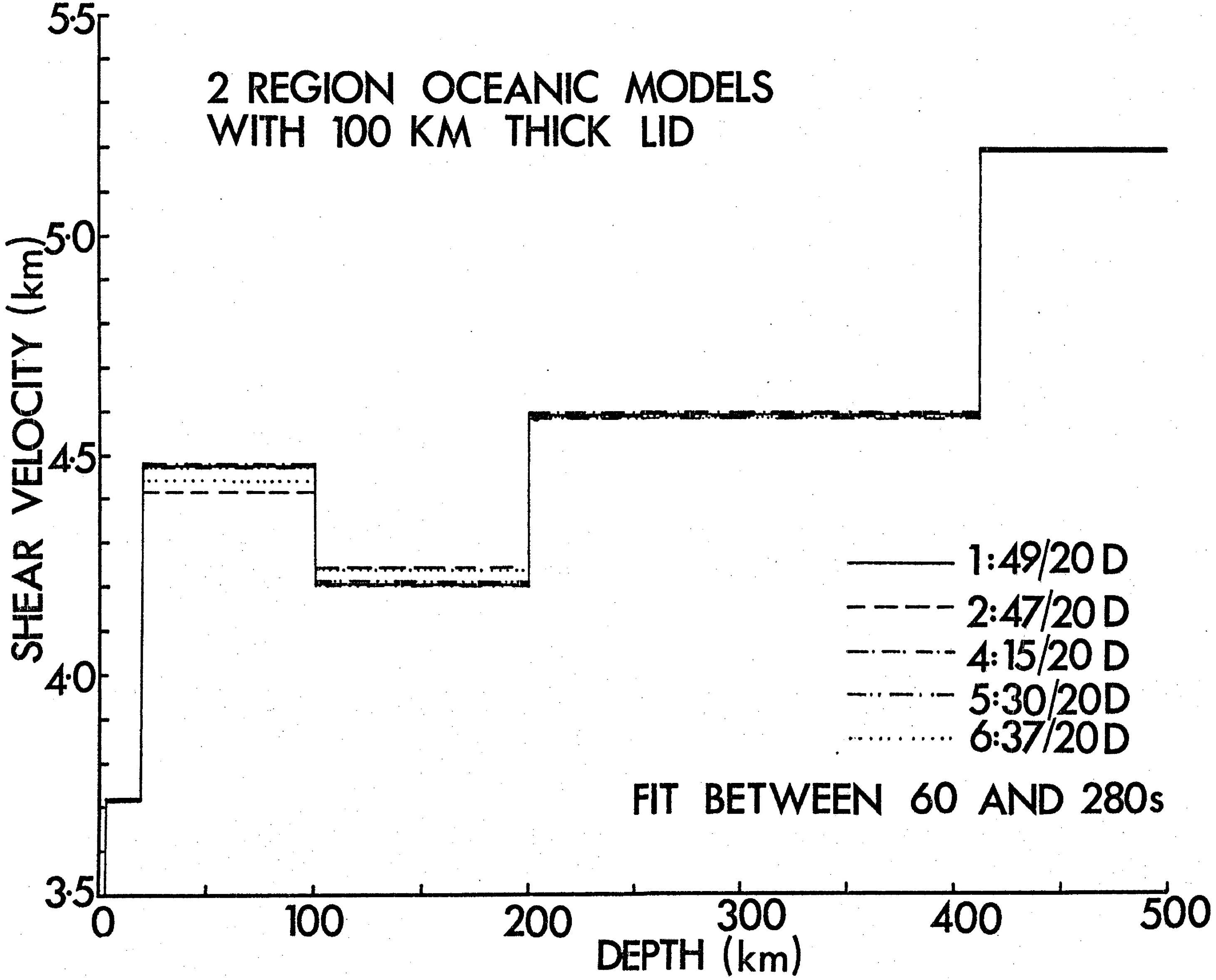
2 REGION OCEANIC MODELS
WITH 100 KM THICK LID
SHEAR VELOCITY (km)
5·5
5·0
4·5
4·0
3·5
0
100
200
300
400
500
DEPTH (km)
1:49/20 D
2:47/20 D
4:15/20 D
5:30/20D
6:37/20D
FIT BETWEEN 60 AND 280s

Figure 7.7(e) SHEAR VELOCITY MODELS DERIVED FROM A CONSTANT VELOCITY STARTING MODEL -

A starting model with a constant (4.4 km/s) upper mantle velocity was refined by controlled Monte Carlo inversion. Models which fit the pure path ocean-ridge group velocities from a 2 region pure path separation (Table 7.2(c)) are listed in Table 7.4(a).

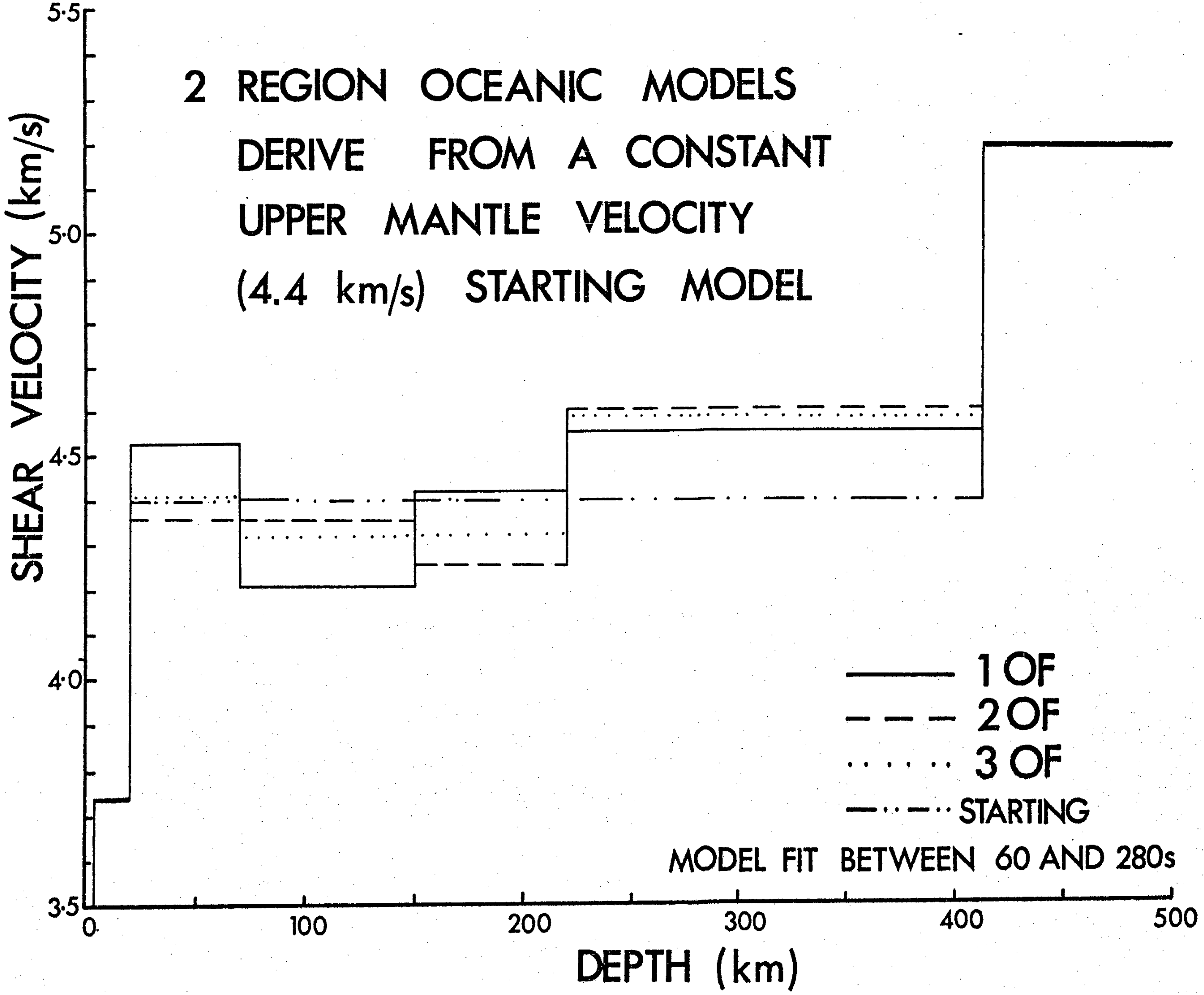
2 REGION OCEANIC MODELS
DERIVE FROM A CONSTANT
UPPER MANTLE VELOCITY
(4.4 km/s) STARTING MODEL
SHEAR VELOCITY (km/s)
5·5
5·0
4·5
4·0
3·5
DEPTH (km)
0
100
200
300
400
500
1 OF
2 OF
3 OF
STARTING
MODEL FIT BETWEEN 60 AND 280s

TABLE 7.3(a) OCEANIC MODELS BASED ON 5.08M

4 REGION OCEANIC MODELS

Depth to Top of Layer	Compressional Velocity	Density	Shear Velocity (km/s)							
(km)	(km/s)	(g/cc)	1:17/40	2:42/40	1:45/40	2:36/40	3:46/40	4:49/40	5:49/40	6:49/40
0.0	1.44	1.02	0.0	0.0	0.0	0.0	0.0	0.0	0.0	0.0
3.0	6.50	2.79	3.72	3.72	3.72	3.72	3.72	3.72	3.72	3.72
21.0	8.37	3.40	4.531	4.503	4.404	4.470	4.642	4.563	4.469	4.483
70.0	8.37	3.40	4.289	4.297	4.355	4.346	4.277	4.282	4.311	4.286
150.0	8.37	3.40	4.256	4.253	4.238	4.235	4.278	4.316	4.287	4.322
220.0	8.37	3.40	4.648	4.647	4.642	4.640	4.631	4.617	4.621	4.608
412.5	9.50	3.80	5.200	5.200	5.200	5.200	5.200	5.200	5.200	5.200
χ^2_r			.348	.347	.311	.304	.307	.300	.302	.313

MODELS FIT FOR PERIODS BETWEEN 60 AND 260s.

TABLE 7.3(b) OCEANIC MODELS BASED ON 5.08M

3 REGION OCEANIC MODELS

Depth to Top of Layer	Shear Velocity (km/s)					
	1:66/30	2:50/30	2:64/30	3:69/30	4:64/30	5:66/30
0.0	0.0	0.0	0.0	0.0	0.0	0.0
3.0	3.72	3.72	3.27	3.72	3.72	3.72
21.0	4.542	4.569	4.459	4.530	4.510	4.460
70.0	4.268	4.297	4.297	4.254	4.264	4.313
150.0	4.334	4.300	4.328	4.369	4.360	4.298
220.0	4.593	4.638	4.597	4.587	4.590	4.605
412.5	5.200	5.200	5.200	5.200	5.200	5.200
χ^2_r	.374	.822	.380	.359	.364	.395

MODELS FIT FOR PERIODS BETWEEN 60 AND 260s.

TABLE 7.3(c) OCEANIC MODELS BASED ON 5.08M.

2 REGION OCEANIC MODELS

Depth to Top of Layer (km)	Shear Velocity (km/s)									
	5:18/20	1:1/20	4:8/20	7:39/20	13:25/20	14:43/20	15:41/20	19:5/20	2:25/20	3:24/20
0.0	0.0	0.0	0.0	0.0	0.0	0.0	0.0	0.0	0.0	0.0
3.0	3.72	3.72	3.72	3.72	3.72	3.72	3.72	3.72	3.72	3.72
21.0	4.576	4.536	4.517	4.526	4.520	4.496	4.530	4.545	4.486	4.491
70.0	4.268	4.303	4.310	4.304	4.302	4.316	4.301	4.295	4.306	4.248
150.0	4.298	4.280	4.252	4.235	4.228	4.289	4.249	4.290	4.265	4.328
220.0	4.594	4.600	4.605	4.611	4.616	4.596	4.606	4.598	4.605	4.593
412.5	5.200	5.200	5.200	5.200	5.200	5.200	5.200	5.200	5.200	5.200
χ^2_r	.160	.191	.191	.256	.299	.211	.213	.188	.158	.228

COMPRESSIONAL VELOCITIES AND DENSITIES ARE SHOWN IN FIGURE 7. (a).

MODELS FIT FOR PERIODS BETWEEN 60 AND 280s.

TABLE 7.3(d)

2 REGION OCEANIC MODELS WITH A 100 KM THICK LID

Depth to Top of Layer (km)	Compressional Velocity (km/s)	Density (g/cc)	Shear Veloicity (km/s) 1:49/20D	2:47/20D	4:15/20D	5:30/20D	6:37/20D
0.0	1.44	1.02	0.0	0.0	0.0	0.0	0.0
3.0	6.50	2.79	3.72	3.72	3.72	3.72	3.72
21.0	8.37	3.40	4.474	4.414	4.477	4.476	4.445
100.0	8.37	3.40	4.203	4.245	4.202	4.210	4.240
200.0	8.37	3.40	4.594	4.592	4.593	4.592	4.582
412.5	9.50	3.80	5.200	5.200	5.200	5.200	5.200
χ^2_r			.211	.172	.218	.192	.172

MODELS FIT FOR PERIODS BETWEEN 60 AND 280S.

TABLE 7. 4(a)

2 REGION OCEANIC MODELS GENERATED FROM A CONSTANT VELOCITY (4.4 km/s) UPPER MANTLE

Depth to Top of Layer (km)	Compressional Velocity (km/s)	Density (g/cc)	Shear Velocity (km/s) 1OF	2OF	3OF
0.0	1.44	1.02	0.0	0.0	0.0
3.0	6.50	2.79	3.72	3.72	3.72
21.0	8.37	3.40	4.527	4.358	4.410
70.0	8.37	3.40	4.207	4.361	4.321
150.0	8.37	3.40	4.423	4.252	4.322
220.0	8.37	3.40	4.565	4.607	4.589
412.5	9.50	3.80	5.200	5.200	5.200
χ^2_r			.264	.177	.259

ALL MODELS FIT FOR PERIODS BETWEEN 60 AND 260S,

TABLE 7. 4(b)

2 REGION CONTINENTAL MODELS GENERATED FROM A CONSTANT VELOCITY (4.4 km/s) UPPER MANTLE

Depth to Top of Layer (km)	Compressional Velocity (km/s)	Density (g/cc)	Shear Velocity (km/s) 1CF	2CF	3CF	4CF
0.0	6.20	2.79	3.60	3.60	3.60	3.60
20.0	6.50	3.35	3.82	3.82	3.82	3.82
40.0	8.00	3.40	4.357	4.311	4.270	4.285
75.0	8.20	3.40	4.486	4.491	4.552	4.473
200.0	8.40	3.40	4.586	4.641	4.552	4.726
317.0	8.90	3.40	4.715	4.638	4.731	4.544
412.5	9.50	3.80	5.20	5.200	5.200	5.200
χ^2_r			.247	.185	.261	.239

ALL MODELS FIT FOR PERIODS BETWEEN 60 AND 260S,

Figure 7.8(a) SHEAR VELOCITY MODELS DERIVED FROM PURE PATH CONTINENTAL GROUP VELOCITIES FROM A 4 REGION PURE PATH SEPARATION - Models have been produced by a controlled Monte Carlo inversion of pure path continental group velocities listed in Table 7.2(a). Models produced from this data are listed in Table 7.5(a).

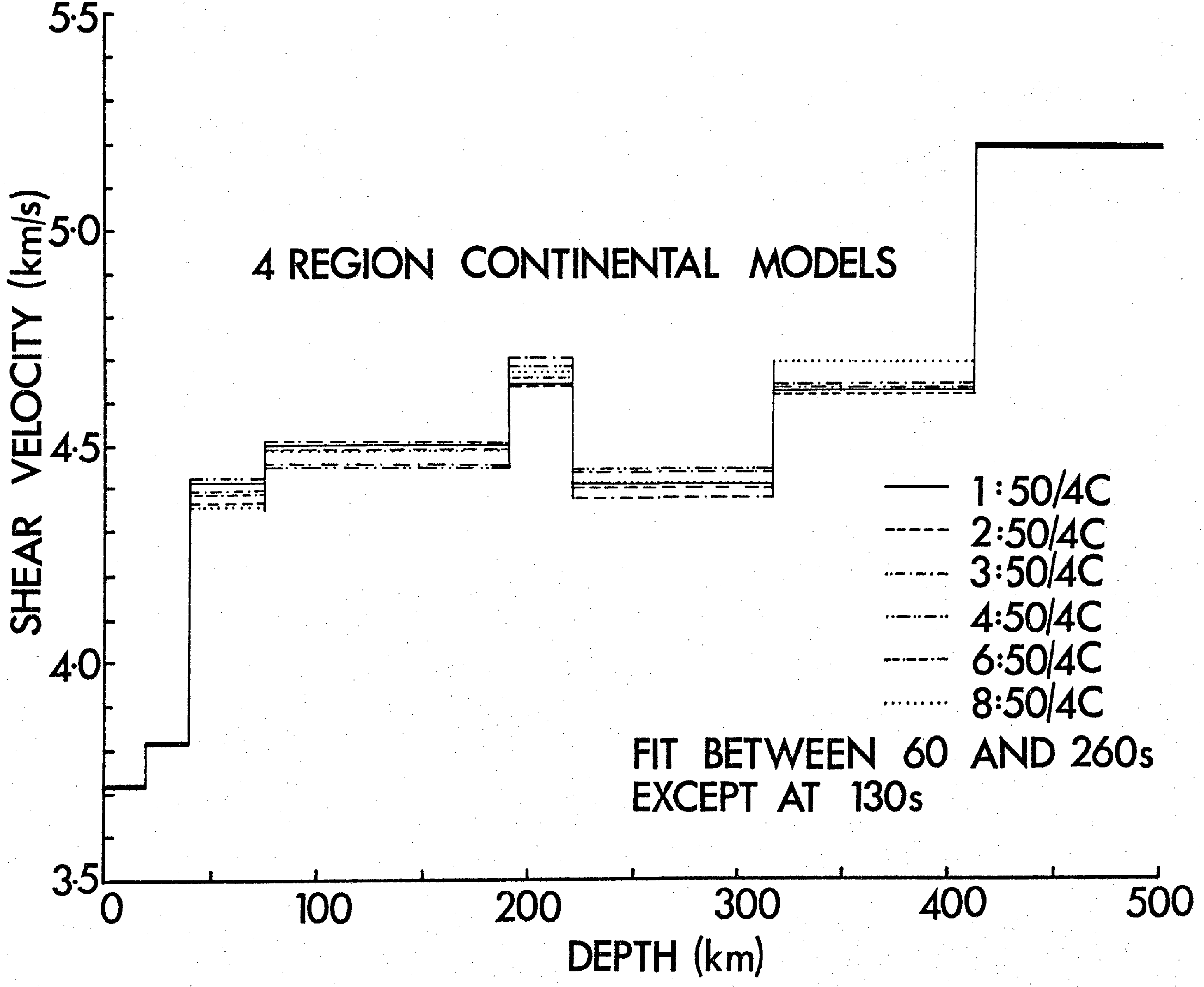
4 REGION CONTINENTAL MODELS
SHEAR VELOCITY (km/s)
5·5
5·0
4·5
4·0
3·5
DEPTH (km)
0
100
200
300
400
500
1:50/4C
2:50/4C
3:50/4C
4:50/4C
6:50/4C
8:50/4C
FIT BETWEEN 60 AND 260s
EXCEPT AT 130s

Figure 7.8(b) SHEAR VELOCITY MODELS DERIVED FROM PURE PATH CONTINENTAL GROUP VELOCITIES FROM A 3 REGION PURE PATH SEPARATION - Models have been produced by a controlled Monte Carlo inversion of pure path continental group velocities listed in Table 7.2(b). Models produced from this data are listed in Table 7.5(b).

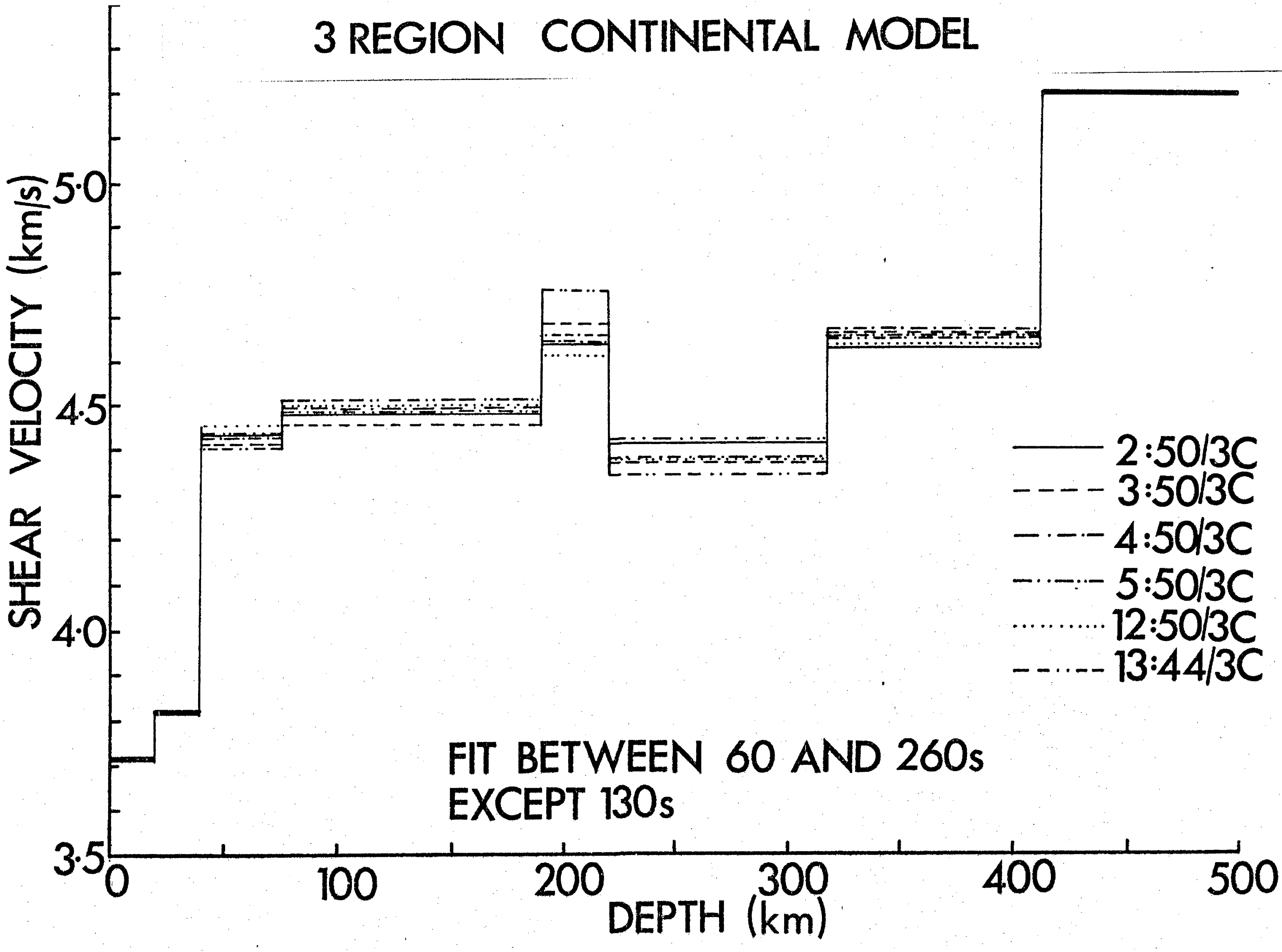
3 REGION CONTINENTAL MODEL
SHEAR VELOCITY (km/s)
5·0
4·5
4·0
3·5
0
100
200
300
400
500
DEPTH (km)
2:50/3C
3:50/3C
4:50/3C
5:50/3C
12:50/3C
13:44/3C
FIT BETWEEN 60 AND 260s
EXCEPT 130s

Figure 7.8(c) SHEAR VELOCITY MODELS DERIVED FROM PURE PATH CONTINENTAL-ARC GROUP VELOCITIES FROM A 2 REGION PURE PATH SEPARATION - Models have been produced by a controlled Monte Carlo inversion of pure path continental-arc group velocities listed in Table 7.2(c). Models produced from this data are listed in Table 7.5(c).

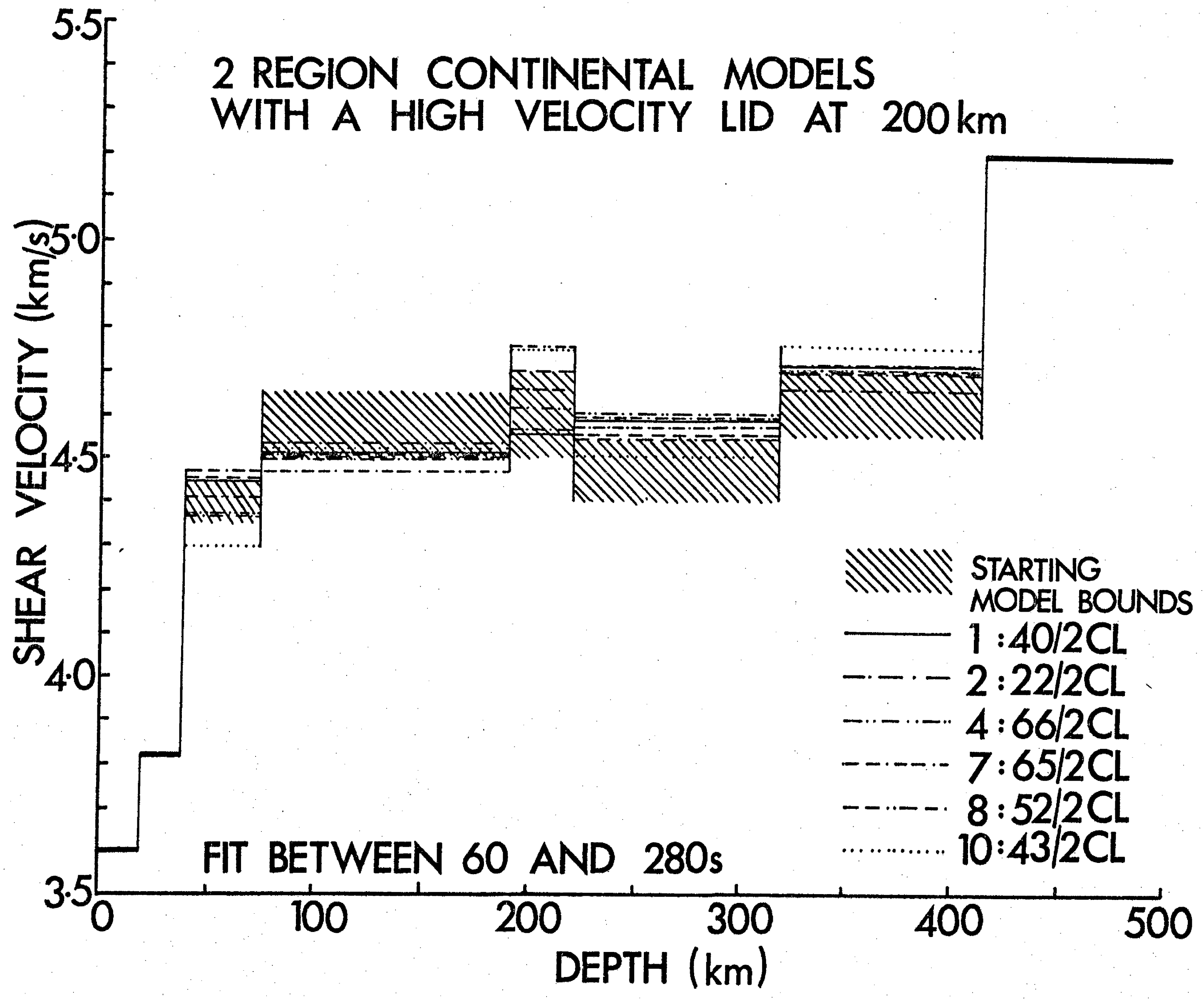
2 REGION CONTINENTAL MODELS
WITH A HIGH VELOCITY LID AT 200 km
FIT BETWEEN 60 AND 280s
SHEAR VELOCITY (km/s)
3·5
4·0
4·5
5·0
5·5
DEPTH (km)
0
100
200
300
400
500
STARTING MODEL BOUNDS
1 : 40/2CL
2 : 22/2CL
4 : 66/2CL
7 : 65/2CL
8 : 52/2CL
10 : 43/2CL

Figure 7.8(d) SHEAR VELOCITY MODELS DERIVED FROM PURE PATH CONTINENTAL-ARC GROUP VELOCITIES FROM A 2 REGION PURE PATH SEPARATION - Models have been produced by a controlled Monte Carlo inversion of pure path continental-arc group velocities listed in Table 7.2(c). Models have high velocity lithospheric lids at a depth of 190 to 220 km but the lid is not present in all models. Table 7.5(d) contains a listing of all models produced which successfully fit the continental-arc data.

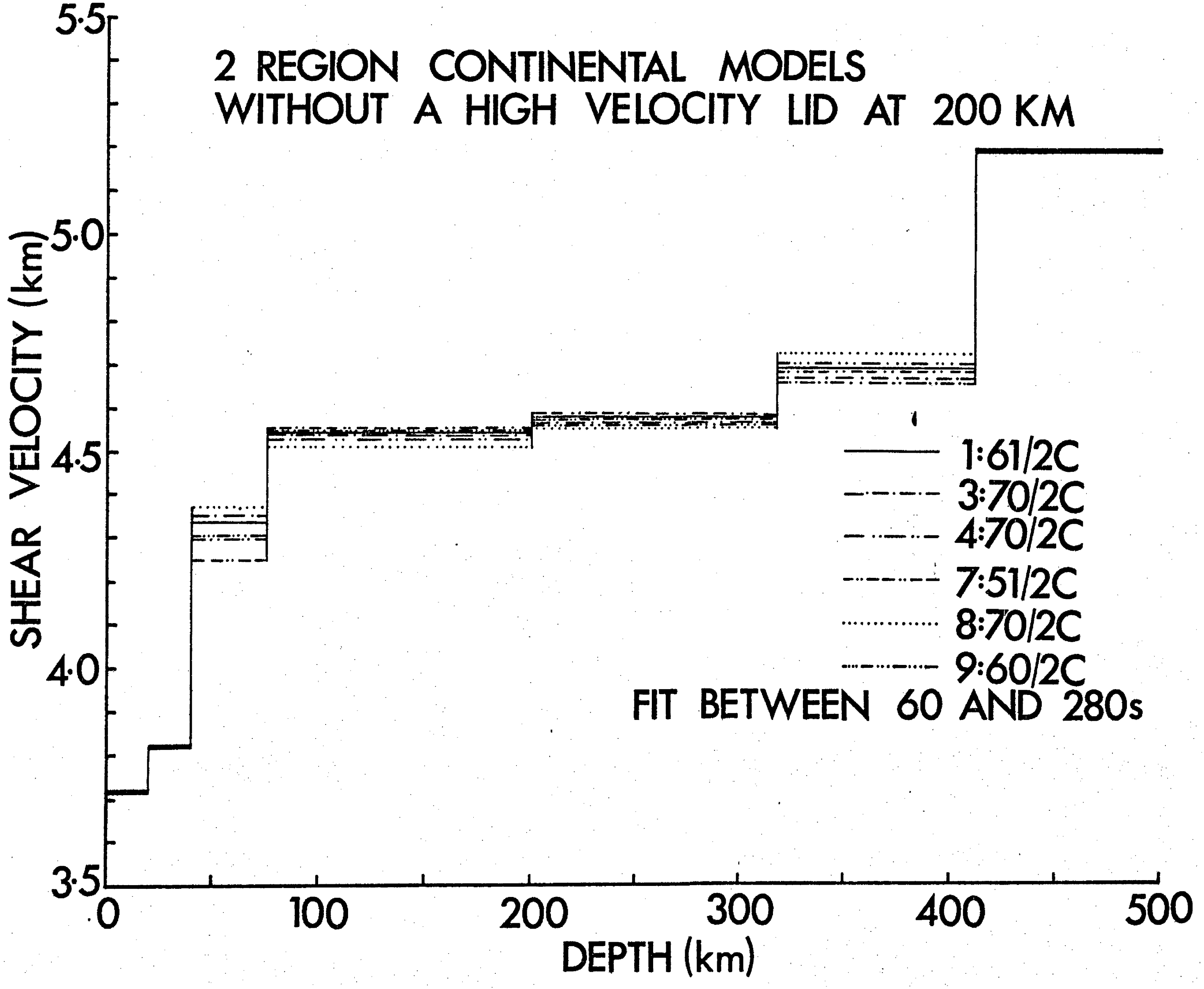
2 REGION CONTINENTAL MODELS
WITHOUT A HIGH VELOCITY LID AT 200 KM
SHEAR VELOCITY (km)
5·5
5·0
4·5
4·0
3·5
0
100
200
300
400
500
DEPTH (km)
1:61/2C
3:70/2C
4:70/2C
7:51/2C
8:70/2C
9:60/2C
FIT BETWEEN 60 AND 280s

Figure 7.8(e) SHEAR VELOCITY MODELS FOR CONTINENTS DERIVED FROM A CONSTANT UPPER MANTLE VELOCITY STARTING MODEL -

Models have been produced by Monte Carlo inversion of pure path continental-arc group velocities (Table 4.2(c)) using a starting model with a constant velocity (4.4 km/s) upper mantle. Models with and without low velocity zones fit the group velocities for continental-arc provinces (Table 7.4(b)).

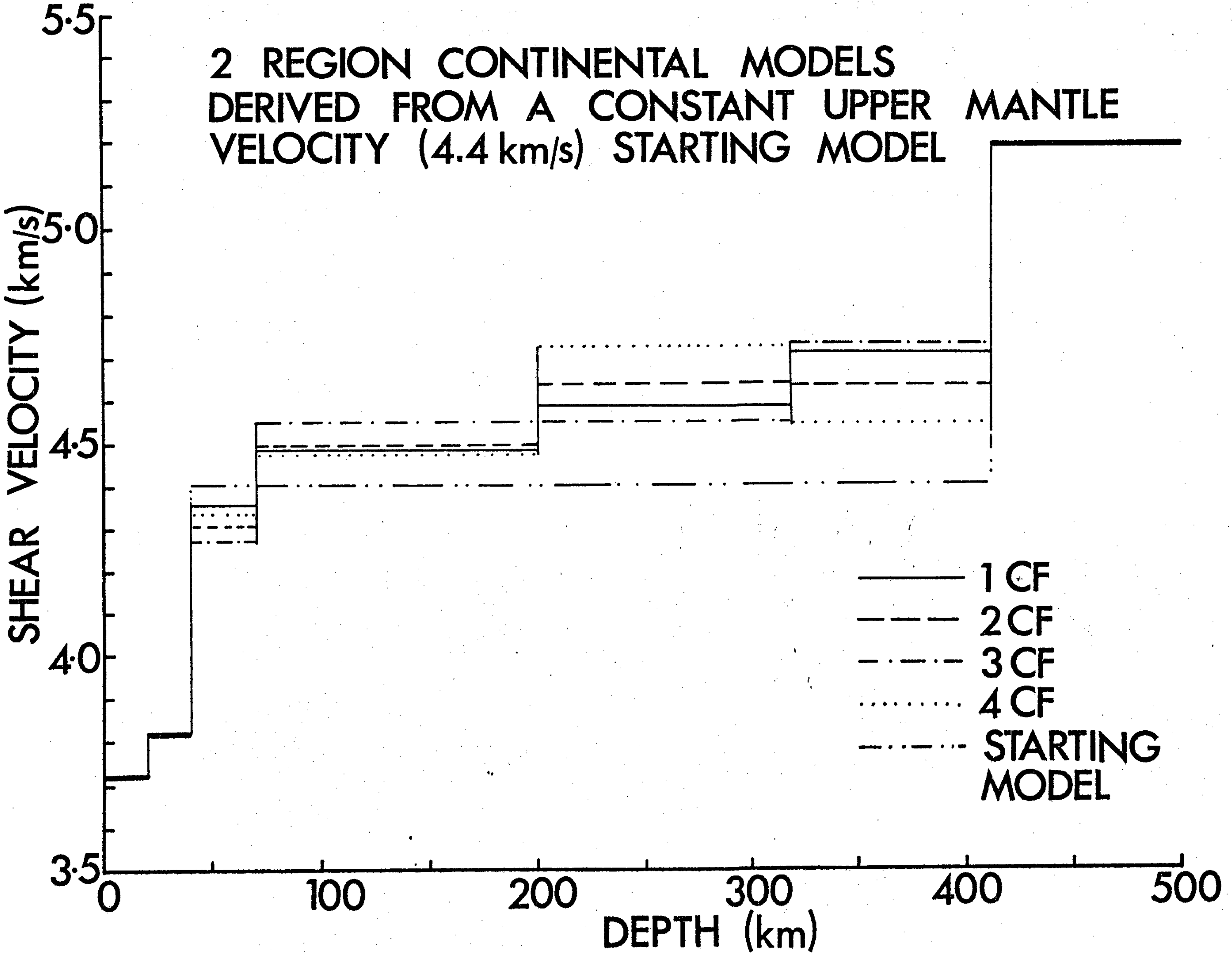
2 REGION CONTINENTAL MODELS
DERIVED FROM A CONSTANT UPPER MANTLE
VELOCITY (4.4 km/s) STARTING MODEL
SHEAR VELOCITY (km/s)
5·5
5·0
4·5
4·0
3·5
0
100
200
300
400
500
DEPTH (km)
1 CF
2 CF
3 CF
4 CF
STARTING MODEL

TABLE 7.5(a) CONTINENTAL MODELS WITH HIGH VELOCITY LIDS AT 200 KM

4 REGION CONTINENTAL MODELS

Depth to Top of Layer (km)	Compressional Velocity (km/s)	Density (g/cc)	Shear Velocity (km/s) 1:50/4C	2:50/4C	3:50/4C	4:50/4C	6:50/4C	8:50/4C
0.0	6.20	2.79	3.72	3.72	3.72	3.72	3.72	3.72
20.0	6.50	3.35	3.82	3.82	3.82	3.82	3.82	3.82
40.0	8.00	3.40	4.415	4.369	4.392	4.428	4.389	4.366
75.0	8.20	3.40	4.506	4.489	4.467	4.450	4.510	4.489
190.0	8.60	3.40	4.646	4.645	4.711	4.684	4.659	4.672
220.0	8.40	3.40	4.413	4.403	4.435	4.444	4.376	4.413
317.0	8.90	3.40	4.624	4.622	4.640	4.636	4.712	4.695
412.5	9.50	3.80	5.200	5.200	5.200	5.200	5.200	5.200
χ^2_r			.688	.657	.518	.493	.536	.471

MODELS FIT FOR PERIODS BETWEEN 60 AND 260S EXCEPT 130S.

TABLE 7.5(b)   CONTINENTAL MODELS WITH HIGH VELOCITY LIDS AT 200 KM

3 REGION CONTINENTAL MODELS

Depth to Top of Layer (km)	Shear Velocity (km/s) 2:50/3C	3:50/3C	4:50/3C	5:50/3C	12:50/3C	13:44/3C
0.0	3.72	3.72	3.72	3.72	3.72	3.72
20.0	3.82	3.82	3.82	3.82	3.82	3.82
40.0	4.431	4.416	4.429	4.428	4.455	4.408
75.0	4.484	4.458	4.493	4.483	4.498	4.516
190.0	4.631	4.683	4.635	4.757	4.613	4.661
220.0	4.413	4.373	4.384	4.423	4.400	4.343
317.0	4.625	4.666	4.667	4.661	4.635	4.649
412.5	5.200	5.200	5.200	5.200	5.200	5.200
χ^2_r	.584	.528	.550	.490	.621	.747

COMPRESSIONAL VELOCITIES AND DENSITIES ARE SHOWN IN FIGURE 7. (a).

MODELS FIT FOR PERIODS BETWEEN 60 AND 260S EXCEPT 130S.

Table 7.5(c) CONTINENTAL MODELS WITH HIGH VELOCITY LIDS AT 200 KM

2 REGION CONTINENTAL MODELS

Depth to Top of Layer (km)	Shear Velocity (km/s)						
	1:40/2CL	2:22/2CL	4:66/2CL	7:65/2CL	8:52/2CL	10:43/2CL	17:52/2CL
0.0	3.72	3.72	3.72	3.72	3.72	3.72	3.72
20.0	3.82	3.82	3.82	3.82	3.82	3.82	3.82
40.0	4.396	4.367	4.368	4.470	4.406	4.296	4.370
75.0	4.511	4.527	4.509	4.469	4.500	4.514	4.469
190.0	4.561	4.550	4.613	4.655	4.757	4.756	4.674
220.0	4.588	4.574	4.603	4.591	4.548	4.503	4.618
317.0	4.712	4.707	4.662	4.706	4.699	4.769	4.657
412.0	5.200	5.200	5.200	5.200	5.200	5.200	5.200
χ^2_r	.206	.257	.224	.185	.227	.179	.169

COMPRESSIONAL VELOCITIES AND DENSITIES ARE SHOWN IN FIGURE 7. (a).

MODELS FIT FOR ALL PERIODS BETWEEN 60 AND 280S.

TABLE 7.5(d)

2 REGION CONTINENTAL MODELS WITHOUT A LID AT 200 KM.

Depth to Top of Layer (km)	Compressional Velocity (km/s)	Density (g/cc)	Shear Velocity (km/s) 1:61/2C	3:70/2C	4:70/2C	7:51/2C	8:70/2C	9:60/2C
0.0	6.20	2.79	3.60	3.60	3.60	3.60	3.60	3.60
20.0	6.50	3.35	3.82	3.82	3.82	3.82	3.82	3.82
40.0	8.00	3.40	4.335	4.355	4.298	4.252	4.371	4.304
75.0	8.20	3.40	4.544	4.531	4.527	4.556	4.513	4.556
200.0	8.40	3.40	4.582	4.568	4.568	4.582	4.560	4.567
317.0	8.90	3.40	4.694	4.670	4.666	4.689	4.727	4.707
412.5	9.50	3.80	5.200	5.200	5.200	5.20	5.200	5.200
χ^2_r			.293	.388	.369	.296	.262	.317

MODELS FIT FIR PERIODS BETWEEN 60 AND 280S.

encourage the formation of a low velocity layer between depths of 220 and 317 km (see Figure 7.8(c)). The lid velocity in these models is not well controlled and varies from 4.55 to 4.8 km/s. In continental models derived from 3 and 4 region pure path separations the shear velocity in the low velocity zone is lower than the shear velocity in the layer immediately shallower than the lid (70 to 150 km). This seems to indicate that even without the high velocity lid, low velocity zone models may be able to fit the pure path continental velocities. Continental models derived from 2 region pure path separations (ocean basin and mid-ocean ridge zones form one region while island arc zones are combined with continents) tend to have low velocity zone velocities which are higher than velocities in the layer immediately above the high velocity lid (Figure 7.8(c)). Models without a high velocity lid derived from this 2 region data set do not have low velocity zones but have a distinct increase in velocity with depth (Figure 7.8(d)). Models which do contain a low velocity channel, but not a high velocity lid are possible as is shown in Figure 7.8(e). In this figure model 4CF contains a low velocity zone between 317 and 412 km. A wide range of models will produce acceptable fits to the 2 region continental group velocities so that no definitive conclusion can be drawn from these data concerning the presence of a low velocity zone beneath the continents. However, models derived from pure path group velocities for 3 and 4 region separations indicate that such zones are likely even if a high velocity lid is absent.

Sec. 7.5 Q^{-1}REGIONALIZATION

The regionalization of the specific attenuation, Q^{-1} is difficult because Q^{-1} is calculated from four observed quantities - group velocities and the amplitudes of two wave phases. Amplitude measurements become inaccurate when signal to noise ratios approach 2 or are smaller. Since the ratio of signal to noise ratios approach 2 or are smaller. Since the ratio of amplitudes is involved, errors are easily compounded. The group velocity regionalization presented in Sec. 7.3 for equally weighted observations depends only on quantities involving single measurements. Pure path Q^{-1}_R's shown in Figure 7.9(b) were calculated directly from individual attenuation coefficients and the corresponding great circle group velocity (which was calculated from the group velocities of two phases as described in Sec. 4.2.2). Each Q^{-1} estimate has received equal weight in the analysis. Large standard errors and lack of smoothness in the pure path Q^{-1}_R result since the multiple linear regression analysis is a least squares fitting process which is heavily influenced by large deviations from the mean. An alternative regionalization of Q^{-1}_R is presented in Figure 7.9(a) in which the path averaged attenuation coefficients and group velocities have been smoothed over 20 second averaging windows. There is no gain in using a pure path separation method in which single observations are equally weighted because the attenuation coefficient measurements are fundamentally great circle measurements so that short nearly pure paths as used in the group velocity regionalization (Sec. 7.3) are not possible.

The pure path separations of Q^{-1}_R presented in Figure 7.9(a) show that most of the dissipation of Rayleigh wave energy occurs beneath the oceans. Attenuation beneath continental regions is low. Island Arc regions have high attenuation at short periods (50 to 100 seconds). At periods between 125 and 175 seconds Q^{-1}_R are negative. These negative Q^{-1}_R values are probably caused by significant lateral refraction and defocusing for path 1 (Figure 5.1) which has the highest proportion of island arc (Table 7.1).

Figure 7.9(a) PURE PATH Q_R^{-1} DERIVED USING THE WU (1972) REGIONALIZATION - Pure path Q_R^{-1}, calculated using the Wu (1972) regionalization with equal weighting of averages for paths, are shows for

4 regions: ocean, continent, arc and ridge provinces (upper right panel),

3 regions: ocean-ridge, continent and arc provinces (upper right panel), and

2 regions: ocean-ridge and continental-arc provinces (lower right panel).

Continental and oceanic Q_R^{-1} determined in the 4 region regression analysis are shown in the lower left panel. Symbols used for regional Q_R^{-1} are the same as the symbols used for group velocities for similar regions in Figure 7.5(a).

WU(1972) REGIONALIZATION PATH AVERAGES - 4 REGIONS

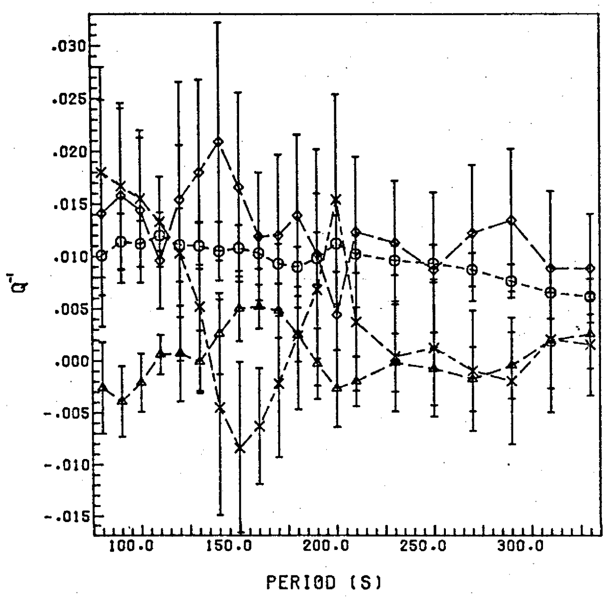

WU(1972) REGIONALIZATION PATH AVERAGES - 3 REGIONS

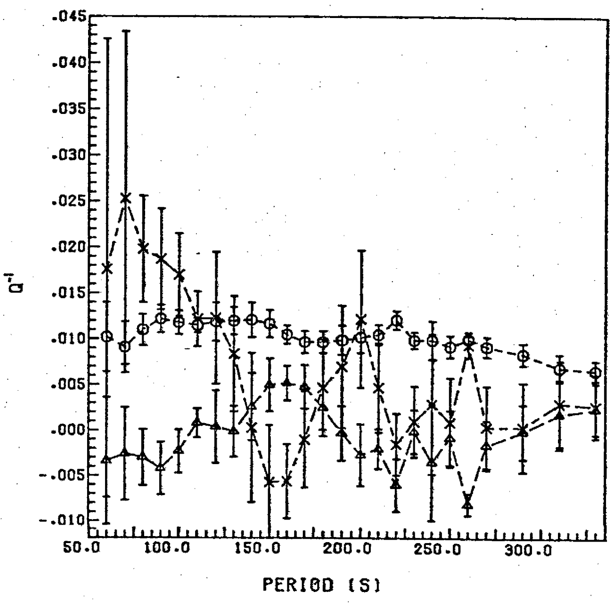

WU(1972) REGIONALIZATION PATH AVERAGES - 4 REGIONS O & C

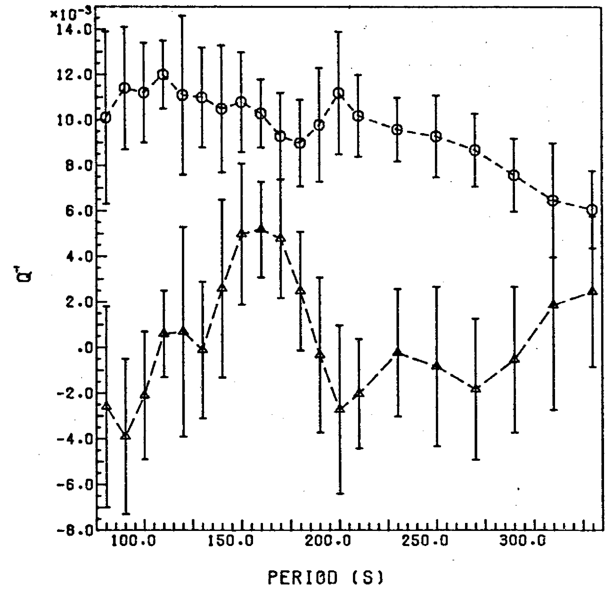

WU(1972) REGIONALIZATION PATH AVERAGES - 2 REGIONS

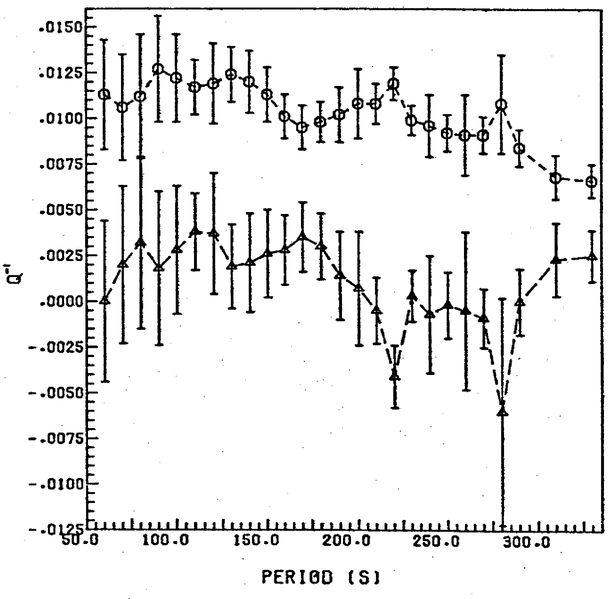

Figure 7.9(b) PURE PATH Q^{-1}_R DERIVED USING THE WU (1972) REGIONALIZATION - Pure path Q^{-1}_R, calculated using the Wu (1972) regionalization with equal weighting of Q^{-1}_R determined from individual pairs of estimates of amplitudes and group velocities, are shown for

4 regions: ocean, continent, arc and ridge provinces (upper left panel),

3 regions: ocean-ridge, continent and arc provinces (upper right panel), and

2 regions: ocean-ridge and continental-arc provinces (lower right panel).

Continental and oceanic Q^{-1}_R determined in the 4 region regression analysis are shown in the lower left panel. Symbols used for pure path Q^{-1}_R are the same as described for pure path group velocities for similar regions in Figure 7.5(a).

WU(1972) REGIONALIZATION INDIVIDUAL OBS - 4 REGIONS

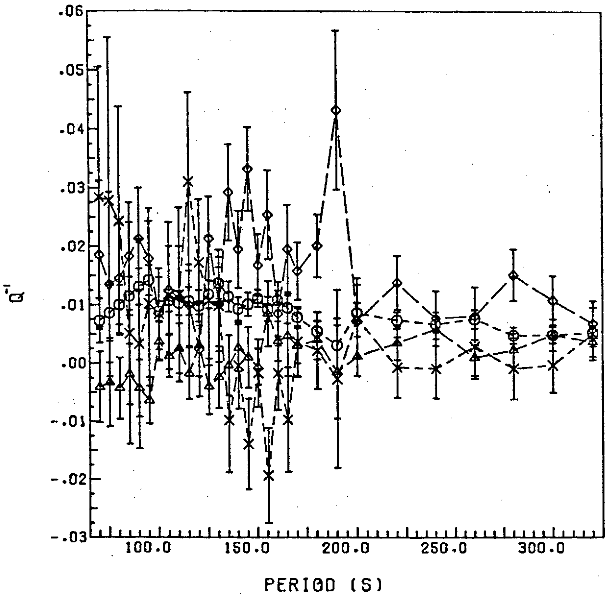

WU(1972) REGIONALIZATION INDIVIDUAL OBS - 3 REGIONS

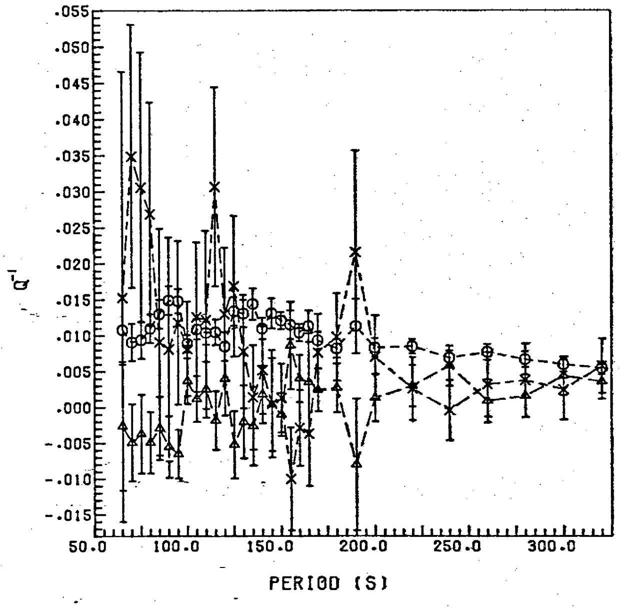

WU(1972) REGIONALIZATION INDIVIDUAL OBS - 4 REGIONS B & C

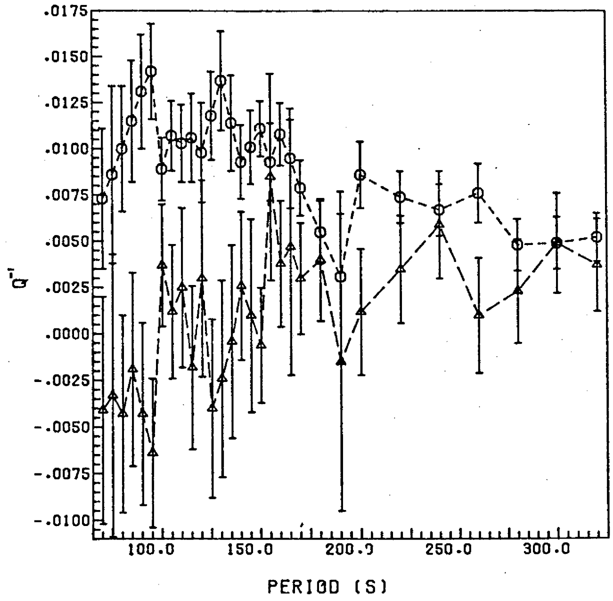

WU(1972) REGIONALIZATION INDIVIDUAL OBS - 2 REGIONS

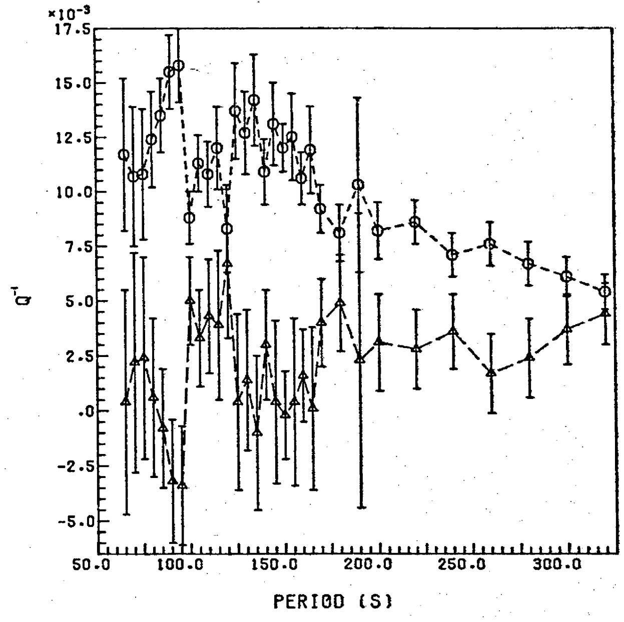

This path as was suggested in Section 7,3, is most likely to produce multipathing since it crosses many island arcs at shallow angles of incidence. The 4 region pure path separation was uncessful for Q^{-1}_R (as was also the case for group velocities) since negative Q^{-1}_R values are predicted for both continental and island arc regions. The 3 region regression analysis produced reasonable results except for island arc Q^{-1}_R at periods greater than 125 seconds. Pure path group velocities for island arc regions determined in 3 region separations were also poorly determined for periods greater than 125 seconds (see Sec. 7.3). The 2 region regression analysis for Q^{-1}_R shows that Q^{-1}_R for both continent-island arc and ocean-ridge provinces are well separated. Only at periods of 220 and 280 seconds do continental Q^{-1}_R estimates deviate substantially from the general trend of the continental Q^{-1}_R values. Models derived from the 2 region regression analysis for both continental and oceanic Q^{-1}_β as a function of depth are discussed in the next section.

Sec. 7.6 Q^{-1}_R INVERSIONS FOR OCEANIC AND CONTINENTAL REGIONS

Models for Q^{-1}_β as a function of depth have been derived in a manner similar to that described for global average Q^{-1}_β models in Section 5.5. For these inversions only the pure path Q^{-1}_R derived for 2 regions was used. Shear velocity models, 19:5/20 for oceanic structures and 8:70/2C for continental structures, were used to generate phase velocity partial derivatives for these inversions. A continental model without a high velocity lid, 8:70/2C was selected because the model parameters, shear velocity and Q^{-1}_β, are poorly resolved for relatively thin layers in this depth range.

Q^{-1}_β models for oceans (Figure 7.10) were found which indicate that the average sub-oceanic mantle has a Q_β of between 80 and 100 to depths of several hundred kilometers. This average Q_β is lower than Q_β's determined by Mitchell (1977) for Pacific Ocean paths. This difference may be caused by the mid-ocean ridge provinces which were included with ocean basins in the twofold Q^{-1}_R regionalization. Layers at depths greater than 400 km in these models are poorly controlled, on the general fit of these models to the oceanic Q^{-1}_R,calculated in the 2 region regression analysis (Sec. 7.5) is also poor. The three models shown in Figure 7.10 have problem variances of 2×10^{-2}, 10^{-2} and 5×10^{-3}. Resolution kernels for model 3/20 are shown in Figure 7.11.

Models for continental Q^{-1}_β were not successful. The models for continental Q^{-1}_R for periods between 60 and 280 seconds and 60 and 230 seconds contained layers at depths greater than 300 km which had negative Q^{-1}_β values. Such models are not physically possible. These problems were primarily caused by the near zero and negative continental Q^{-1}_R values for periods in excess of 200 seconds. It is evident, however, that the dissipation of seismic energy beneath the continents is much smaller than dissipation beneath the oceans.

Figure 7.10 OCEANIC MODELS FOR SPECIFIC ATTENUATION FOR SHEAR WAVES - as a function of depth are shown for models 2/20, 3/20 and 3.6/20 which have problem variances of 2×10^{-3}, 10^{-3} and 5×10^{-4} respectively. All models fit ocean-ridge province Q^{-1}_{R} for periods between 60 and 280 seconds. All models were devised using phase velocity partial derivatives generated from shear velocity model 19:5/20. The Q_{β} for the upper 200 km of the mantle for models 2/20 and 3/20 ranges from 85 to 100.

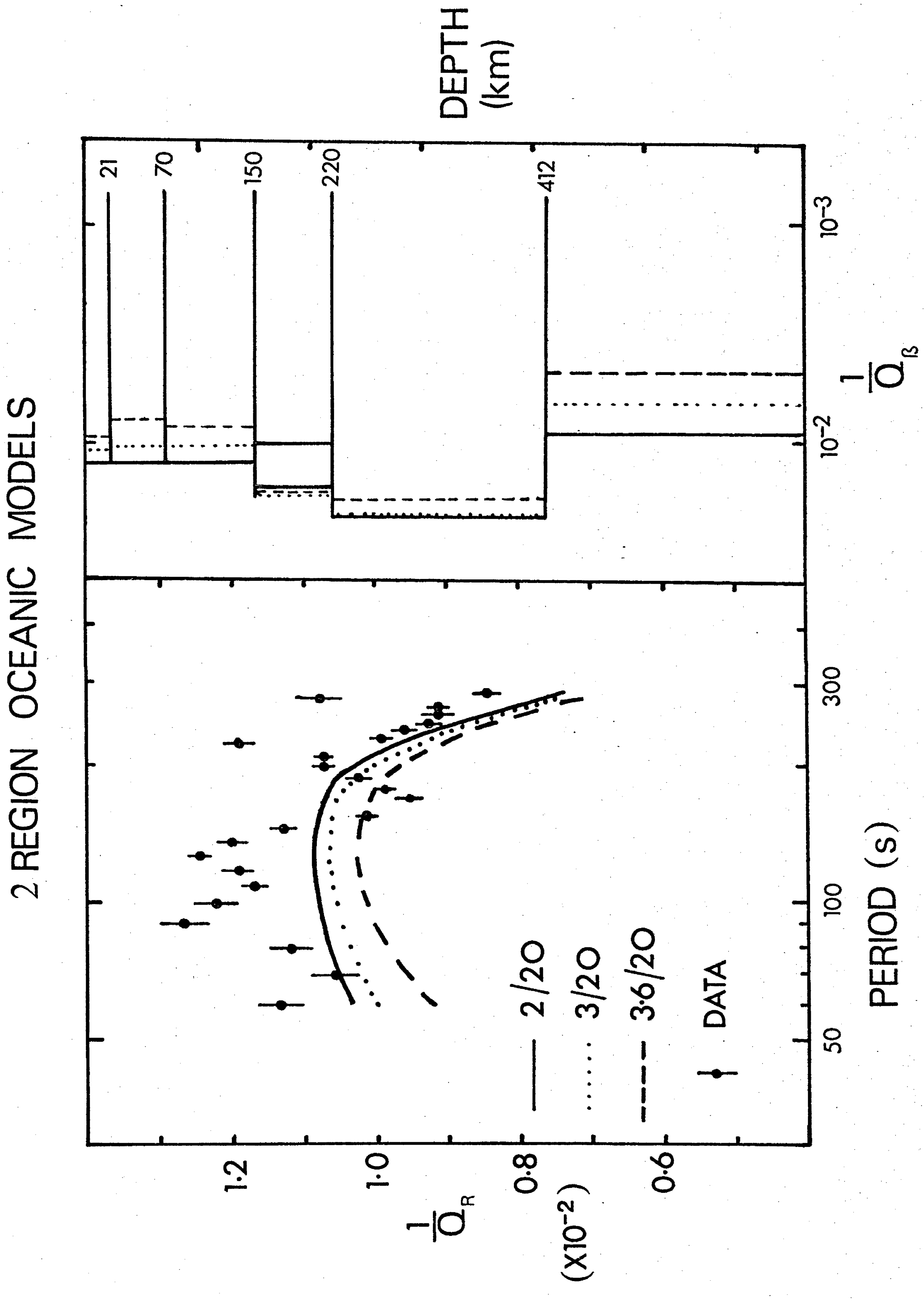
2 REGION OCEANIC MODELS
DEPTH (km)
21
70
150
220
412
10⁻³
10⁻²
1/Q_β
1.2
1.0
0.8
0.6
1/Q_R (X10⁻²)
50
100
300
PERIOD (s)
2/20
3/20
3.6/20
DATA

TABLE 7.6 2 REGION OCEANIC MODELS FOR ATTENUATION BASED ON 19:5/20

Depth to Top	Compressional Velocity (km/s)	Shear Velocity (km/s)	$1/Q_\beta$ $(\times 10^{-2})$		
			2/20	3/20	3.6/20
0	6.50	3.72	1.114	1.050	0.972
21	8.37	4.545	1.117	1.022	0.921
70	8.37	4.295	1.101	1.023	0.951
150	8.37	4.290	1.193	1.250	1.247
220	8.37	4.598	1.363	1.358	1.286
412.5	9.50	5.200	0.977	0.833	0.700

Figure 7.11 RESOLUTION KERNELS -

for model 3/20 are shown for depths shallower than 400 km.

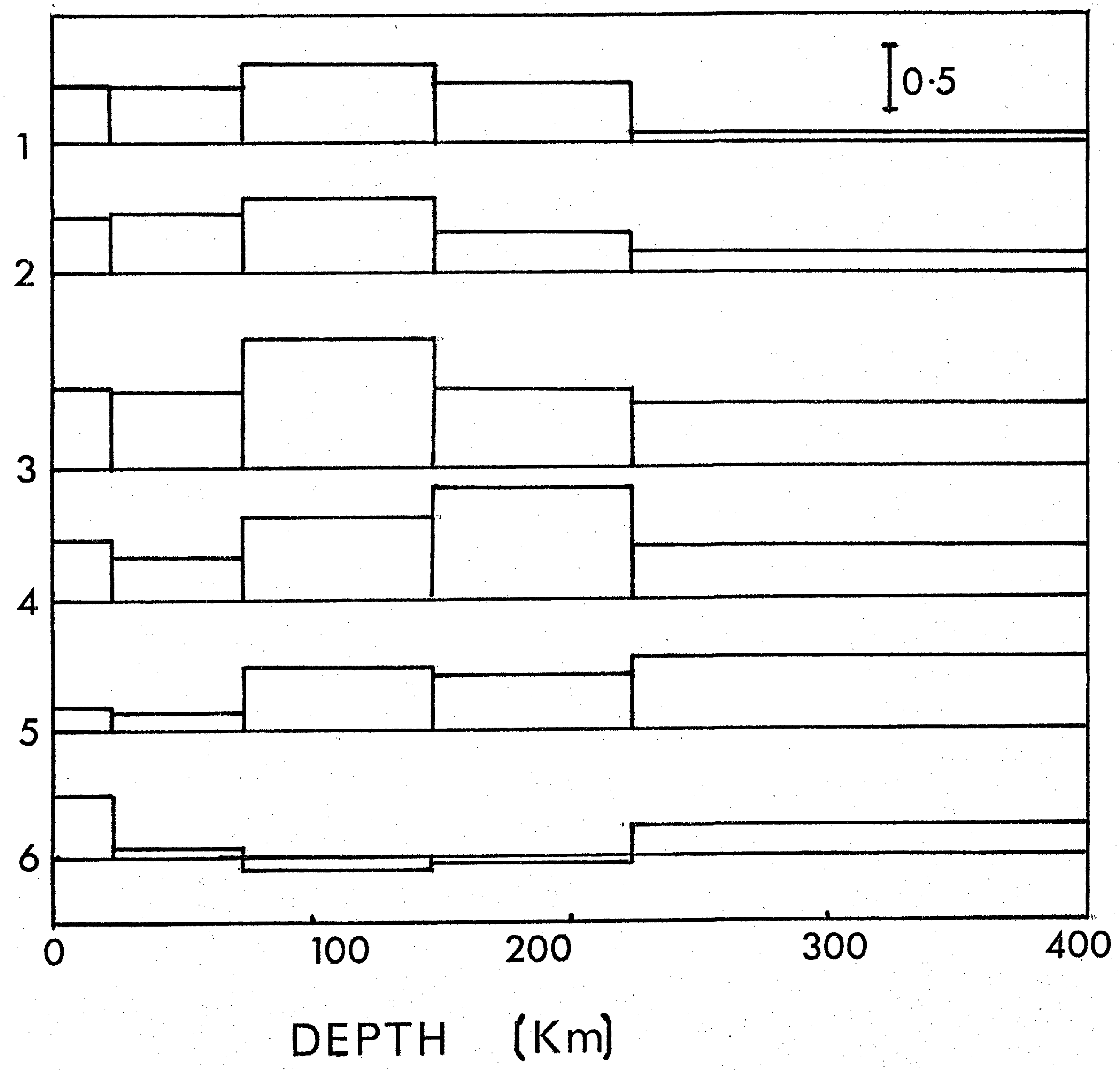

RESOLUTION KERNELS FOR Q_β^{-1} MODEL 3/20

CHAPTER 8

SUMMARY

The analysis of group velocities and attenuation coefficients for Rayleigh waves in the period range 50 to 600 seconds provides information on the average elastic and anelastic properties of the earth. The Direct Filtering Method has been developed which provides estimates of group arrival times and spectral amplitudes from Gaussian filtered seismograms. Two estimates of the standard error of the group arrival time are based on the regression statistics of parabolas which are fitted to each envelope maximum. One estimate reflects the quality of the fit to the maximum while the other is determined by the half amplitude width of the maximum. Estimates of the period at the envelope maximum are also available in order to estimate the purity of the filtered signal at the envelope maximum. Estimates of group velocities and spectral amplitudes determined by the Direct Filtering Method are comparable to those provided by other multiple filter analyses, but the Direct Filtering Method provides objective estimates of the standard errors of group velocity measurements. Spectral amplitudes and attenuation coefficients determined from seismograms filtered with narrow band-pass Gaussian filters do not require a correction for geometric spreading if filters are sufficiently sharp.

The Direct Filtering Method has been applied to seismograms of 4 Kurile Island earthquakes ranging in magnitude from 6.6 to 8.3. These events are all located within a small region so that Rayleigh waves from all events traverse the same great circle paths. All events have focal mechanism solutions which show that the fault motion is predominantly dip-slip.

Great circle group velocities have been determined for the surface wave magnitude 8.3 event by averaging of group velocities of Rayleigh phases arriving after R_3. Errors in the great circle group velocities caused by averaging group velocities of arrivals later than R_3 are much smaller than the standard errors of the estimates for individual Rayleigh phases. These group velocities extend from 100 to 600 seconds in period. Kanamori's (1970a) estimates for the same great circle paths are in good agreement with these estimates. Attenuation coefficients have also been determined from spectral amplitude ratios estimated by 2 methods:

1. from the rate of decay of envelope maxima of Gaussian filtered Rayleigh phases, and
2. from the rate of decay of spectral amplitudes taken as the sum of products of a pure sine wave with segments of each Rayleigh phase within a group velocity window. Both methods provide attenuation coefficients which agree well with attenuation coefficients derived from Kanamori's (1970a) group velocities and Q's, but those derived from the envelopes of the filtered seismograms show less scatter.

Group velocities and spectral amplitudes determined for the smaller 3 Kurile Islands earthquakes have extended the range of accurate measurements to periods as short as 50 seconds. These measurements, taken with those for the larger event, provide averages for group velocities and attenuation coefficients for 9 great circle paths. These 9 paths are evenly distributed in azimuth at the source. The averaging of the path group velocities and attenuation coefficients over all paths provides a reliable estimate of global average group velocities for periods between 50 and 600 seconds and attenuation coefficients for periods between 50 and 450 seconds. Global average phase velocities, determined by integration of the global average group velocities, agree well with oceanic phase velocities determined by Weidner (1974) for periods between 50 and 120 seconds. The global average group velocities are in good agreement with oceanic velocities determined by Forsyth (1985b) and Landisman _et al_. (1969). These group velocities are, however, much lower than those predicted by several recent earth models.

zone) cannot be determined with precision. Global average models for shear wave attenuation (Q^{-1}_{β}) indicate that a zone of high attenuation is coincident with the low velocity zone. Models for attenuation which have lithospheric thicknesses of 70 km place the highest attenuation layer in the lower half of the low velocity zone which indicates that on the average the lithosphere is thicker than 70 km. Average Q_{β} for the lithosphere, low-velocity zone and sub-low velocity layer (asthenosphere) are approximately 200, 85 to 110 and 170 to 200 respectively. Although losses caused by elastic scattering have not been taken into account, they are small compared to anelastic attenuation in the 50 to 300 second period range.

Pure path averages for group velocities and specific attenuation have been calculated from path averages and from individual observations for 2 regionalization schemes, one original to this study and the other devised by Wu (1972). Both regionalization schemes are based on 4 upper mantle provinces: continent, ocean basin, island arc and mid-ocean ridge. Pure path group velocities and specific attenuation have also been calculated for combinations of regions, namely, ocean basin plus mid-ocean ridge and continent plus island arc provinces. Several of these regionalizations have provided well separated regional group velocities for such composite regions. Results of regionalizations using Wu's (1972) choice of regions have given pure path group velocities for continent, ocean basin, continent plus island arc and ocean basin plus mid-ocean ridge provinces which are in good agreement with group velocity dispersion observed at periods shorter than 100 seconds and which also agree with the pure path group velocities derived from great circle measurements of Dziewonski (1971a) and Wu (1972). Dziewonski's pure path group velocities for shields lie at most less than one standard error above continental group velocities derived in this study, while his oceanic group velocities lie slightly more than one standard error below ocean basin plus mid-ocean ridge province group velocities. Shear velocity models derived from pure path group

Equivalent spheroidal oscillation periods derived from the global average phase velocities are also progressively **longer** in period, for periods less than 150 seconds, than fundamental spheroidal mode periods calculated for model QM2 (Hart et al. 1977b) which incorporates corrections for anelastic dispersion for free oscillation periods. In the future, data sets for average earth models should include equivalent free oscillation periods or surface wave phase or group velocities in the period range 50 to 150 seconds since body wave travel times together with free oscillation data for periods in excess of 140 seconds do not adequately constrain the upper mantle structure of such models.

Q^{-1}_R which are calculated from global average attenuation coefficients and group velocities are similar to the largest Q^{-1}_R computed from fundamental mode spheroidal oscillations by Jobert and Roult (1976) and are lower than those predicted by model MM8 of Anderson et al. (1965). Q^{-1}_R from Ben-Menahem's (1965) measurements lie between the global average Q^{-1}_R and those predicted by model MM8 periods between 50 and 100 seconds. For For periods between 50 and 100 seconds, attenuation coefficients of Mitchell et al. (1975) for Pacific Ocean paths and by Mitchell (1973a) and Hermann and Mitchell (1975) for the central United States are all within a factor of 2 of the global average attenuation coefficients. From the agreement of the global average attenuation coefficients and group velocities with other long and short period measurements it is concluded that these measurements are estimates of global average properties.

The global average group velocities and attenuation coefficients provide a basis for modelling the shear velocity and attenuation structure of the average earth. Shear velocity models for the upper mantle which fit 50 to 300 second global average group velocities within one standard deviation require, the presence of a low velocity zone. Models have been produced from the global average group velocities alone which have the top of the low velocity zone at depths of both 70 and 100 km, so that the average thickness of the lithosphere (taken as the depth to the top of the low velocity velocities for pure and combined regions indicate that low velocity zones are required beneath the oceans, but are not required beneath the continents, although 3 and 4 region separations produce a range of models which include low velocity zones at depths greater than 200 km. A regional study of group velocity dispersion and thrust faulting in eastern Australia shows that a low velocity zone is required at depths greater than 140 km and probably greater than 180 km in order to fit observed fundamental and higher mode Love and Rayleigh waves and ScS travel times.

Specific attenuation for shear waves, Q_β^{-1}, determined from path average group velocities and attenuation coefficients has also been regionalized successfully for 2 and 3 region combinations. The resulting pure path specific attenuation for continents is much lower than that for ocean basins and ocean basin plus mid-ocean ridge provinces. Island arc and mid-ocean ridge provinces both show higher attenuation than ocean basins for periods shorter than 100 seconds for the 4 region separation, but results deteriorate at longer periods due to multipathing and defocusing. Models derived for ocean basin plus mid-ocean ridge province specific attenuation show that the sub-oceanic mantle has an average Q_β of about 80 to 100 for the upper 200 km. The results of the attenuation studies show that with additional data it will be possible to obtain significantly higher precision estimates of the differences between different types of upper mantle provinces.

REFERENCES

Aki, K., 1966. Generation and propagation of G waves from the Niigata earthquake of June 16, 1964. Part 2: Estimation of earthquake moment, released energy and stress-strain drop from the G-wave spectrum. Bull. Earthq. Res. Inst. Tokyo Univ., 44, 73-88.

Alexander, S.S., 1963. Surface wave propagation in the western United States, Ph.D. thesis, Calif. Inst. of Tech.

Alterman, Z., Jarosch, H. and Pekeris, C.L., 1961. Propagation of Rayleigh waves in the earth. Geophys. J.R. Astr. Soc., 4, 219-241.

Anderson, D.L., 1966. Recent evidence concerning the structure and composition of the Earth's mantle. Physics and Chemistry of the Earth, 6, 1-131, ed. L.H. Ahrens, F. Press, S.K. Runcorn and H.C. Urey, Pergamon Press, New York.

Anderson, D.L., 1966. Earth's viscosity, Nature, 151, 321-322.

Anderson, D.L. and Archambeau, C.B., 1964. The anelasticity of the earth. J. Geophys. Res., 69, 2071-2084.

Anderson, D.L., Ben-Menahem, A. and Archambeau, C.B., 1965. Attenuation of seismic energy in the upper mantle. J. Geophys. Res., 70, 1441-1448.

Anderson, D.L. and Hart, R.S., 1976. An earth model based on free oscillations and body waves. J. Geophys. Res., 81, 1461-1475.

Anderson, D.L., Kanamori, H., Hart, R.S. and Liu, H.-P., 1977. The earth as a seismic absorption band. (In Press).

Archambeau, C.B., 1968. General theory of elastodynamic source fields. Rev. Geophys. Sp. Phys., 6, 241-288.

Backus, G. and Gilbert, F., 1976. Uniqueness in the inversion of inaccurate gross earth data. Phil. Trans. R. Soc. London, Ser. A., 266, 123-192.

Backus, G. and Gilbert, F., 1967. Numerical applications of a formalism for geophysical inverse problems. Geophys. J.R. Astr. Soc., 13, 247-276.

Backus, G. and Gilbert, F., 1968. The resolving power of gross earth data. Geophys. J.R. Astr. Soc., 16, 169-205.

Ben-Menahem, A., 1961. Radiation of seismic surface-waves from finite moving sources. Bull. Seism. Soc. Am., 51, 401-435.

Ben-Menahem, A., 1965. Observed attenuation and Q values of seismic surface waves in the upper mantle. J. Geophys. Res., 70, 4641-4651.

Ben-Menahem, A. and Harkrider, D.G., 1964. Radiation patterns of seismic waves from buried dipolar point sources in a flat stratified earth. J. Geophys. Res., 69, 2605-2620.

Biswas, N.N. and Knopoff, L., 1970. Exact earth flattening calculation for Love waves. Bull. Seism. Soc. Am., 66, 1123-1137.

Biswas, N.N. and Knopoff, L., 1974. Structure of the upper mantle under the United States from the dispersion of Rayleigh waves. Geophys. J.R. Astr. Soc., 36, 515-539.

Bolt, B.A. and Dorman, J., 1961. Phase and group velocities of Rayleigh waves in a spherical gravitating earth. J. Geophys. Res., 66, 2965-2981.

Bolt, B.A. and Niazi, M., 1964. Dispersion of Rayleigh waves across Australia. Geophys. J.R. Astr. Soc., 9, 21-35.

Braile, L.W. and Keller, G.R., 1975. Fine structure of the crust inferred from linear inversion of Rayleigh-wave dispersion. Bull. Seis. Soc. Am., 65, 71-83.

Brune, J.N., 1960. Radiation pattern of Rayleigh waves from the southern Alaska earthquake of July 10, 1958. Publ. Dominion Obs. Ottawa, 24, 373-383.

Brune, J.N., 1962. Attenuation of dispersed wave trains. Bull. Seis. Soc. Am., 52, 109-112.

Brune, J.N. and Allen, C.R., 1967. A low stress-drop, low-magnitude earthquake with surface faulting: the Imperial California earthquake of March 4, 1966. Bull. Seism. Soc. Am., 57, 501-514.

Burkhard, N.R. and Jackson, D.D., 1976. Density and surface wave inversion. Geophys. Res. L., 3, 637-638.

Burton, P.W., 1972. Upper mantle zone of low Q. Nature Phys. Sci., 238, 87-90.

Burton, P.W., 1974. Estimations of Q^{-1} from seismic Rayleigh waves. Geophys. J.R. Astr. Soc., 36, 167-189.

Burton, P.W., 1977. Inversion of high frequency $Q_{\gamma}^{-1}(f)$. Geophys. J.R. Astr. Soc., 48, 29-51.

Canitez, N., 1977. Optimum filter for surface-wave group-velocity determination. Bull. Seis. Soc. Am., 67, 79-85.

Capon, J., 1970. Analysis of Rayleigh-wave multipath propagation at LASA. Bull. Seis. Soc. Am., 6, 1701-1731.

Capon, J., 1971. Comparison of Love- and Rayleigh-wave multipath propagation at LASA. Bull. Seis. Soc. Am., 61, 1327-1344.

Cara, M., 1973. Filtering of dispersed wave trains. Geophys. J.R. Astr. Soc., 33, 65-80.

Cleary, J., 1973. Australian Crustal Structure. In Müeller, S., ed., The Structure of the Earth's Crust Based on Seismic Data., Tectonophysics, 20, 241-248.

Connelly, J.B. and Collins, C.D.N., 1973. Bowen Basin seismic refraction survey, May - June, 1973; operational report. Bur. Min. Resour. Aust. Rec., 1973/212 (unpublished).

Denny, M.D. and Chin, R.C.Y., 1976. Gaussian filters for determining group velocities. Geophys. J.R. Astr. Soc., 45, 495-525.

Derr, J.S., 1969. Free oscillation observations through 1968. Bull. Seis. Soc. Am., 59, 2079-2099.

Doyle, H.A., Everingham, I.B. and Hogan, T.K., 1959. Seismic recordings of large explosions in south-eastern Australia. Aust. J. Phys., 12, 222-230.

Doyle, H.A., Underwood, R. and Polak, E.J., 1966. Seismic velocities from explosions off the central coast of New South Wales. J. Geol. Soc. Aust., 13, 355-372.

Drake, L.A., 1972a. Love and Rayleigh waves in non-horizontally layered media. Bull. Seis. Soc. Am., 62, 1241-1258.

Drake, L.A., 1972b. Rayleigh waves at a continental boundary by the finite element method. Bull. Seis. Soc. Am., 62, 1259-1268.

Dziewonski, A.M., 1972a. On regional differences in dispersion of mantle Rayleigh waves. Geophys. J.R. Astr. Soc., 22, 289-325.

Dziewonski, A.M., 1971b. Upper mantle models from "Pure Path" dispersion data. J. Geophys. Res., 76, 2587-2601.

Dziewonski, A.M., Bloch, S., and Landisman, M. 1969. A technique for the analysis of transient seismic signals. Bull. Seis. Soc. Am., 59, 427-444.

Dziewonski, A.M. and Hales, A.L., 1972. Numerical analysis of dispersed seismic waves, in Methods of Comput. Phys., vol. 11, ed., B.A. Bolt, Academic Press, New York, pp. 39-85.

Dziewonski, A.M., Mills, J.M. and Bloch, S. 1972. Residual Dispersion Measurement - a new method of surface-wave analysis. Bull. Seis. Soc. Am., 62, 129-139.

Dziewonski, A.M., Hales, A.L., and Lapwood, E.R., 1975. Parametrically simple earth models constent with geophysical data. Phys. Earth. Planet. Int., 10, 12-48.

Ewing, M., Jardetzky, W.S. and Press, F., 1957. Elastic Waves in Layered Media, McGraw-Hill, New York.

Fitch, T.J., 1976. The Picton earthquake of March 9, 1973: a seismic view of the source. Bur. Miner. Resour. Aust. Bull., 164, 11-14.

Fitch, T.J. and Rynn, J.M.W., 1976. Inversion for V_p/V_S in shallow source regions. Geophys. J.R. Astr. Soc., 44, 253-267.

Fix, J.E., 1975. The crust and upper mantle of central Mexico. Geophys. J.R. Astr. Soc., 43, 453-499.

Franklin, J.N., 1970. Well-posed stochastic extensions of the ill-posed linear problems. J. Math. Anal. Appl., 31, 682-716

Forsyth, D.W., 1975a. A new method for the analysis of multi-mode surface wave dispersion: application to Love wave propagation in the East Pacific. Bull. Seis. Soc. Am., 65, 323-342.

Forsyth, D.W., 1975b. The early structural evolution and anisotropy of the oceanic upper mantle. Geophys. J.R. Astr. Soc., 43, 103-162.

Fukao, Y., 1972. Source process of a large deep-focus earthquake and its tectonic implications - the western Brazil earthquake of 1963. Phys. Earth Planet. Int., 5, 61-76.

Gilbert, F., 1971. Ranking and winnowing gross earth data from inversion and resolution. Geophys. J.R. Astr. Soc., 23, 125-128.

Gilbert, F., Dziewonski, A.M. and Brune, J.N., 1973. An informative solution to a seismological inverse problem. Proc. Nat. Acad. Sci. USA, 70, 1410-1413.

Gilbert, F. and Dziewonski, A.M. 1975. An application of normal mode theory to the retrieval of structural parameters and source mechanisms from seismic spectra. Philos. Trans. R. Soc. London, Ser. A., 278, 187-269.

Goncz, J.H., 1974. Surface wave studies of the Australian upper mantle. Ph.D. thesis, Australian National University, 170 pp.

Goncz, J.H. and Cleary, J., 1976. Variations in the structure of the upper mantle beneath Australia, from Rayleigh wave observations. Geophys. J.R. Astr. Soc., 44, 507-516.

Gough, D.I. and Gough, W.I., 1970. Stress and deflection in the lithosphere near Lake Kariba - I. Geophys. J.R. Astr. Soc., 21, 65-78.

Green, D.H. and Ringwood, A.E., 1967. Genesis of basaltic magmas. Beitr. Mineral. Petrog., 15, 103-190.

Griggs, D. and Handin, J., 1960. Rock deformation. Geol. Soc. Am. Mem., 79.

Gupta, H.K., Nyman, D.C. and Landisman, M., 1977. Shield-like upper mantle structure inferred from long-period Rayleigh- and Love-wave dispersion investigation in the Middle East and southern Asia. Bull. Seis. Soc. Am., 67, 103-119.

Hagiwara, T., 1958. A note on the theory of the electromagnetic seismograph. Bull. Earthq. Res. Inst. Tokyo Univ., 36, 139-164.

Hales, A.L., 1969. Gravitational sliding and continental drift. Earth Planet. Sci. L., 6, 31-34.

Hamada, K., 1972. Regionalized shear-velocity models for the upper mantle inferred from surface-wave dispersion data. J. Phys. Earth, 20, 301-326.

Harkrider, D.G., 1964. Surface waves in multilayer elastic media, I. Rayleigh and Love waves from buried sources in a multilayered elastic half-space. Bull. Seism. Soc. Am., 54, 627-680.

Harkrider, D.G., 1970. Surface waves in multilayered elastic media. Part II: Higher mode spectra and spectral ratios from point sources in plane layered earth models. Bull. Seism. Soc. Am., 60, 1937-1987.

Hart, R.S. and Press, F., 1973. S_n velocities and the composition of the lithosphere in the regionalized Atlantic. J. Geophys. Res., 78, 407-411.

Hart, R.S., Anderson, D.L. and Kanamori, H. 1977a. Shear velocity and density of an attenuating earth. (In press).

Hart, R.S., Anderson, D.L. and Kanamori, H. 1977b. The effect of attenuation on gross earth models. (In press).

Harrington, H.J., 1974. The Tasman Geosyncline in Australia. The Tasman Geosyncline - a symposium, 383-407, Geol. Soc. Aust., Queensland Division

Hayes, D.E. and Ringis, J., 1973. Seafloor spreading in the Tasman Sea, Nature, 243, 454-458.

Herrman, R.B. and Mitchell, B.J., 1975. Statistical analysis and interpretation of surface-wave anelastic attenuation data for the stable interior of North America. Bull. Seis. Soc. Am., 65, 115-1128.

Hess, H.H., 1962. History of ocean basins. In Engel, A.E.J., James, H.L. and Leonard, B.F., eds., Petrologic Studies: a volume to Honor A.F. Buddington, Geol. Soc. Am., 599-620.

Hodgson, J.H., 1957. The nature of faulting in large earthquakes. Bull. Geol. Soc. Am., 68, 611-644.

Honda, H., 1962. Earthquake mechanisms and seismic waves. J. Phys. Earth, 10, 1-97.

Inston, H.H., Marshall, P.D. and Blamey, C., 1971. Optimization of filter band width in spectral analysis of wave trains. Geophys. J.R. Astr. Soc., 23, 243-250.

Jackson, D.D., 1971. The attenuation of Love waves and toroidal oscillations of the earth. Geophys. J.R. Astr. Soc., 25, 25-34.

Jackson, D.D., 1972. Interpretation of inaccurate, insufficient and inconsistent data. Geophys. J.R. Astr. Soc., 28, 97-109.

Jaeger, J.C., 1970. Heat-flow and radioactivity in Australia. Earth Planet. Sci. Lett., 8, 285-292.

Jaeger, J.C. and Lesley Read, 1969. Seismicity of southeast Australia. The Earth's Crust and Upper Mantle. p. 145-147, ed. P.J. Hart, Am. Geophys. Union, Geophys. Mono., 13.

Jeffreys, H., 1965. Damping of S waves. Nature, 208, 675.

Jeffreys, H., 1967. Radius of the earth's core. Nature, 215, 1365-1366.

Jenkins, G.M. and Watts, D.G., 1968. Spectral Analysis and its Applications, Holden Day, San Francisco, 525 pp.

Jobert, N. and Roult, G., 1976. Periods and damping of free oscillations observed in France after sixteen earthquakes. Geophys. J.R. Astr. Soc., 45, 155-176.

Johnson, L.E. and Gilbert, F., 1972. Inversion and inference for teleseismic ray data. Methods in Comput. Phys., 12, 231-266.

Jordan, T.H. and Franklin, J.N., 1971. Optimal solutions to a linear inverse problem in geophysics. Proc. Nat. Acad. Sci., 68, 291-293.

Jordan, T.H. and Anderson, D.L., 1974. Earth structure from free oscillations and travel times. Geophys. J.R. Astr. Soc., 36, 411-459.

Kanamori, H., 1967. Spectrum of P and PcP in relation to the mantle - core boundary and attenuation in the mantle. J. Geophys. Res., 72, 559-571.

Kanamori, H., 1970a. Velocity and Q of mantle waves. Phys. Earth Planet. Int., 2, 259-275.

Kanamori, H., 1970b. Synthesis of long-period surface waves and its application to earthquake source studies - Kurile Islands earthquake of October 12, 1963. J. Geophys. Res., 75, 5011-5027.

Kanamori, H. and Abe, K., 1968. Deep structure of island arcs as revealed by surface waves. Bull. Eartq. Res. Inst. Tokyo Uni., 46, 1001-1025.

Kanamori, H. and Press, F., 1970. How thick is the lithosphere? Nature, 226, 330-331.

Kanamori, H. and Anderson, D.L., 1975. Theoretical basis of some empirical relations in seismology. Bull. Seism. Soc. Am., 65, 1073-1096.

Kausel, E.G., Leeds, A.R. and Knopoff, L., 1974. Variations of Rayleigh wave phase velocities across the Pacific Ocean. Science, 186, 139-141.

Keilis-Borok, V.I. and Yanovskaja, T.B., 1967. Inverse problems of seismology (structural review). Geophys. J.R. Astr. Soc. 13, 223-234.

Knopoff, L., 1958. Energy release in earthquakes. Geophys. J.R. Astr. Soc., 1, 44-52.

Knopoff, L., 1972. Observation and inversion of surface-wave dispersion. In Ritsema, A.R., ed., The Upper Mantle, Tectonophysics, 13, 497-519.

Knopoff, L., Müeller, S. and Pilant, W.L., 1966. Structure of the crust and upper mantle in the Alps from the phase velocity of Rayleigh waves. Bull. Seis. Soc. Am., 56, 1009-1044.

Knopoff, L. and Fouda, A.A., 1975. Upper-mantle structure under the Arabian peninsula. Tectonophysics, 26, 121-134.

Lanczos, C., 1961. Linear Differential Operators, D. Van Nostrand Co., London, 564 pp.

Landisman, M., Dziewonski, A.M. and Satô, Y. 1969. Recent improvements in the analysis of surface wave observations. Geophys. J.R. Astr. Soc., 17, 369-403.

Lee, W.B. and Solomon, S.C., 1975. Inversion schemes for surface wave attenuation and Q in the crust and the mantle. Geophys. J.R. Astr. Soc., 43, 47-71.

Leeds, A.R., Knopoff, L. and Kausel, E.G., 1974. Variations of upper mantle structure under the Pacific Ocean. Science, 186, 141-143.

Le Pichon, X., 1968. Sea-floor spreading and continental drift. J. Geophys. Res., 73, 3661-3687.

Levshin, A.L., Pisarenko, V.F. and Pogrebinsky, G.A., 1972. On a frequency-time analysis of oscillations. Ann. Geophys., 28, 211-218.

Liu, H.-P., Anderson, D.L. and Kanamori, H., 1976. Velocity dispersion due to anelasticity; implications for seismology and mantle composition. Geophys. J.R. Astr. Soc., 47, 41-58.

McGarr, A., 1969a. Amplitude variations of Rayleigh waves - progagation across a continental margin. Bull. Seis. Soc. Am., 59, 1281-1305.

McGarr, A., 1969b. Amplitude variations of Raylwigh wave - horizontal refraction. Bull. Seis. Soc. Am., 59, 1307-1334.

McGarr, A. and Alsop, L.E., 1967. Transmission and reflection of Rayleigh waves at vertical boundaries. J. Geophys. Res., 72, 2169-2180.

McGarr, A., 1972. Comments on some papers concerning amplitudes of seismic surface waves. J. Geophys. Res., 77, 3823-3826.

McKenzie, D.P., 1969a. The relation between fault plane solutions for earthquakes and the direction of the principle stresses. Bull. Seism. Soc. Am., 59, 591-601.

McKenzie, D.P., 1969b. Speculations on the consequences and causes of plate motions. Geophys. J.R. Astr. Soc., 18, 1-32.

McKenzie, D.P. and Parker, R.L., 1967. The North Pacific: an example of tectonics on a sphere. Nature, 216, 1276-1280.

Mitchell, B.J., 1973a. Radiation and attenuation of Rayleigh waves from the southeastern Missouri earthquake of October 21, 1965. J. Geophys. Res., 78, 886-899.

Mitchell, B.J., 1973b. Surface-wave attenuation and crustal anelasticity in central North America. Bull. Seism. Soc. Am., 63, 1057-1071.

Mitchell, B.J., 1975. Regional Rayleigh wave attenuation in North America. J. Geophys. Res., 80, 4912-4924.

Mitchell, B.J., Leite, L.W.B., Yu, Y.K. and Herrmann, R.B., 1976. Attenuation of Love and Rayleigh waves across the Pacific at periods between 15 and 110 seconds. Bull. Seis. Soc. Am., 66, 1189-1204.

Mitchell, B.J., 1977. Anelasticity of the crust and upper mantle beneath the Pacific Ocean from the inversion of observed surface wave attenuation. (In press).

Mitchell, B.L. and Landisman, M., 1969. Electromagnetic seismograph constants by least-squares inversion. Bull. Seism. Soc. Am., 59, 1335-1348.

Molnar, P. and Oliver, J., 1969. Lateral variations of attenuation in the Upper Mantle and discontinuities in the lithosphere. J. Geophys. Res., 74, 2648-2682.

Morgan, W.J., 1968. Rises, trenches, great faults, and crustal blocks. J. Geophys. Res., 73, 1959-1982.

North, R.G. and Dziewonski, A.M., 1976. A note on Rayleigh-wave flattening corrections. Bull. Seis. Soc. Am., 66, 1873-1879.

O'Connell, R.J., 1977. On the scale of mantle convection. Tectonophysics, 38, 119-136.

Olgers, F., 1972. Geology of the Drummond Basin, Queensland Dept. Min. Energy, Bur. Miner. Resour. Aust., Bull. 132, pp. 78. Australian Government Publishing Service, Canberra.

Oversby, B., 1971. Palaeozoic plate tectonics in the southern Tasman Geosyncline. Nature Phys. Sci., 234, 45-47.

Papoulis, A., 1962. The Fourier Integral and its Applications, McGraw-Hill, New York, 318 pp.

Parker, R.L., 1970. The inverse problem of electrical conductivity in the mantle. Geophys. J.R. Astr. Soc., 22, 121-138.

Parker, R.L., 1972. Inverse theory with grossly inadequate data. Geophys. J. R. Astr. Soc., 29, 123-138.

Penrose, R., 1955. A generalized inverse for matrices. Proc. Camb. Phil. Soc., 51, 406-413.

Pilant, W.L. and Knopoff, L., 1964. Observations of multiple seismic events. Bull. Seis. Soc. Am., 54, 19-34.

Pomeroy, P.W., Nade, G., Savino, J. and Chander, R., 1969. Preliminary results from high-gain wide-band long-period electromagnetic seismograph systems. J. Geophys. Res., 74, 3295-3298.

Press, F., 1959. Some implications on mantle and crustal structure from G waves and Love waves. J. Geophys. Res., 64, 565-568.

Press, F., 1968. Density distribution in Earth. Science, 160, 1218-1221.

Press, F., 1969. The sub-oceanic mantle. Science, 165, 174-176.

Press, F., 1970. Earth models consistent with geophysical data. Phys. Earth Planet. Int., 3, 3-22.

Randall, M.J., 1976. Attenuative dispersion and frequency shifts of the earth's free oscillations. Phys. Earth Planet. Int., 12, P1-P4.

Reiter, L., 1973. Reflection, refraction and mode conversion of long-period surface waves and the measurement of Q^{-1} for free oscillations. Bull. Seis. Soc. Am., 63, 1709-1722.

Ringwood, A.E., 1969. Composition and evolution of the upper mantle. The Earth's Crust and Upper Mantle, p. 1-17, ed. P.J. Hart, Am. Geophys. Union, Geophys. Mono., 13.

Ringwood, A.E, and Green, D.H., 1966. An experimental investigation of the gabbro-eclogite transformation and some geophysical implications. Tectonophysics, 3, 383-427.

Rothe, J.P., 1969. Earthquakes and Reservoir Loading. Vol. 1, Proc. Fourth Cont. on Earthquake Engineering, Santiago, Chile.

Roult, G., 1974. Attenuation des ondes sismiques de tres basse freguence. Ann Geophys., 30, 141-167.

Roult, G., 1975. Attenuation of seismic waves of very low frequency. Phys. Earth Planet. Int., 10, 159-166.

Rynn, J.M.W., 1971. High-gain long-period seismograph station installation report, Charters Towers, Australia, Technical Report, 77 pp. ARPA Order 1513, Lamont-Doherty Geol. Observ., Palisaides, New York.

Sass, J., 1964. Heat-flow values from eastern Australia. J. Geophys. Res., 69, 3889-3893.

Satô, Y., 1958. Attenuation, dispersion, and the wave guide of the G wave. Bull. Seis. Soc.Am., 48, 231-251.

Scheibner, E., 1973. A plate tectonics model of the paleozoic tectonic history of New South Wales. J. Geol. Soc. Aust., 20, 405-426.

Sherburne, R.W., 1975. Crust-mantle structure in continental South America and its relation to sea floor spreading. Ph.D. thesis, Pennsylvania State University, 145 pp.

Smith, M.L. and Franklin, J.N. 1969. Geophysical application of generalized inverse theory. J. Geophys. Res., 74, 2783-2785.

Smith, S.W., 1972. The annelasticity of the mantle. In Ritsema, A.R., ed., The Upper Mantle, Tectonophysics, 13, 602-622.

Solomon, S.C., 1972. Seismic-wave attenuation and partial melting in the upper mantle of North America. J. Geophys. Res., 77, 1483-1502.

Stauder, W. and Bollinger, G.A., 1966. The S-wave project for focal mechanism studies, earthquakes of 1963. Bull. Seis. Soc. Am., 56, 1363-1371.

Starr, A.T., 1928. Slip in a crystal and rupture in a solid due to stress. Proc. Cambridge Phil. Soc., 24, 489-499.

Stephenson, B.R. and Murray, K.J., 1970. Application of the strain rosette relief method to measure principal stresses throughout a mine. Inst. J. Rock Mech. Min. Sci., 7, 1-22.

Thomas, L., 1969. Rayleigh wave dispersion in Australia. Bull. Seism. Soc. Am., 59, 167-182.

Umbgrove, J.H.F., 1947. The Pulse of the Earth, 2nd ed., Nijhof, The Hague.

Underwood, R., 1969. A seismic refraction study of the crust and upper mantle in the vicinity of Bass Strait. Aust. J. Phys., 22, 573-587.

Underwood, R., 1970. A large cooperative seismic experiment: Project BUMP. Aust. Phys., 7, 21-22.

Vine, F.J. and Matthews, D.H., 1963. Magnetic anomalies over oceanic ridges. Nature, 199, 947-949.

Walsh, J.B., 1968. Attenuation in partially melted material. J. Geophys. Res., 73, 2209-2216.

Wegener, A., 1929. Die Enstehung der Kontinente und Ozeane, 4th ed., Vieweg and Shon, Brauschweig.

Weissel, J.K. and Hayes, D.E., 1971. The Australian-Antartic discordence: New results and implications. J. Geophys. Res., 79, 2579-2587.

Wellman, P. and McDougall, I., 1974. Cainozoic igneous activity in eastern Australia. Tectonophysics, 23, 49-65.

Whitcomb, J.H., Allen, C.R., Gramany, J.D. and Hileman, J.A., 1973. San Fernando earthquake series, 1971: focal mechanics and tectonics. Rev. Geophys. Sp. Phys., 11, 693-730.

Wiggins, R.A., 1969. Monte Carlo inversion of body-wave observations. J. Geophys. Res., 74, 3171-3181.

Wiggins, R.A., 1972. The generalized inverse problem: implications of surface waves and free oscillations for earth structure. Rev. Geophys. Sp. Phys., 10, 251-238.

Wiggins, R.A., McMechan, G.A. and Toksöz, M.N., 1973. Range of earth structure non-uniqueness implied by body wave observations. Rev. Geophys. Sp. Phys., 11, 87-113.

Wilson, J.T., 1965. A new class of faults and their bearing on continental drift. Nature, 207, 343-347.

Worthington, M.H., Cleary, J.R. and Anderssen, R.S. 1974a. Upper and lower mantle shear velocity modelling by Monte Carlo inversion. Geophys. J. R. Astr. Soc., 36, 91-103.

Worthington, M.H., Cleary, J.R. and Anderssen, R.S., 1974b). Density modelling by Monte Carlo inversion - II comparison of recent earth models. Geophys. J.R. Astr. Soc., 29, 445-457.

Wu, F.T., 1972. Mantle Rayleigh wave dispersion and tectonic provinces. J. Geophys. Res., 77, 6445-6453.

Yoshii, T., 1975. Regionality of group velocities of Rayleigh waves in the Pacific and thickening of the plate. Earth Planet. Sci. L., 25, 305-312.

ADDITIONAL REFERENCES

Backus, G. and Gilbert, F., 1970. Uniqueness in the inversion of inaccurate gross earth data. Phil. Trans. R. Soc. London, A266, 123-192.

Forsyth, D.W., 1977. The evolution of the upper mantle beneath the mid-ocean ridges. Tectonophysics, 38, 89-118.

Stauder, W. and Mauchlin, L. 1976. Fault motion in the larger earthquakes of the Kurile-Kamchatka Arc and of the Kurile-Hokkaido Corner. J. Geophys. Res., 81, 297-308.

Toksöz, M.N., and Anderson, D.L., 1966. Phase velocities of long period surface waves and structure of the upper mantle. J. Geophys. Res., 71, 1649-1658.

Toksöz, M.N., Chinnery, M.A. and Anderson, D.K., 1967. Inhomogeniety in the earth's mantle. Geophys. J.R. Astr. Soc., 13, 31-59.

Weidner, D.J., 1974. Rayleigh wave phase velocities in the Atlantic Ocean. Geophys. J.R. Astr. Soc., 36, 105-139.